Enhanced Ultrasonic Techniques for Inspection of Pressure Tubes

Huan Zhao

Department of Electronic and Electrical Engineering

University of Strathclyde

A Thesis submitted for the degree of

Doctor of Philosophy

May 2019

Copyright

This Thesis is the result of the author's original research. It has been composed by the author and has not been previously submitted for examination which has led to the award of a degree.

Signed:

Date:

Acknowledgements

I would like to express my foremost gratitude to my supervisor Professor Anthony Gachagan for giving me the opportunity to do my PhD and providing invaluable guidance, patience and encouragement throughout my studies. I could have not finished this work without his support.

I would like to sincerely thank my co-supervisor Dr Gordon Dobie for his endless ideas to inspire me to do my research. Through his support, I was able to find a part-time job in the fourth year of my PhD that helped me to finish my study.

I gratefully acknowledge the Hawthorne PhD Studentship, which fully funded my PhD for three years.

I would like to extend my thanks to Dr Richard O'Leary, who helped me for my modelling work with tremendous patience. Thanks especially to Dr Timothy Lardner, Dr Jerzy Dziewierz, Dr Jeff Dobson, Dr Gongzhang Rui and Dr Bo Xiao who I worked with intensively and shared me with useful knowledge. Thanks to John Mackersie, Tommy McCunnie, Alexander Ward and Walter Galbraith for their technical support with my experiments. Thanks to Lynn Morrison and Rhona Nicholson for their very kind support.

My gratitude extends to all my colleagues in CUE. Thanks to Dr Carmelo Mineo, Dr Marcus Ingram, Dr Zhen Qiu, Dr Haoyu Fang, Dr Jie Gao, Xiaotong Li, Botong Zhu and Shuang Chen for sharing invaluable experience and knowledge with me.

Special thanks to Mrs Anne-Marie Hughes who is always friendly and encouraging either in running club or gym class that made me stronger both physically and mentally.

I would like to thank my friend Dr Mengni Long. It is her experience inspired me to do a PhD and she provided huge support since the application and valued suggestions when I encountered challenges. Thanks to my friends Fen Wang, Yunxia Tu, Mie Wang and Shengwen Wang for their support and sharing of thoughts.

I would like to thank my Master supervisor Professor Yuenong Fei. It is his dedicated attitude to work and his spirit of pursuing new knowledge that has deeply affected me.

I would like to thank my friends Dr Hongling Liang, Gary Steele and Pisco who treated me like a family that helped me feel warmth in the Scottish weather.

Finally, I would like to thank my family for their endless love and letting me do what I want to do.

Abstract

Pressure tube inspection within CANDU nuclear reactors is a critical maintenance operation to identify and track the growth of defects. Current inspection approaches utilising ultrasonic techniques are technically challenging due to transducer alignment caused by the tube dimensional changes. This Thesis focuses on enhancing ultrasonic techniques to improve the inspection accuracy by introducing signal processing algorithms and phased array technology. This work is motivated by the nuclear industry desire to reduce the time and cost consuming replica processes.

The Synthetic Aperture Focusing Technique (SAFT) has been applied to industrial inspection data where the ultrasonic image performance is poorly-focused. The transducer focal point operates as a virtual source to transmit ultrasound with a corresponding beam angle. Subsequently, the refocused image demonstrates a distinct improvement in the measurement of defect width. Regarding to the defect depth measurement, this Thesis proposes a wavelet analysis method, which employs the Haar wavelet to decompose the original poorly-focused A-scan signal and reconstruct the defect information from selected frequency components within the transducer operational bandwidth. Compared to the original image characterisation, this method provides an improved estimate of defect depth within an acceptable error ±0.04 mm.

A hybrid simulation platform for ultrasonic phased array transducer inspection has been developed and experimentally validated, which combines the benefits of finite element modelling and analytical extrapolation. This approach has been used to study a range of phased array imaging solutions based on both the Total Focusing Method and array SAFT processing. The phased array technique is predicted to improve the accuracy of characterising defects on the inner and outer surfaces of the pressure tube and a dual array system incorporating 32-element 5 and 10 MHz arrays is proposed as a potential future sensor head configuration. The results conclude there is significant potential to improve the quality of the inspection data.

Contents

List of Figures

List of Tables

Abbreviations

aID	axial Inner Diameter
aOD	axial Outer Diameter
APC	Axial Pitch-Catch
ATF	Acoustic Transfer Function
BPF	Bearing Pad Fretting
CAFA	Combined Analytical Finite element model Approach
CANDU	CANadian Deuterium Uranium
cID	circumferential Inner Diameter
CIGAR	Channel Inspection and Gauging Apparatus for Reactors
cOD	circumferential Outer Diameter
CPC	Circumferential Pitch-Catch
CUE	Centre for Ultrasonic Engineering
DAS	Dealy-And-Sum
DF	Debris Fretting

FBH	Flat-Bottom Holes
FE	Finite Element
FMC	Full Matrix Capture
FT	Fourier Transform
ID	Inner Diameter
LISA	Local Interaction Simulation Approach
LSM	Linear Systems Model
NB	Normal Beam
NDE	Non-Destructive Evaluation
NDT	Non-Destructive Testing
OD	Outer Diameter
OECD	Organisation for Economic Co-operation and Development
PCI	Phased-Coherent Imaging
PHTS	Primary Heat Transport System
PHWR	Pressurized Heavy-Water-Moderated and Cooled Reactor
PML	Perfectly Matched Layer
POD	Probability of Detection

ROI	Region of Interest
SAFE	Semi-Analytical Finite Element
SAFT	Synthetic Aperture Focusing Technique
SCI	Spatial Compounding Imaging
SDH	Side-Drilled Holes
SNR	Signal to Noise Ratio
STFT	Short Time Fourier Transform
TFM	Total Focusing Method
TOFD	Time of Flight Diffraction
WA	Wavelet Analysis
WB	Waved Based

Symbols

F_N	Force
m	Mass
a	Acceleration
$\mathrm{y}(x,t)$	Wave function
$v_{\mathrm{y}}(x,t)$	Transverse velocity
$a_{\mathrm{y}}(x,t)$	Acceleration of particle
k	Wavenumber
ω	Angular frequency
c	velocity of the wave propagation
c_L	Longitudinal wave velocity
c_S	Shear wave velocity
c_w	Wave velocity in water
c_{t}	Wave velocity in tube
E	Young's modulus

ρ	Density of the material
σ	Poisson’s ratio
Z	Acoustic impedance
I	Wave intensity
μ	Wave attenuation coefficient
A	Wave Amplitude
λ	Wavelength
T_{coef}	Wave transmission coefficient
R_{coef}	Wave reflection coefficient
T	Thickness of piezoelectric material
d	Size of elements
D	Diameter/Aperture of a transducer
α_h	Half angle of beam divergence
H	Element height of array transducer
p	Pitch of array transducer
e	Element width of array transducer
g	Spacing between array elements

N_{field}	Near field length
N	Number of array transducer elements
S_{SAFT}	Summed echo signal for SAFT processing
WT	Wavelet transform
ψ	Mother wavelet
a_{wt}	Scale parameter of wavelet transform
b_{wt}	Shift parameter of wavelet transform
A_{WT}	Approximation of wavelet transform
D_{WT}	Detail of wavelet transform
S_{WT}	Decomposition signal of wavelet transform
T_d	Time delay
n	Refraction index
$\mathcal{F}$	Fourier transform
$\mathcal{F}_\tau$	Short Time Fourier Transform

Chapter 1

Introduction

1.1. Project Context

As the world's population increases, the demand for energy is also increasing significantly. Since the first commercial nuclear station started operation for the supply of electrical power in the 1950s, nuclear energy has become one of the most important energy industries that contributes hugely to the supply of carbon-free electricity. In 2017, the world nuclear energy consumption was 596.4 million tonnes of oil equivalent[1]. Nuclear power stations provide 18% of the electricity to Organisation for Economic Co-operation and Development (OECD) countries[2] and contributed to 10.3% of the world electricity consumption[3].

Nuclear reactors are the core of the nuclear power plants for electricity generation. Currently, there are 448 commercial nuclear reactors under operation across the world, which provide 391,721 MWe of total net capacity and an additional 59 reactors are under construction[4]. In the operational reactors, 49 of them are Pressurized Heavy-Water-Moderated and Cooled Reactor (PHWR), which are fuelled by natural uranium and use heavy water (deuterium oxide D_2O) as its coolant and moderator[5].

The CANadian Deuterium Uranium (CANDU) reactor is a type of PHWR. Using the same basic principle as other types of nuclear reactors, it produces heat by splitting uranium atoms and then converts the heat into electricity. The specific feature of the CANDU reactor is that it uses heavy water to assist the fission process, which keeps a continuous nuclear reaction. The pressure tubes of the CANDU reactor can be visualized from Figure 1.1, and shows the CANDU reactor core[6] that consists of 380 to 480 horizontal fuel channels.

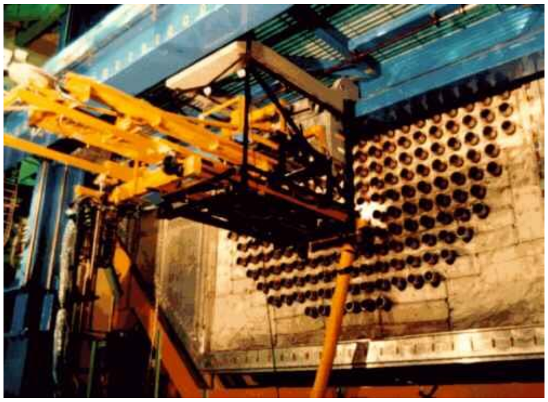

Figure 1.1 Fuel channels of CANDU reactor[6]

The fuel channels are part of the Primary Heat Transport System (PHTS) within a CANDU reactor, which are the places that the coolant flows through the fuel bundles to transport the nuclear heat to the stream generators[7]. They are the most significant feature of the CANDU design aiming at executing their function for 30 years and play the key role to maintain the reliability of the reactor performance. Therefore, regular inspection of the fuel channels is particularly important to ensure their condition is qualified for their intended function. A fuel channel mainly consists of a pressure tube, two end fittings and four annulus spacers, where the pressure tube is surrounded by a calandria tube and they are separated through the use of the annular spacers. The process of the general configuration of the fuel bundles passing through a pressure tube is shown in Figure 1.2[7].

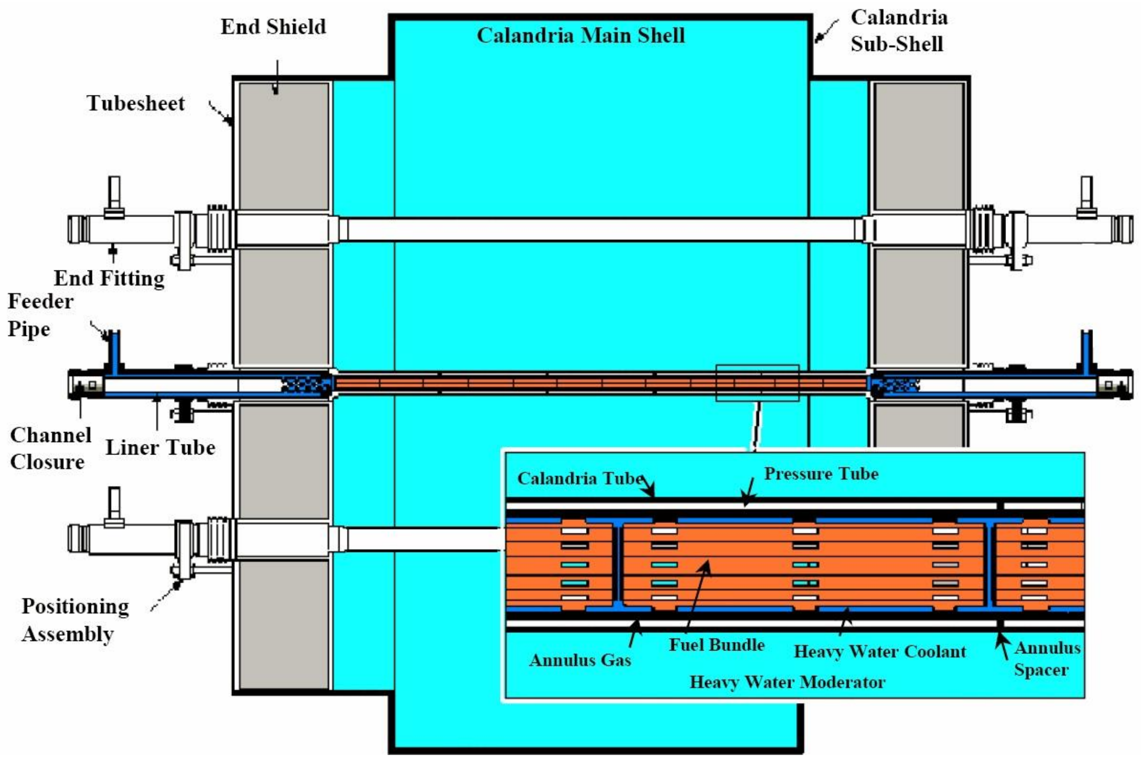

Figure 1.2 Schematic of the general configuration of fuel bundles passing through a pressure tube[7]

As the key component of the fuel channel, the zirconium alloy (Zr-2.5%Nb) pressure tubes are used to locate the fuel bundles for the reaction and support the coolant passing through to remove the heat from the fuel. The zirconium alloy has the features of low capture cross-section for thermal neutrons, which combines with its good corrosion properties to bring benefits for use in water reactors[8]. The pressure tubes are about 6.3 m long, 104 mm inner diameter and 4.3 mm wall thickness. During the operation, they are exposed to a pressure of approximately 10 MPa and at a temperature ranging from approximately 250℃ to 310℃[9]. Due to the harsh environment of high temperature, pressure and neutron flux, the tube dimensions can alter during service, for example axial elongation, diametric expansion, sagging and wall thinning. Hence, the inspection of the pressure tubes faces environmental and automation challenges in order to provide a high level of inspection accuracy.

The fuel channel inspection is executed by a tool named Channel Inspection and Gauging Apparatus for Reactors (CIGAR)[6], as shown in Figure 1.3, which is a remotely automated inspection system including an ultrasonic sensor head for pressure tube defect detection and wall thickness and diameter measurements, an eddy current system for detecting the annular spacers and measuring the spacing between pressure tube and the calandria tube, and a servo-accelerometer for estimating the sag of the fuel channels[10]. The ultrasonic transducers are located in the red circle in Figure 1.3.

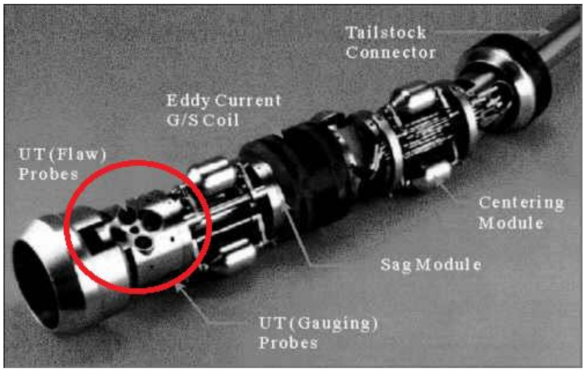

Figure 1.3 CIGAR sensor head with red circle indicating ultrasonic devices[6]

1.2. Project Overview

1.2.1. Background

This PhD project investigated ways to improve the ultrasonic inspection of CANDU pressure tubes through two avenues: simulating ultrasonic phased array transducer technology to replace the current sensor head (Figure 1.3) which uses multiple single element transducers; and exploring signal processing methods to enhance the reliability of the current industrial inspection data.

The most common defect found in the pressure tubes are Bearing Pad Fretting (BPF) defects resulting from the fuel bundle vibration during transportation and Debris Fretting (DF) defects due to the wear caused by debris such as a weld electrode or spatter[9]. Other defect types, for example, crevice corrosion marks, erosion-corrosion defects, mechanical damage flaws, manufacturing defects, also produce detrimental effects on the performance of the pressure tubes.

Currently, the ultrasonic sensor head applied for pressure tube inspection is comprised of 6 single element focused transducers, where one of them has a central frequency of 20 MHz and the others are 10 MHz transducers[6][11][12]. All the transducers are immersed in heavy water during the operation. As shown in Figure 1.4, the 20 MHz transducer and one 10 MHz transducer are working on pulse-echo mode for the tube Inner Diameter (ID) surface and Outer Diameter (OD) surface inspection (Figure 1.4 (a) and (d)), respectively. A pair of 10 MHz shear wave transducers situated in the circumferential direction (Figure 1.4 (b)) are working on full skip pitch-catch mode for defect detection on the tube ID and

OD surfaces, while another shear wave pair scan along the axial direction (Figure 1.4 (c)). The 20 MHz transducer is focusing on the tube ID surface. Regulation dictates full tube inspection of ID and OD surfaces are necessary, while the ID surface is of particular interest as this is where defects occur – notably bearing pad fretting and debris fretting[9][11].

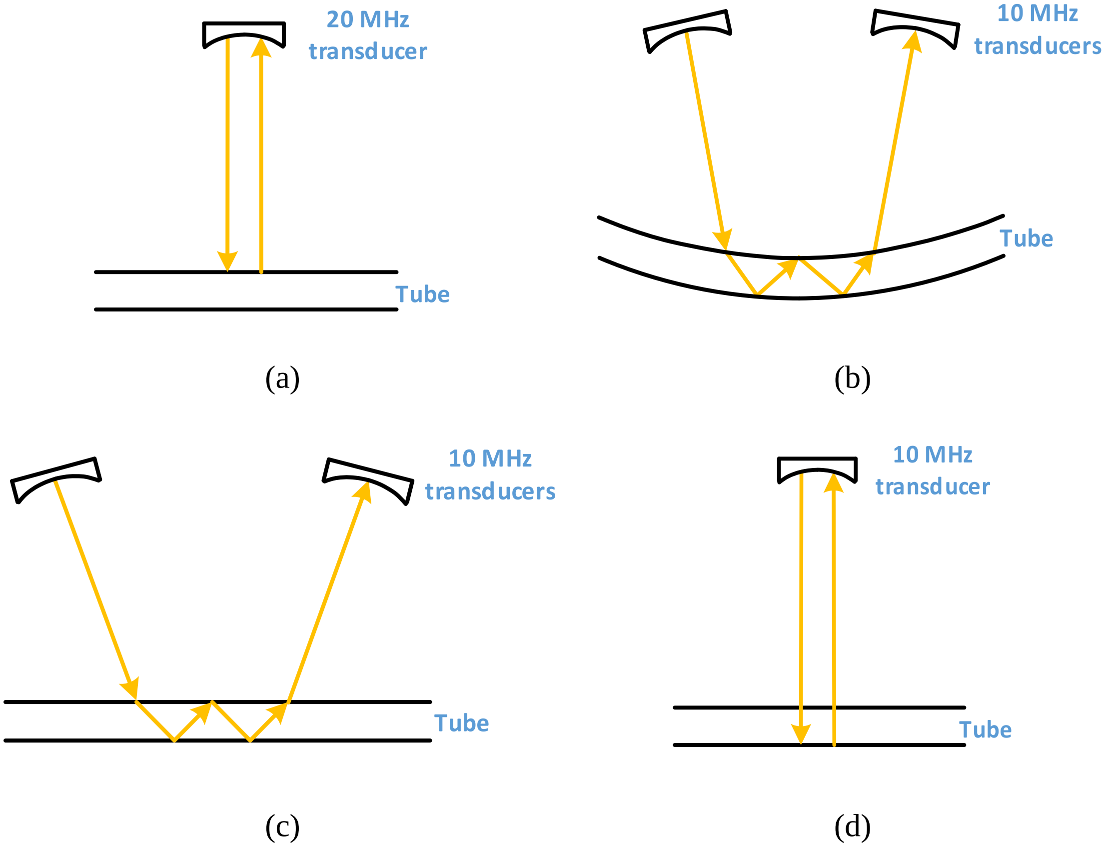

Figure 1.4 Schematics of ultrasonic inspection of CANDU pressure tubes using CIGAR Sensor Head (a) ID inspection; (b) circumferential material inspection; (c) axial material inspection; (d) OD inspection

An Analyst specialises in evaluation of the ultrasonic inspection data and follows this general process.

- In terms of the defect depth measurement
    - if the measurement result is bigger than 0.1 mm, it will be flagged as ‘reportable’.
    - if the measured defect depth is greater than 0.15 mm, it should be flagged as ‘dispositionable’, which means further action such as replication must be taken to provide more information for result validation[12][13].
    - when the defect depth exceeds 2 mm (about half of the tube thickness), the tube will be removed from the reactor.
    - the inspection accuracy is described as a measurement error either within 0.04 mm or below 5% of the actual defect depth.
- With regard to defect width and length
    - the accuracies are expected to have a 0.5 mm accuracy on the defect size or an uncertainty of 5% to 10 %[9].
- A combination of all the size information is used to analyse short length and high depth defects.

One important aspect in this inspection process is the requirement for replicas to be taken of defects which are difficult to classify[12][13]. This is time consuming and can become a significant burden on the operational downtime of the nuclear reactor associated with an inspection outage. Hence, the potential to improve defect classification accuracy would have the additional benefit in a reduction requests from an Analyst for the replication process to be deployed.

1.2.2. Motivation

The pressure tubes are operated in an environment of high temperature, high pressure and radiation flux that leads to dimensional changes in length and diameter[7][10]. One example is tube sag as a result from the weight of the fuel bundle and heavy water. Such dimensional changes make it difficult for the current ultrasonic inspection to be implemented as designed, which affects the accuracy of the measurement and results in additional replica processes. For example, the 20 MHz transducer focus is intended to inspect the tube inner surface, but as the device is held rigidly in the sensor head, then any dimensional deviation in the tube will result in the transducer focus not being on the desired tube wall surface. The question that this Thesis will address is whether the application of signal processing to the data from such poorly-focused inspection scenarios could improve the quality of the data presented to an Analyst and hence, improve the accuracy and repeatability of the defect quantification process.

Considering the high requirements associated with the defect size measurement specification, an improvement in ultrasonic inspection is strongly desired for both time and cost savings. For more than ten years, ultrasonic phased array technology has been applied in the nuclear power industry for reactor components inspection[14][15]. Due to the composition of an array of small elements, which can independently transmit and receive ultrasonic signals, it is able to electronically steer the sound beam in different directions and can therefore be a substitute approach mimicking several transducer configurations. Moreover, this technology has become a foundation of many sophisticated signal processing algorithms[16][17], which can offer enhanced performance in terms of defect detection and characterization[18][19]. This Thesis will explore the operational flexibility offered by a phased array transducer inspection configuration and analyse its potential to improve the defect/feature detection accuracy for the CANDU pressure tube inspection scenario. Moreover, it also has the potential to overcome the poorly-focused problem, resulting from tube dimensional changes, in the current sensor system implementation.

In terms of researching the application of phased array technology in the pressure tube inspection, simulation methods offer a convenient approach with minimum expense to determine potential solutions to improve inspection accuracy. Generally, in a finite element model, the number of the wavelength exceeding 100 will cause accumulated errors which significantly affect the model’s convergence. Due to the high frequency ultrasound used in this application, propagation path lengths in excess of 169 wavelengths require to be simulated. This can be challenging to combine both high resolution around the areas of interest (transducer and component) and accommodation these long path lengths. Hence, a hybrid modelling platform will be developed.

Overall, there is a great potential to employ ultrasonic phased array technology combining advanced post-processing algorithms in future sensor deployment configurations used in the pressure tube inspection. However, there is also a need to improve the quality of acquired field inspection data using the current sensor head. These two topics will now be addressed in this Thesis, with the aim to provide high quality information to support the important role of the Analyst in the inspection cycle.

1.3. Knowledge Contribution

- A novel method applying SAFT on single element focused transducer to correct the poorly-focused industrial data has been developed. The main contribution is the concept to use SAFT on the CIGAR focused transducer datasets where the target area is located a short distance beyond the natural focal point of the transducer. Importantly, an investigation into the effect of focal length value on algorithm performance has demonstrated that using an appropriate focal length value leads to a matched synthetic aperture curvature, which improves image focusing with respect to the original poorly-focused B-scan image.
- A modification to the wavelet analysis method has been applied to extract defect depth information from the poorly-focused industrial data. The main contribution is to take advantage of the high frequency component of the filter which has not been used previously, since most wavelet analysis applications for noise reduction and characteristic detection are based on the low frequency components.
- A hybrid simulation method to model the pressure tube inspection both for single element transducer and phased array transducer has been developed. The main contribution is to combine the FE method and analytical extrapolation to solve the

dispersion problem caused by high frequency transducer and long wave propagation distances. This multi-stage modelling approach provides the platform to investigate pressure tube inspection scenarios.

- A new scheme for phased array transducer inspection of pressure tubes has been developed using the hybrid simulation methodology. The main contribution is to provide appropriate imaging algorithms covering both ID and OD surfaces on axial direction as well as circumferential direction, combined with the full-skip TFM for defect feature detection.
- A novel analytical time map calculation for the TFM algorithm has been developed to accommodate wave propagation through this two-layer system (heavy water and pressure tube).
- An array SAFT processing algorithm is developed to improve the inspection accuracy. The main contribution is to calculate the synthetic aperture area for different array inspection configurations.

1.4. Publications

The author has presented the research work at three high regarded conferences and the following have been published in the proceedings of these conferences.

- H. Zhao, A. Gachagan, G. Dobie, C. Wallace, and G. West, “Synthetic Aperture Focusing Technique for Correction of Poorly-Focused Ultrasonic Pressure Tube Inspection Data,” in *9th European Workshop on Structural Health Monitoring Series*, 2018, p. 12.

- H. Zhao, A. Gachagan, G. Dobie, and T. Lardner, “Wavelet Analysis of Poorly-Focused Ultrasonic Signal of Pressure Tube Inspection in Nuclear Industry,” in *44th Annual Review of Progress in Quantitative Nondestructive Evaluation*, 2018, p. 9.
- H. Zhao, J. Dobson, A. Gachagan, T. Lardner, and G. Dobie, “Hybrid simulation model of ultrasonic inspection of pressure tubes in nuclear industry,” in *55th Annual Conference of the British Institute for Non-Destructive Testing*, 2016, p. 10.

1.5. Thesis Structure

The Thesis is organized over six Chapters.

The ultrasonic NDT theory including phased array technology and a number of signal processing techniques and simulation methods are reviewed in Chapter 2. This starts with the ultrasound fundamentals from the wave equation through to signal to noise ratio definition. Next, the basics of ultrasonic transducers and the testing system are presented in detail. Followed by an overview of the phased array imaging algorithms and signal processing techniques, such as wavelet analysis and SAFT, used in this Thesis. Finally, finite element analysis and hybrid simulation methods are reviewed.

In Chapter 3, the signal analysis and processing of industrial data is described to deal with the poorly-focused problem during the inspection caused by tube dimensional changes. A SAFT algorithm for application with focused transducers is introduced to improve the defect width measurement, where the relationship between the focal length and the curvature of synthetic aperture is analysed. Likewise, a wavelet analysis method is introduced to extract the defect depth information from the poorly-focused signal by considering the high frequency components. Moreover, the application of different wavelets are also discussed.

In Chapter 4, the hybrid simulation platforms for a single element transducer inspection and a phased array transducer inspection are both presented. The methodology to decompose a large model into a combination of FE method and analytical extrapolation aspects are explained. The phased array inspection model can generate FMC data, with a number of configurable parameters, such as the number of elements and transducer operational frequency. In addition, both hybrid simulation methods are experimentally validated.

The analysis of the future inspection scenarios using phased array sensor systems are presented in Chapter 5. Two array transducers are utilized to replace the current single element transducers with five display modes including axial and circumferential direct ID and OD images and axial full-skip image. The comparison of inspection results between single element transducer and array transducer is discussed. In addition, an array SAFT processing algorithm is demonstrated with the purpose to improve the inspection accuracy and a full-skip TFM algorithm is presented to identify defect features. A potential transducer configuration using phased array sensor system is discussed.

Chapter 6 presents a summary of the key results in the Thesis and includes a discussion on potential future work opportunities.

Chapter 2

Review of Ultrasonic Non-Destructive Testing

One of the main techniques in ultrasonic Non-Destructive Testing (NDT), also called Non-Destructive Evaluation (NDE), is applying ultrasound to perform an inspection on a test object, which does not result in damage to the object[20]. It can also measure other characteristics of the object, such as size, dimension or structure. Ultrasonic NDT is widely used in industry and plays an important role in the examination of materials throughout the component lifecycle; from the material state prior to processing through to in service inspection.

In this Chapter, the fundamental knowledge of ultrasonic NDT is introduced, including the ultrasonic transducer and the testing system, to give an overview of how it works for defect detection. The phased array technology and signal processing techniques are presented to show the potential improvement in inspection accuracy. At the end of the Chapter, the simulation methods of ultrasonic inspection are discussed.

2.1. Ultrasonic Non-Destructive Testing Basics

2.1.1. Ultrasound Fundamentals

Ultrasound is a mechanical wave with particles vibrated at frequencies of 20 kHz or above, which can not been heard by humans[21]. It has been applied broadly in science and engineering fields as a testing tool for many kinds of materials. This Section discusses the basic principles of ultrasound.

2.1.1.1. Wave Equation

The wave equation is a second-order partial differential equation and describes the motion of mechanical waves. Assume that a mechanical wave is propagating in an isotropic media within the elastic limit, the wave equation can be derived by Newton's second law given by Equation 2.1[22].

$$F_N = m\,a \tag{2.1}$$

F_N – Force, m – Mass, a – Acceleration.

Firstly, a wave function $\mathrm{y}(x,t)$ can be described in such a way (Equation 2.2) to express the displacement of any particle in a transverse wave. The wave function indicates the displacement of the particle at a particular position x and at time t.

$$\mathrm{y}(x,t) = A\cos(kx - \omega t) \tag{2.2}$$

where A is the amplitude of the particle movement, k is the wavenumber and ω is the angular frequency. Figure 2.1 displays a graphical representation of the wave propagation.

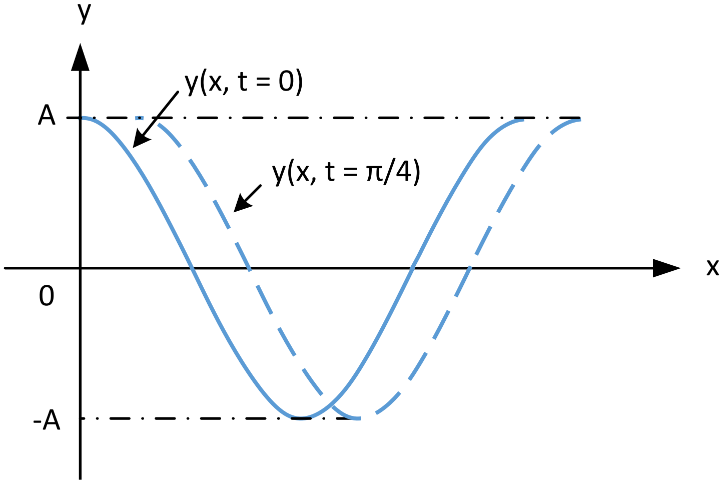

Figure 2.1 Graphical representation of wave propagation

The transverse velocity, $v_{\mathrm{y}}(x,t)$, can be derived by a partial derivative of the wave function with respect to t.

$$v_{\mathrm{y}}(x,t) = \frac{\partial y(x,t)}{\partial t} = \omega A \sin(kx - \omega t) \tag{2.3}$$

Then, the acceleration of any particle is the partial derivative of $v_{\mathrm{y}}(x,t)$ with respect to t:

$$a_{\mathrm{y}}(x,t) = \frac{\partial^2 y(x,t)}{\partial t^2} = -\omega^2 A \cos(kx - \omega t) = -\omega^2 \mathrm{y}(x,t) \tag{2.4}$$

On the other hand, calculating the partial derivatives of $\mathrm{y}(x,t)$ with respect to x indicates the slope of the wave at position x and at time t.

$$\frac{\partial y(x,t)}{\partial x} = -kA \sin(kx - \omega t) \tag{2.5}$$

The second partial derivative with respect to x is the curvature of the wave, which is given by:

$$\frac{\partial^2 y(x,t)}{\partial x^2} = -k^2 A\cos(kx - \omega t) = -k^2 \mathrm{y}(x,t) \tag{2.6}$$

Through equations 2.4 and 2.6 and considering the relationship $\omega = c\,k$ (where c is the velocity of the wave propagation),

$$\frac{\partial^2 y(x,t)/\partial t^2}{\partial^2 y(x,t)/\partial x^2} = \frac{\omega^2}{k^2} = c^2 \tag{2.7}$$

This equation can be rewritten as:

$$\frac{\partial^2 y(x,t)}{\partial x^2} = \frac{1}{c^2}\frac{\partial^2 y(x,t)}{\partial t^2} \tag{2.8}$$

The Equation 2.8 is called the wave equation that describes how a disturbance can propagate as a wave along an axis with a wave velocity of c. It is the fundamental equation for waves propagating in an isotropic material.

2.1.1.2. Wave Modes of Propagation

There are several modes of propagation associated with mechanical waves. For this work, the longitudinal wave and shear wave are the main waves considered to be relevant to the pressure tube inspection scenario. Longitudinal waves cause the particles of the media to vibrate parallel to the direction of the wave, whereas the particle motion associated with shear waves is perpendicular to the direction of wave propagation[23].

The velocities of the longitudinal wave and shear wave can be calculated from the elastic constants of the media, which are given by equations 2.9 and 2.10, respectively.

$$c_L = \left[\frac{E(1+\sigma)}{\rho(1+\sigma)(1-2\sigma)}\right]^{1/2} \tag{2.9}$$

$$c_s = \left[\frac{E}{2\rho(1+\sigma)}\right]^{1/2} \tag{2.10}$$

Where c_L is the longitudinal wave velocity, c_s is the shear wave velocity, E is Young's modulus (Nm^{-2}), ρ is the density of the material and σ is Poisson's ratio.

2.1.1.3. Transmission and Reflection

When an ultrasonic wave is perpendicularly incident on a boundary between two different media (from medium 1 to medium 2), some ultrasonic energy is transmitted into medium 2 and some is reflected directly back to medium 1[23]. The percentage of the energy transmitted and reflected is dependent on the acoustic impedance, Z, which is defined by Equation 2.11, associated with each medium.

$$Z = \rho\, c_L \tag{2.11}$$

where ρ is the density of the material and c_L is the longitudinal velocity of the wave.

The transmission coefficient T_{coef} defines the wave pressure which passes through the interface and continues to propagate in medium 2 and can be written as Equation 2.12[24].

$$T_{coef} = \frac{2Z_2}{Z_1 + Z_2} \tag{2.12}$$

The reflection coefficient R_{coef} is the proportion of incident pressure which is reflected back into medium 1 at the interface

$$R_{coef} = \frac{Z_2 - Z_1}{Z_1 + Z_2} \tag{2.13}$$

where Z_1 and Z_2 are acoustic impedances in medium 1 and medium 2 respectively.

2.1.1.4. Snell’s Law

When an ultrasonic wave is incident with an angle to a surface between two different media, it can produce both refracted and reflected longitudinal and shear waves[23]. This is following Fresnel equations that describe the light’s reflection and transmission when the light incidents on an interface between two media[25]. A rule describing the relationship between the angle of the refraction and the wave incidence angle is known as Snell’s law, which is derived from Fermat’s principle that states the optical path length of a light ray passing from point A to B is the length of the shortest optical path between the same point[26]. However, Snell’s law is valid for any stationary point rather than only the minimum time of flight. Figure 2.2 illustrates the refraction and reflection phenomenon when a propagating wave is incident at the interface between medium 1 (liquid) to medium 2 (solid). The following relationship relates to Snell’s law,

$$\frac{\sin\alpha}{c_{1L}} = \frac{\sin\beta_L}{c_{2L}} = \frac{\sin\beta_S}{c_{2S}} \tag{2.14}$$

where α, β_L and β_S are the incident angle, the refracted angle of the longitudinal wave and the refracted angle of the shear wave respectively. c_{1L} is the velocity of the incident longitudinal wave (in the liquid medium) and c_{2L} and c_{2S} are the velocities associated with the refracted longitudinal and shear waves in the solid medium.

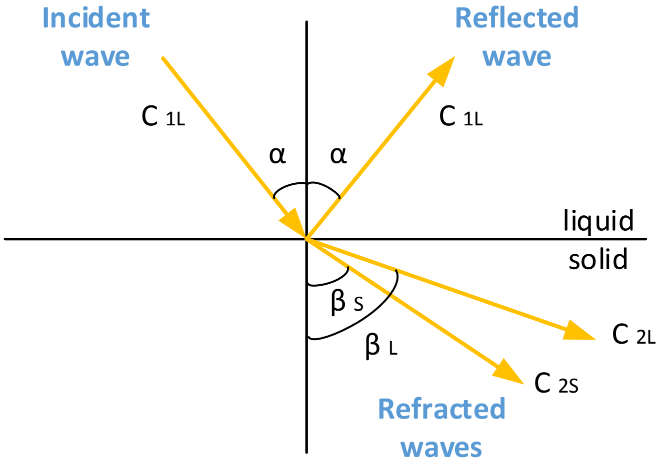

Figure 2.2 Illustration of wave transmission, reflection and refraction for an angled incident wave at the boundary between liquid and solid media

In the situation depicted in Figure 2.2, the critical angle indicates that the incident angle leads to a refracted angle which is 90 degrees, i.e. that particular refracted wave does not propagate within the solid medium itself. Regarding the situation in Figure 2.2, there are two critical angles associated with the longitudinal and shear refracted waves. When the incident angle increases to the first critical angle, the refracted longitudinal wave will converted to an interface wave[24]. Further increase to the incident angle will reach the second critical angle and at this point there will be no propagating waves within the solid medium. The incident wave will be either reflected or propagated as interface wave. The critical angle can be calculated by Snell's law, as described by Equation 2.14, with β_L or β_S equal to 90^o.

In addition, in terms of the transmission and reflection coefficients with an angle incidence, the reflection coefficient is present in Equation 2.15[27].

$$R_{coef} = \frac{1}{M}\left[\left(\frac{c_{2s}}{c_{2L}}\right)^2 \sin 2\beta_L \sin 2\beta_S + \cos^2 2\beta_S - \frac{Z_1}{Z_2}\frac{\cos\beta_L}{\cos\alpha}\right] \tag{2.15}$$

with the abbreviation

$$M = \left(\frac{c_{2s}}{c_{2L}}\right)^2 \sin 2\beta_L \sin 2\beta_S + \cos^2 2\beta_S + \frac{Z_1}{Z_2}\frac{\cos\beta_L}{\cos\alpha} \tag{2.16}$$

and the transmission coefficients for longitudinal wave and shear wave are described in Equations 2.17 and 2.18 respectively.

$$T_{coef\_L} = \frac{2}{M}\cos 2\beta_S \tag{2.17}$$

$$T_{coef\_S} = -\frac{2}{M}\left(\frac{c_{2s}}{c_{2L}}\right)^2 \sin 2\beta_L \tag{2.18}$$

where Z_1 and Z_2 are the acoustic impedances of liquid and solid respectively.

2.1.1.5. Ultrasonic Attenuation

Ultrasound propagates in a medium with an intensity which is reduced due to the effect of scattering and absorption[23]. Scattering is caused by the sudden change of the impedance at internal boundaries since any material is not ideally homogeneous inside and many are heterogeneous. When the wavelength of ultrasound is smaller than or similar to the material grain size, the waves may split into various transmitted and reflected wave types and the process will repeat at the next grain boundary, while a larger wavelength brings about wave transmission with deviated route. Therefore, the original waves are gradually converted into heat[27]. In terms of the absorption, it is a direct conversion of sound energy into heat which is mainly due to the oscillations of the material particles that relates to the ultrasonic frequency of the propagating wave [27].

The ultrasonic attenuation is described in Equation 2.19[23].

$$I = I_0 e^{-\mu s} \tag{2.19}$$

where I is the wave intensity at a distance s from an initial intensity I_0 and μ is the attenuation coefficient.

2.1.1.6. Signal to Noise Ratio

Signal to Noise Ratio (SNR) is used to compare the level of the received signal intensity with respect to the level of background noise. In the ultrasonic field, SNR is dependent on the frequency of the transducer[28]. When higher frequencies are utilized in an inspection, the energy density can be focused on a smaller point since they allow the generation of a tighter focal spot size. This leads to an increase of SNR in an idealised scenario ignoring the effects of attenuation and/or scattering. However, higher frequencies result in stronger scattering and oscillation due to shorter wavelength and fast vibration, which results in bigger signal attenuation.

SNR is often expressed using the logarithmic decibel scale due to many signals having a wide dynamic range[23][28]. Equation 2.20 describes SNR by utilizing signal intensity.

$$SNR = 10log_{10}\frac{I_{signal}}{I_{noise}} \tag{2.20}$$

I_{signal} – the intensity of the signal, I_{noise} – the intensity of the noise.

Because the acoustic intensity (or power) is proportional to $(\text{signal amplitude})^2$, when comparing the corresponding amplitudes, A_{signal} and A_{noise}, Equation 2.20 can be written as:

$$SNR = 20log_{10}\frac{A_{signal}}{A_{noise}} \tag{2.21}$$

2.1.2. Traditional Ultrasonic Transducers

2.1.2.1. Piezoelectric Effect

The piezoelectric effect was observed by Jacques Curie and Pierre Curie in 1880[29]. It is a property of piezoelectric materials related to when the material is subjected to external pressure, an electric charge is generated on the surfaces of the material. The converse of the energy conversion is called inverse piezoelectric effect. This characteristic of conversion between pressure and electrical signal domains is the foundation of piezoelectric ultrasonic transducers.

Figure 2.3 (a) and (b) graphically present the piezoelectric effect and inverse piezoelectric effect, respectively[30]. When an external pressure is applied to a piezoelectric material, electricity is produced. Conversely, applying an electrical signal to a piezoelectric material can lead to the generation of pressure. Importantly, the material shape will change due to the influence of Poisson's ratio.

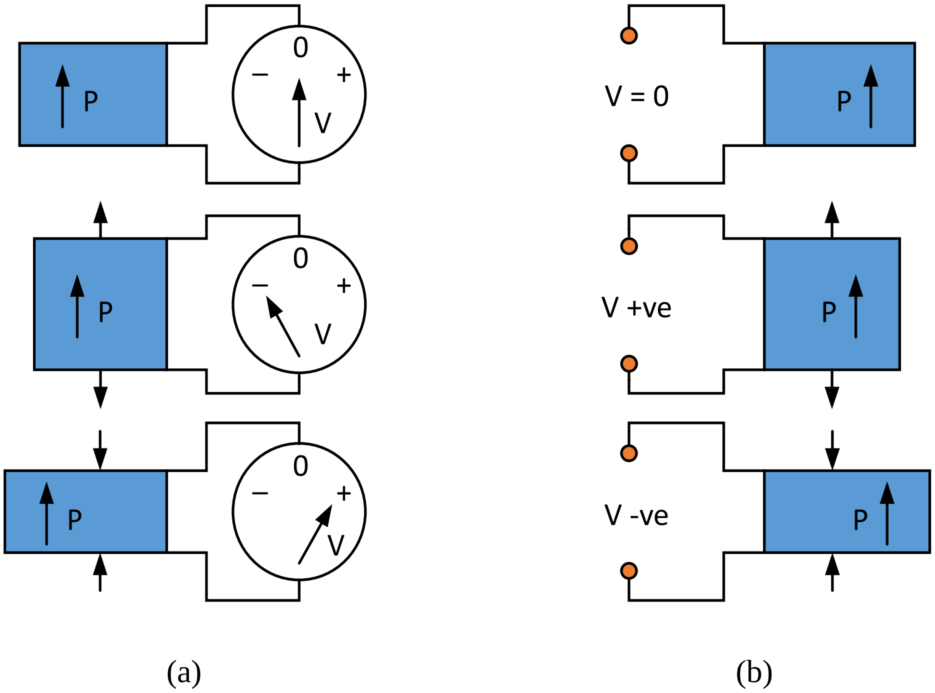

Figure 2.3 Graphical representation of the piezoelectric effect with P indicates the poling direction (a) Direct piezoelectric effect; (b) Inverse piezoelectric effect[30]

2.1.2.2. Piezoelectric Materials

Currently, piezoceramic is typically used as the piezoelectric material within a transducer structure[30]. The archetypal material is Lead Zirconate Titanate (PZT), which is applied in many forms. They can be divided into two groups, piezoelectrically hard and soft types. For example, PZT-4 is hard and PZT-5H is soft:

- the piezoelectric coefficients and permittivity of PZT-4 is lower than that of PZT-5H;

- PZT-4 is more suitable for the situation that high average output ultrasound intensities are necessary;
- PZT-5 is better for providing higher sensitivity as a transmitter and for applications using the device as both a transmitter and a receiver.

A modified form of the piezoelectric family, named a piezoelectric ceramic composite or piezocomposite, can be used to solve the mismatch problem of the acoustic impedance between piezoceramic and low acoustic impedance test objects[30]. Typically, piezoceramic elements are encapsulated within a polymer matrix to produce an active piezoelectric material with modified properties compared to the original piezoceramic material. There are three main types of dimensional connectivity which are 1-3 piezocomposite, 2-2 piezocomposite and 0-3 piezocomposite (Figure 2.4). Generally, m-n piezocomposite defines the dimensional connectivity of the piezoelectric ceramic (m, blue in Figure) and polymer (n, grey in Figure) phases.

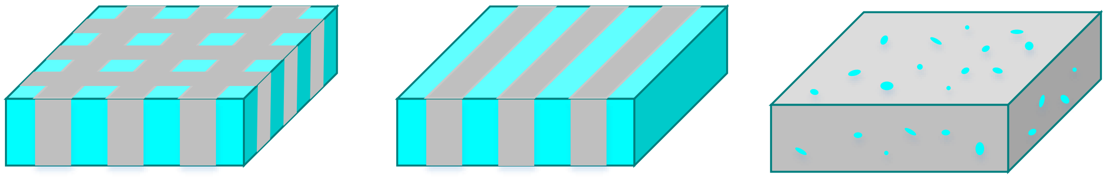
(a) 1-3 piezocomposite (b) 2-2 piezocomposite (c) 0-3 piezocomposite

Figure 2.4 Piezocomposite material structures[30]

2.1.2.3. Piezoelectric Transducers

In a piezoelectric ultrasonic transducer, there are two electrodes on the opposite faces of the piezoelectric material. When apply an electric field to the electrodes on the piezoelectric material, the polarised molecules of the material align with the direction of the field. The alignment will lead to a deformation of the piezoelectric material. If this electric field is time varying then the material vibrates and mechanical energy, propagating ultrasound waves, are generated[31].

The typical structure of a conventional ultrasonic transducer is shown in Figure 2.5. It primarily consists of a piezoelectric material, a backing material and a matching or wear layer[23][28]. The backing material is used to dampen the vibrational activity at the rear face of the transducer. Ideally, it should have similar acoustic impedance with the piezoelectric material to avoid reflections of the ultrasonic energy at the transducer/backing material interface and have a property of high absorption with respect to the frequency of the generated ultrasonic waves. The wear plate is utilized to protect the piezoelectric material from mechanical degradation and can also promote efficient transfer of energy between the piezoelectric element and the load medium. This wear layer is also known as a matching layer and usually has a thickness of a quarter of wavelength. As an approximation, the wavelength of the ultrasound λ can be determined from the thickness of the piezoelectric material, which is given by

$$\lambda = 2\,\mathrm{T} \tag{2.22}$$

where T is the thickness of the piezoelectric material.

In addition, the electrical connector connects the external cable and the piezoelectric material. A case houses the whole transducer. The electrical leads link piezoelectric material through internal wire interconnects to provide connection to external instrumentation. For many industrial applications, a protective workface prevents the transducer from damage.

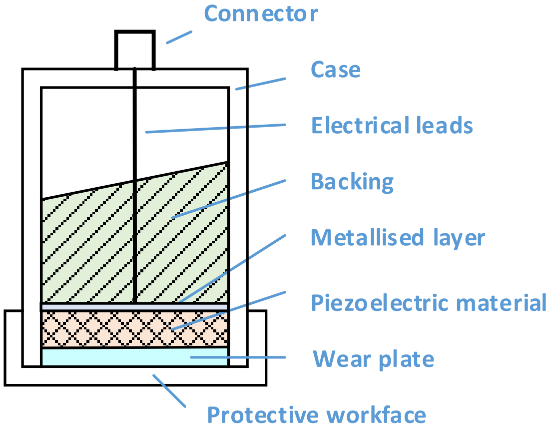

Figure 2.5 The structure of a conventional industrial ultrasonic transducer[23]

2.1.2.4. Transducer Performance

Ultrasound Field Characteristic

The ultrasonic waves transmitted from a transducer are not typically from a point source. For most applications, they originate from the surface of large aperture piezoelectric elements with respect to the ultrasonic wavelength. According to Huygens' principle, which states that every point on a wave-front may be considered as a source of secondary spherical wavelets[22], the ultrasonic field can be thought as a superposition of the wave-front. Effectively, there are two components generated by a regular plate or disc shaped piezoelectric element: a plane wave emitted from the surface of the material; and edge waves from the extremities of the element. These then interfere in the load medium and create areas of constructive and destructive interference close to the transducer. The generated ultrasonic field can be divided into near field and far field regions. In the near field, the interference is severe and it therefore can be difficult to obtain reliable information on the load characteristics. While in the far field, the ultrasonic energy decays steadily with increasing propagation paths. Hence, under ideal circumstances, the ultrasonic system would be configured to operate in this region. The length of the near field N_{field} is given by Equation 2.23[23].

$$N_{field} = \frac{D^2}{4\,\lambda} \tag{2.23}$$

where D is the diameter of the transducer, λ is the wavelength of the ultrasound.

Figure 2.6 illustrates the near/far field concept through an example ultrasonic field along the transducer central axis. This graph has been generated using a 1 MHz transducer with a diameter of 15mm and water as the load medium.

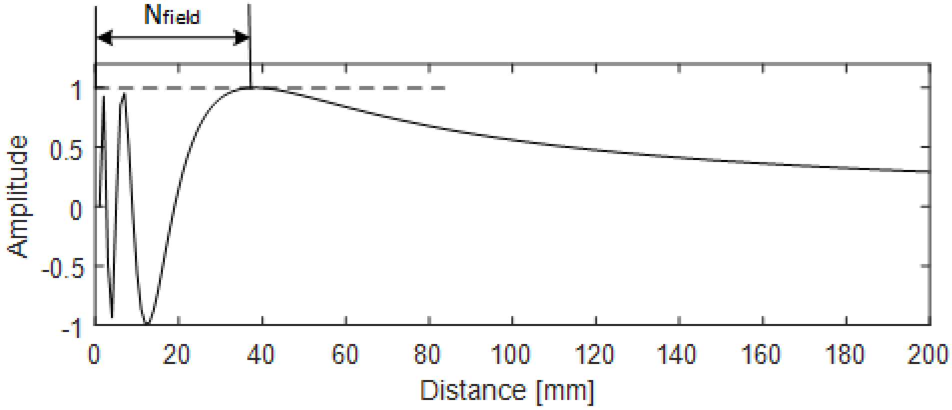

Figure 2.6 Ultrasonic field along the axis for a 15 mm diameter transducer, operating at 1 MHz in water

Beam Divergence

The energy of the waves does not only transmit directly in the direction of wave propagation, but will also spread into other angles. Beam divergence is a measure of this angular spread and is used to indicate the relative intensity distribution of the ultrasonic beam in the far field[24]. The half angle of the beam divergence α_h is defined using the following description. Construct a cylinder with the same diameter as the transducer and extend the cylinder from the transducer through the ultrasonic field. Where this cylinder intersects with the near field distance, N_{field}, is used to determine α_h. Take a 2-D case for example, as shown in Figure 2.7, the angle between the intersection beam and the centreline of the transducer is the half angle of the beam divergence.

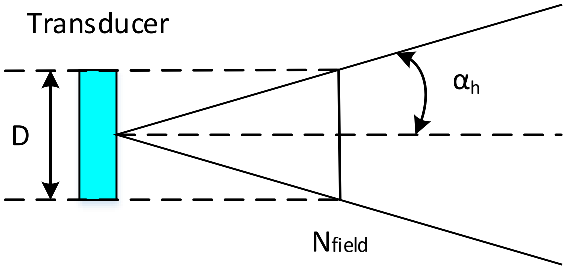

Figure 2.7 Illustration of ultrasonic beam divergence

The half angle of the beam divergence α_h can be calculated by Equation 2.24.

$$\sin \alpha_h = \frac{1.2\,\lambda}{D} \tag{2.24}$$

Side Lobes

In the ultrasonic field, there exists a main lobe and a number of unwanted side lobes. The main lobe is the beam on the primary path, which contains the main ultrasonic energy. Other unwanted radiations in undesired directions are called side lobes. The energy of the side lobes is normally much less than that of the main lobe.

Increasing the wave frequency f or the size of the piezoelectric element d will augment the number of side lobes[24]. Figure 2.8 shows the increased side lobes with the augment of d/λ ratio, where the ultrasound field in water is generated by a 1 MHz transducer. The main lobe can be seen in each of these images emanating directly from the top and centred around 0 on the x-axis. Directional energy outside of the main lobe can be considered side lobe activity. In order to decrease these unwanted side lobes, it is necessary to decrease the frequency f of the transducer as well as the size of the elements d.

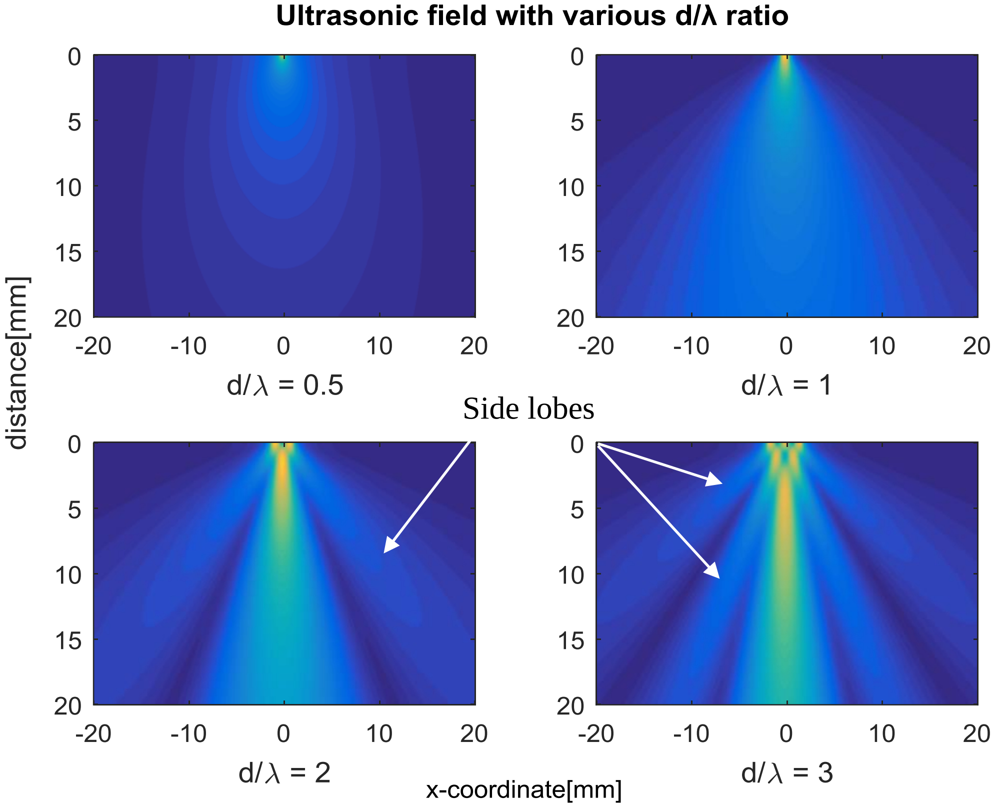

Figure 2.8 Ultrasonic field predictions with various d/λ ratio. The transducer is centred around 0 on the x-axis and located at the top of each image.

2.1.3. Ultrasonic Testing System

2.1.3.1. Basic Structure

A standard ultrasonic testing system consists of a user interface, a display, a pulser-receiver, an ultrasonic transducer, a motion controller and a scanner (the motion parts are applied in an automatic ultrasonic NDT system), as depicted in Figure 2.9. The user interface is a link between the operator and the testing system. Operators can use it to control the testing process. The display shows the ultrasonic echo signal indicating the internal structure of the test specimen. The pulser-receiver and the motion controller/scanner are utilized to control the generation of the ultrasound energy and control its delivery into the test specimen and subsequent acquisition of ultrasonic echoes.

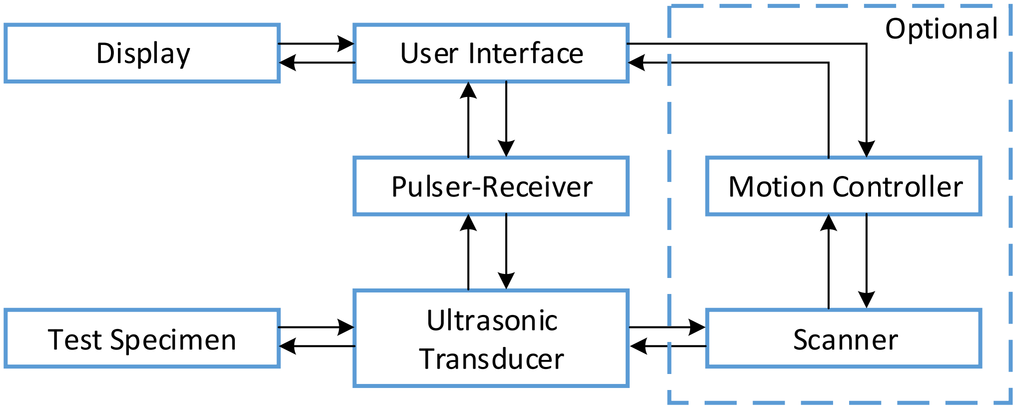

Figure 2.9 Basic components of an ultrasonic testing system

2.1.3.2. Testing Configurations

Pulse-echo and pitch-catch modes are the two main testing configurations in ultrasonic NDT.

In pulse-echo mode, a transducer transmits ultrasonic waves which travel through a test specimen until they interact with a feature or the boundary of the specimen[32]. The waves are reflected and scattered by such features and these echo waves are subsequently received by the same transducer, as shown in Figure 2.10 (a). Consequently, the size and location of the feature, which is typically a defect, are related to the amplitude of the echo signal and the time when the signal arrives at the transducer, now working as a receiver. The advantage of the pulse-echo technique is its ability to determine defects' position and height from a one-side inspection[33]. However, there is a disadvantage that it has low sensitivity for defects near the surface of the specimen in contact testing, called the dead zone, due to the coupling between the transducer and the specimen, and the transducer ring-down time.

In a pitch-catch mode, one transducer (also called transmitter) is utilized for transmitting ultrasonic waves into the test specimen and the echo signals are received by a second transducer (also called receiver). Figure 2.10 (b) presents an example of the pitch-catch inspection, where an angle wedge is typically used with each transducer to use refraction at the wedge/solid interface to generate or receive refracted waves after interaction with features in the sample[34]. In this case, the time delay before receiving an echo from a defect will be longer due to the increased propagation path between the two transducers and in many cases, the generation of shear waves in the sample. This is only one example of a pitch-catch inspection mode and the pair of transducers can be placed in many different positions, such as on the opposite side of the test specimen to facilitate through-thickness scanning[23].

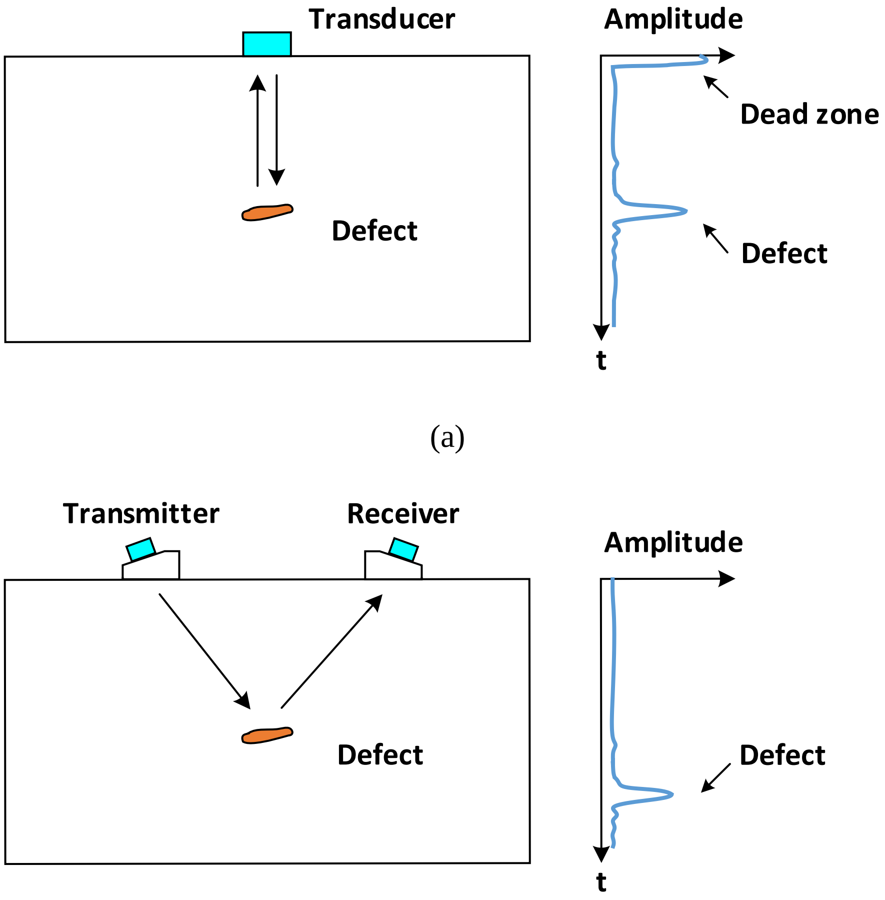

(a)

(b)

Figure 2.10 Common ultrasonic testing configurations (a) pulse-echo (b) pitch-catch

2.1.3.3. Scan Views

The ultrasonic signals can be presented in different display modes. In this Section, A-scan, B-scan, C-scan and D-scan display modes will be introduced.

A-scan mode presents the raw received ultrasonic energy as a function of time of flight. Figure 2.10 contains two examples of an A-scan on the right hand side of each image. The vertical axis indicate the time of the propagation of ultrasonic waves. The relative amount of the received energy (generally the amplitude of the quantized received voltage is used) are plotted along the horizontal axis. The distances between the defect and the transducer can be calculated by using the time of flight and the knowledge of the ultrasound velocity in the sample under investigation.

All of the B-scan, C-scan and D-scan display modes are 2-D views, effectively using multiple, raw A-scan ultrasonic signals in different ways, as illustrated in Figure 2.11[35]. The red axis (Ultrasound) indicates the time associated with ultrasound propagation, the green axis (Index axis) and the blue axis (Scan axis) correspond to the raster scan pattern moving the transducer over the sample surface.

In terms of a B-scan mode, the ultrasonic data is displayed as a side view of the test specimen. The horizontal axis is the index axis and the vertical axis is the ultrasonic path or time[35]. The amplitude of the received signal is presented by colour code of the image, while the defect is indicated by red colour in the Figure. Substantially, a B-scan is a collection of several A-scan signals. The size of a defect can be measured in a B-scan image by extracting high amplitude signals.

For a C-scan mode, the ultrasonic data is displayed as a top view of the test specimen. One of the axes is index axis (same as the horizontal axis of B-scan) and the other axis is the scan axis. The colour code of the image presents the maximum amplitude of the A-scan signal received at each position.

Regarding a D-scan mode image, the ultrasonic data is displayed as an end view of the test specimen. It is similar to B-scan that the vertical axis is the ultrasonic path or time but it uses the scan axis as the horizontal axis of the image. The amplitude of the received signal is presented in the same way as the B-scan image.

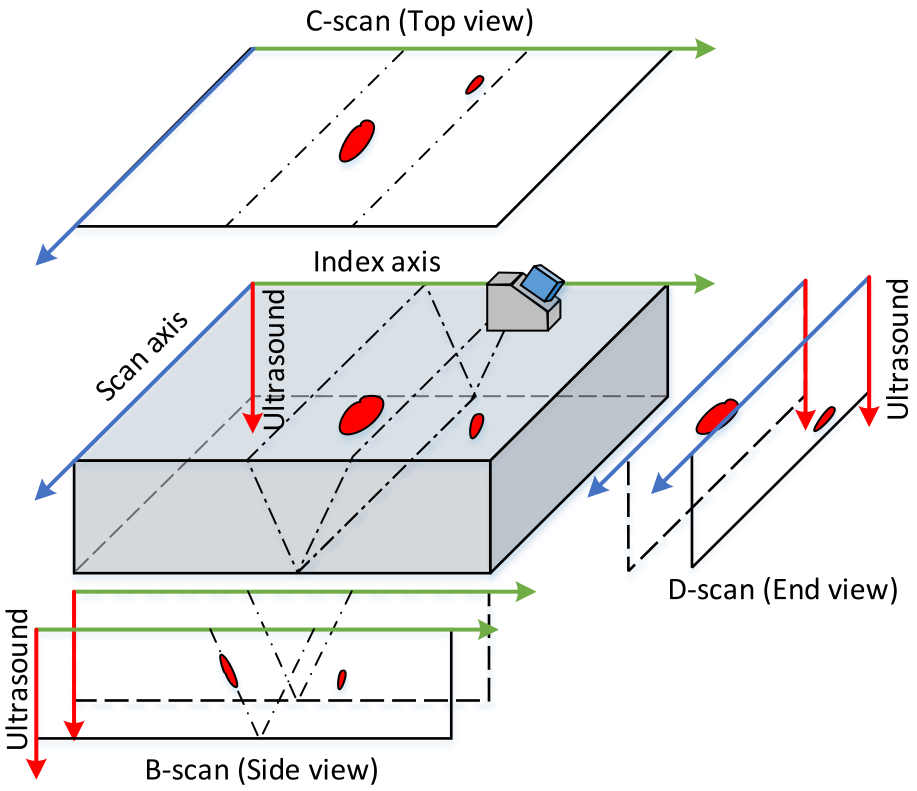

Figure 2.11 Scan views for B-scan, C-scan and D-scan illustrations for an ultrasonically inspected sample[35]

2.2. Phased Array Technology

Phased array technology was first used in radar and sonar fields. From 1980s, it started to be utilized in industrial NDT[35].

2.2.1. Principles

An ultrasonic phased array transducer has a number of individual piezoelectric elements, with commonly used number of elements for NDT applications ranging between 8 to 128. A typical 1-D linear array structure is shown in Figure 2.12, where e is the width of an individual element, H is the element height, g is the spacing between active elements, p is the pitch (centre-to-centre distance between the successive elements) and D is the aperture of the phased array transducer. Each element can be controlled independently to transmit and receive an ultrasonic signal. All the ultrasound energy generated by these elements can be steered and focused by setting relative transmission and reception times, known as a delay law[17][28]. Then, the wave front is specifically defined due to interference phenomenon in the ultrasonic field. When an ultrasonic array transducer is fixed in a single position, it can scan over different depths and angles of a sample using this electronic beam steering approach. Figure 2.13 demonstrates the normal and angular incidences of a focused beam from a phased array transducer generated by different delay laws.

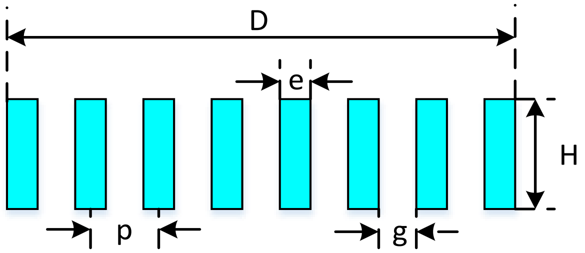

Figure 2.12 A typical 1-D linear array structure[35]

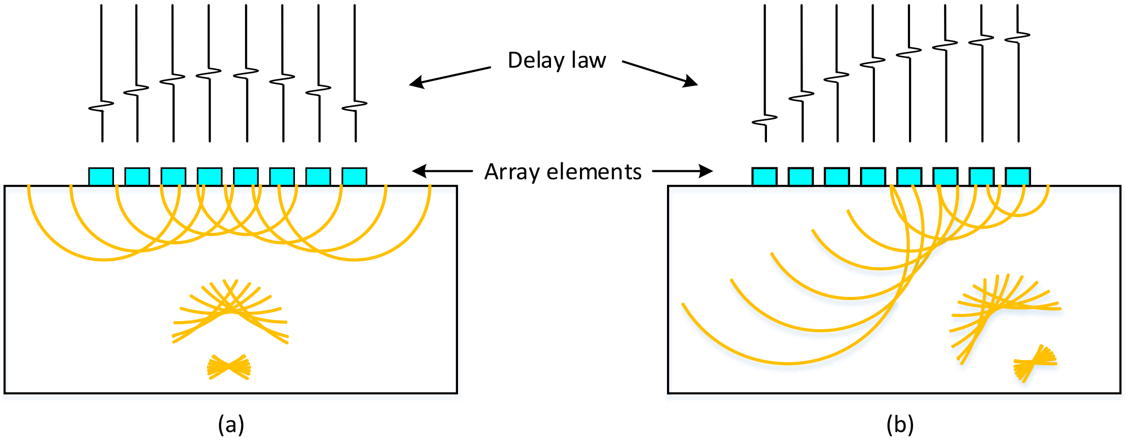

Figure 2.13 Beam focusing principle for (a) normal and (b) angular incidences[35]

The transducer can be expanded into a second dimension to create more advanced array configurations, including 2-D matrix array, cross array and circular array[16][35][36]. All these transducers provide additional operational flexibility compared to 1-D linear array, but simultaneously require more complex imaging methodology and significantly greater data processing time.

Comparing to conventional ultrasonic transducers, a special case of side lobes exists in the ultrasound generated by phased array transducers when the element pitch is greater than a half wavelength[31]. These special side lobes are called as grating lobes. Its production is due to a spatial aliasing effect, which causes some side lobes to become much larger in amplitude[35]. Importantly, the amplitude of these grating lobes can approach the level of the main lobe.

2.2.2. Phased Array Imaging

2.2.2.1. Imaging Techniques

There are many types of widely used phased array imaging techniques that are illustrated in Figure 2.14[18]. When all the array elements are triggered at the same time, the transmitted waves take a shape of a plane wave, which has the same performance as a single element transducer scanning on a straight line. Importantly, in this case, each receiver element individually acquires the returning echoes and provides additional spatial resolution compared to a single element transducer. This is called a plane B-scan (Figure 2.14 (a)). The focused B-scan (Figure 2.14 (b)) applies delay law to make the transmitted waves focus at a specific depth that works similar to a focused single element transducer, but has an advantage of focusing at desired depths. In terms of a single element transducer, the ultrasound energy focuses on a plane with a circular shape, while it focuses on a plane with an oval shape for a linear phased array transducer. The major axis of the oval focal region is along the transducer width direction and the minor axis is along the transducer elevation direction. A sector B-scan (Figure 2.14 (c)) is steering a range of angular beams through the test object, where each angular beam generates a scan line in the image. The Total Focusing Method (TFM) (Figure 2.14 (d)) focuses the beam at every point of the image and is implemented through post-processing.

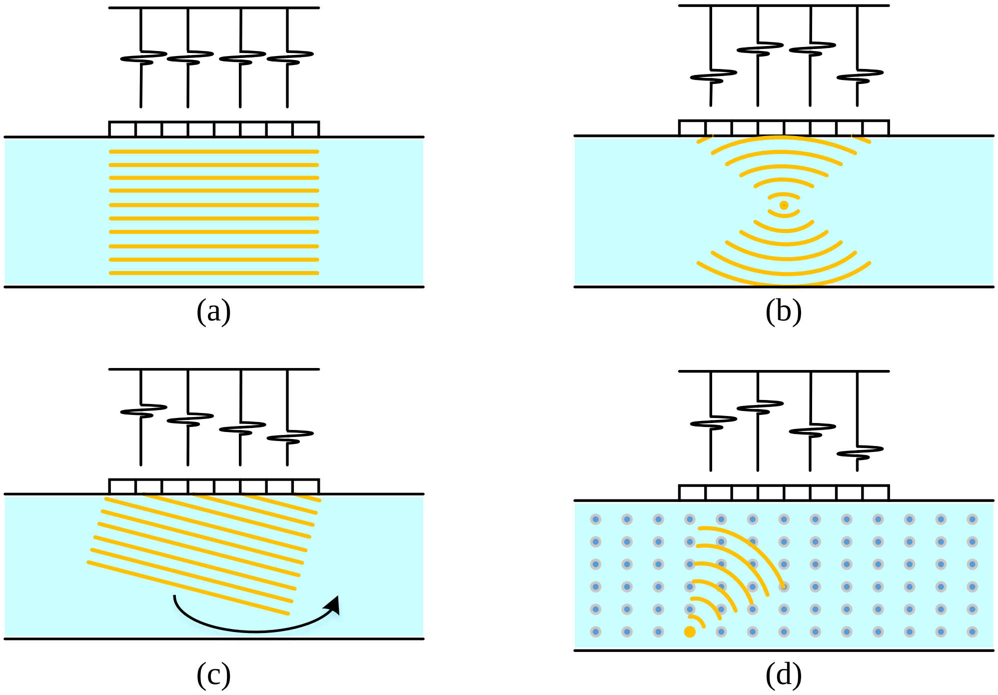

Figure 2.14 Phased array imaging techniques.

(a) plane B-scan; (b) focused B-scan; (c) sector B-scan and (d) fully focused TFM[18]

To generate a TFM image, an acquisition of Full Matrix Capture (FMC) data is required by triggering the first element of an array transducer to emit ultrasound into the load medium, receiving the echo signals by all the elements and then triggering the second element to repeat the process until all the elements have been triggered. TFM uses the echo data focusing at every point in a Region of Interest (ROI) to aggregate the effect from all the elements[18]. The intensity of the arbitrary pixel, $I(x,y)$, in the image in Figure 2.15 (a) is given by:

$$I_{TFM}(\mathrm{x},\mathrm{y}) = \sum_{\mathrm{i}=1}^{\mathrm{N}}\sum_{\mathrm{j}=1}^{\mathrm{N}} \mathrm{f}_{\mathrm{Tx,Rx}}\left(\frac{\sqrt{\left(\mathrm{x}_{\mathrm{Tx,i}}-\mathrm{x}\right)^{2}+\mathrm{y}^{2}}+\sqrt{\left(\mathrm{x}_{\mathrm{Rx,j}}-\mathrm{x}\right)^{2}+\mathrm{y}^{2}}}{\mathrm{c}}\right) \tag{2.25}$$

where N is the number of the elements of the array transducer, Tx means transmitter, Rx means receiver, $\mathrm{f}_{\mathrm{Tx,Rx}}(\mathrm{t})$ is the wave propagation function and c is the wave velocity in the test object. Here, the array transducer is assumed to be situated at coordinate $y = 0$.

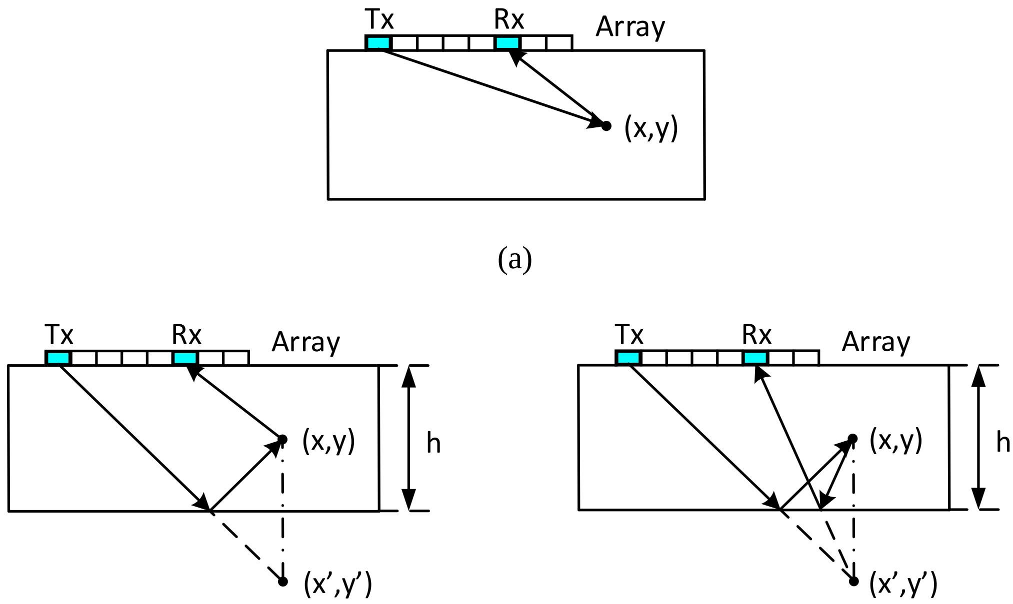

(b) (c)

Figure 2.15 TFM modalities (a) direct TFM; (b) half-skip TFM;(c) full-skip TFM

2.2.2.2. Multi-Mode TFM

Direct TFM, as illustrated in Figure 2.15 (a), directly uses the beam path towards and away from the ROI and produces good image for defect detection of vertical discontinuities. For defects situated at an angle, multi-mode TFM using either half-skip or full-skip approaches can be used to enhance information on the feature of interest[37][38][39].

Figure 2.15 (b) presents the half-skip TFM approach that calculates the transmitted wave through a reflection from the back wall and then the received wave is the direct path from the ROI. Considering the geometric symmetry of the image pixel to the back wall, the intensity of the pixel for the half-skip TFM is:

$$I_{HSTFM}(\mathrm{x},\mathrm{y}) = \sum_{\mathrm{i}=1}^{\mathrm{N}}\sum_{\mathrm{j}=1}^{\mathrm{N}} \mathrm{f}_{\mathrm{Tx,Rx}}\left(\frac{\sqrt{\left(\mathrm{x}_{\mathrm{Tx,i}}-\mathrm{x}'\right)^{2}+\mathrm{y}'^{2}}+\sqrt{\left(\mathrm{x}_{\mathrm{Rx,j}}-\mathrm{x}\right)^{2}+\mathrm{y}^{2}}}{\mathrm{c}}\right) \quad (2.26)$$

where $\mathrm{x}' = \mathrm{x}$, $\mathrm{y}' = 2 * (-h) - \mathrm{y}$, h is the thickness of the test sample.

Full-skip TFM is presented in Figure 2.15 (c) and receives both transmitted and received waves through a reflection from the back wall. The intensity of the image pixel for the full-skip TFM can be described by:

$$I_{FSTFM}(\mathrm{x},\mathrm{y}) = \sum_{\mathrm{i}=1}^{\mathrm{N}}\sum_{\mathrm{j}=1}^{\mathrm{N}} \mathrm{f}_{\mathrm{Tx,Rx}}\left(\frac{\sqrt{\left(\mathrm{x}_{\mathrm{Tx,i}}-\mathrm{x}'\right)^{2}+\mathrm{y}'^{2}}+\sqrt{\left(\mathrm{x}_{\mathrm{Rx,j}}-\mathrm{x}'\right)^{2}+\mathrm{y}'^{2}}}{\mathrm{c}}\right) \quad (2.27)$$

The direct TFM, half-skip TFM and full-skip TFM imaging algorithms can be utilized separately to detect different defect types. Half-skip TFM and full-skip TFM demonstrate good performance to improve surface-braking cracks measurement[38] and defect characterization[39]. An improvement of multi-faceted defect detection is able to be achieved through a combination of all of the three TFM imaging algorithms[40].

2.3. Signal Processing Techniques

In the last three decades, digital signal processing has played a significant role in NDT[41] and it has been aimed at the localization, sizing and classification of the defects. Now sophisticated signal processing algorithms are broadly used in NDT such as Fourier Transform (FT) and Short Time Fourier Transform (STFT), wavelet analysis and SAFT (Synthetic Aperture Focusing Technique). FT and STFT transform the time domain signal into frequency domain to analyse the signal by spectral characteristics. STFT and wavelet analysis provide time-frequency analysis to the signals. SAFT is commonly used to enhance SNR of an image and improve the sizing accuracy of the defects. In this Section, application of these algorithms in NDT will be reviewed.

2.3.1. FT and STFT

The Fourier Transform (FT) is a mathematical operation to represent the signal in the form of its frequency spectrum. In the frequency domain, the frequency components of the signal can be observed and analysed for feature extraction and filtering processing. Only considering the simplest time varying signal, as given by Equation 2.28, its FT representation can be expressed by Equation 2.29[42].

$$f(t) = A\cos(\omega t) \tag{2.28}$$

$$\mathcal{F}(\omega) = \int f(t)\, e^{-j\omega t} dt \tag{2.29}$$

where A is the amplitude of the signal and ω is the angular frequency.

An inverse FT is the opposite operation that transforms signal from frequency domain into time domain, which is given by Equation 2.30.

$$f(t) = \frac{1}{2\pi} \int \mathcal{F}(\omega)\, e^{j\omega t} d\omega \tag{2.30}$$

This pair of operations provides the foundation for analysis and processing of ultrasonic signals.

Compared to FT, the Short Time Fourier Transform (STFT) is more commonly utilized for non-stationary signal analysis[43]. For example, there is ten minutes of music including guitar at the beginning and piano at the end. By applying FT to the whole music signal, we know guitar and piano are playing but do not know when they are playing. STFT can segment the whole signal into small time pieces and execute FT to every segment to acquire the individual frequency spectra. Therefore, the guitar and piano sound can be time localized.

The segmentation of a signal can be achieved by multiplying the original signal by a window function. Equation 2.28 can be segmented by a window function $h(\tau)$, as described by Equation 2.31[43].

$$f_\tau(t) = f(t)\, h(t - \tau) \tag{2.31}$$

where $f_\tau(t) = \begin{cases} f(t), & for\ t\ near\ \tau \\ 0, & for\ t\ far\ away\ from\ \tau \end{cases}$

Then, the STFT is the FT of the segment signal which is given by

$$\mathcal{F}_\tau(\omega) = \int f_\tau(t)\, e^{-j\omega t} dt \tag{2.32}$$

and the inverse STFT is

$$f_\tau(t) = \frac{1}{2\pi} \int \mathcal{F}_\tau(\omega)\, e^{j\omega t} d\omega \tag{2.33}$$

Figure 2.16 (a) demonstrates an example of a 1000 points time domain signal with 2 MHz and 4 MHz components located in different time regions. Figure 2.16 (b) shows its Fourier transform and Figure 2.16 (c) and (d) show the short time Fourier transform using different window lengths of 32 and 128 respectively.

STFT brings about the ability of time-frequency analysis but has limitations due to the uncertainty principle[43][44]. The uncertainty principle of signal analysis, as stated by Skolnik, was that 'a narrow waveform yields a wide spectrum and a wide waveform yields a narrow spectrum and both the time waveform and frequency spectrum cannot be made arbitrarily small simultaneously'[45]. This can be observed in Figure 2.16 (c) and (d) when a shorter window length is applied, there is a wider spectrum and conversely a longer window leads to a narrower spectrum.

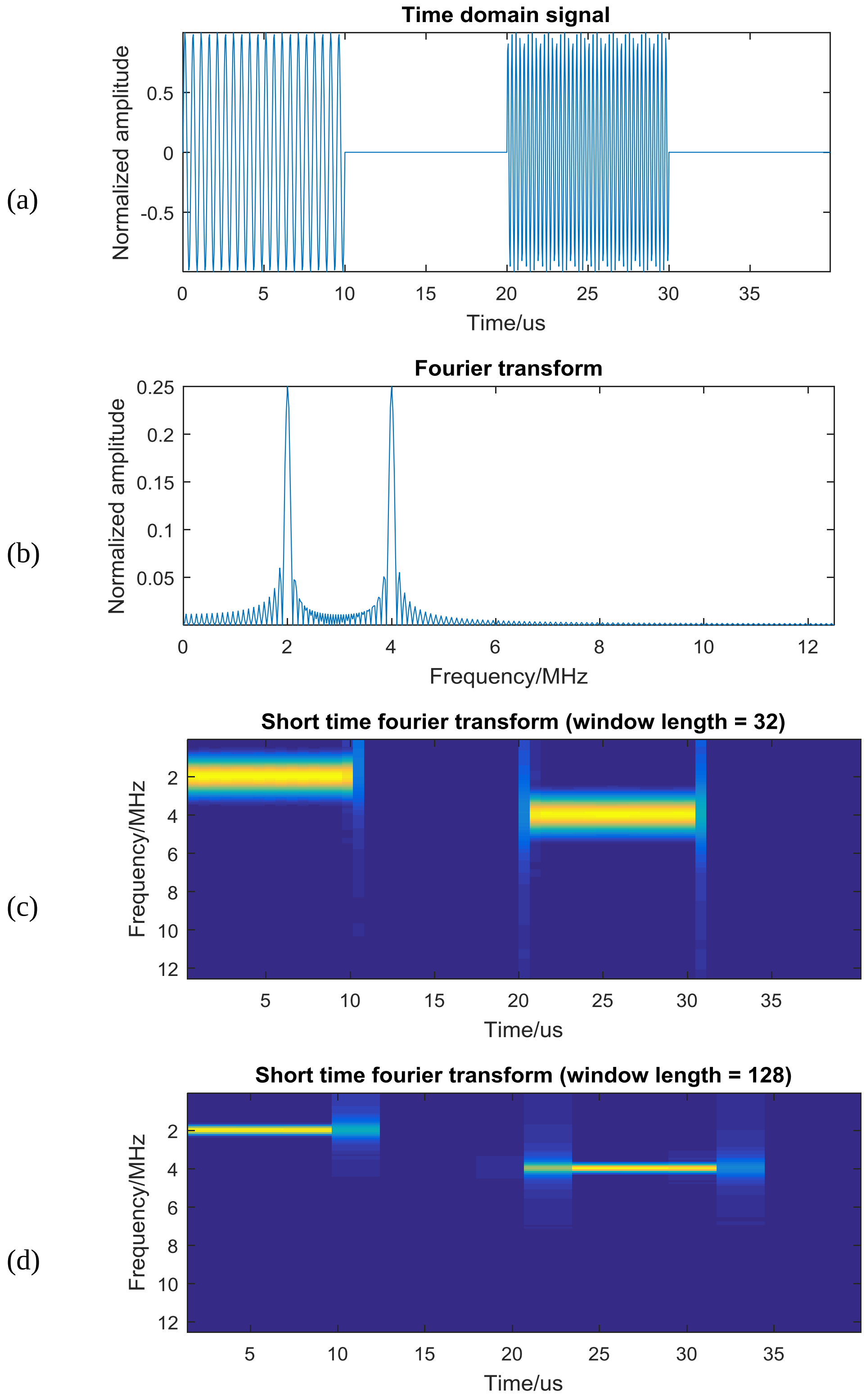

Figure 2.16 Time and frequency domain signal representations (a) Time domain signal – 2 MHz and 4 MHz; (b) FT; STFT using window length (c) 32 and (d) 128

2.3.2. Wavelet Analysis

Wavelet analysis has been widely used in ultrasonic NDT for SNR enhancement[46], weak defect signals extraction[47] and flaw signal classification[48]. This approach has demonstrated excellent improvement in identifying target signals by extracting signal features in the frequency domain, whilst maintaining the temporal information.

The wavelet transform is an analysis method to segment data into different frequency ranges and investigate each frequency component using the corresponding time information. The operation involves two variables – frequency and time, which offers an efficient tool for time-frequency localization[49]. The primary difference between the wavelet transform and STFT is that the former has an adaptive frequency resolution as opposed to the uniform resolution associated with the latter[50][51]. A description of the wavelet transform of a given function $f(t)$ can be expressed by

$$WT(a_{wt}, b_{wt}) = \frac{1}{\sqrt{a_{wt}}} \int_{-\infty}^{+\infty} f(t) \cdot \psi\left(\frac{t - b_{wt}}{a_{wt}}\right) dt \tag{2.34}$$

where the functions ψ are called wavelets,

$$\psi_{a_{wt}, b_{wt}}(\mathrm{s}) = \frac{1}{\sqrt{a_{wt}}} \psi\left(\frac{s - b_{wt}}{a_{wt}}\right) \tag{2.35}$$

and the function $\psi_{a_{wt}, b_{wt}}$ is called mother wavelet. Values a_{wt} and b_{wt} are the scale and shift parameters respectively. Here, it is assumed that the mother wavelet $\psi_{a_{wt}, b_{wt}}$ satisfies the condition

$$\int_{-\infty}^{+\infty} \psi_{a_{wt},b_{wt}}(t)\, dt = 0 \tag{2.36}$$

When the parameter a_{wt} changes, the wavelets cover different frequency ranges and parameter b_{wt} brings about movement of the wavelets across the frequency domain. By applying different parameters, the product of the wavelet transform is the coefficients for different frequency ranges. Thus, a signal is decomposed into approximations (A_{WT}) and details (D_{WT}) on different levels according to frequency. A_{WT} indicates the low frequency component, while D_{WT} indicates the high frequency component. The decomposed signal S_{WT} into level n can be expressed by

$$S_{WT} = (A_{WT})_n + \sum_{j=1}^{n} (D_{WT})_j \tag{2.37}$$

where j is an integer.

In ultrasonic NDT, many researchers have applied the wavelet transform to improve inspection results. Song and Que applied the wavelet transform as a band-pass filter to reduce noise within the ultrasonic inspection signal[46]. The interesting thing is they used an optimal scale of a daughter wavelet to match the central frequency of the ultrasonic signal, which removed white noise to improve SNR. The optimal scale wavelet transform method is also proposed to identify a weak defect echo from within noisy signals[47]. Wang proposed a classification method based on the wavelet transform that is used for ultrasonic inspection of carbon fibre reinforced polymer[48]. Different features relating to delamination, debonding and void regions in the test sample can be extracted by using Daubechies wavelet and then be classified through further processing. Siqueira et al.

applied the wavelet analysis method to analyse ultrasonic guided wave signals used in low-carbon steel pipe inspection[52]. After employing the Daubechie 3 wavelet to filter the noise signal, the guided waves are able to travel long distances with an acceptable SNR. An adaptive Morlet wavelet filter was demonstrated by Chen et al. to enhance the reflected echo from a crack tip in an ultrasonic Time of Flight Diffraction (TOFD) inspection[53]. White et al. proposed a closed-form analytical solution to parameterize the wavelet transformed ultrasonic signals and subsequently, implemented statistical analysis method to evaluate the inspection data, which showed potential for defect classification[54].

2.3.3. SAFT

SAFT was first applied in the radar field and it has been performed for over 30 years in ultrasonic NDT to improve the detected performance in terms of horizontal resolution, defect sizing and also SNR[55][56]. It does not only exist in pulse echo and pitch-catch techniques, but also can be combined with the phased array technique[19][57].

The SAFT theory is based on the standard delay and sum approach. Here, a single element transducer working in pulse-echo mode is used as an example. As shown in Figure 2.17, the transducer moves horizontally to collect A-scan signals. The echo signals from the discontinuity in the test object are situated at different time ranges of the A-scan signals due to the different propagation distances between the transducer position and the discontinuity. All the information can be superimposed as described in Equation 2.38:

$$S_{SAFT}(t) = \sum_{i} A_i(t - t_i) \tag{2.38}$$

where $S_{SAFT}(t)$ is the summed echo signal, $A_i(t)$ is the returned signal from the transducer at position i and t_i is the time delay for transducer at position i relative to central position.

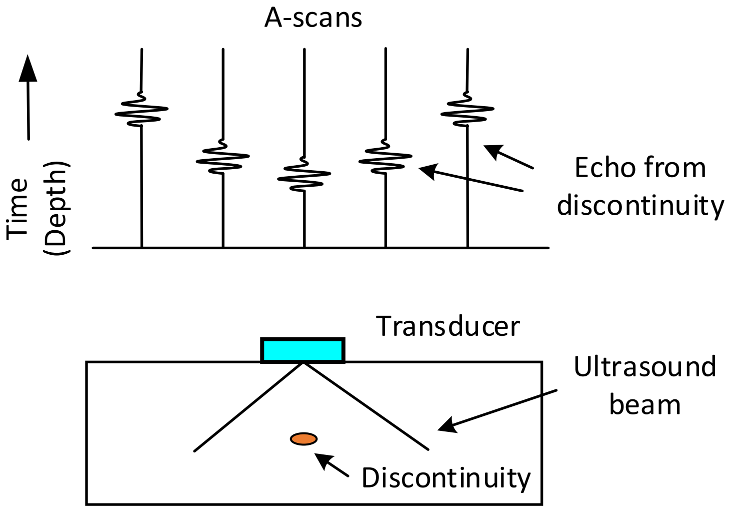

Figure 2.17 Illustration of SAFT theory

SAFT has been researched in anisotropic and strongly attenuating material. Spies analysed the methods for modelling of ultrasonic NDT in anisotropic media that was simulated by a Gaussian beam and a point source superposition technique[58]. Jager and Spies did experiments on carbon-fiber reinforced composites containing Side-Drilled Holes (SDH) and Flat-Bottom Holes (FBH) to validate the algorithm[59]. In addition, Spies and Rieder used SAFT in a study of the Probability of Detection (POD) in a strongly attenuating material[60].

Furthermore, research on SAFT has been implemented using data collected from phased array transducers because the small size of each transducer element brings about the wide beam width to provide more information for focusing within the synthetic aperture. Boehm et al. modelled phased array inspection with different angles of incidence to collect data for SAFT analysis[19] and provided experimental validation. They concluded that compared to SAFT using a small conventional transducer, the advantage was much larger SNR, while the disadvantage was the increased amount of raw data.

Researchers also made comparisons between SAFT, TFM and TOFD. Holmes et al. used a typical synthetic aperture sonar approach, Range-Doppler algorithm, to process pulse-echo data which could reduce the imaging time compared to TFM[61]. Compared with TOFD, SAFT is better in the capabilities of detection and sizing due to its superior spatial resolution[62].

The applications in concrete inspection also show SAFT's advantages in ultrasonic imaging processing[63]. In addition, SAFT in the frequency domain is investigated including the main aspects of Phase Shift Migration (PSM) algorithm[64][65] and ω-k algorithm[66][67].

In the recent years, SAFT algorithm with a virtual source has been researched by many scholars with a concept to take advantage of the transducer focal point, either for focused transducer or phased array transducer working with a focused delay law. Frazier and O'Brien proposed a virtual source synthetic aperture technique for a focused transducer to test wire and cyst objects with different weighting functions[68]. They proved that the method could achieve a better resolution and the image SNR could be increased with the test object 3, 5 and 7 mm beyond the focal point. Another weighting method was presented by Li et al. for virtual source SAFT, which considered the ultrasound energy in frequency domain[69]. Scharrer et al. showed a new method for data acquisition which entailed executing an angular scan at each position to ensure the transducer was focused at the surface of the test object[70]. The SAFT processing of the acquired data demonstrated good performance to identify the inner structural edges. The application of a virtual source SAFT for phased array transducer configurations was introduced by Bae and Jeong[71]. They utilized the virtual source for both forward and back directions and showed the result of SAFT algorithm for medical use that improved the image SNR and penetration depth but had limitation for moving objects. Furthermore, a virtual source SAFT method in the frequency domain was presented by Wu et al. for improving the image lateral resolution[72].

2.4. Simulation of Ultrasonic Inspection

The simulation of ultrasonic systems has been the subject of research by scholars for many decades[73][74]. Techniques have evolved from analytical solutions to computer based software to analyse the behaviour of ultrasonic waves propagating in one or more media and interacting with a discontinuity, if it exists. With advances in computing efficiency, simulation is a significantly faster process nowadays and therefore can bring about benefits of time and cost savings when researching a new technique or application.

2.4.1. Finite Element Method

Finite Element (FE) methods have been extensively used for the analysis of ultrasonic NDT[75][76][77][78][79][80]. Some FE analysis tools provide efficient solution of ultrasound relevant problems such as PZFlex (OnScale Inc, Cupertino, CA)[71][72], COMSOL (Comsol Inc., Burlington, MA)[73][74], Abaqus (Abaqus Inc., Waltham, MA)[83], POGO (Imperial College London, London, UK)[80] and ANSYS (ANSYS, Inc., Canonsburg, USA)[84][85][86], as well as FE modules used in CIVA (Extende, Massy FR)[87]. In this Section, the basic concept of FE methodology and the advantages of this approach are introduced.

The Finite Element method is a numerical solution of the mathematic equations to physical problems. The basic concept is dividing the whole domain into numerous subdomains (called finite element), solving the algebraic equations of each subdomain, providing relations among the solution at selected points (called nodes) and finally assembling all the parts into the whole domain[88][89]. The main process can be summarised in Figure 2.18.

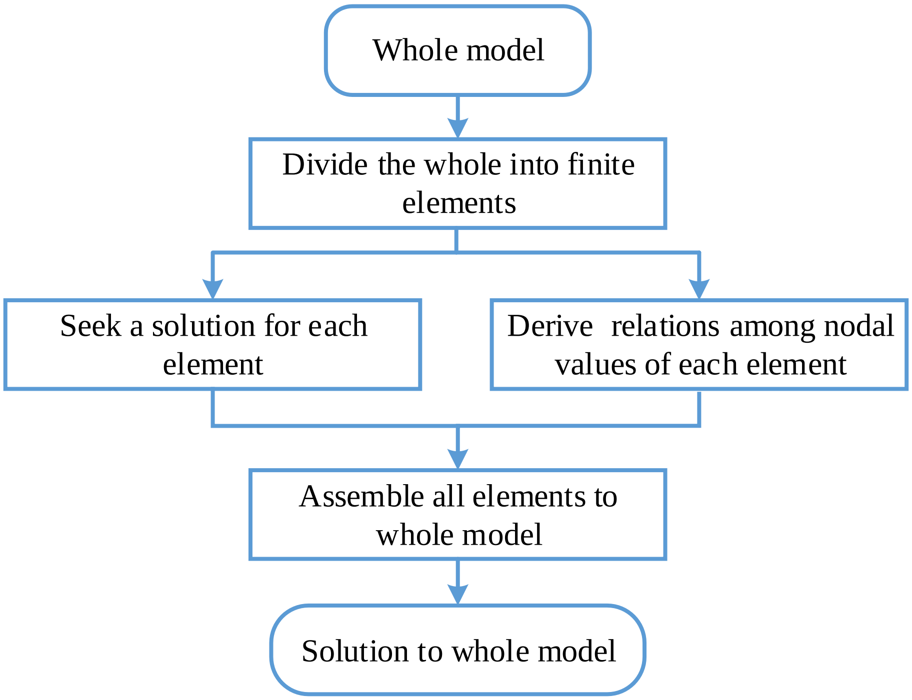

Figure 2.18 Fundamental process of FE method

Firstly, the whole model is represented as many finite elements. This operation is called discretization of the domain. Secondly, for each element, an approximation of the solution to element equations is calculated for a linear combination of the nodal values. Finally, all the element equations and solutions are assembled together as a solution of the whole model. Smaller finite elements can produce higher accuracy, but will result in a longer simulation time.

There are many advantages of the FE method for engineering applications[89]:

- it is easy to model complex shapes;
- the model can be composed of different materials;
- various finite element sizes can be used;

- different boundary conditions can be defined for different applications;
- model configuration modifications are very simple.

When the mesh size of the model becomes smaller, the FE model size increases, which will lead to a non-convergency of the model due to numerical dispersion errors[90][91]. While a bigger element size also increases simulation error since fewer details are provided for modelling. There is a trade-off between the simulation error and mesh size. An illustration of the relationship between element size and simulation error in FE model is shown in Figure 2.19. Considering the high frequency simulation requirements in this Thesis, 3-D simulation would lead to extra computational burden and convergence problems due to small mesh size. Therefore, only 2D simulations were performed. In the next Section, hybrid simulation methods applied in ultrasonic NDT are reviewed.

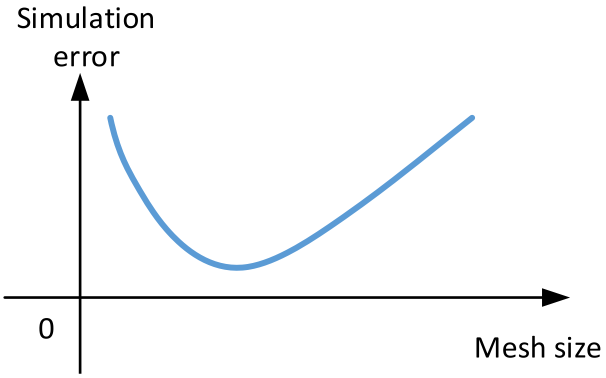

Figure 2.19 Relationship between mesh size and simulation error in FE model

2.4.2. Hybrid Simulation

Hybrid simulation methods have been developed and used for ultrasonic NDT inspection scenarios to solve simulation problems where a single model cannot be used reliably.

Zhang et at. described a hybrid approach to predict the scattering coefficient matrices of defects[37]. A combination of the FE package Abaqus and the Kirchhoff model were used to simulate the interactions between the wave and the defect, with a ray-based approach used to model the wave propagation region. This method was able to simulate longitudinal waves, shear waves and wave mode conversion effects. A generic hybrid model for analysing the ultrasonic wave propagation in bulk electrodynamics was introduced by Rajagopal et al.[92]. An interface between two FE model-domains (modelled in Abaqus) was applied through the use of a generic wave propagator. The usefulness of this method was demonstrated in its application to an ultrasonic wave propagation and scattering problem. Han et al. presented modelling work of pipe inspection by utilizing a hybrid 2-D acoustic transfer function (ATF) approach to simulate the cross-sectional area individually and then assemble the multiple sections[93]. This method was shown to have an accurate estimation of the longitudinal, torsional and flexural wave modes in the pipe. A 3D hybrid model was developed by Masmoudi and Castaings to simulate air-coupled inspection of composite samples, combining a fast 3D simulation in COMSOL with the Kirchhoff integral[94]. Another hybrid simulation combined both FE and Waved Based (WB) methods for analysing poroelastic materials[95]. The FE-WB modelling technique contained three parts: FE model, WB model and direct coupling between them. This approach benefited from the advantages of the WB method and FE model to improve the convergence rates for the model of the analysis of poroelastic materials. Zuo et al. proposed a Semi-Analytical Finite Element (SAFE) method coupled with a Perfectly Matched Layer (PML) to investigate guided wave behaviour in embedded waveguides with arbitrary cross sections[96]. Shen and Giurgiutiu made use of a Combined Analytical Finite element model Approach (CAFA) to simulate a Lamb wave damage detection technique[97]. This method utilized frequency and direction dependent complex-valued coefficients to model the Lamb wave damage interaction, which achieved good performance in accuracy and efficiency comparing to full-scale FE simulation and experiments. Shi et al. presented a hybrid simulation method by using numerical code combined with boundary integration formulae to calculate the received waves in the time domain, while the simulation performance is largely dependent on the reliability of the coupled numerical integration[98]. Dobie et al. proposed a combination of Linear Systems Model (LSM)[99] and Local Interaction Simulation Approach (LISA)[100] propagation model to simulate an air-coupled ultrasonic scanning platform[101], which provided a solution for the high computational time associated with complex geometries. An efficient hybrid FE modelling linking CIVA and Abaqus simulation modules through an interface was presented by Choi et al.[77]. They improved the boundary absorption, meshing algorithm and computational efficiency of the FE modelling to achieve a fast 3D simulation in ultrasonic NDT.

2.5. Summary

Ultrasound technology applied in NDT has been reviewed in this Chapter. Ultrasonic transducer and data acquisition system are the key components for ultrasonic inspection. Compared to traditional single element transducer, ultrasonic phased array technology offers excellent potential through a range of post-processing signal analysis techniques. This Thesis focuses on researching ultrasonic phased array inspection of pressure tubes and analysing industrial data currently collected by single element transducers. The review of phased array technology and signal processing techniques is considered to show potential to improve the accuracy of pressure tube inspection. Finally, the simulation of ultrasonic inspection was reviewed as this will be used for modelling of the pressure tube inspection.

Chapter 3

Analysis of Poorly-Focused Ultrasonic Signal of Pressure Tube Inspection

3.1. Introduction

Ultrasonic inspection can encounter operational challenges when the transducer is not aligned as expected to the component being tested. In the case of CANDU pressure tube inspection, this is typically due to the tube dimensional changes. As discussed in Section 1.2.1, a focused transducer is incorporated into the CIGAR sensor head, immersed in heavy water and used to perform a helical scan inside of the tube, focusing on the tube inner surface. However, a poorly-focused transducer can produce a defocused B-scan image, which can lead to the oversizing of defects. This effect is worse in the middle of the tube where sagging causes the biggest difference from the ideal position. Defects beyond a specific dimensional threshold are then sized in more detail through a time and cost consuming replica process[13]. Obviously, more accurate ultrasonic sizing would reduce the need for replicas, where defect width and depth are the main factors for making a decision of whether to execute the replica process or not[12]. In terms of the pressure tube inspection, the ultrasonic transducer is fixed on a module inside the tube and moved with a helical scan motion. Therefore, it is not straightforward to mechanically adjust the transducer position to solve the focusing problem. Applying appropriate signal processing to compensate for the defocusing effect would be a more practical method and provide more representative information for use in the sizing process.

In this Chapter, signal post-processing methods are used on poorly-focused industrial data to improve the inspection accuracy. A Synthetic Aperture Focusing Technique (SAFT) method is described in Section 3.2 for correction of the poorly-focused B-scan data to improve the defect width measurement. Moreover, analysis of the effect of the focal length value on the SAFT algorithm performance is also undertaken. In Section 3.3, a Wavelet Analysis (WA) method used to extract precise defect depth information is presented. For both signal processing approaches, multiple datasets have been applied to validate the algorithms and importantly, both of the methods show a clear improvement in the defect measurement accuracy.

3.2. SAFT Analysis on B-scan Image

In the inspection of pressure tubes within a CANDU reactor, ultrasonic single element focused transducers are employed to collect normal beam pulse-echo data (10 MHz and 20 MHz transducers) and full-skip shear wave pitch-catch data (10 MHz transducers)[11]. Currently, only the 10 MHz transducers are applied by the Analyst for defect width measurement by using either the ‘visual’ sizing or the amplitude drop method[12]. ‘visual’ sizing method is visually identifying and boxing a defect for investigation and interpreting defect edges by applying a greyscale display. These approaches have limited accuracy due to human error and ‘jitter’ interference, respectively. The 20 MHz transducer provides higher frequency inspection data and an intuitive B-scan image for defect detection and sizing. It therefore has a huge potential for accurate defect width measurement. However, the in-service tube dimensional changes led to the transducer being poorly-focused with respect to the tube inner surface which causes poor inspection results. Thus, a SAFT algorithm is proposed to overcome this system focus challenge to improve the inspection accuracy.

3.2.1. SAFT Theory

3.2.1.1. Basic SAFT Theory

SAFT theory extends the aperture of a physical source by processing multiple sequential echo signals. The basic concept of SAFT involves manipulating a single element transducer across the sample being inspected to collect a number of pulse-echo signals. Importantly, each point in the ROI can be inspected at multiple transducer positions due to the divergence associated with the ultrasonic beam.

The usual implementation method utilises delay-and-sum (DAS) in the time domain to summarize all the signal values on the aperture to one pixel value[102], which was been briefly introduced in Section 2.3.3. As shown in Figure 3.1 (a), a transducer is moved step by step to collect echo information from point P. The echoes from P can be received at many transducer positions and relate to different time delays in the B-scan image, as presented in Figure 3.1 (b). Summing all the pixel values on the aperture to produce a pixel value at P is called the DAS method and the SAFT B-scan image executes this process for all the pixels in the image.

The calculation of new pixel value p can be determined using Equation 3.1, where $A_i(t)$ is the echo signal acquired at position i; j is the length of the aperture (also considered as the number of transducer positions within the aperture); r_i is the distance from the transducer to the target point at position i; and c is the longitudinal wave velocity in the medium.

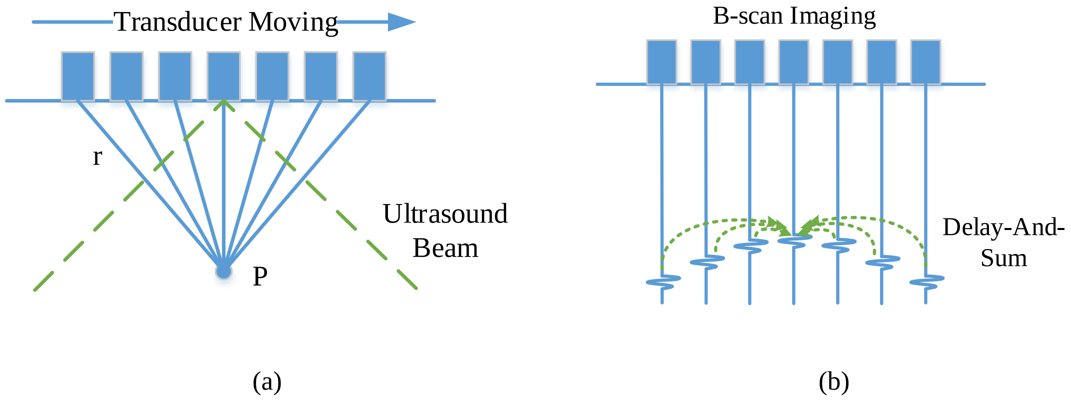

Figure 3.1 SAFT theory, (a) inspection data collection; (b) delay-and-sum on B-scan image

$$p = \sum_{i=1}^{j} A_i(\frac{2r_i}{c}) \tag{3.1}$$

3.2.1.2. SAFT Theory for Focused Transducer

When a focused transducer is employed in the SAFT algorithm, the wave propagation path for delayed time calculation is different from that of an unfocused transducer. In terms of a focused transducer, the ultrasound beam beyond the focal point is utilised for synthetic aperture processing[68]. As Figure 3.2 (a) shows, the wave propagation paths to P from two transducer positions are ACP and BDP respectively. The time difference can be calculated from paths CP and DP, since the focused transducer has same propagation distance from the transducer surface to the focal point. However, for an unfocused transducer, the wave propagation path is determined from the transducer centre point to P, which are shown as A'C'P' and B'D'P' in Figure 3.2 (b). The difference between paths ACP and A'C'P' is clearly presented in Figure 3.2 and therefore the DAS approach needs to be adjusted to accommodate the focal point plane for focused transducer applications.

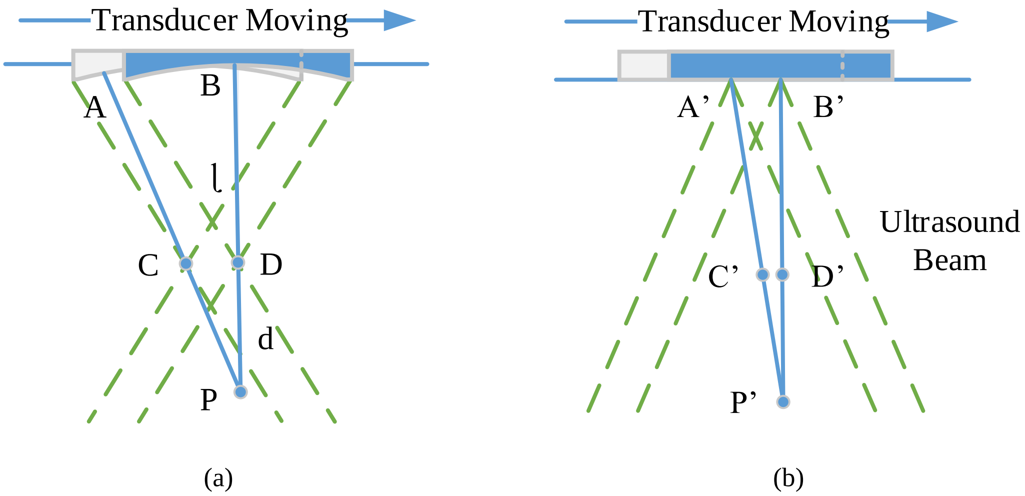

(a)

(b)

Figure 3.2 Wave propagation path, (a) focused transducer; (b) unfocused transducer

The calculation of new pixel value p_f can be described by Equation 3.2, where l is the focal length of the transducer and d_i is the distance from the focal point at transducer position i to the target point.

$$p_f = \sum_{i=1}^{j} A_i\left(\frac{2(l+d_i)}{c}\right) \tag{3.2}$$

3.2.1.3. Focal Length and Synthetic Aperture Curvature

When the transducer focal length changes, it results in time differences between data collected at neighbouring positions. Since the transducer used for our industrial application is reported to have a Focal Length (FL) of 10.4 mm, a selection of FL equal to 10.4 mm, 12 mm and 13.5 mm is used in this work, as shown in Figure 3.3, in which the red line indicates the synthetic aperture. When applying SAFT to the same point of a B-scan image, a longer focal length value produces a shorter length and higher curvature aperture, as shown in Figure 3.3 (b) and (c). Here, shorter equates to less sample points on the moving axis. Moreover, in Section 3.2.2.4, the theoretically calculated synthetic apertures for different focal length values are drawn on the B-scans to facilitate visual comparison.

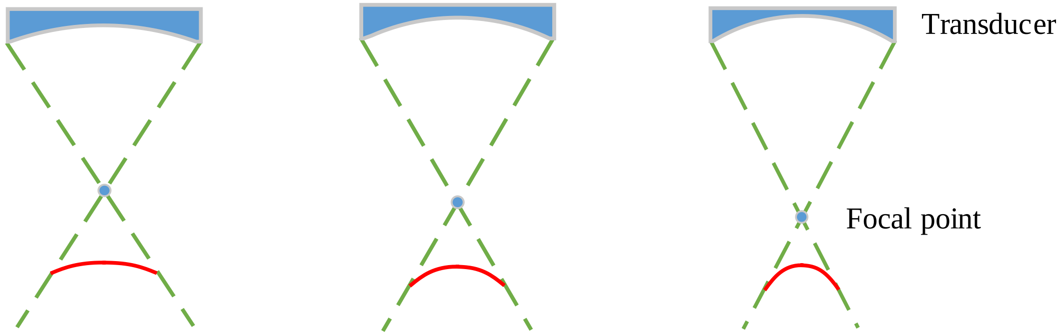

(a) FL = 10.4 mm (b) FL = 12 mm (c) FL = 13.5 mm

Figure 3.3 Relationship between focal length and synthetic aperture (red line), (a) FL = 10.4 mm; (b) FL = 12 mm; (c) FL = 13.5mm

3.2.2. SAFT Processing of Industrial Data

3.2.2.1. Data Acquisition

As previously described, the 20 MHz transducer is working in normal beam pulse-echo mode, through heavy water, to acquire A-scan signals. The data is then utilized to produce a B-scan image for SAFT processing, which will be further processed using SAFT.

3.2.2.2. SAFT Processing Parameters

Data supplied by the industrial sponsor for the 20 MHz focused transducer stated it had a diameter of 6.3 mm and a focus at 10.4 mm. Different virtual focal lengths are considered in the following SAFT processing to show the effect of focal length value to the algorithm performance and the inspection system has a sample frequency of 100 MHz, with a cable signal delay of 700 ns. The wave velocity in heavy water is 1420 m/s. Table 3.1 lists all the parameters used for SAFT processing.

Table 3.1 Parameters for SAFT processing

Parameter	**Value**
Transducer frequency	20 MHz
Transducer diameter	6.3 mm
Transducer focal length	10.4/12/13.5 mm
Sample frequency	100 MHz
Cable signal delay	700 ns
Wave velocity in heavy water	1420 m/s

3.2.2.3. Flowchart

The SAFT algorithm is executed in MATLAB R2016b (The MathWorks, Inc.) and the flowchart is presented in Figure 3.4. Since the transducer is performing a helical scan inside of the tube to collect data, the tube surface on the B-scan image is not straight. In the software analysis package, FLAW (Ontario Power Generation Inc., Toronto, Canada), used for CIGAR data analysis, a wave straightening function is typically applied to align the B-scan image presented to the NDE Analyst. Here, prior to applying the SAFT algorithm, the tube surface is straightened by using the Random Sample Consensus (RANSAC) method[103].

In the inspection system's display mode, the horizontal axis of the B-scan image indicates time and the vertical axis indicates the rotational degree. Therefore, the B-scan data is a 2-D matrix with each column showing the echo signal at a specific time and each row showing time domain signal received at a specific position. The steps of SAFT processing as illustrated in Figure 3.4 are listed as follows:

- For each column, evaluate if the pixel depth is bigger than focal length. The pixel depth is the distance between the target pixel and the transducer surface.
- If larger, calculate the length of the synthetic aperture according to the transducer beam width.
- Calculate the shift points within the synthetic aperture corresponding to the delayed time. The shift points are all the pixels on the aperture with respect to the central pixel

(it has a distance d_0 to the focal point) that can be calculated by $\Delta t_i * f = \left[\frac{2(l+d_i)}{c} - \frac{2(l+d_0)}{c}\right] * f$ for each transducer position i (f is the sample frequency).

- For each pixel, sum all the signal values on the aperture and record as the new pixel value.

After all the pixels on the B-scan image have been replaced by the new pixel values, a SAFT B-scan image is obtained.

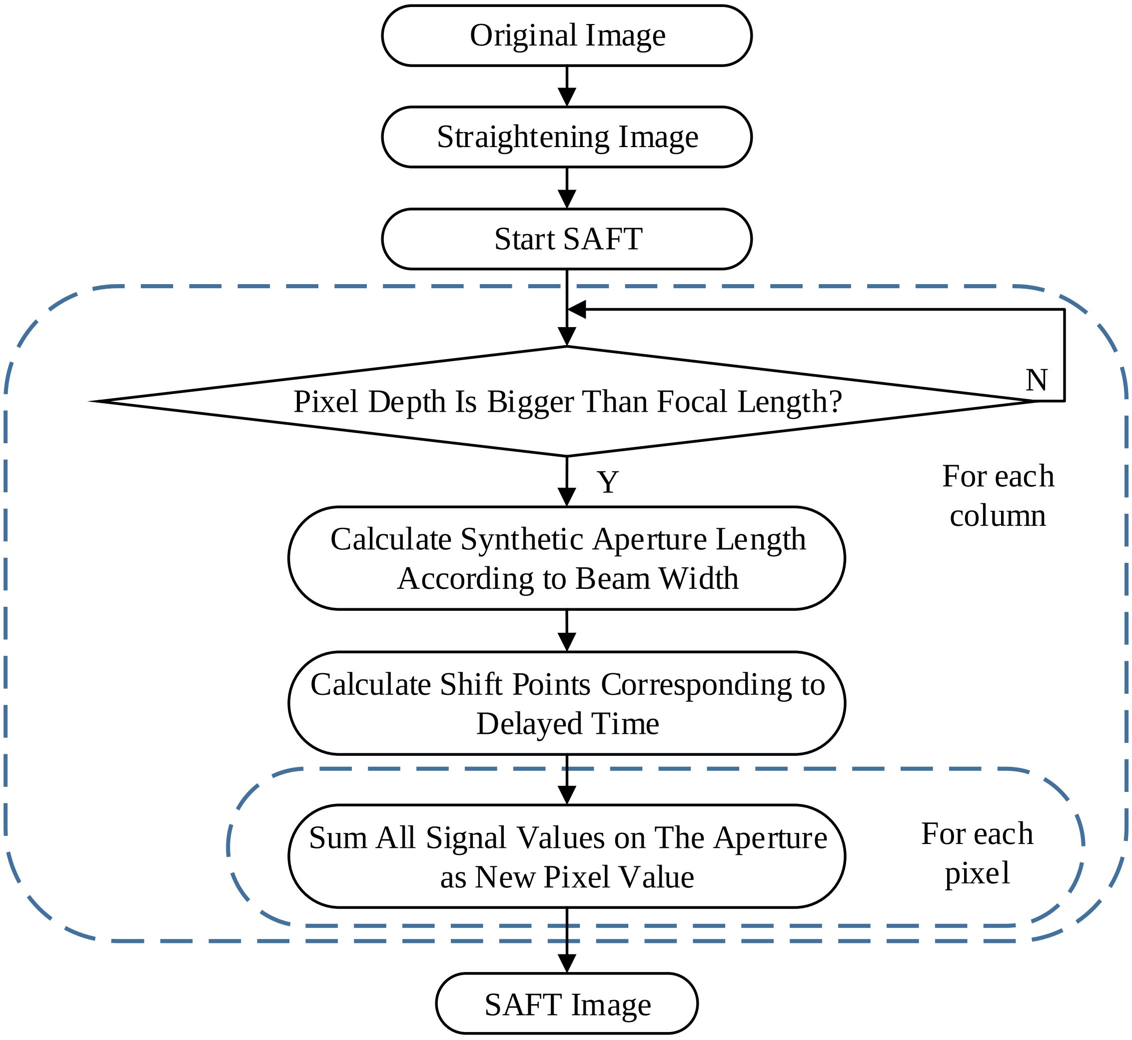

Figure 3.4 Flowchart of SAFT algorithm on inspection data from a focused transducer

3.2.2.4. Effects of Using Different Focal Length Values

Figure 3.5 presents a CIGAR data example of calculated apertures overlaid on a B-scan image with the 3 different focal length values. In this B-scan example, the potential defect is detected and the corresponding echo signals can be seen as curved lines beneath the tube surface in the grey-scale image. The calculated transducer apertures are indicated by the red dotted lines. When using 10.4 mm as focal length value for the aperture calculation, the aperture length is a reasonably close match to the length of the echo signal, but the curvature is smaller. While the 12 mm focal length value produces an aperture curvature very well matched to the echo signal. Finally, for the case of the focal length value equal to 13.5 mm, the aperture curvature is larger than the practical one and the length is the shortest. In Figure 3.5 (c), since the aperture length is too short to illustrate the curvature, an extension of aperture is indicated by the green dotted line. Therefore, 12 mm is considered correspond to the actual transducer focal length.

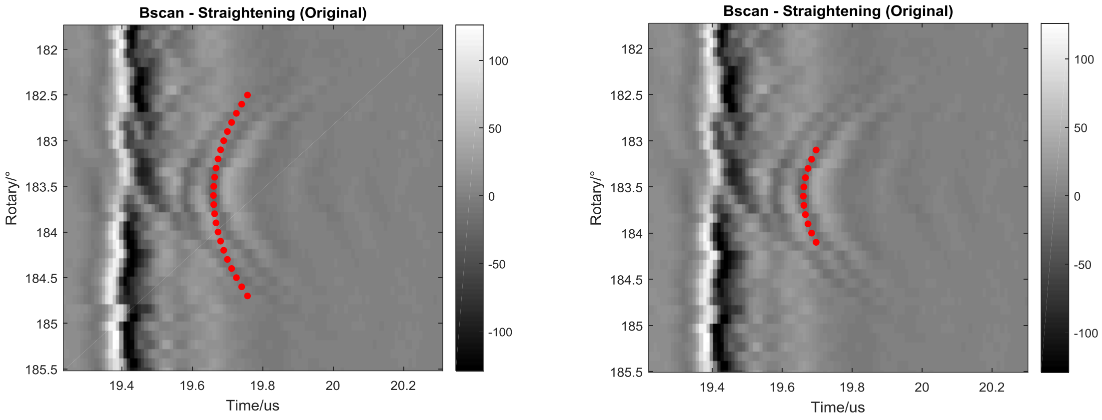

(a) FL = 10.4 mm

(b) FL = 12 mm

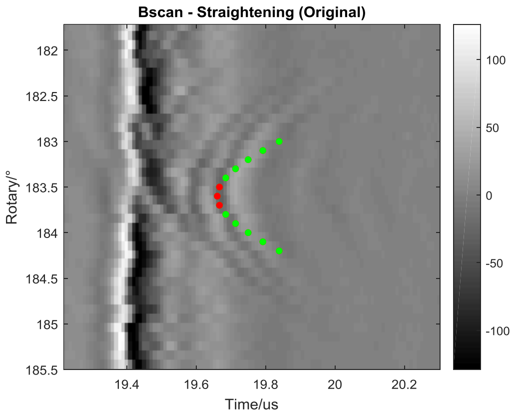

(c) FL = 13.5 mm

Figure 3.5 Calculated aperture on B-scan image by different focal length values, (a) FL = 10.4 mm; (b) FL = 12 mm; (c) FL = 13.5 mm

3.2.3. Result Analysis of Different Focal Length Values

Figure 3.6 presents SAFT processing results with different focal length values and the corresponding -6 dB defect contour plots. The contour plots are based on the -6 dB values of the defect echoes. The propagation time for ultrasound reaching the tube surface is approximately 19.4 us. The left column shows the B-scan images and the right column displays the -6 dB defect contour plot.

In this CIGAR data example, an obvious ‘over-correction’ phenomenon can be found in SAFT B-scan by applying focal length value of 10.4 mm (Figure 3.6 (b)), but importantly the first reflected echo from the defect is no longer visible in the corresponding contour plot. This ‘over-correction’ phenomenon indicates the change of the defect’s curved direction. It is caused by the accumulation of additional echo signals not belonging to the target. In other words, the theoretical synthetic aperture and the practical one should be matched to take the advantage of the SAFT algorithm. Then, the accumulation of the pixel values on the aperture is considered to be accurate or ‘true’ focusing. Likewise, for the case of utilizing a focal length value of 13.5 mm, because the theoretical synthetic aperture and the practical one are not matched, as shown in Figure 3.5 (c), a poor focusing result is produced, as illustrated in Figure 3.6 (d). The focal length value of 12 mm demonstrates a well matched synthetic aperture, as shown in Figure 3.5 (b), and this produces the well-focused SAFT B-scan image presented in Figure 3.6 (c), which results in a defect width measurement result of 0.3 mm. Comparing this to the original 0.8 mm result, SAFT has produced a significantly enhanced image quality from which an Analyst can size the defect more accurately and repeatedly.

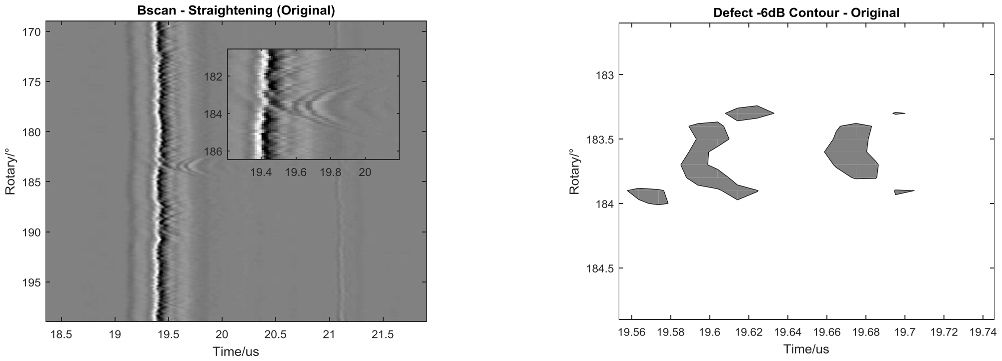

(a) Original B-scan and -6 dB contour shows typical 'poorly-focused frown'

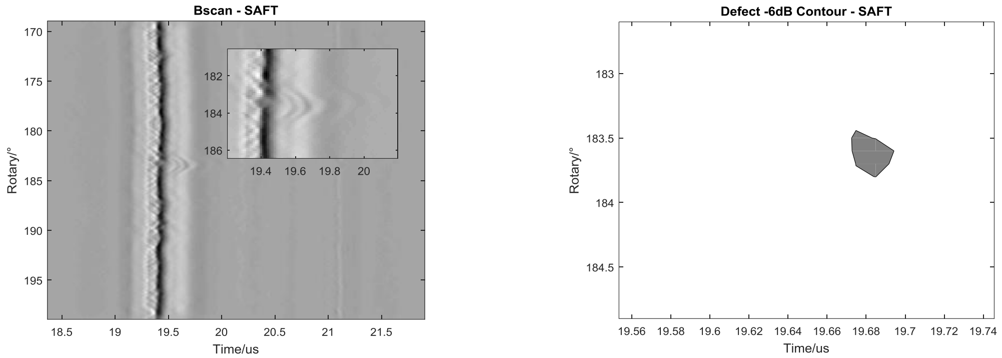

(b) SAFT B-scan (FL = 10.4 mm) and -6 dB contour shows 'over-correction'

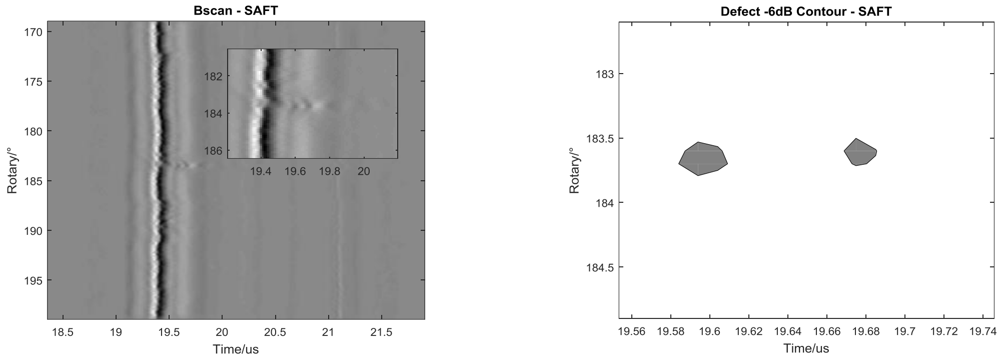

(c) SAFT B-scan (FL = 12 mm) and -6 dB contour shows good correction

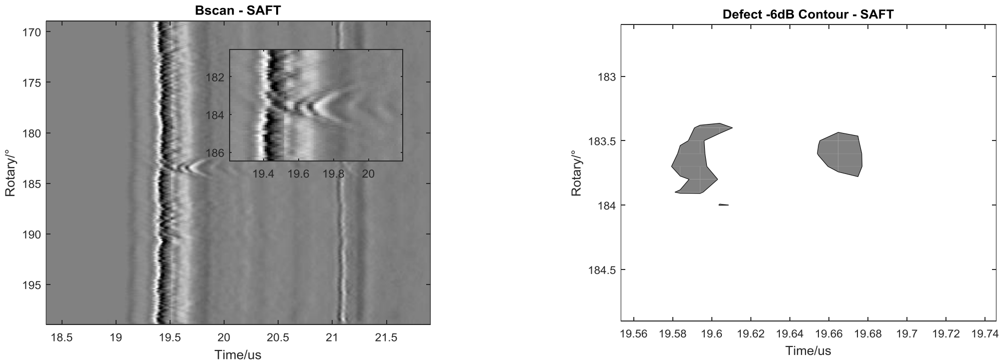

(d) SAFT B-scan (FL = 13.5 mm) and -6 dB contour shows poor correction

Figure 3.6 Example SAFT processing result and corresponding -6 dB defect contour

3.2.4. Synthetic Aperture Length

When the tube surface and transducer focal point have a greater separation, the synthetic aperture is larger and more apparent in an image. Consequently, when applying SAFT on such B-scan images, more directly relevant information can be utilized to get a better correction performance. Figure 3.7 shows inspection data examples of the defects situated at different positions along the tube, where the B-scan images are listed on the left-hand side and the -6 dB defect contours are shown on the right-hand side. Since the tube centre is more susceptible to sagging, the tube surface is farthest from the transducer focal point (Example 1), while Example 2 presents the inspection at one quarter of the tube length and Example 3 presents the result at the end of the tube. The respective times to reach the tube surface are 19.4 us, 18.95 us and 17.7 us. In terms of the 20 MHz transducer with a focal length of 12 mm, the time to reach the tube surface should be approximately 16.9 us for a well-focused inspection.

In Figure 3.7 (a), when the tube surface is the furthest from the focal point, the SAFT image has the best resolution compared to the original image, which can be found in the defect -6 dB contour plot. The defect width has a much smaller size on SAFT B-scan than on the original B-scan which indicates a better focusing effect. In terms of the tube surface being closer to the focal point (Figure 3.7 (b)), the SAFT image has a good degree resolution comparing to the original image, but is not that well-focused as discussed for Example 1. Therefore, a smaller defect width can be found on the SAFT B-scan but this is not significantly different from the original size. Finally, when the tube surface is the closest to the focal point, the SAFT image has the similar degree of resolution compared to the original image with small differences between the defect widths, where the defects are indicated by red dashed ovals (Figure 3.7 (c)).

In order to show the ability of the SAFT algorithm on poorly-focused inspection data of pressure tubes, a group of datasets from another tube are presented in Figure 3.8. Generally, the tube centre has the most serious sagging situation which leads to tube surface seperated from the focal point of transducer. However, different positions on the tube cross-section influences the surface and focal point seperation as well. Hence, for the data examples from this tube, the order is arranged by time to tube surface, which are 19 us, 18.7 us and 17.6 us for Example 4, Example 5 and Example 6 respectively. It is easily found from the -6 dB defect contour that all the cases have distinct improvement in the defect width measurement.

All the results and errors of the defect width measured using the -6 dB method can be found in Table 3.2. An important thing needs to emphasize is that the Analyst' results are based on a combination of General Helical data[13], pitch-catch data and inspection experience. Therefore, the defect size measurement result from the Analyst is different from the result in this Thesis. However, after comparing the industial verified results to the measured defect size using -6 dB method, it is approximate 5 to 6 times value of the latter. That means an improvement of 0.2 mm of the width measurement indicating an accuracy enhancement of more than 1 mm from an Analyst's view.

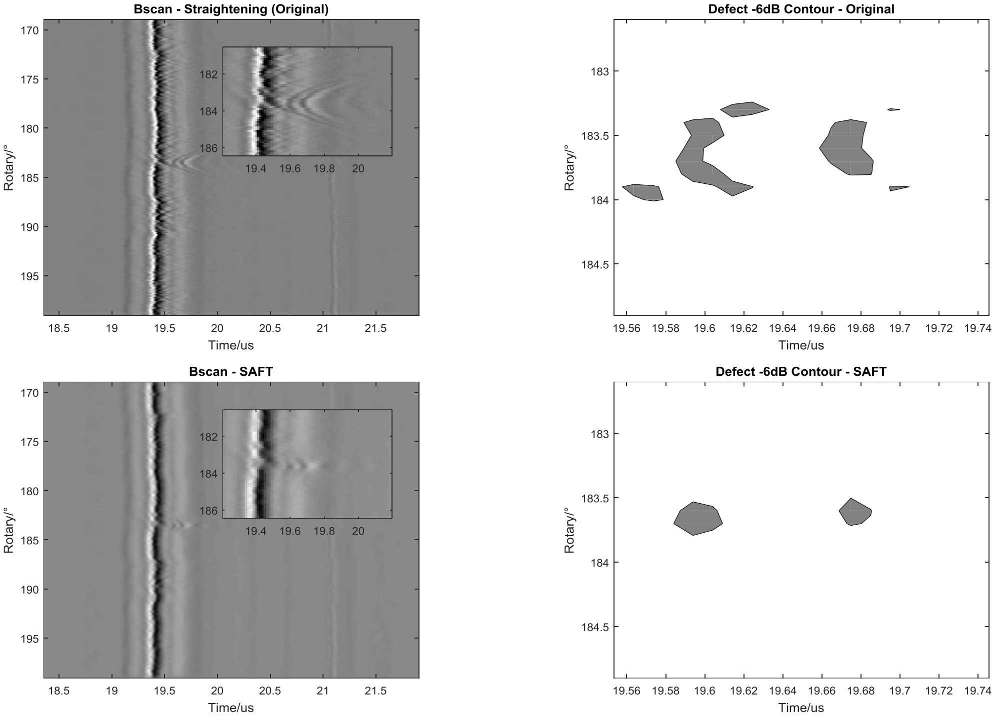
Bscan - Straightening (Original)

Defect -6dB Contour - Original

Bscan - SAFT

Defect -6dB Contour - SAFT

(a) Example 1: middle of the tube

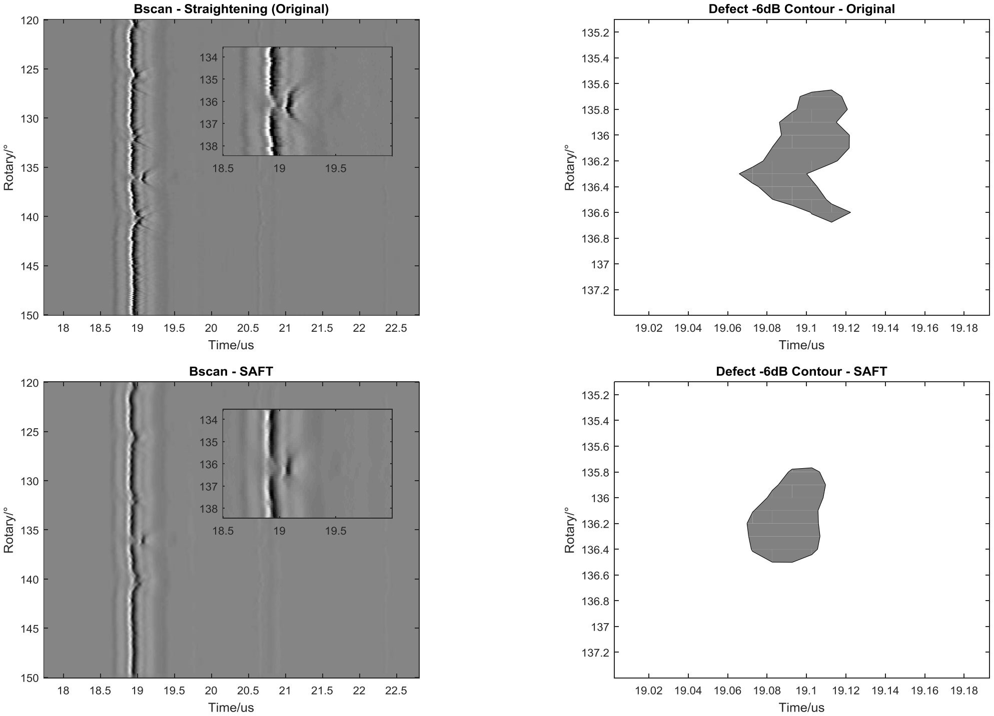
Bscan - Straightening (Original)

Defect -6dB Contour - Original

Bscan - SAFT

Defect -6dB Contour - SAFT

(b) Example 2: one quarter length of the tube

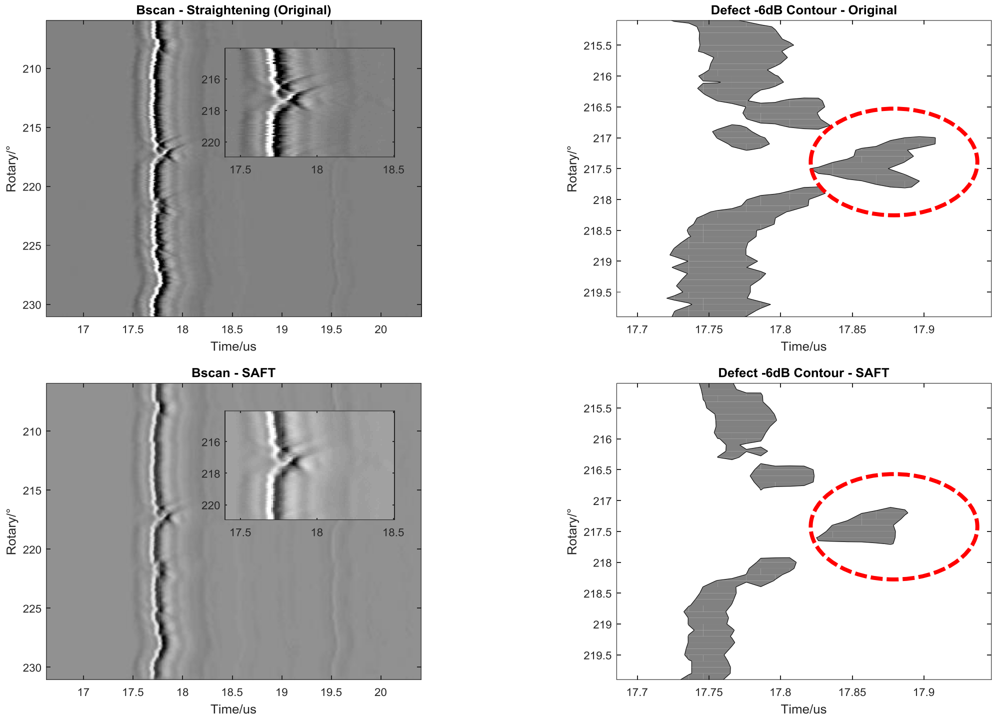

(c) Example 3: end of the tube

Figure 3.7 Original B-scan and defect -6 dB contour comparing to SAFT results

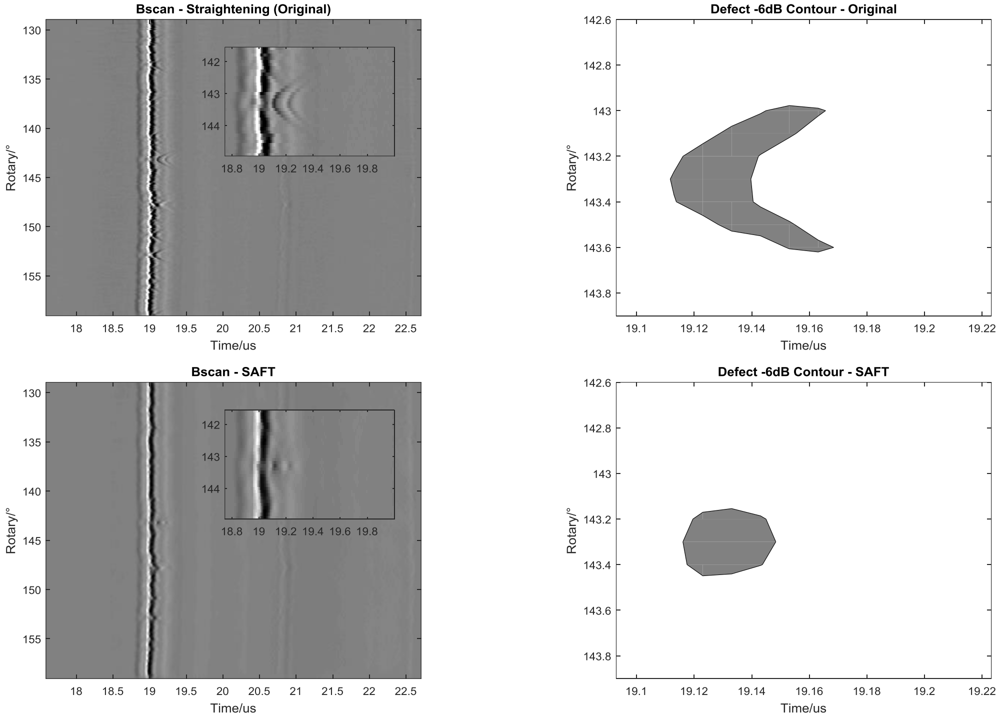

(a) Example 4: time to reach tube surface – 19 us

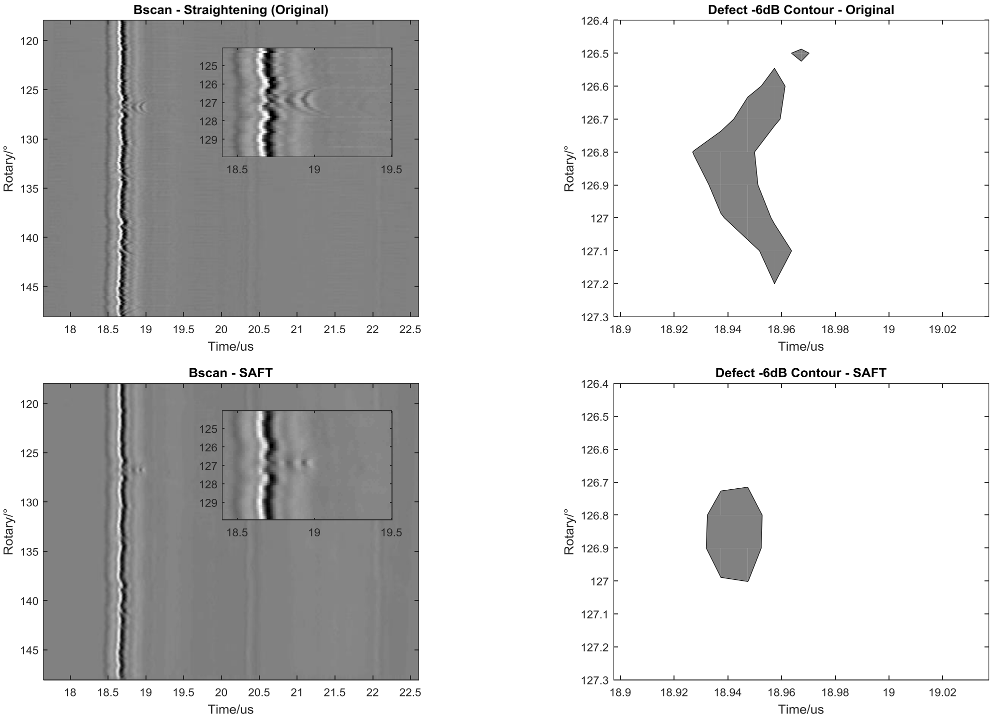

(b) Example 5: time to reach tube surface – 18.7 us

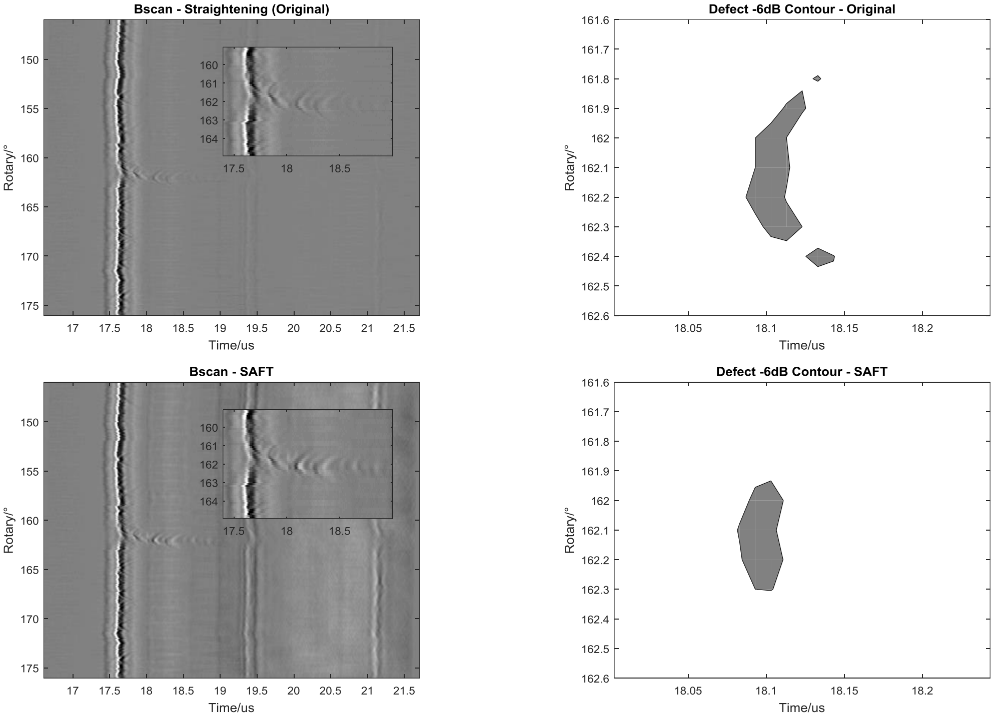

(c) Example 6: time to reach tube surface – 17.6 us

Figure 3.8 Original B-scan and defect -6 dB contour comparing to SAFT results from dataset with time to reach tube surface

The results demonstrate the defect width measurement on the SAFT image has better focusing compared to the original image data with an improvement of more than 0.2 mm, and the farthest distance (Example 1) separated from the tube surface brings about the best focusing result improving by 0.5 mm. Hence, there is a confidence that SAFT algorithm will contribute benefits for the correction of poorly-focused inspection, especially for ageing pressure tubes.

Table 3.2 Defect width -6 dB contour comparison – rotation degree axis

Example No.	Original Image (°)	SAFT Image (°)	|Δ| (°)
1	0.8	0.3	0.5
2	1.1	0.8	0.3
3	0.8	0.6	0.2
4	0.6	0.3	0.3
5	0.7	0.3	0.4
6	0.6	0.4	0.2

3.2.5. Summary of SAFT Processing Approach

In this Section, SAFT processing of a poorly-focused B-scan image from a CANDU pressure tube inspection was presented and the effect of different values of transducer focal length on the SAFT algorithm was analysed. Importantly, the SAFT algorithm for a focused transducer is different from the conventional unfocused transducer scenario.

Hence, the SAFT algorithm was modified to account for differences in the calculation of time difference between the neighbouring spatial positions.

Importantly, the transducer's focal length is a significant parameter for the SAFT processing, which determines if the calculated synthetic aperture is matched with the practical defect echo curve on B-scan image. A mismatched aperture could cause an 'over-correction' phenomenon in the SAFT processing result.

SAFT processing can improve the defect width measurement with a matched synthetic aperture. It increases resolution without any modification or extension to the CANDU inspection. Therefore, it provides a competitive solution for higher resolution defect width measurement and has potential to bring more accurate analysis for ageing tubes which may have serious sag issues.

3.3. Wavelet Analysis for Depth Measurement

In situations when the ultrasonic inspection of CANDU pressure tubes produces poorly-focused images of the tube surface, it results in difficulties to precisely measure the defect depth from the superimposed A-scan echo signals[104]. The A-scan signals acquired by CIGAR tool considered in this work are from a 20 MHz normal beam used for detection of inner tube wall defects. To match the stringent requirements for the depth measurement accuracy (minimum defect depth size of 0.1 mm), conventional frequency analysis, such as STFT, does not produce sufficient accuracy due to the trade-off between time and frequency resolution. Wavelet analysis has demonstrated excellent improvement in identifying target signals by extracting signal features in the frequency domain, whilst maintaining the temporal information. However, to date, wavelets have mainly focused on signals in the low frequency regime. Hence, in this Section, wavelet analysis of ultrasonic signals will focus in the high frequency level regime (10-20 MHz) to enhance the extraction of the defect echo characteristics associated with the CANDU pressure tube inspection.

3.3.1. Wavelet Transform

The wavelet transform has been described in Section 2.3.2., where applying different parameter values of scale a_{wt} and shift b_{wt} can obtain a series of coefficients related to the different frequency ranges. Therefore, a signal can be described by approximations A_{WT} and details D_{WT} on different levels according to frequency.

The ultrasonic echo signal received from the pressure tube inspection is a high frequency signal, exhibiting low levels of noise. The detail signal for the wavelet analysis is reconstructed using these acquired ultrasonic echoes and used for defect observation within an appropriate frequency range. The decomposition of Discrete Wavelet Transform (DWT) operation in MATLAB can be found in Figure 3.9. With regard to decomposition on more levels, the process is shown in Figure 3.10[105]. The detail signal can be reconstructed directly from the wavelet coefficients on any level.

Considering the uncertainty principle[106] of signal processing, the selection of the wavelet for the poorly-focused A-scan signal is more likely to have a high time resolution.

A number of wavelet options will be considered to achieve the best balance between time and frequency resolution.

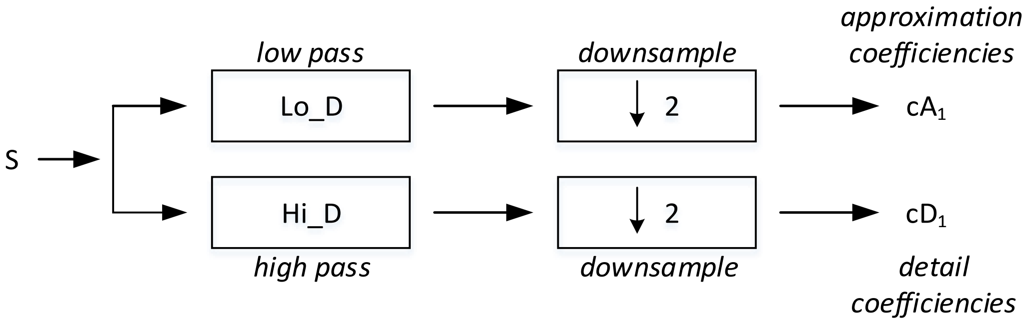

Figure 3.9 Process of decomposition of DWT in MATLAB

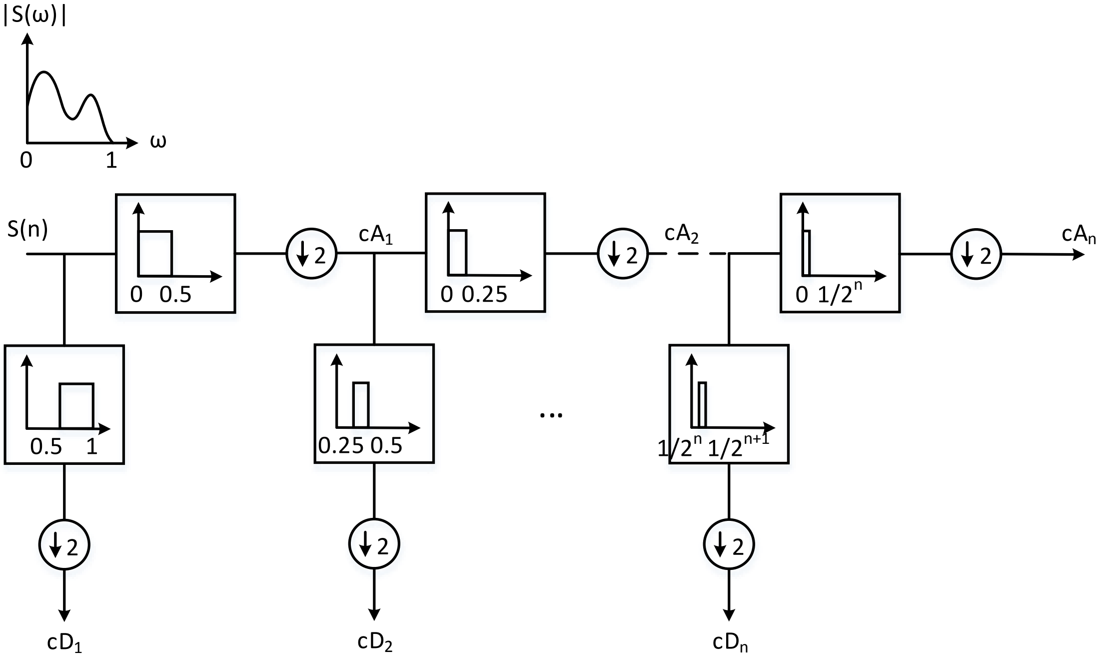

Figure 3.10 Process of an n-level wavelet decomposition.

3.3.2. Analysis of Industrial Data

3.3.2.1. Data Acquisition

The CIGAR sensor head is employed to inspect the pressure tubes by executing a helical scan immersed in heavy water inside the tubes. The ultrasonic inspection system experiences high damping, which results in a filtering effect of the central frequency of the received echoes from the 20 MHz excitation frequency, as shown in Figure 3.11, where the frequency response of a group of A-scan signals can be found. Nevertheless, in a standard operation the time difference between the peaks in the received pulse-echo signals from the measured tube inner surface (no defect case) and the echo from the bottom of the defect is used to calculate the defect depth, as described in the next Section.

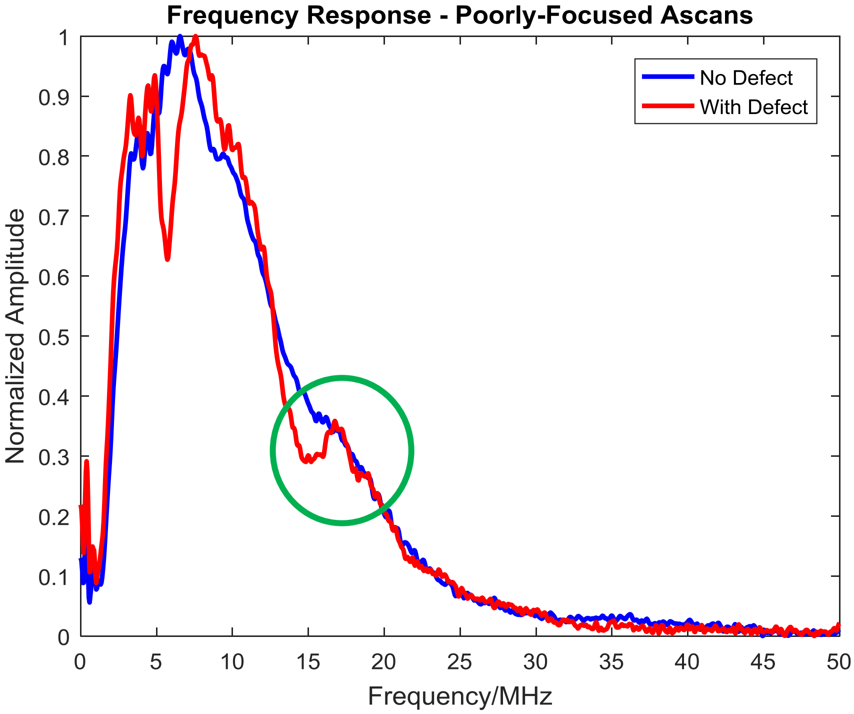

Figure 3.11 Frequency response from typical A-scan signals

3.3.2.2. Defect Depth Measurement in FLAW

The software analysis package FLAW has one function is specific to defect depth measurement. Initially, the acquired ultrasonic signal is presented as a B-scan image. Due to the movement during the helical scan, a wave straightening function within FLAW is applied to align the B-scan image, as shown in Figure 3.12. This is an example of well-focused ultrasonic signal. The Analyst will select the most relevant A-scan signal (Signal 1) to measure the defect depth, and another A-scan signal not containing defect information (Signal 0) is selected to represent the image back wall and used as a reference. The defect depth can be obtained through the time difference of the peaks in the two A-scan data, also presented in the Figure.

In terms of the inspection configuration, the transducer focal length is about 12 mm, and the wave velocity in heavy water is 1420 m/s. For the inspection of the tube surface, the propagation time (plus the cable signal delay in FLAW display) to reach the tube surface should be approximately 17.6 µs. However, for a poorly-focused B-scan image, this time can be extended. Taking the inspection data in Figure 3.13 as an example with a wave straightening applied, the time of ultrasonic wave reaching the tube surface is greater than the expected time, and the defect echo signal is difficult to clearly identify from both the A-Scan and B-Scan associated with Signal 1, due to the superposition of the scatterings from the defect bottom and the defect edge near the tube surface.

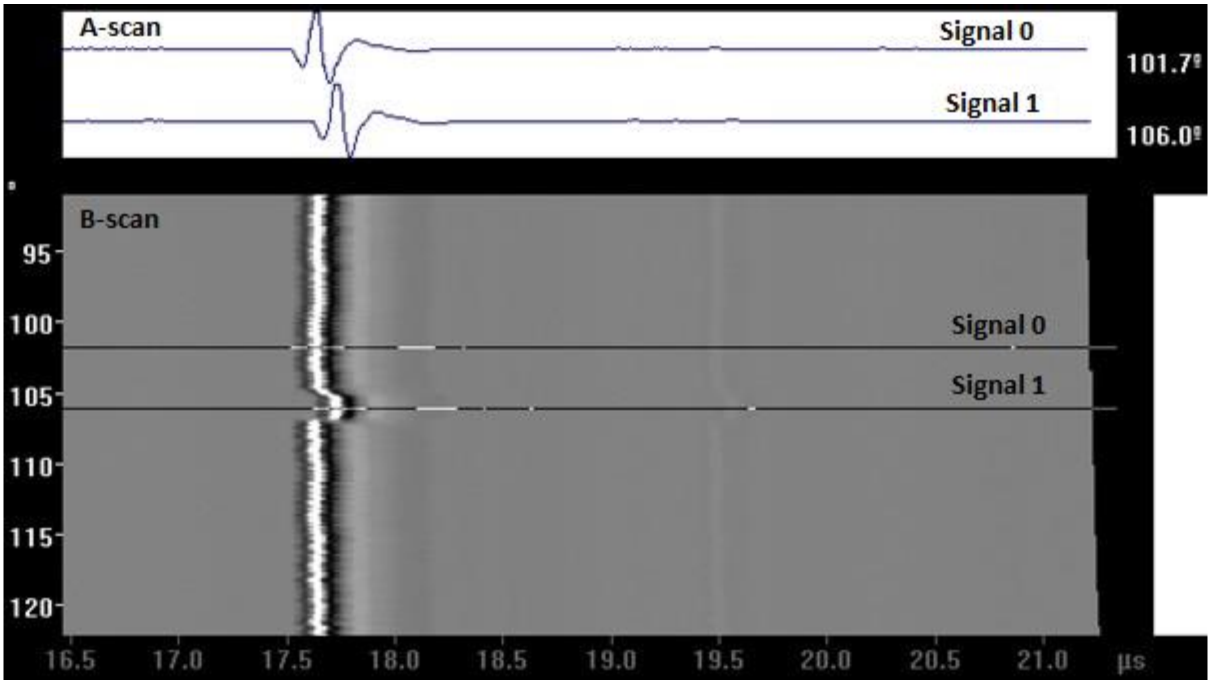

Figure 3.12 An example of well-focused ultrasonic signals presented using the FLAW analysis package

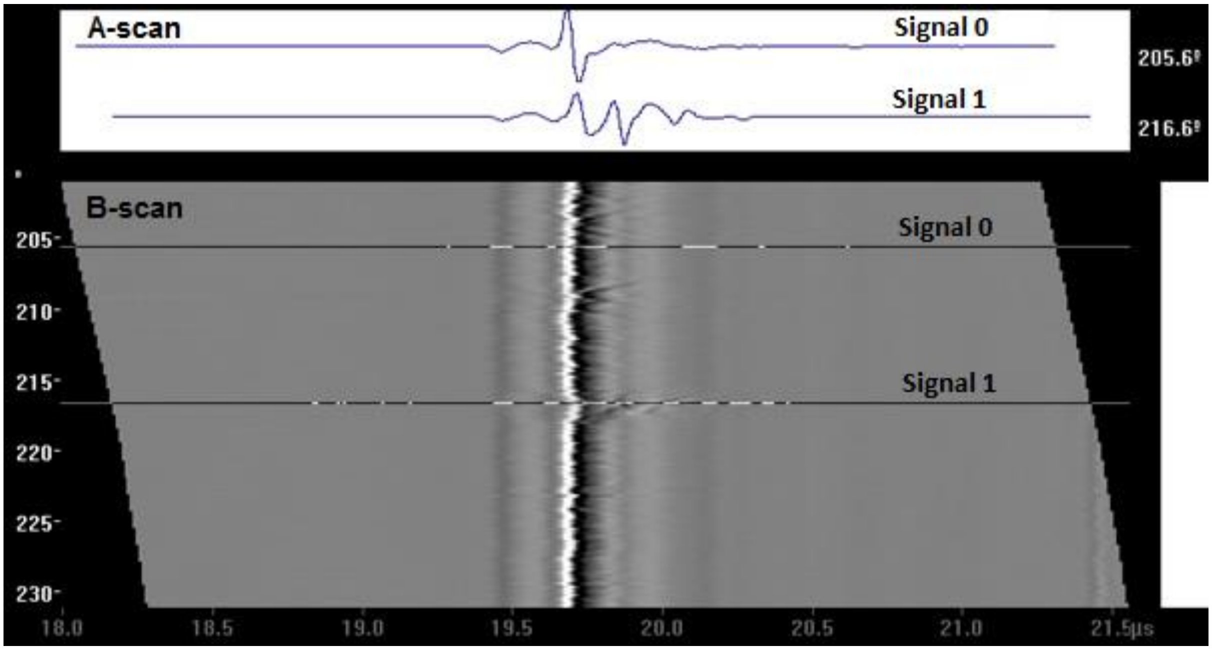

Figure 3.13 An example of poorly-focused ultrasonic signals presented using the FLAW analysis package

3.3.2.3. Wavelet Processing

A-scan signals from this inspection have spectral characteristics (shown in Figure 3.11) for two regions associated with the inner surface of the tube with and without the presence of a defect. These spectra are the average from a number of ultrasonic echo signals identified as belonging to either category. Each spectrum contains multiple peaks over the frequency range 2-20 MHz. The majority of these peaks lie in the 2-10 MHz region, but there is a distinct spectral feature associated with the presence of a defect close to 20 MHz (identified using a green circle), which offers potential for defect analysis. Furthermore, for the specific A-scan signals identified in Figure 3.13, the calculated frequency spectra are presented in Figure 3.14. It can be clearly seen that the spectral peaks in the 2-10 MHz range are reasonably consistent between these two signals and the frequency component around 16.7 MHz demonstrates a different characteristic from the no defect case. Therefore, this suggests that filtering of the spectral content may lead to the generation of useful information in terms of the defect response.

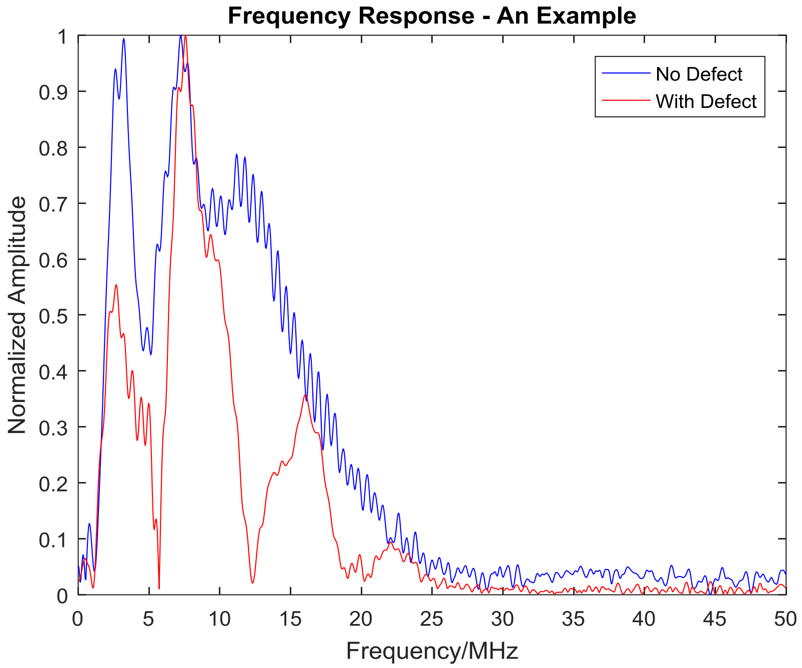

Figure 3.14 Frequency response for A-scans from a no defect (Signal 0) and defect (Signal 1) regions from Figure 3.13

Wavelet decomposition can be considered as applying groups of low pass and high pass filters to the signal of interest, with the group number dependent on the number of decomposition levels. The following wavelet analysis is based on the Haar wavelet[107], with alternative wavelets compared in the next Section. After convolving the A-scan signal with the Haar wavelet, the coefficients can be used to reconstruct the approximation and detail separately. The two A-scan signals (*S*) from Figure 3.13 are used as an example to demonstrate this processing approach. The approximation (*A3*) and detail signals (*D1*, *D2* and *D3*) are presented in Figure 3.15. From the decomposed signals, the detail signal on level 1 (*D1*) is identified as containing defect information due to the high frequency signal extracted from the inspection data. There are two peaks in the detail signal with defect on level 1 (*D1*). The first peak indicates the echo information from the near tube surface while the second one is an indication of the defect bottom location. The second level detail signal (*D2*) contains the defect signal as well, but with a poor time resolution due to using half the number of coefficients for signal reconstruction and a narrower spectral band compared to D1. Figure 3.16 presents both levels 1 and 2, Haar filter (high pass) transfer functions with a green dashed line indicating the defect echo frequency of 16.7 MHz. It can be found that more low frequency components (grey area) will be filtered on level 2 than on level 1, which means *D2* signal contains more low frequency echo information which can mask the higher frequency information associated with the defect. In addition, the depth resolution obtained from *D1* and *D2* are 0.0071 mm and 0.0142 mm respectively. Considering the inspection error tolerance is 0.04 mm[9], using *D1* to find the defect depth information has a higher accuracy.

Unfortunately, the third level detail signal (*D3*) and the approximation signal (*A3*) contain significantly less information of the defect, as observed from Figure 3.15. As a result of the application of wavelet analysis, the low frequency information has effectively been filtered out and the high frequency components are utilized to highlight the temporal characteristics of the defect in signal *D1*.

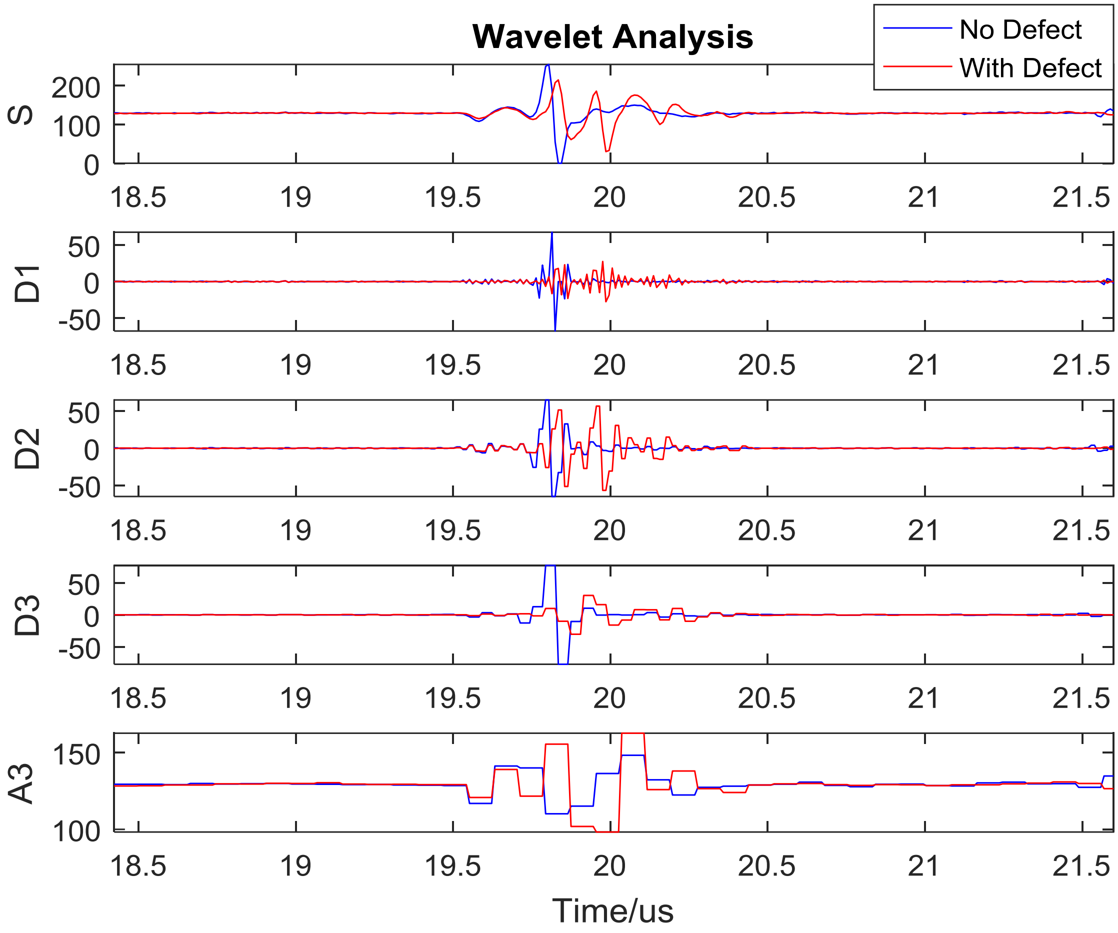

Figure 3.15 Wavelet analysis of no-defect signal and with-defect signal; S: original signal, D1: detail signal on level 1, D2: detail signal on level 2, D3: detail signal on level 3, A3: approximation signal on level 3

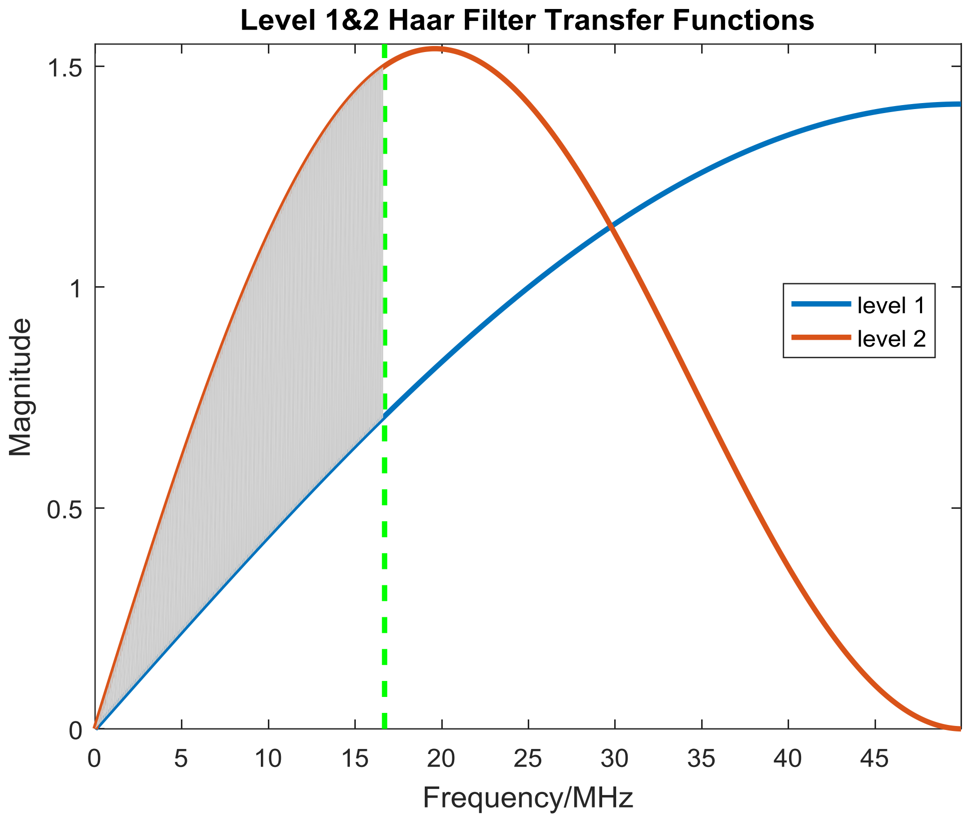

Figure 3.16 Level 1&2 Haar filter transfer functions (green dashed line indicates a frequency of 16.7 MHz)

Figure 3.17 displays the original A-scan signals and the corresponding wavelet analysis results. Firstly, a Hilbert transform is used to process these waveforms to generate the envelope representations. Then, the time of flight information between the peaks from the tube surface and defect is used for defect depth calculation. The original time domain signal from the defect, identified as red line in Figure 3.17 (a), poses significant challenges in selecting which peak accurately represents the defect depth. Whereas, the peaks in the envelope signal, presented in Figure 3.17 (b), can be clearly identified and used to calculate the defect depth. Subsequently, the depth calculation produced a depth 0.1207 mm. The original verified estimate of this defect depth from an experienced Analyst was 0.12 mm; hence, there is a measurement error less than 1% in this case, which is well within the expectation that defect depth errors should be within 0.04 mm.

(a) Original Signal

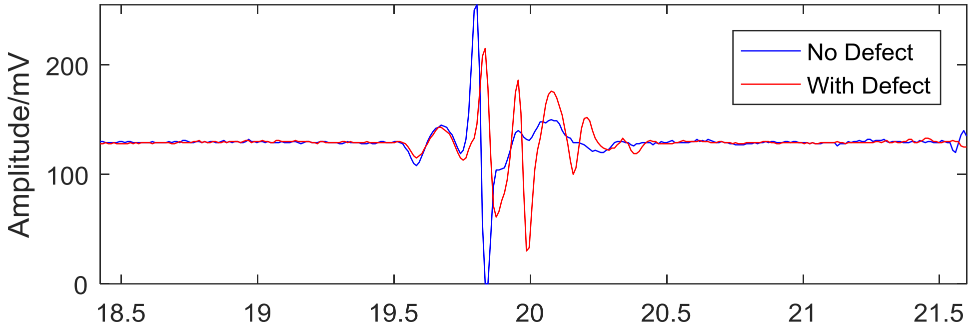

(b) Haar Wavelet Envelope Result

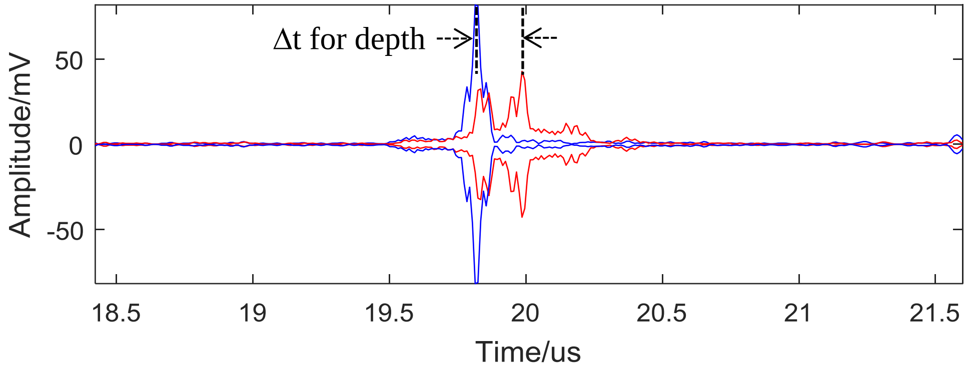

Figure 3.17 Original A-scan signals and envelopes of wavelet analysis detail signals on level 1 (no-defect signal and with-defect signal respectively)

3.3.2.4. Comparison between Wavelet Options

The selection of the wavelet used for signal processing is a compromise between time resolution and frequency resolution. Here four wavelets – Haar wavelet, db4 wavelet, sym6 wavelet and coif4 wavelet[49] – are selected for comparison, where their scaling functions and wavelet functions are presented in Figure 3.18. *Phi* is the scaling function and *psi* is the wavelet function. As the simplest known orthonormal wavelet, the Haar wavelet has extremely good time resolution, which should contribute to accurate time information for the extracted defect echo signal. While db4, sym6 and coif4 wavelets have similar wave shapes as ultrasonic signals with an expectation to take advantage of their time domain characteristics.

The transfer functions of the high pass filter on level 1 of all the wavelets are shown in Figure 3.19 with a green dashed line indicating a frequency of 16.7 MHz. With regard to the Haar wavelet, it illustrates the low frequency filtering effect as a gradual process as opposed to a rapidly changing characteristic presented by other wavelets. Importantly, in this implementation, the frequency resolution is sacrificed. Therefore, db4, sym6 and coif4 wavelets are considered further to compare the time and frequency balance.

The wavelet analysis approach was utilised on the data illustrated in Figure 3.13 and the results by employing all four wavelets are shown in Figure 3.20. All the signals with defect and without defect can easily be identified. Table 3.3 shows the defect depth measurements by utilizing Haar, sym6 and coif4 wavelets that have the same high accuracy while db4 wavelet does not show good performance. It is simple to find the signal amplitude has the largest value when using Haar wavelet, which is more than twice that of the other wavelets.

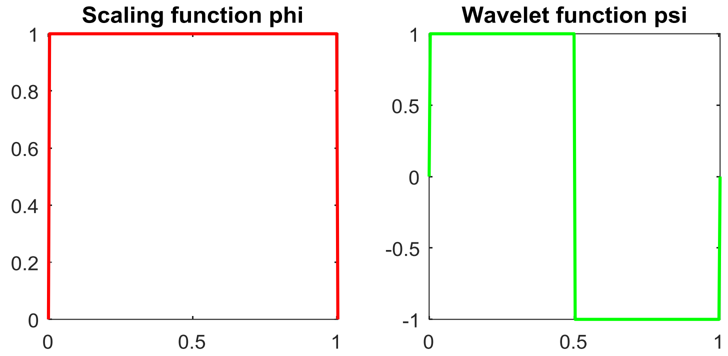

(a) Haar wavelet

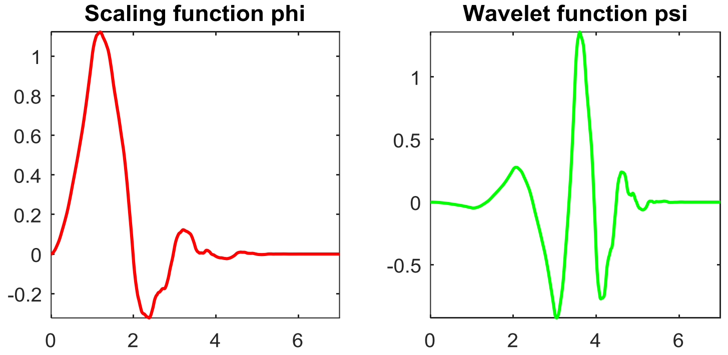

(b) db4 wavelet

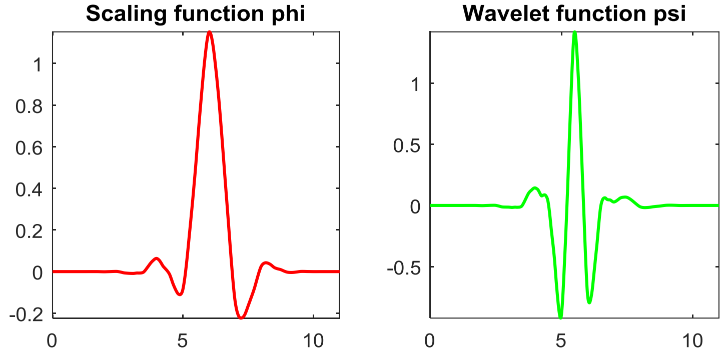

(c) sym6 wavelet

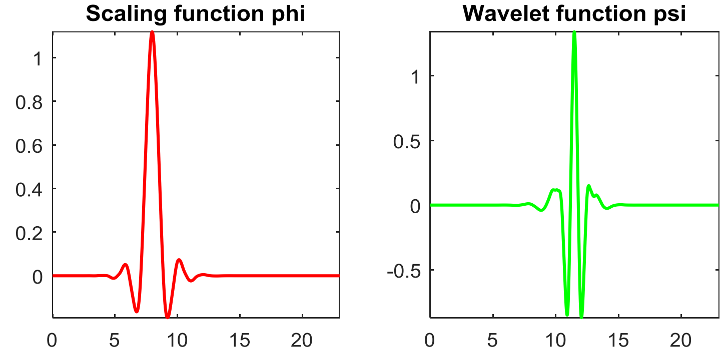

(d) coif4 wavelet

Figure 3.18 scaling function and wavelet function

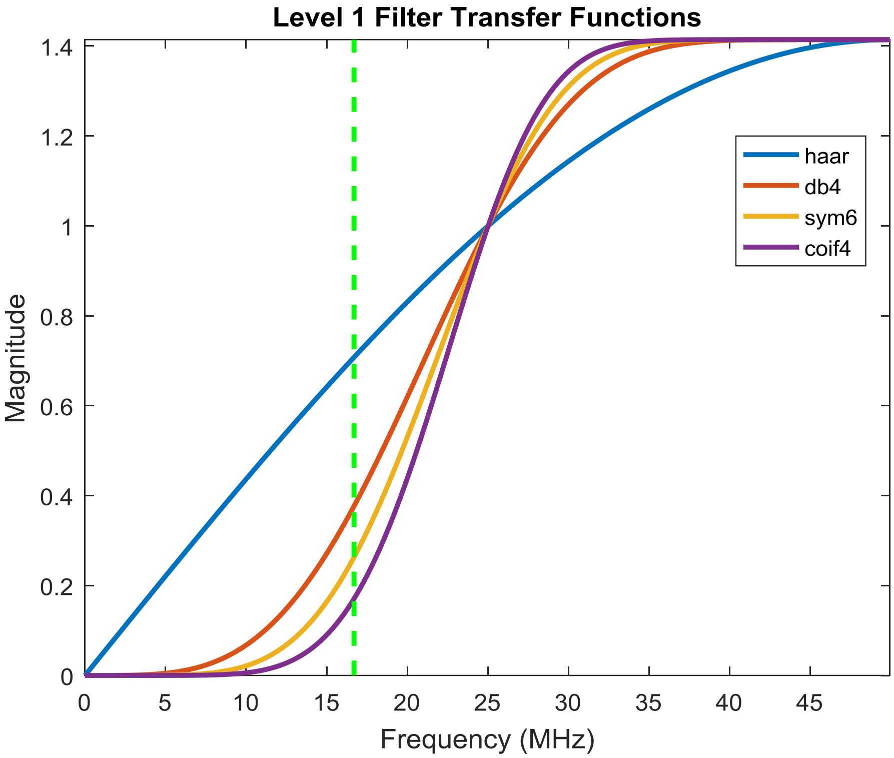

Figure 3.19 Level 1 filter transfer function – high pass

Table 3.3 Wavelet analysis results comparison

Wavelet	**haar**	**db4**	**sym6**	**coif4**	**Verified measurement**
Depth Result (mm)	0.1207	0.0994	0.1207	0.1207	0.12
Error (mm)	+0.0007	-0.0206	+0.0007	+0.0007	-
Defect Max Abs Amplitude (mV)	27.5	12.67	13.23	10.96	-

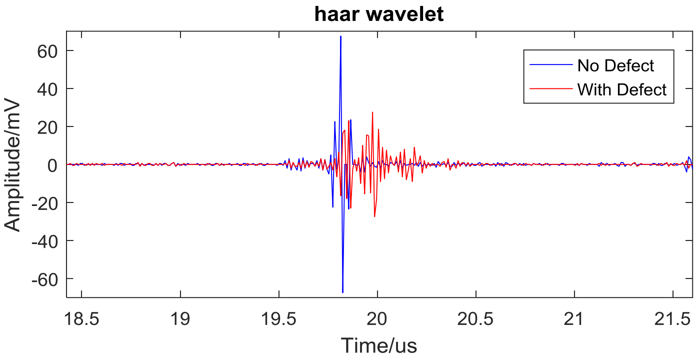

(a) haar wavelet

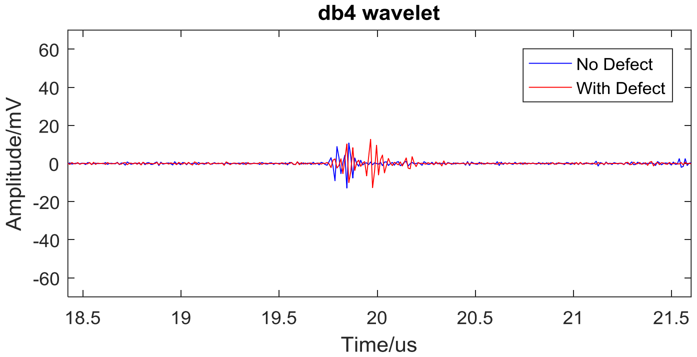

(b) db4 wavelet

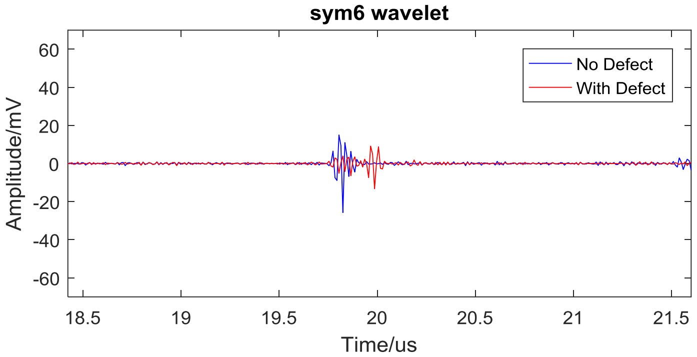

(c) sym6 wavelet

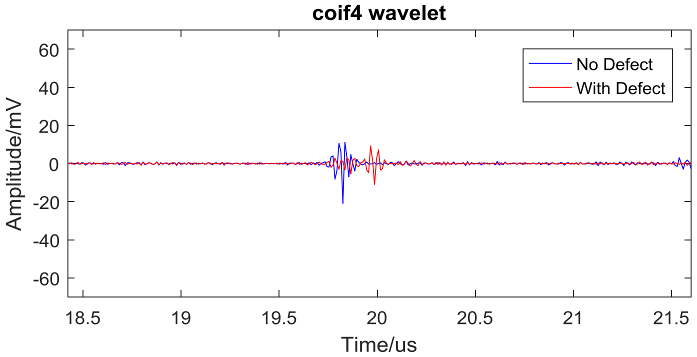

(d) coif4 wavelet

Figure 3.20 Wavelet analysis results – detail 1

Through application of the Haar wavelet, more details about high frequency components are maintained, which are particularly relevant to the defect information. In addition, a good time resolution can be obtained which is suitable for the requirement of measuring small defect depths. Hence, Haar wavelet has been chosen for evaluation of the wavelet analysis approach using a number of real industrial datasets.

3.3.3. Application on Industrial Datasets

To evaluate this approach further, 46 data acquisitions from 8 pressure tube scans have been selected and subjected to this wavelet analysis approach. The datasets were provided through Strathclyde's Advanced Nuclear Research Centre (ANRC) partnership with Bruce Power (Ontario, Canada). Importantly, 38 out of the 46 now show improved defect detection and defect depth calculations within the expected error range.

Table 3.4 compiles the results from all the datasets, presenting defect depth measurement results and the corresponding errors as compared to the verified results generated by an Analyst. The method still faces challenges to be able to reduce all the errors within the defined industrial requirement, which are highlighted by shading the background in the Table. These poor analysis results have weak frequency components near the transducer central frequency, while the good results show strong frequency components. The shape of the defects may cause difficulties for the reflected echo to be received by the ultrasound transducer, which can be additionally inspected by the pair of 10 MHz full-skip pitch-catch transducers. The author would like to compare the measurement results between using wavelet analysis and without processing for more direct comparison. However, more than half of the original datasets do not contain clear peaks for defect depth calculation. Therefore, comparing the processing result to industrial verified result is able to demonstrate that the wavelet analysis method can make the defect depth easier to be measured and provide an accurate result with acceptable the industrially accepted maximum error of 0.04 mm.

Table 3.4 Defect depth measurement results and errors

No.	**Bruce Power Identification Name**	**Defect Position (mm)**	**Wavelet Analysis Result (mm)**	**Verified Results (mm)**	**Errors |Δ| (mm)**
1	A1241 C07 (2603-2614)	2607.6	0.4686	0.32	0.1486
2	A1241 C07 (2944-2955)	2949.2	0.2982	0.28	0.0182
3	A1241 C07 (3752-3763)	3756.8	0.1775	0.18	0.0025
4	A1241 C07 (6321-6329)	6325.4	0.142	0.14	0.002
5	A1241 D15 (7381-7419)	7412.4	0.0852	0.12	0.0348
6	A1241 D15 (8322-8562)	8474.4	0.1207	0.1	0.0207
7	A1241 G12 (2568-2607)	2576.8	0.1136	0.13	0.0164
8	A1241 G12 (4126-4135)	4130	0.142	0.11	0.032
9	A1241 G12 (5440-5449)	5445.2	0.3408	0.32	0.0208
10	A1241 G12 (7397-7405)	7401.2	0.1633	0.15	0.0133
11	A1241 G12 (8412-8422)	8417.2	0.1775	0.15	0.0275
12	A1241 G12 (8475-8485)	8478.8	0.1065	0.1	0.0065
13	A1241 G12 (8630-8640)	8635.6	0.2485	0.21	0.0385
14	A1241 G12 (6874-6887)	6881	0.1775	0.2	0.0225
15	A1241 G12 (6874-6887)	6880.4	0.2627	0.27	0.0073
16	A1241 Q14 (2838-2849)	2844.2	0.2698	0.28	0.0102
17	A1241 Q14 (3250-3266)	3259.8	0.1775	0.12	0.0575

18	A1241 Q14 (4593-4620)	4612.8	0.2272	0.23	0.0028
19	A1241 Q14 (8606-8657)	8618.4	0.1136	0.12	0.0064
20	A1241 Q14 (6127-6135)	6130	0.1562	0.17	0.0138
21	A1431 D16 (5608-5890)	5853	0.1846	0.38	0.1954
22	A1431 D16 (5608-5890)	5873	0.1349	0.16	0.0251
23	A1431 D16 (5847-5857)	5851.4	0.4757	0.38	0.0957
24	A1431 D16 (5869-5878)	5873.2	0.1278	0.16	0.0322
25	B1381 D17 (3152-3155)	3153	0.1207	0.12	0.0007
26	B1381 D17 (4302-4305)	4303	0.1775	0.11	0.0675
27	B1381 D17 (4478-4484)	4479.6	0.213	0.11	0.103
28	B1381 D17 (4548-4552)	4549.4	0.3195	0.32	0.0005
29	B1381 D17 (5171-5174)	5173.6	0.1136	0.11	0.0036
30	B1381 D17 (6308-6320)	6313.8	0.1491	0.15	0.0009
31	B1561 C14 (3690-3700)	3694.2	0.142	0.11	0.032
32	B1561 C14 (4973-4983)	4976.2	0.2485	0.21	0.0385
33	B1561 C14 (4996-5008)	4998.4	0.1136	0.11	0.0036
34	B1561 C14 (5356-5379)	5361.2	0.1562	0.11	0.0462
35	B1561 C14 (5482-5488)	5484.6	0.1775	0.15	0.0275
36	B1561 C14 (5513-5523)	5517.8	0.1988	0.19	0.0088
37	B1561 C14 (8208-8216)	8212	0.1562	0.15	0.0062
38	B1561 C14 (8707-8727)	8716.6	0.0994	0.11	0.0106
39	B1561 C14 (7119-7128)	7124.8	0.2769	0.11	0.1669
40	B1561 N10 (8715-8722)	8717.2	0.1491	0.15	0.0009
41	B1561 N10 (5659-5670)	5662.2	0.1349	0.11	0.0249
42	B1561 N10 (5720-5731)	5724	0.1065	0.11	0.0035
43	B1561 N10 (5720-5731)	5727	0.1349	0.12	0.0149
44	B1561 N10 (6359-6367)	6362.4	0.1917	0.18	0.0117
45	B1561 N10 (6377-6386)	6380.2	0.1917	0.19	0.0017
46	B1561 N10 (6385-6392)	6387.2	0.1704	0.16	0.0104

3.3.4. Summary of Wavelet Analysis Approach

The wavelet analysis method of extracting defect depth information from poorly-focused A-scan signals associated with pressure tube inspection was proposed in this Section. The spectral characteristics associated with ultrasonic echoes from the tube wall and the defect have similarities in the low frequency range (2-10 MHz), but the defect signal has a distinct spectral peak between 15-20 MHz. The use of different wavelets was analysed including Haar, db4, sym6 and coif4 to find the best defect depth information. A Haar wavelet approach has been adopted to exploit this difference in the frequency domain, whilst maintaining good temporal accuracy. Results on 48 datasets demonstrate the success of this signal processing approach, with good agreement between the processed defect depth and the reported defect depth by an experienced Analyst in over 80% of cases. It is envisaged that utilization of this advanced processing method could improve depth measurements from poorly-focused A-scan datasets and thereby save on the cost of further inspection processes, for example precise depth measurement from replicas.

3.4. Summary

In this Chapter, SAFT processing of poorly-focused B-scan images and wavelet analysis of A-scan signals for CANDU pressure tube inspection were presented with the objective to improve the accuracy of defect width and depth measurements.

The SAFT algorithm for focused transducer required modification from the standard unfocused transducer approach to include accurately calculated time difference between the neighbouring positions. Importantly, the approach is sensitive to the transducer focal length value used in the algorithm. The effect of different focal length values was analysed and the corresponding results show that SAFT processing can improve the defect width measurement more than 0.2 mm using a matched synthetic aperture. In Chapter 5, the SAFT approach will be extended for use with the ultrasonic phased array techniques proposed as a potential replacement for the single element transducers currently used in the CIGAR sensor head.

Wavelet analysis method was shown to improve defect depth information from poorly-focused A-scan signals by extracting signal's spectral characteristics associated with ultrasonic echoes from the tube wall and the defect. Four different wavelets were analysed to find a trade-off between time and frequency resolution. The Haar wavelet was chosen as most appropriate for this inspection scenario as it was able to obtain more defect relevant information, whilst maintaining a good temporal accuracy.

Chapter 4

Hybrid Simulation of Ultrasonic Inspection of Pressure Tube

4.1. Introduction

Currently, single element ultrasonic transducers are used for the inspection of the pressure tubes in the CANDU reactor[11]. With the advances in the design and processing associated with phased array technology[16], there is scope for the current single element approach to be replaced using an array system. The performance of phased array technology has been demonstrated in a number of NDT applications, for example, testing of welds[108], railway wheel inspection[109] and turbine blade inspection[14]. Moreover, the combination of array technology and advanced signal processing has been applied to complex geometry components[15][110][111]. A key advance in phase array inspection was the introduction of FMC approach and the accompanying post-processing algorithm TFM[18][112]. As a gold standard imaging algorithm, TFM has played a significant role in NDT such as inspecting complicated geometries[113] and crack depth measurement[38]. This approach has also been extended to consider multi-mode operation[18] and angled wedge transduction[114]. Importantly, Zhang et al compared

TFM to two other imaging algorithms, phased-coherent imaging (PCI) and Spatial Compounding Imaging (SCI), with TFM outperforming these other approaches for a variety of defect types[112]. In order to determine the potential benefits of applying phased array technology in the inspection of CANDU pressure tubes, a simulation programme is required to consider the performance of an ultrasonic array transducer operating in FMC data acquisition mode and subsequent imaging implemented using TFM.

However, the challenge of the modelling of the pressure tube inspection is that high frequency transducers (10 MHz and 20 MHz) are currently used in the process, with a two-way propagation path in heavy water of approximately 40 mm for 10 MHz transducer and 25.4 mm for 20 MHz transducer. For a conventional Finite Element (FE) modelling approach, this creates two serious issues: unreliable simulation results due to numerical dispersion errors[90][91] and prohibitively long simulation times when modelling the entire system.

In this Chapter, 2-D hybrid models were developed by combining a FE package and a simplified but accurate analytical extrapolation approach to provide a solution to overcome the inherent restrictions in employing a full-scale FE model. In Section 4.2, a feasibility study of the hybrid modelling approach is evaluated by simulating a single element focused transducer inspection. The pulse-echo signals of simulation and experiment are compared and the model's capability for defect depth measurement is studied. The extension to a phased array hybrid model is presented in Section 4.3. FMC data is acquired from the model and the TFM algorithm is applied to image tube ID and

OD surfaces. A range of array element configurations are explored in the model and all the simulation results are validated by experiment.

4.2. Single Element Transducer Inspection Model

4.2.1. Single Element Hybrid Model - Problem Definition

The simulation of the ultrasonic inspection of the pressure tubes is essential for the analysis of potential techniques to improve the accuracy and/or efficiency of the inspection. The pressure tube is a zirconium alloy which has an inside diameter of 104 mm and a thickness of 4.3 mm[11]. Currently, a CIGAR tool, which contains six focused ultrasonic transducers with frequencies of 10 MHz and 20 MHz, is immersed in heavy water during the inspection and the water path is around 20 mm for 10 MHz transducer and 12.7 mm for 20 MHz transducer. A wave propagation distance of 20 mm in water contains 133 wavelengths for 10 MHz transducer and that 12.7 mm contains 169 wavelengths for 20 MHz transducer. A simulation platform of the existing testing method forms the basis of the development of phased array methods to improve the accuracy of the inspection. PZFlex is used for the simulation. This software package has been applied to NDT problems using its explicit time-domain approach which brings about rapid simulation time[79][115][116]. However, the serious numerical dispersion phenomenon associated with the large size model impacts on the accuracy of this approach. To decrease the influence of the numerical dispersion, the FE simulation will be restricted to model both the transducer and pressure tube sections and will be combined with analytical extrapolation of wave propagation in the fluid.

In order to simplify the process of developing this hybrid model and make the validation process simpler to be realized at the initial development stage, water and titanium, which has the same crystal structure as zirconium, are used in the simulation as well as experiment.

4.2.2. Hybrid Single Element Model Simulation

The hybrid model of single element transducer inspection contains five subsequent components: ultrasound transmission; transmission extrapolation (wave propagation); target interaction; echo wave extrapolation and ultrasonic reception. The ultrasound transmission, target interaction and ultrasonic reception parts are simulated using the FE method to take advantage of its accurate analysis of the wave interaction parts of the model, while the analytical extrapolation analysis method is employed for the wave propagation between the transducer and the pressure tube for computational efficiency.

The complete model is decomposed into five parts as shown in Figure 4.1.

- H1 (Ultrasound transmission)
- H2 (Transmission extrapolation)
- H3 (Target interaction)
- H4 (Reception extrapolation)
- H5 (Ultrasonic reception).

The model simulates a focused transducer immersed in a water load, with a titanium tube used as the target feature for the inspection. Only the longitudinal section of the tube inspection is analysed in this initial model validation section.

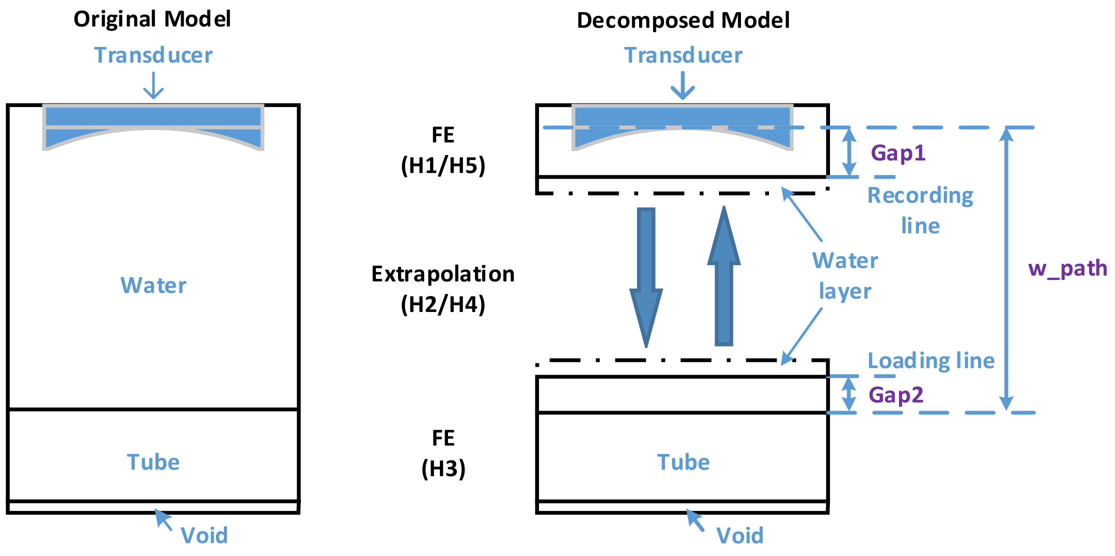

Figure 4.1 Hybrid model decomposition - single element transducer inspection

4.2.2.1. Finite Element Modelling

The simulation of ultrasound transmission, target interaction and ultrasonic reception are executed in PZFlex.

Ultrasonic transmission is shown in Figure 4.1 as H1 is defined as a FE process. The diameter of the transducer is 9.5 mm, with the transducer represented using two solid blocks of transducer material with the outer layer being a lens with a focal length of 33 mm attached to the transducer front face. These transducer parameters have been used as they relate to a physical transducer available within CUE and will enable experimental validation of the modelled scenario. The calculation of lens geometry in the model is introduced in Appendix A. The model excitation will be a mechanical pressure loading applied at the interface between these two solid blocks representing the transducer, with reflection at the outer surface (top) block minimised by application of an absorbing boundary condition. After excitation, the FE model records the received signals across the full aperture width at a specified distance from the transducer, this distance is defined as *Gap1* in Figure 4.1, and these signals are then stored for use by the extrapolation phase, H2, of the model. *Gap1* should be longer than the excitation signal and the lens edge to ensure the entire wave is recorded. The minimum running time of the model H1 $t_{m1,min}$ should guarantee that the wave transmitted from the full aperture can be received by any position through the ROI. This can be expressed by Equation 4.1 and Figure 4.2 provides the geometric configuration of the modelling time calculation.

$$t_{m1,min} = \frac{L_{m1}}{c_w} \tag{4.1}$$

Since $\frac{L_{m1}}{L_s} = \frac{Gap1}{L_w}$, then we have $t_{m1} = \frac{Gap1 * Ls}{L_w * c_w} = \frac{Gap1 * \sqrt{{L_w}^2 + {L_a}^2}}{L_w * c_w}$, where L_s is the bevel edge of the triangle composed of the water path L_w and transducer aperture L_a. L_{m1} is the bevel edge of the triangle cut off by the recording line and c_w is the wave velocity in water.

Ultrasonic reception is effectively the reciprocal with respect to the transmission process, with H4 the extrapolation phase and H5 defined as the FE receiver model.

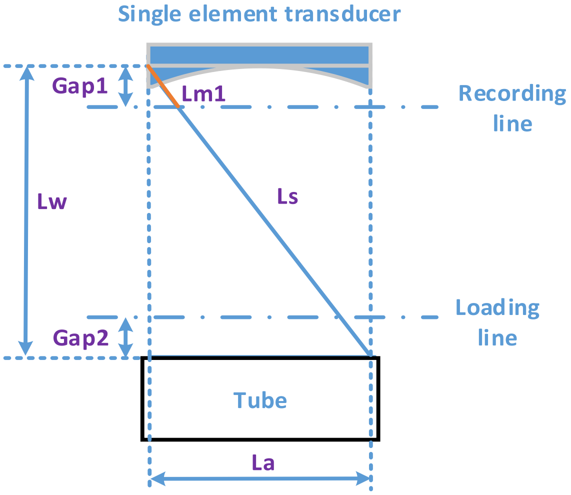

Figure 4.2 Geometric configuration of modelling time calculation – single element transducer

The final FE model part represents the target interaction, H3, for the inspection of the pressure tube. The transmitted waves after the process of extrapolation (H2) are loaded as the input to this FE model, with a small water channel included prior to the tube wall itself – this is defined in Figure 4.1 with a thickness of *Gap2*. Since the loading line is used for recording the echo wave as well, *Gap2* should be long enough to let the recorded transmitted wave be completely loaded into model H3 to avoid unwanted signals being recorded. After that, the recording can start. The minimum length of *Gap2* can be obtained by Equation 4.2. The FE model will simulate the ultrasonic interaction with the component, including defects if included, and the returning echoes will be recorded at the same interface for use by the receive extrapolation model, H4.

$$Gap2_{min} = t_{m1} * c_w \tag{4.2}$$

where t_{m1} is the running time of model H1.

To avoid corner and boundary effects caused by loading of waves on the boundary, an additional water layer is augmented onto each of the sub-models H1 (bottom), H3 (top) and H5 (bottom).

4.2.2.2. Extrapolation Method

The modelled parts of wave propagation, H2 and H4, employ the extrapolation method which combines the Green's functions and Huygen's principle[117] to deal with the high frequency wave propagation in the homogeneous water load. The details of this method are given in Appendix B. Importantly, there is an extrapolation function in PZFlex which can realize the extrapolation for both the outward transmitted wave and the returned echo wave(s) from the titanium tube target.

4.2.3. Simulation Example

The use of the analytical extrapolation of the wave propagation in the water reduces the complexity of the FE model used to simulate this inspection scenario. This is a computationally efficient approach and can improve the accuracy of the simulation by decreasing the influence of the numerical dispersion phenomenon associated with the FE method. These analytical modules are combined with the previously described FE models to produce a full pulse-echo simulation framework. Figure 4.3 displays the excitation signal used to drive the transducer in the model and a snapshot of the ultrasonic wave propagating in the water load. The simulation parameters associated with the excitation signal are 10 MHz focused transducer with a diameter of 9.5 mm and a focal length of 33 mm. All of the simulation parameters are detailed in Table 4.1. The modelled result from the transmitted wave propagation shows the waveform at a distance about 30 mm in front of the transducer. Note that this is close to the focal point of the transducer. The -6 dB width of this signal is 0.58 mm and the thickness is 0.04 mm, which provides a reference for the setting of the defect size in the model to test the capability of the defect depth measurement.

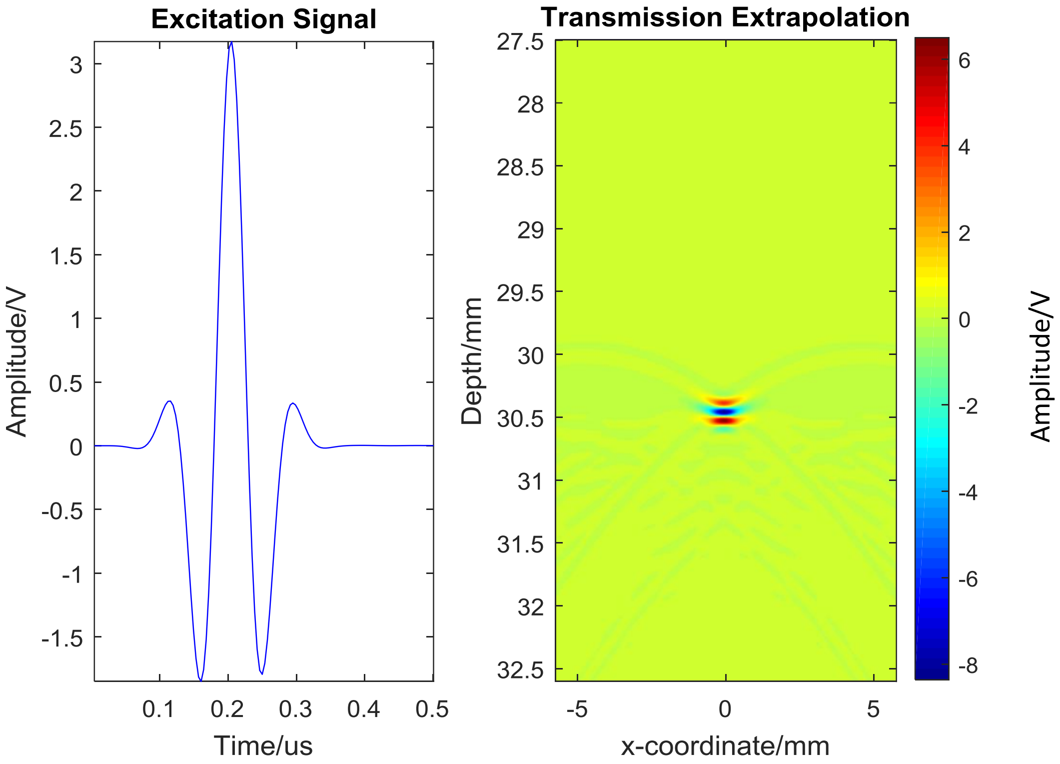

Figure 4.3 Illustration of the transducer excitation signal and a snapshot of the propagating wave close to the focal point.

Table 4.1 Parameters of simulation configuration – single element transducer

Items	**Parameters**	**Values**
Transducer	Central frequency	10 MHz
	Diameter	9.5 mm
	Focal length	33 mm
	Wavelength in water	0.148 mm
Water layer	Gap1	2.5 mm
	Gap2	2.5 mm
Water path	Length	33 mm
Titanium plate	Thickness	5 mm

4.2.4. Capability of Defect Depth Measurement

In order to test the defect inspection capability of the hybrid model, a slot is introduced into the target part of the hybrid model. The slot is situated at the centre of the tube surface with both depth and width of 1mm, as illustrated in Figure 4.4 (a), and the centre of the transducer is axially aligned with the centre of the defect. Again, the simulation parameters are as described in Table 4.1. The received signals from the hybrid model with and without the slot are shown in Figure 4.4 (b). The blue solid line in the Figure indicates the received signal from a model without defect on the tube surface. The red dashed line in the Figure indicates the received signal from a model with a defect.

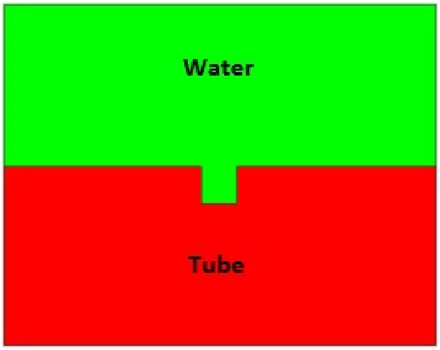

(a) Target part of the hybrid model with a slot

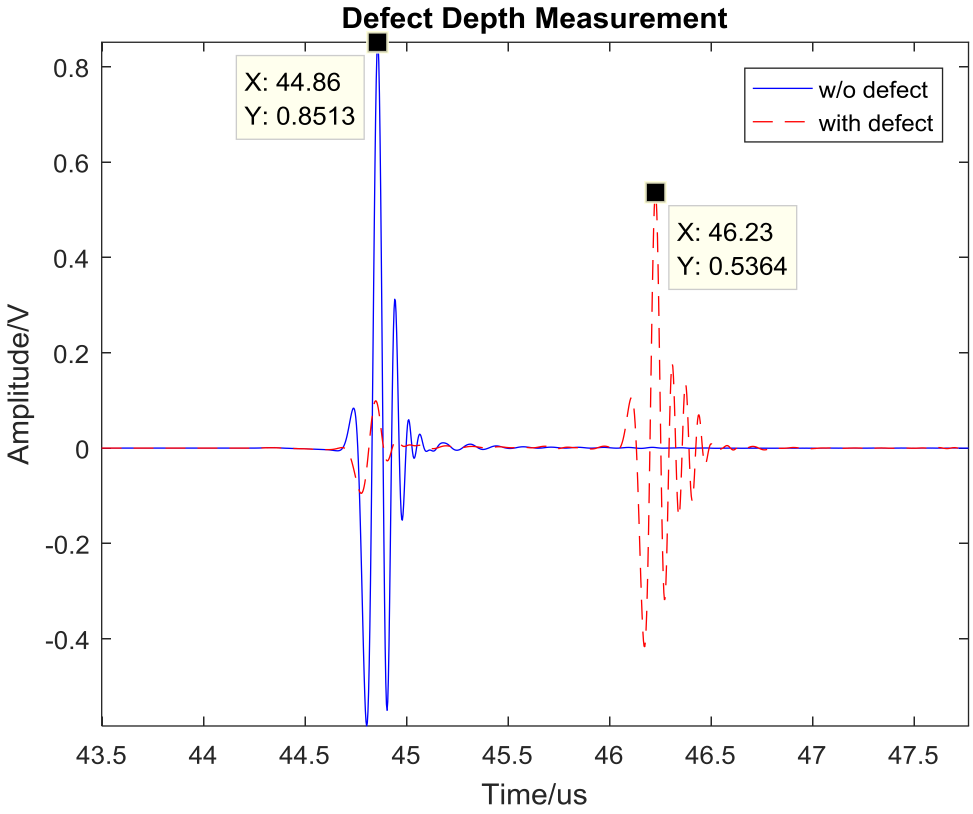

(b) Comparison of 10 MHz single element model with and without a defect

Figure 4.4 Simulation of pulse-echo response from a slot defect

Two signal peaks have been identified using data cursors in Figure 4.4 (b) to illustrate the reflected signals from the tube surface and the backface of the slot, respectively. The depth information is calculated from the time difference between the reflections of the tube surface and of the bottom of the slot. Table 4.2 presents the depth information obtained from 10 MHz and 20 MHz transducers as well as the measurement errors. Note, the 20 MHz device has the same parameters as shown in Table 4.1 for the 10 MHz device, but is driven at a higher frequency. The wave speed for water used in the model is 1480 m/s. According to the calculated results, the defect depths are 1.0138 mm and 1.0064 mm from the hybrid model for 10 MHz and 20 MHz transducers, giving measurement errors of +13.8 µm and +6.4 µm respectively.

Table 4.2 Depth information obtained from hybrid model

Transducer Frequency	**Peak Time**		**Depth**	**Error**
	w/o defect	**with defect**		
10 MHz	44.86 µs	46.23 µs	1.0138 mm	+13.8 µm
20 MHz	44.74 µs	46.10 µs	1.0064 mm	+6.4 µm

In terms of these results, it can be found that the error of the inspection simulated in the hybrid model is less than 1.5% for both transducer configurations. Therefore, the validity of this hybrid model has been demonstrated and it is reliable for simulating high frequency inspection of a pressure tube.

4.2.5. Experimental Verification

The transducer illustrated in Figure 4.1 is not fully represented in the model as this is a commercial device and full details of the construction and materials are unknown. Hence, in the first iteration of the model a generic excitation waveform was used. However, in order to maintain suitable accuracy in the model, the transducer response is experimentally measured and subsequently used as the input excitation function. To achieve this a membrane hydrophone, as illustrated in Figure 4.5 (a), was positioned at the focal length of 33 mm, for the 10 MHz transducer and the waveform measured in a water load. The acquired signal is presented in Figure 4.6, in both the time (note: DC offset has been removed) and frequency domain representations.

To experimentally validate the hybrid modelling approach, a pulse-echo experiment setup was used, as shown in Figure 4.5 (b) (c) and (d). Here, the 10 MHz transducer is immersed in the water and the first echo recorded from a flat titanium plate with a thickness of 5 mm. The reflected signal from the surface of the titanium plate in the experiment is recorded and compared to that predicted by the hybrid model, where the input excitation to the model is the measured transducer response, as presented in Figure 4.6. Comparisons of the received signals are presented in Figure 4.7, with normalized amplitudes, and show the time-domain signals and their frequency spectra, respectively. Good correlation is demonstrated in the time-domain result, albeit the initial half cycle is not well aligned and the simulation demonstrates a slightly longer ringdown. These issues are clearly evident from the frequency spectra comparison, in which both spectra have similar profiles but the predicted result seems to have undergone additional attenuation/damping.

Nevertheless, the accuracy of the temporal characteristic is considered sufficient for the intended purpose of evaluation of the CANDU transduction system used for pressure tube inspection.

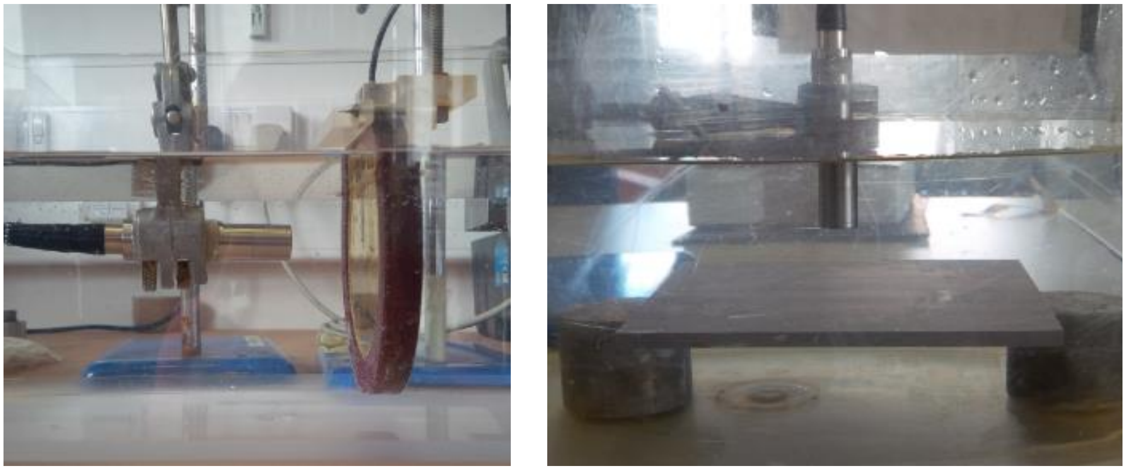

(a) hydrophone reception;

(b) pulse-echo configuration using a 5mm thick titanium plate

(c) oscilloscope

(d) pulser-receiver

Figure 4.5 Experimental setup used to validate single element simulation model

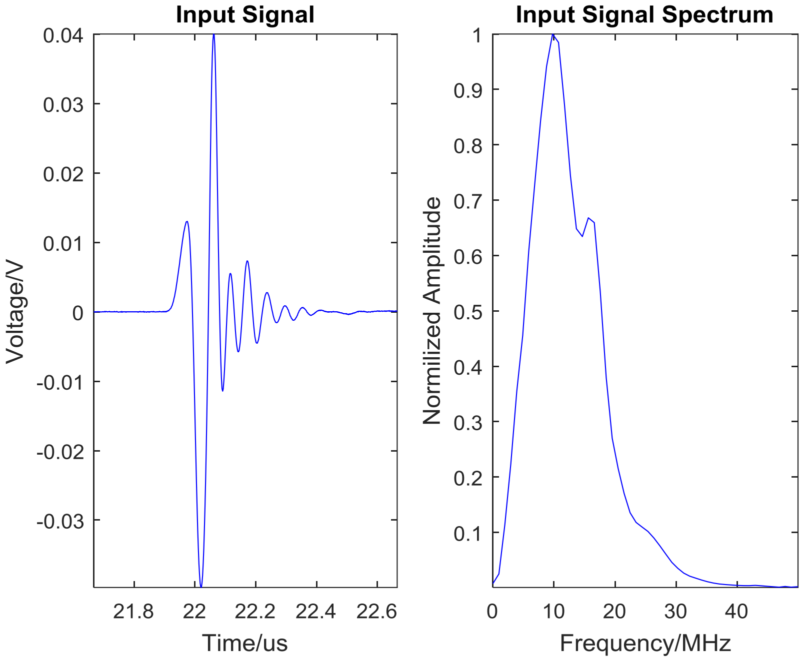

Figure 4.6 The input signal used in the hybrid model recorded by a hydrophone situated at the focal point of the transducer

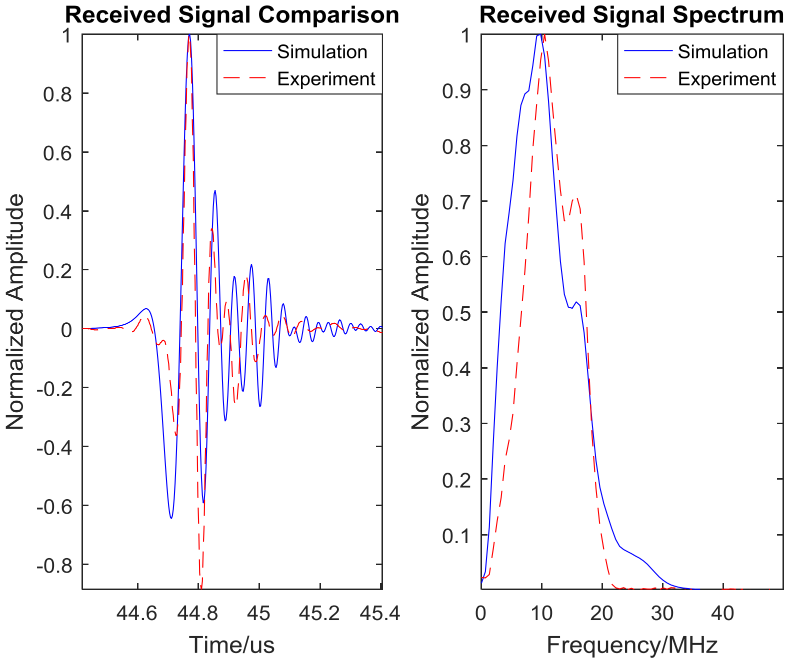

Figure 4.7 Comparison of the signals received from the front face of a titanium plate: both the simulation and the experimental signals in time-domain and the corresponding spectra are shown

4.3. Phased Array Transducer Inspection Model

In this Section, a simplified inspection scenario will be used to develop an efficient hybrid simulation platform to overcome the influence of numerical dispersion errors associated with high frequency ultrasonic phased array inspection of thin metallic tubes with large diameter with respect to the ultrasonic wavelength. To validate the model, a flat plate geometry will be utilised, which assumes the transducer is aligned axially along the length of the tube, as depicted by the longitudinal section in Figure 4.8. Accurate representation of the ID and OD surface condition is the goal of these pressure tube inspections and Figure 4.8 presents the cross section and longitudinal section geometries. FMC will be acquired from the platform for signal post-processing using the TFM algorithm. The key contribution in this work is in the application of hybrid simulation models for high frequency ultrasonic phased array inspection to produce high resolution TFM images of the ID and OD surfaces. Importantly, this Section develops the simulation model and describes the model validation, which will be utilised as the simulation platform for the ongoing research and development of phased array technology for use in pressure tube inspection applications and described in Chapter 5.

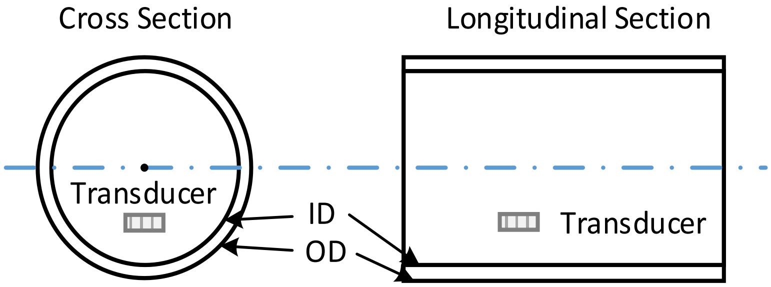

Figure 4.8 ID and OD surfaces of a pressure tube shown in both cross section and longitudinal section representations

4.3.1. Phased Array Hybrid Model - Problem Definition

In order to overcome the inherent restrictions in using a full-scale FE model, the focused transducer hybrid simulation platform described in Section 4.2 is extended to simulate a phased array transducer inspection. This 2-D hybrid array model contains the same five components as described in Section 4.2.2. for the single element modelling approach: ultrasound transmission; transmission extrapolation (wave propagation); target interaction; echo wave extrapolation and ultrasound reception. The key difference is the definition of array elements at the transducer location and the data acquisition methodology (i.e. FMC), which excites each element of the phased array transducer individually and in sequence, while all the elements are used to receive the echo signals.

4.3.2. Hybrid Array Model Simulation

The complete phased array simulation platform is decomposed into five parts as shown in Figure 4.9. These match the methodology used in the focused transducer hybrid model: H1 (Ultrasound transmission), H2 (Transmission extrapolation), H3 (Target interaction), H4 (Reception extrapolation) and H5 (Ultrasound reception). Again, PZFlex is applied to model the simulation of ultrasound transmission, target interaction and ultrasonic reception; and the wave propagation is calculated through an analytical extrapolation method.

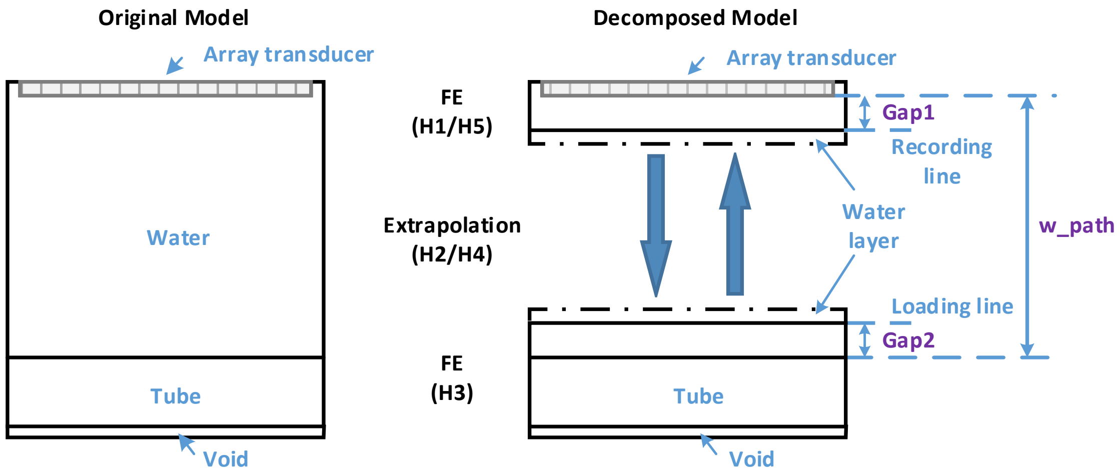

Figure 4.9 Decomposition of phased array hybrid simulation platform

In Figure 4.9, H1 is defined as the ultrasonic transmission which simulates multiple elements generating ultrasound. The number of the elements is configurable and simulated using a mechanical pressure loading technique in which each element is driven using a Ricker wavelet[118], with specified frequency, to simulate the generation of ultrasonic pressure at the front face of the array. A 1 mm water layer is added onto both sides of the transducer to extend the width of the model and an absorbing boundary is set to eliminate reflections from the model sides. When the waves are transmitted, a recording line is located at a specified distance *Gap1* from the transducer and across the full aperture to record the propagating signals at each iteration of the FMC data acquisition. *Gap1* should be longer than the length of Ricker wavelet to ensure the entire wave is recorded. The minimum running time of the model H1 is $t_{m1,min}$ and should guarantee that the wave transmitted from the first element can be received by the last element through ROI. The geometric configuration of the modelling time calculation is visualised in Figure 4.10 and can be expressed using Equation 4.1, where L_a is the array transducer aperture in this case.

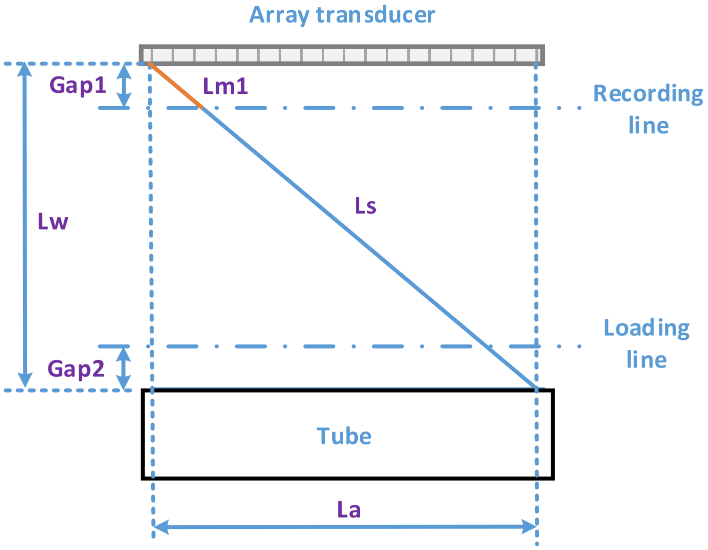

Figure 4.10 Geometric configuration of modelling time calculation – array transducer

All these signals are saved for use by the extrapolation phase, H2, of the model. The ultrasonic reception model H5 uses reciprocity with respect to the transmission process, while the extrapolation waves from H4 are loaded into the model from the recording line and every array element records the returning ultrasonic echoes from the pressure tube.

The final FE model H3 simulates the target interaction of the pressure tube inspection. After the operation of extrapolation through H2, the transmitted waves are loaded as an input of the H3 model, where a thickness of *Gap2* between the loading line and the tube wall is included. Since the loading line is used for recording the echo wave as well, *Gap2* should be long enough to let the recorded transmitted wave be completely loaded into model H3 to avoid unwanted signals being recorded. The minimum length of *Gap2* can be obtained through Equation 4.2.

For the purpose of avoiding corner and boundary effects due to the loading waves on the boundary between the FE and the extrapolation layer, an additional water layer of about 10 wavelengths is supplemented onto each of the sub-models H1 (bottom), H3 (top) and H5 (bottom).

4.3.3. Surface Imaging Algorithm

The main defects of interest in the CANDU reactor pressure tubes are situated on the tube surfaces. TFM is a popular and reliable phased array imaging algorithm and can be used for the imaging of the tube inner and outer surfaces. The acquired FMC dataset from the hybrid array model is used in post-processing to generate a desired TFM image. TFM uses the FMC echo data to focus all contributions from each array pair onto a high resolution mesh of the target area of interest, as described in Section 2.2.2.1. The intensity of an arbitrary pixel in the TFM image is described in Equation 2.25.

The resolution for imaging the near wall defects is 0.01 mm in this Thesis. The high resolution is aiming at showing the accurate defect size information especially for defect depth which should be reported when it is larger than 0.1 mm. However, when a lower resolution is used for presenting the defects, the imaging results are not able to show the accurate defect size. Based on the test of imaging using different resolution, a resolution higher than one fifth of the wavelength of the medium (water) is recommended for more accurate size measurement.

4.3.3.1. Inner Tube Diameter

The TFM algorithm in Equation 2.25 can be applied to image the ID wall surface directly by using water as the only medium in the algorithm. This method makes the defects on the inner surface visible and the defect depth information can be determined by taking measurements from the defect bottom and the tube inner surface.

4.3.3.2. Outer Tube Diameter

OD imaging algorithm involves two materials - water and zirconium (or titanium), which requires a more complex calculation and Equation 2.25 cannot be applied directly. Snell's law provides a solution to determine the relevant time of flight information through the use of ray tracing[119]. Figure 4.11 presents an array element situated at point *A* which is triggered to transmit an ultrasonic wave to reach point *B* within the tube wall via point *P* on the interface. Following the application of Snell's law, the x-coordinate of *P* can be obtained by solving Equation 4.3, where c_w and c_t are the wave velocity in water and tube respectively.

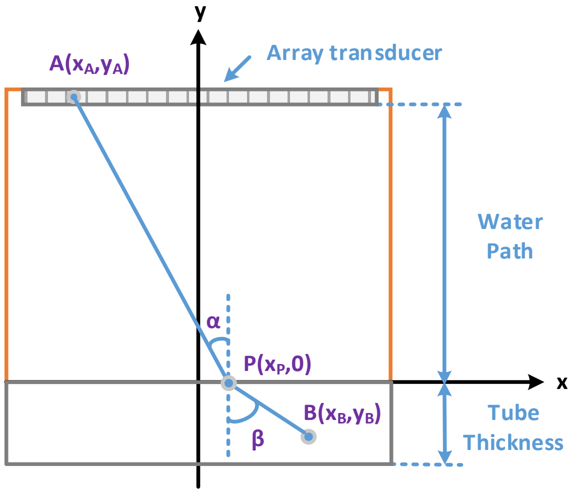

Figure 4.11 Geometric illustration of outer diameter imaging

$$\frac{(x_P - x_A)/\sqrt{(x_A - x_P)^2 + {y_A}^2}}{(x_B - x_P)/\sqrt{(x_B - x_P)^2 + {y_B}^2}} = \frac{c_w}{c_t} \tag{4.3}$$

Once the time information of the ray tracing of the target area is calculated, the TFM algorithm for the second layer medium as described in Equation 4.4 can be employed to image the OD surface.

$$\begin{aligned} I_{2nd}(x,y) &= \sum_{i=1}^{N}\sum_{j=1}^{N} f_{Tx,Rx}\left(\frac{\sqrt{\left(x_{A,i} - x_{p,i}\right)^2 + {y_{A,i}}^2} + \sqrt{\left(x_{A,j} - x_{p,j}\right)^2 + {y_{A,j}}^2}}{c_w}\right. \\ &\left. + \frac{\sqrt{\left(x_B - x_{p,i}\right)^2 + {y_B}^2} + \sqrt{\left(x_B - x_{p,j}\right)^2 + {y_B}^2}}{c_t}\right) \end{aligned} \tag{4.4}$$

However, the solution of Equation 4.3 encounters difficulty when the denominator is infinitely small. A computationally efficient solution was developed by Dziewierz and Gachagan[120] that offered a time map to support the ray tracing function. In this context, the time map represents the time of flight from an array element to every pixel in the desired image space. This is repeated for every array element, with the reception time of flight implemented using reciprocity. Hence, when determining the overall path length during the TFM imaging algorithm, these time maps are used as an effective look-up table instead of the mathematical approach utilised in Equation 4.4. Figure 4.12 shows a time map of the 1st element of a 32 element array transducer in a target area below tube inner surface with a pixel resolution of 10 µm (water path = 12.7 mm). The x-coordinate covers a width equivalent to the array transducer length and is symmetrical to the centre of the transducer, while the y-coordinate sets the zero position on the tube inner surface. The Figure presents the time spent from the element to any pixel in the target area. The upper left-hand corner involves a shorter transit time that relates to an area close to the transmit element and the transit time varies across this area until it becomes a maximum in the bottom right-hand corner. This approach enhances the TFM algorithm efficiency when imaging through a second material layer. In this work, the ID and OD imaging are kept separate to simplify the modelling approach and to mimic the way in which an Analyst would review such datasets.

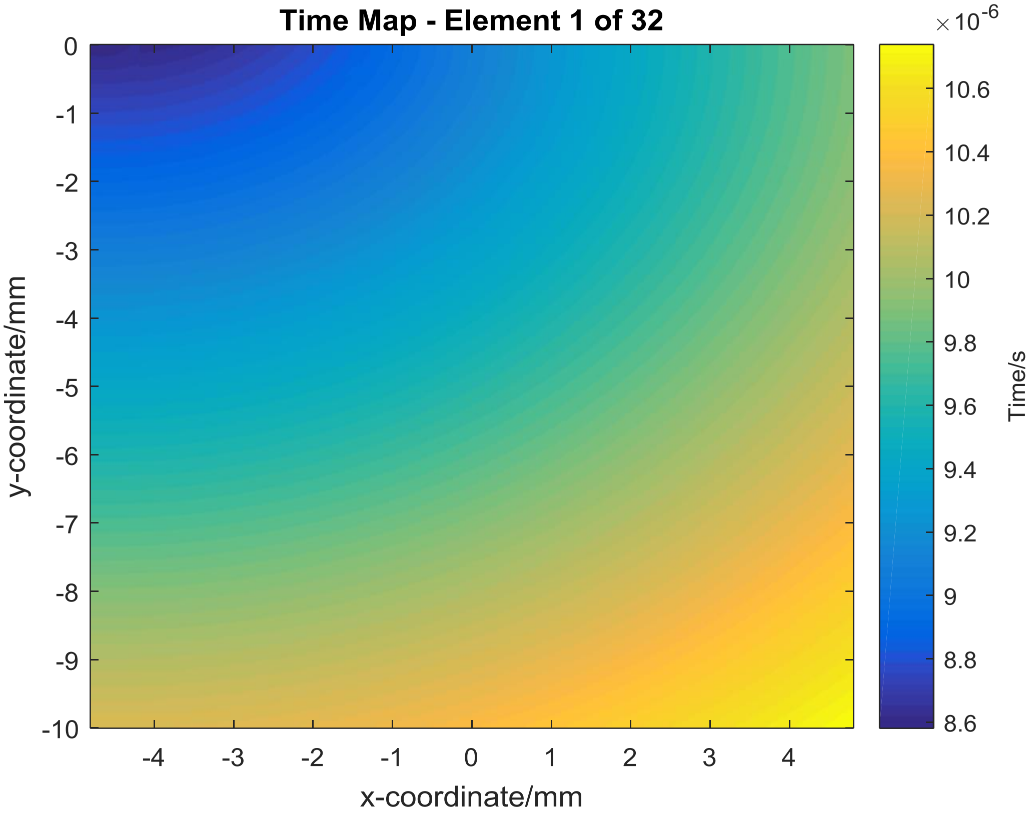

Figure 4.12 Time map of array element 1 of a 32 element array transducer with a TFM pixel resolution of 10 μm

4.3.4. ID and OD Inspection: Simulation and Experimental Verification

In this Section, the parameters for the ID and OD inspection simulations and the corresponding experiment verifications are described. A 10 MHz phased array transducer is immersed in water to inspect a titanium plate with a small defect on the ID or OD surface. Array sub-apertures between 8 to 32 elements are utilised. Full parameter details for the simulations and experimental work are displayed in Table 4.3.

Table 4.3 Parameters of simulation configuration – array transducer

Items	Parameters	Values
Transducer	Element number	8/16/32
	Central frequency	10 MHz
	Element size	0.275 mm
	Pitch	0.3 mm
	Wavelength in water	0.148 mm
Titanium plate	Thickness	5 mm
Water layer	Gap1	2.5 mm
	Gap2	2.5 mm
Defect	Depth	0.5 mm
	Width	0.3 mm
Water path	Length	12.7 mm

4.3.4.1. Hybrid Array Simulation Parameters

Figure 4.13 illustrates the simulation configuration of ID inspection with a defect on the inner surface, while OD inspection has a defect on the outer surface instead. As only the axial direction is considered here, a 5 mm thick flat titanium plate is employed as the test object with a defect size of 0.5 mm depth and 0.3 mm width which relates to the CANDU reportable defect sizes[12]. In the experimental work, the defect size has been verified by a replication process combined with the use of an optical microscope and was measured to be 0.504 x 0.300 mm^2. Appendix C presents an example of the defect size measurement by replication process. The mesh size of FE model is set to 20 points per wavelength. In order to minimize the model size for computational efficiency, the tube wall width matches the transducer length plus an additional 1 mm water layer on each side of the transducer is built into the model.

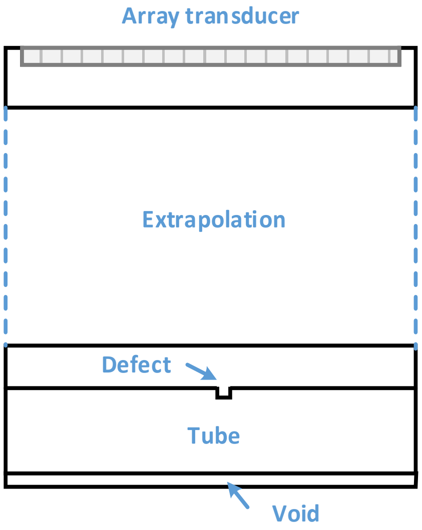

Figure 4.13 ID inspection simulation configuration (OD inspection has a defect on the outer surface instead)

4.3.4.2. Experimental Verification Arrangement

The experimental setup is shown in Figure 4.14 and includes a water tank with a titanium plate, a phased array transducer connected to an array controller and a computer as the user interface. The transducer was manufactured by Vermon (France) and has 128 elements. The array elements are excited by the FI Toolbox array controller from Diagnostic Sonar Ltd (Livingstone, UK). The user interface uses a proprietary software tool cueART[121] to configure the array data acquisition. When the FMC data is stored, the surface imaging algorithms described in Section 4.3.3 are applied on the ID and OD inspection images, as required.

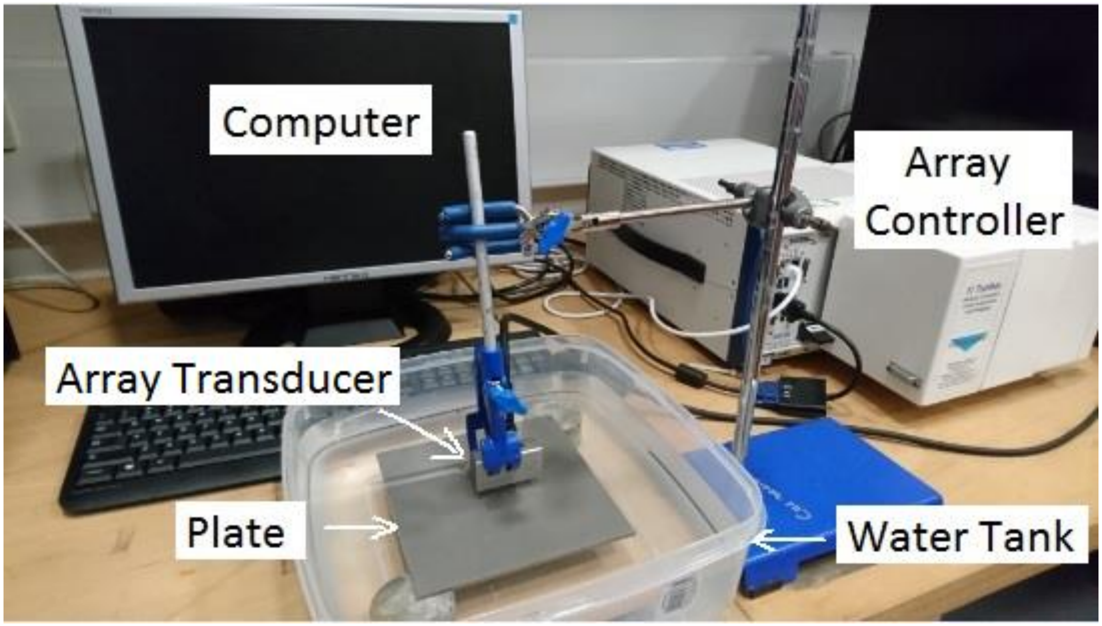

Figure 4.14 Experimental setup to validate hybrid array model

4.3.5. Results Analysis

Figure 4.15 - Figure 4.17 present the simulation and experimental results of ID and OD inspection by using 8, 16 and 32 element phased array active sub-aperture configurations to detect the notch defect on the wall surfaces of the titanium plate. The left-hand side images present the simulation results while the right-hand side shows the corresponding experimental results. The TFM images cover the transducer length on the horizontal direction. Due to the wave velocity in titanium being higher than that in water, a longer

wavelength can be found in the OD images. In each Figure, the defect position has been indicated by a magenta dotted rectangular box in the image.

When an 8 element array transducer aperture is used for the inspection, both the simulation and the experimental ID images have a clear view of the defect below the surface, as shown in Figure 4.15 (a) and (b), but this reduced resolution configuration shows no indication on the surface. However, the defect on the OD images (Figure 4.15 (c) and (d)) is difficult to discern due to a combination of resolution and transmitted energy issues with this 8-element configuration. Good correlation between the simulated and experimental images has been achieved, although there is an observable difference in the characteristic response from the defect in the ID case.

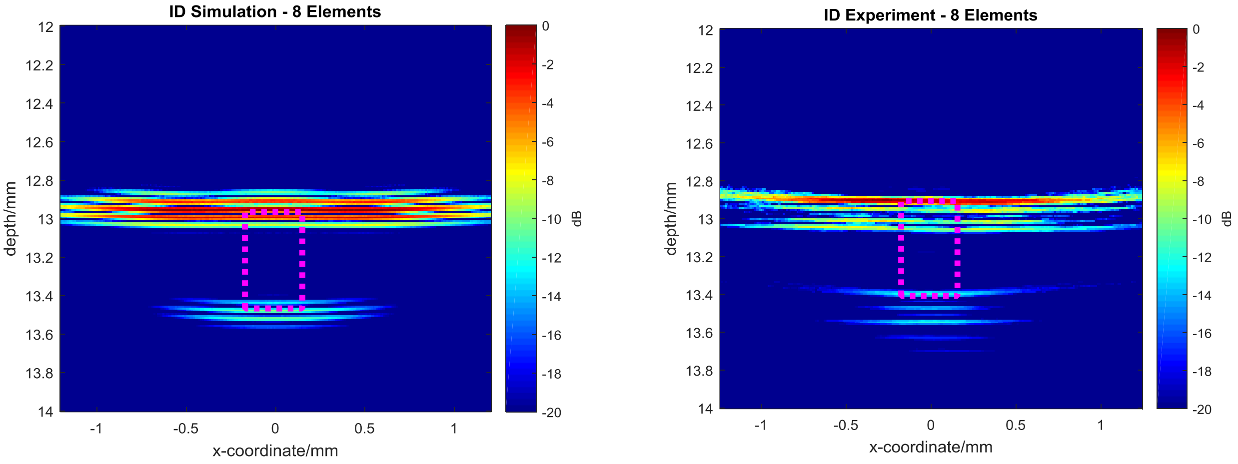

(a) ID surface simulation

(b) ID surface experiment

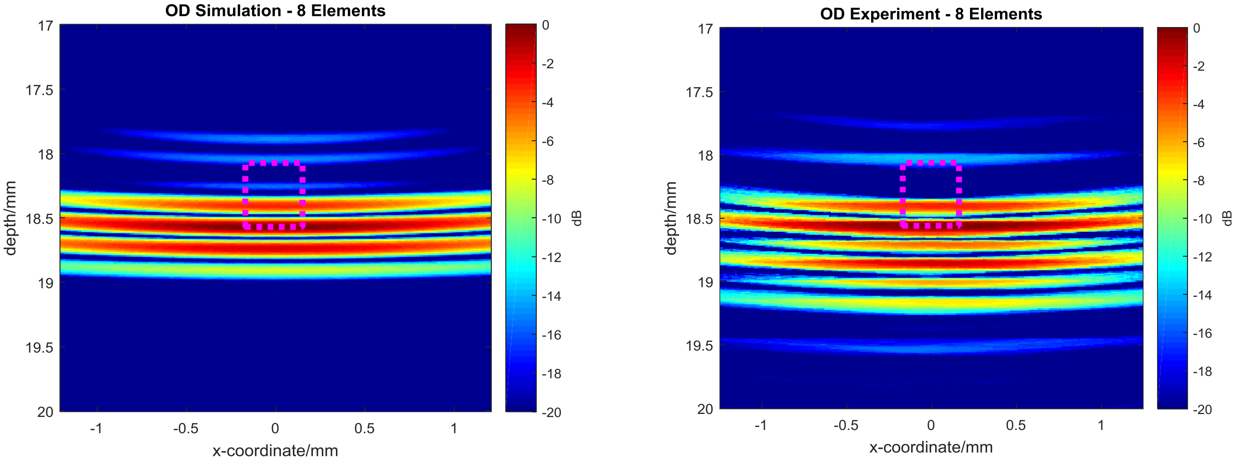

(c) OD surface simulation *(d) OD surface experiment*

Figure 4.15 TFM images comparison – 8 elements transducer inspection

The 16 element sub-aperture array transducer provides a clearer indication of the defect on both ID and OD images (Figure 4.16). The indications are located where expected, with a good contrast between the defect indication and the front wall/back wall signals. Excellent correlation between the simulated and experimental results has been achieved, with accurate positioning of the defects in all cases.

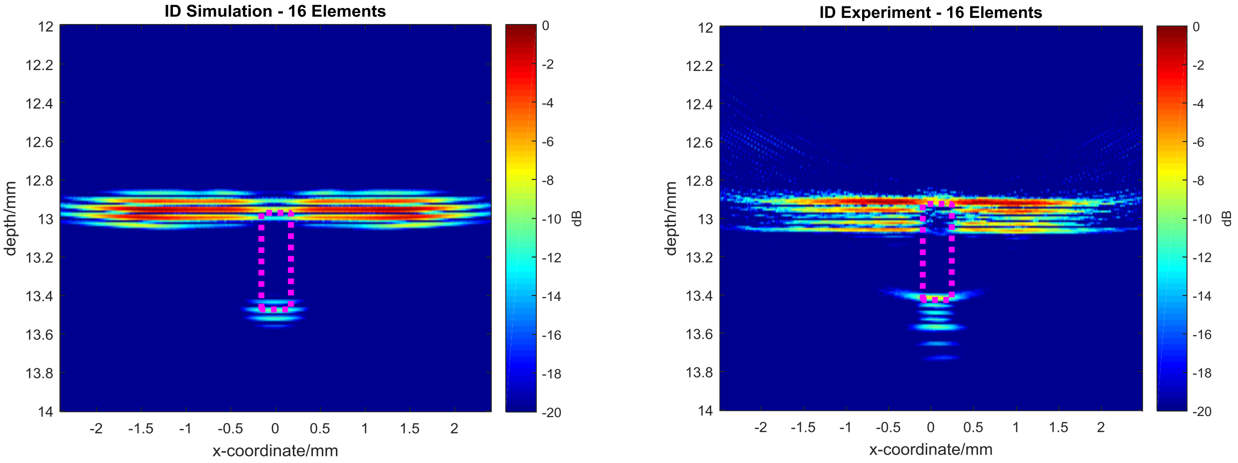

(a) ID surface simulation *(b) ID surface experiment*

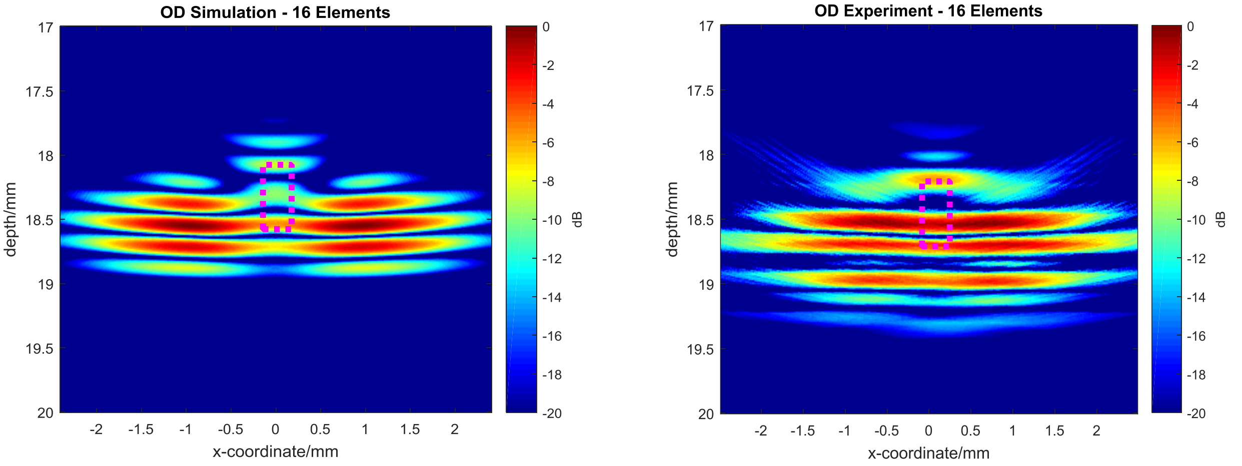

(c) OD surface simulation *(d) OD surface experiment*

Figure 4.16 TFM images comparison – 16 elements transducer inspection

The highest resolution images in both ID and OD surface cases have been produced using the 32 element array inspection configurations (Figure 4.17). Importantly, the defect has a strong echo and the clear indications of surface breaks. Again, excellent correlation between the simulated and experimental datasets has been demonstrated, with the potential to more accurately measure the defect dimensions.

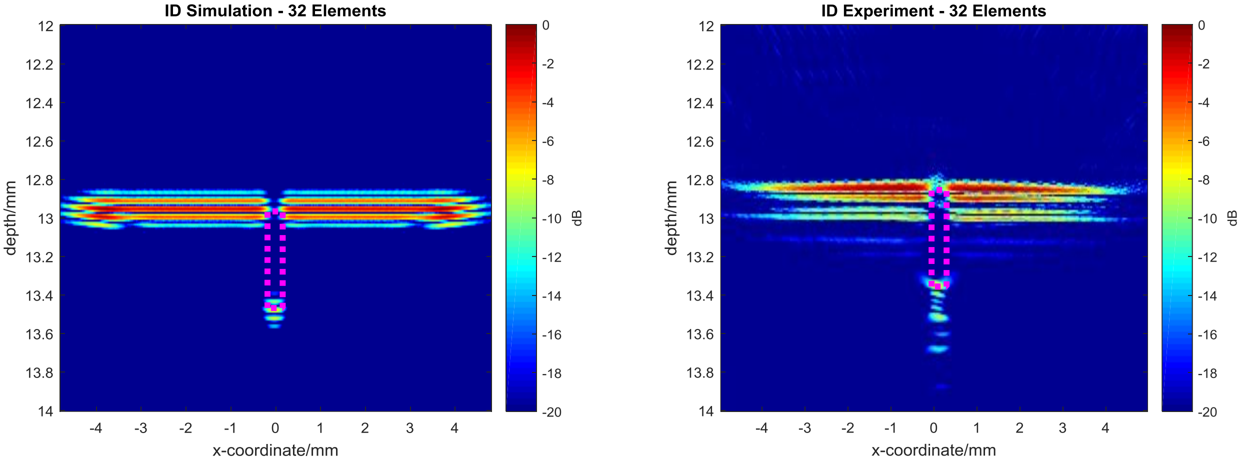

(a) ID surface simulation *(b) ID surface experiment*

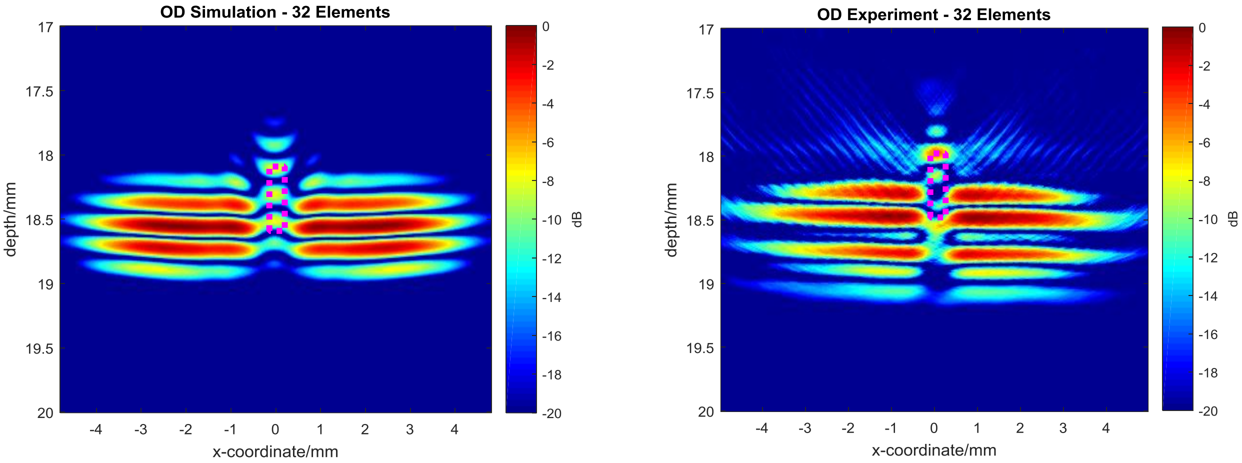

(c) OD surface simulation

(d) OD surface experiment

Figure 4.17 TFM images comparison – 32 elements transducer inspection

The measurement results and errors of defect size information are shown in Table 4.4. The defects' size is measured through a -6 dB method. The errors (compare to experiment) is used for validation of the simulation, while the errors (compare to real size) provides the practical inspection errors. All element configurations for the ID inspection simulation (in 1st column) have very close depth results when compared to the corresponding experimental measurement (in 3rd column), while the width results show differences (in 2nd and 4th columns) with the correlation improves with the increase in element numbers. The defect width measurement of OD inspection has a big difference in the 8 element transducer configuration (in 2nd and 4th columns), due to poor lateral resolution caused by the smaller active array aperture, which makes both the simulation and experimental results unreliable. When the number of elements is increased, the width results are closer to the real size for simulation as well as experiment. However, the OD defect depth measurement (in 1st and 3rd columns) is not as sensitive to the number of elements. Both simulation and experiment results are close to the real defect size within a reasonable error range. In a 32 elements configuration, the simulation errors comparing to the real defect depth are 0.03 mm and -0.04 mm for ID and OD inspection, respectively.

Table 4.4 Simulation and experimental defect sizing results and errors

Defect Position	**Elem -ents**	**Simulation**		**Experiment**		**Errors (compare to experiment)**		**Errors (compare to real size)**	
		Defect Depth (mm)	**Defect Width (mm)**	**Defect Depth (mm)**	**Defect Width (mm)**	**Depth (mm)**	**Width (mm)**	**Depth (mm)**	**Width (mm)**
ID	8	0.53	0.9	0.5	0.92	0.03	-0.02	0.03	0.6
	16	0.53	0.61	0.51	0.53	0.02	0.08	0.03	0.31
	32	0.53	0.42	0.51	0.36	0.02	0.06	0.03	0.12
OD	8	0.54	1.71	0.53	2.09	0.01	-0.38	0.04	1.41
	16	0.48	0.82	0.51	1.47	-0.03	-0.65	-0.02	0.52
	32	0.46	0.68	0.51	0.71	-0.05	-0.03	-0.04	0.38

Figure 4.18 provides a convenient way to compare the errors between the simulation results and actual defect size for different transducer element configurations, which shows that the defect depth measurement errors are insignificant for both ID and OD inspection. While for defect width measurement, configurations with increased numbers of elements facilitates lower measurement errors.

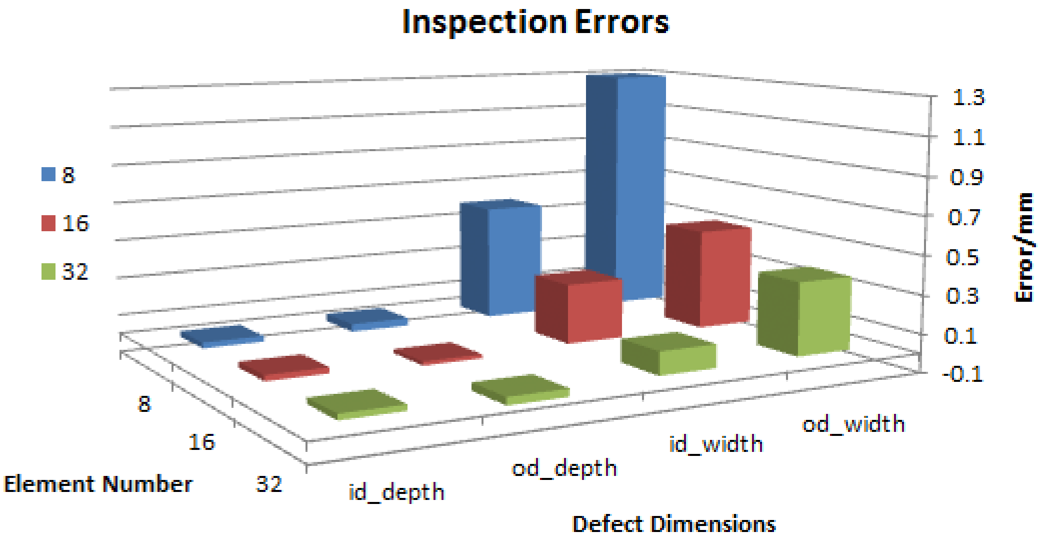

Figure 4.18 Defect sizing errors from simulation data (comparing to real defect size)

4.4. Summary

A hybrid model, incorporating the PZFlex finite element software package, to overcome the influence of numerical dispersion error in a large single model has been presented in this Chapter. This method is used for simulation of both single element transducer and phase array transducer configurations immersed in water to inspect a tube or thin plate. The FE approach has utilised an extrapolation method to simulate wave propagation in water.

In the single element transducer inspection model, the capability of the defect depth measurement of the hybrid model has been demonstrated and the errors are shown to be minimal for the 10 MHz and 20 MHz transducer samples used in this work. Importantly, the simulation result correlates well with experiment giving confidence that the hybrid model approach is able to be used as the platform to investigate advances in transducer technology. The simulation time for a 10 MHz transducer configuration takes 3.5 hours by using a computer with two 2.1 GHz processors and 16 GB memory.

A hybrid simulation platform to determine FMC datasets for ultrasonic phased array inspection over long propagation path lengths has been presented. The work concentrated on the longitudinal section of a CANDU reactor pressure tube. The simulation model combines both FE simulation and analytical extrapolation to overcome the influence of numerical dispersion errors which would occur in a large single FE model. Subsequently, the TFM algorithm is used to image both the inner and outer surfaces of the tube wall. Moreover, a computationally efficient solution provides a ray tracing time map to solve the refraction problem associated with TFM imaging in a dual-layer configuration.

The validation results demonstrate that the simulation platform produces images which have an excellent correlation with experimentally measured TFM images. This hybrid simulation approach generates images which are less damped than in practice, but correlates well with the actual defect sizes. The defect depth measurement is the most critical parameter for the nuclear industry and importantly, this is not sensitive to the number of elements used in the array configuration. This software platform will now be used to evaluate different array configurations to determine a practical replacement for the existing multi-transducer tool currently used. The limitation of the 2-D simulation platform is that it is less realistic than 3-D simulation. For example, in a 2-D model, each element of a 1-D linear array is working as a narrow source which has a wide beam width. While in a 3-D model, the element is simulated along the cross section as well, which brings about a narrower beam width. Therefore, in this situation, 3-D simulation will have a more concentrated beam than 2-D simulation. However, at the initial stage, a 2-D simulation platform is sufficient for investigating the inspection of pressure tube.

Chapter 5

Future Pressure Tube Inspection Scenarios Using Phased Array Sensor Systems

5.1. Introduction

The inspection of CANDU pressure tubes may benefit by utilizing phased array technology to replace the current multiple focused transducer sensor arrangement, as discussed in Section 4.3. Phased array systems offer more flexibility in terms of implementation, but also can take advantage of advanced post-processing algorithms such as TFM and SAFT. However, due to the inspection of pressure tubes focusing on the Inner Diameter (ID) and Outer Diameter (OD) surfaces, on both axial and circumferential directions, there are challenges for array system implementation. Firstly, the configuration of the transducer should maximise defect detection capability, at both ID and OD locations, as well as the array system efficiency in terms of practical operability. Secondly, any array imaging algorithms would have to be able to account for propagation through a non-planar interface for inspection of the OD surface. Finally, SAFT processing of phased array data for tube inspection is more complex due to the multi-layer propagation path. This Chapter will use the simulation tool developed in Chapter 4 to investigate the implementation of advanced phased array systems for inspection of CANDU pressure tube components. Importantly, all three of the identified problems need to be addressed in the simulation programme.

In this Chapter, two phased array transducers located on the axial and circumferential directions of the pressure tube are presented as the inspection system in Section 5.2. In Section 5.3, validation of the data post-processing methodology, including both simulation and experimental results, is presented. Comparison between single element transducer inspection and phased array transducer inspection is then demonstrated in Section 5.4. In Section 5.5, the simulation platform developed in Chapter 4 is applied to generate phased array inspection data for a range of array configurations, including different transducer operating frequencies, number of array elements and target defect types. The advantages and disadvantages of the different configurations are then analysed for application in pressure tube inspection scenarios. A suggested solution of using array sensor system for the pressure tube inspection is discussed in Section 5.6.

5.2. Methodology

In Chapter 1, see Figure 1.4, the current deployment of six single element transducers to inspect in both axial and circumferential directions was introduced. Two implementations of an individual array transducer are described in this Section to replicate the inspection regime facilitated by this CIGAR sensor head. In addition, this Section will describe the evolution of the direct TFM algorithm to incorporate full-skip TFM and the SAFT algorithm implementation for use with array transducers is also discussed.

5.2.1. Array Transducer System Configuration

Figure 1.4 depicts the four inspection configurations associated with the six single element focused transducers currently deployed in the CIGAR sensor head. The inspection modalities are illustrated in Table 5.1 and can be summarised as follow:

- Only one transducer operates at 20 MHz and is used for pulse-echo ID surface inspection (Figure 1.4 (a))
- A 10 MHz transducer also works in pulse-echo mode, but for OD surface inspection (Figure 1.4 (d)). This is termed Normal Beam (NB).
- One pair of 10 MHz devices work in shear wave pitch-catch mode on the circumferential direction (Figure 1.4 (b)). This is termed Circumferential Pitch-Catch (CPC).
- Another pair of 10 MHz devices work in shear wave pitch-catch mode on the axial direction (Figure 1.4 (c)). This is termed Axial Pitch-Catch (APC).

Since the tube material was rigorously tested before being installed in the nuclear reactor, the in-service ultrasonic inspection focusses on defects on the ID and OD tube wall surfaces. The 20 MHz B-scan image is employed to obtain the ID defect depth and length information, while the 10 MHz Normal Beam (NB) B-scan image takes responsibility to measure the OD defect size of depth, width and length. In addition, the 10 MHz shear wave Circumferential Pitch-Catch (CPC) B-scan is utilized for defect depth and length measurement of both ID and OD surfaces, whereas the Axial Pitch-Catch (APC) B-scan is applied for defect depth and width measurement[12].

Table 5.1 Inspection functions of single element transducers in the CIGAR sensor head

Scan mode	**ID defect measurement**			**OD defect measurement**		
	Depth	**Width**	**Length**	**Depth**	**Width**	**Length**
20 MHz B-scan	x		x			
10 MHz shear wave CPC	x		x	x		x
10 MHz shear wave APC	x	x		x	x	
10 MHz NB B-scan				x	x	x

Considering that the typical phased array system has a more complex signal excitation, data acquisition and data processing compared to the single element transducer inspection, two array transducers are proposed to replace the inspection modalities detail in Table 5.1, with one array transducer aligned with the tube's axial direction and the other one aligned along the circumferential direction, as presented in Figure 5.1. The concept is for the two separate array transducer pairs to inspect both the tube ID and OD surfaces on the axial and circumferential directions. This method covers the inspection of targets on both directions and does not affect the defect size measurement caused by increased focal spot size in the passive axis due to flat linear array transducer. Moreover, similar to single element APC pitch-catch mode, the array transducer in the axial direction will perform a full-skip inspection to assist in the identification of defect features, which is helpful to recognize angled defects. These two array transducers are proposed to collect ultrasonic data containing defect information for all the ID and OD defect measurements of depth, width and length, as listed in Table 5.2. In this Chapter, the upper array transducer frequency investigated is 10MHz, which was shown in Chapter 4 to provide sufficient imaging performance to detect and size pressure tube defects.

Table 5.2 Inspection function of array transducers

Scan mode	**ID defect measurement**			**OD defect measurement**		
	Depth	**Width**	**Length**	**Depth**	**Width**	**Length**
Array transducer 1	x	x	x	x	x	x
Array transducer 2	x	x	x	x	x	x

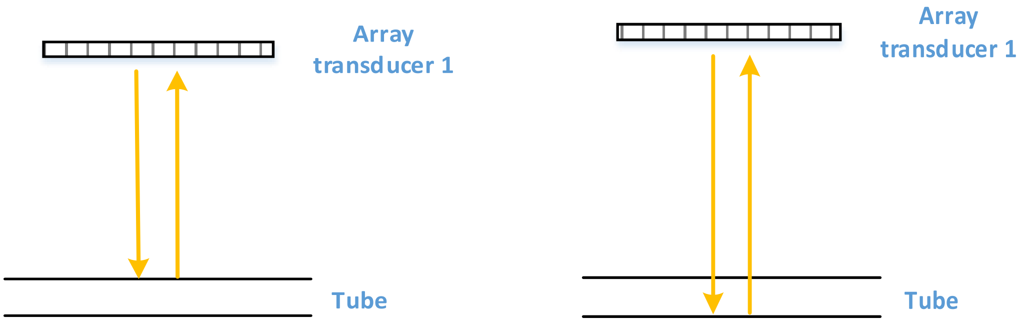

(a) (b)

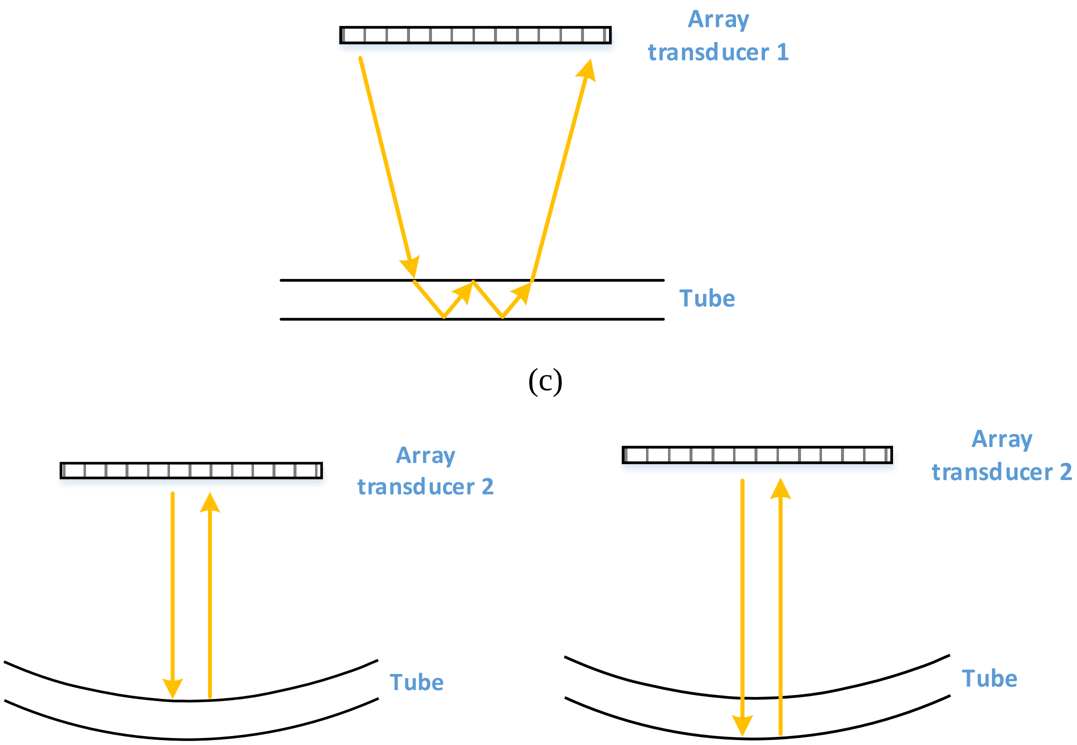

(c)

(d)

(e)

Figure 5.1 Schematics of array transducer replacement (a) axial ID inspection; (b) axial OD inspection; (c) axial full-skip inspection; (d) circumferential ID inspection; (e) circumferential OD inspection

5.2.2. Array Imaging Method

For this work, the phased array imaging method applied is the TFM algorithm for defects located on both the ID and OD surfaces and on both axial and circumferential directions. This will require the acquisition of Full Matrix Capture (FMC) data from the array. In Chapter 4, the direct TFM algorithm was introduced for imaging the ID surface on the axial direction, see Section 4.3.3. This approach can obviously be used for the circumferential direction as well. In terms of the OD surface inspection on the axial direction, the TFM imaging algorithm was extended in Section 4.3.3.2 to take into account propagation through the liquid/solid interface (at the ID surface) and the derived equation to calculate the value of each image pixel is expressed in Equation 4.4.

5.2.2.1. Circumferential OD TFM Imaging

The TFM imaging of circumferential OD surface utilizes the same equation (Equation 4.4), but has the additional difficulty in acquiring the time information from the second medium. In order to obtain the accurate time information for TFM image, a combination of Snell's law and cross product is proposed to get the analytical solution of the time map for TFM imaging. This innovative analytical solution is based on the coordinate system in Figure 5.2 with the origin O situated at the centre of the tube cross-section. The transducer is located symmetrically to the y-axis and immersed in water with sound velocity, c_1. The sound velocity in tube is c_2 and R is the inner diameter of the tube. In terms of arbitrary point in the second medium, such as point B, ultrasound is transmitted from transducer at point A to point B via the point P on the tube inner surface. The following process is to acquire the time information of wave propagating from A to B. The x-coordinate of P, x_P, is the target value. After having x_P, the time map can be easily obtained.

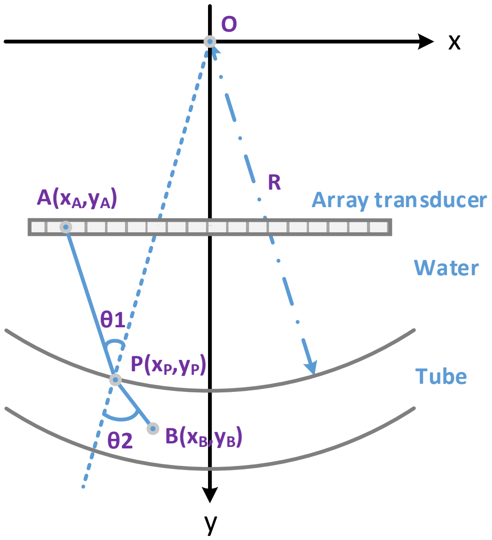

Figure 5.2 Time map calculation for circumferential OD TFM image

For this scenario, Snell's law from Equation 2.14 can be simplified to Equation 5.1:

$$\frac{\sin\theta_1}{\sin\theta_2} = \frac{c_1}{c_2} \tag{5.1}$$

According to the principle of cross product, Equation 5.2 can be acquired.

$$\frac{\left|\overrightarrow{PO} \times \overrightarrow{PA}\right|}{\left|\overrightarrow{OP} \times \overrightarrow{PB}\right|} = \frac{\left|\overrightarrow{PO}\right| \cdot \left|\overrightarrow{PA}\right| \cdot \sin\theta_1}{\left|\overrightarrow{OP}\right| \cdot \left|\overrightarrow{PB}\right| \cdot \sin\theta_2} = \frac{\left|\overrightarrow{PA}\right|}{\left|\overrightarrow{PB}\right|} \cdot \frac{\sin\theta_1}{\sin\theta_2} \tag{5.2}$$

Put Equation 5.1 into Equation 5.2, we have

$$\frac{\left|\overrightarrow{PO} \times \overrightarrow{PA}\right|}{\left|\overrightarrow{OP} \times \overrightarrow{PB}\right|} = \frac{\left|\overrightarrow{PA}\right|}{\left|\overrightarrow{PB}\right|} \cdot \frac{c_1}{c_2} \tag{5.3}$$

In order to solve this equation, some vectors are defined as below shown:

$\overrightarrow{PO} = (-x_P, -y_P),\ \overrightarrow{PA} = (x_A - x_P, y_A - y_P);$

$\overrightarrow{OP} = (x_P, y_P),\ \overrightarrow{PB} = (x_B - x_P, y_B - y_P).$

Then, the left-hand side of Equation 5.3 can be changed to:

$$\begin{aligned}\frac{\left|\overrightarrow{PO}\times\overrightarrow{PA}\right|}{\left|\overrightarrow{OP}\times\overrightarrow{PB}\right|} &= \frac{\begin{vmatrix}\vec{x} & \vec{y} & \vec{z}\\ -x_P & -y_P & 0\\ x_A-x_P & y_A-y_P & 0\end{vmatrix}}{\begin{vmatrix}\vec{x} & \vec{y} & \vec{z}\\ x_P & y_P & 0\\ x_B-x_P & y_B-y_P & 0\end{vmatrix}}\\ &= \frac{|\vec{z}\cdot(-x_P(y_A-y_P)+y_P(x_A-x_P))|}{|\vec{z}\cdot(x_P(y_B-y_P)-y_P(x_B-x_P))|}\\ &= \frac{|\vec{z}\cdot(-x_Py_A+y_Px_A)|}{|\vec{z}\cdot(x_Py_B-y_Px_B)|} = \frac{|\vec{z}|\cdot|-x_Py_A+y_Px_A|}{|\vec{z}|\cdot|x_Py_B-y_Px_B|}\\ &= \frac{|-x_Py_A+y_Px_A|}{|x_Py_B-y_Px_B|}\end{aligned} \tag{5.4}$$

And the right-hand side of Equation 5.3 can be changed to:

$$\frac{\left|\overrightarrow{PA}\right|}{\left|\overrightarrow{PB}\right|}\cdot\frac{c_1}{c_2} = \frac{\sqrt{(x_A-x_P)^2+(y_A-y_P)^2}\cdot c_1}{\sqrt{(x_B-x_P)^2+(y_B-y_P)^2}\cdot c_2} \tag{5.5}$$

Let Equation 5.4 equals to Equation 5.5, we have:

$$\frac{|-x_Py_A+y_Px_A|}{|x_Py_B-y_Px_B|} = \frac{\sqrt{(x_A-x_P)^2+(y_A-y_P)^2}\cdot c_1}{\sqrt{(x_B-x_P)^2+(y_B-y_P)^2}\cdot c_2} \tag{5.6}$$

To make it simple to solve the equation, we use the square of Equation 5.6:

$$\frac{(-x_Py_A+y_Px_A)^2}{(x_Py_B-y_Px_B)^2} = \frac{(x_A-x_P)^2+(y_A-y_P)^2}{(x_B-x_P)^2+(y_B-y_P)^2}\cdot\frac{{c_1}^2}{{c_2}^2} \tag{5.7}$$

After executing the cross multiplication of Equation 5.7, we have:

$$(-x_P y_A + y_P x_A)^2[(x_B - x_P)^2 + (y_B - y_P)^2] \cdot {c_2}^2 \\ = (x_P y_B - y_P x_B)^2[(x_A - x_P)^2 + (y_A - y_P)^2] \cdot {c_1}^2 \tag{5.8}$$

When the wave incidence is vertical to the tube surface, the situation is $\theta_1 = \theta_2 = 0$. Using the condition described in Equation 5.9, we can ensure that the vertical incidence condition is satisfied in Equation 5.8.

$$\frac{x_A}{y_A} = \frac{x_P}{y_P} = \frac{x_B}{y_B} \tag{5.9}$$

Accordingly, Equation 5.8 can be changed to:

$$[{x_P}^2 {y_A}^2 - 2x_P y_P x_A y_A + {y_P}^2 {x_A}^2][(x_B - x_P)^2 + (y_B - y_P)^2] \cdot {c_2}^2 \\ = [{x_P}^2 {y_B}^2 - 2x_P y_P x_B y_B + {y_P}^2 {x_B}^2][(x_A - x_P)^2 \\ + (y_A - y_P)^2] \cdot {c_1}^2 \tag{5.10}$$

There is a known condition about R, which is:

$${x_P}^2 + {y_P}^2 = R^2 \tag{5.11}$$

Since $y_P < 0$, we have:

$$y_P = -\sqrt{R^2 - {x_P}^2} \tag{5.12}$$

Substituting Equation 5.12 into Equation 5.10, then it becomes:

$$\begin{aligned}
&[x_P{}^2 y_A{}^2 - 2x_A y_A \left(-\sqrt{R^2 - x_P{}^2}\right) x_P + \left(R^2 - x_P{}^2\right) x_A{}^2][x_B{}^2 - 2x_B x_P + x_P{}^2 \\
&\qquad + y_B{}^2 - 2y_B \left(-\sqrt{R^2 - x_P{}^2}\right) + \left(R^2 - x_P{}^2\right)] \cdot c_2{}^2 \\
&\qquad = [x_P{}^2 y_B{}^2 - 2x_B y_B (-\sqrt{R^2 - x_P{}^2}) x_P + (R^2 - x_P{}^2) x_B{}^2]\ [x_A{}^2 \\
&\qquad - 2x_A x_P + x_P{}^2 + y_A{}^2 - 2y_A \left(-\sqrt{R^2 - x_P{}^2}\right) + (R^2 - x_P{}^2)] \cdot c_1{}^2
\end{aligned} \tag{5.13}$$

Equation 5.13 can be simplified as the following:

$$\begin{aligned}
&\left[\left(y_A{}^2 - x_A{}^2\right) x_P{}^2 + 2x_A y_A \sqrt{R^2 - x_P{}^2}\, x_P + x_A{}^2 R^2\right]\left[-2x_B x_P + 2y_B \sqrt{R^2 - x_P{}^2}\right. \\
&\qquad \left. + \left(x_B{}^2 + y_B{}^2 + R^2\right)\right] \cdot c_2{}^2 \\
&\qquad = \left[\left(y_B{}^2 - x_B{}^2\right) x_P{}^2 + 2x_B y_B \sqrt{R^2 - x_P{}^2}\, x_P + x_B{}^2 R^2\right]\left[-2x_A x_P\right. \\
&\qquad \left. + 2y_A \sqrt{R^2 - x_P{}^2} + \left(x_A{}^2 + y_A{}^2 + R^2\right)\right] \cdot c_1{}^2
\end{aligned} \tag{5.14}$$

To simplify the calculation, the factors not containing the variable x_P will be replaced by:

$A_1 = x_A{}^2 R^2,\ A_2 = x_A{}^2 + y_A{}^2 + R^2,$

$A_3 = x_B{}^2 R^2,\ A_4 = x_B{}^2 + y_B{}^2 + R^2.$

Therefore, Equation 5.14 can be deformed to:

$$
\begin{aligned}
&{c_2}^2\Big[-2x_B({y_A}^2-{x_A}^2){x_P}^3-4x_Ay_Ax_B\sqrt{R^2-{x_P}^2}\,{x_P}^2-2A_1x_Bx_P \\
&\qquad +2y_B({y_A}^2-{x_A}^2)\sqrt{R^2-{x_P}^2}\,{x_P}^2+4x_Ay_Ay_B(R^2-{x_P}^2)x_P \\
&\qquad +2A_1y_B\sqrt{R^2-{x_P}^2}+A_4({y_A}^2-{x_A}^2){x_P}^2 \\
&\qquad +2A_4x_Ay_A\sqrt{R^2-{x_P}^2}\,x_P+A_1A_4\Big] \\
&\qquad = {c_1}^2\Big[-2x_A({y_B}^2-{x_B}^2){x_P}^3-4x_Ax_By_B\sqrt{R^2-{x_P}^2}\,{x_P}^2 \\
&\qquad -2A_3x_Ax_P+2y_A({y_B}^2-{x_B}^2)\sqrt{R^2-{x_P}^2}\,{x_P}^2 \\
&\qquad +4y_Ax_By_B(R^2-{x_P}^2)x_P+2A_3y_A\sqrt{R^2-{x_P}^2} \\
&\qquad +A_2({y_B}^2-{x_B}^2){x_P}^2+2A_2x_By_B\sqrt{R^2-{x_P}^2}\,x_P+A_2A_3\Big]
\end{aligned}
\tag{5.15}
$$

For the purpose of solving Equation 5.15, it can be simplified to an equation of descending powers of x_P.

$$
\begin{aligned}
&\{{c_2}^2[-2x_B({y_A}^2-{x_A}^2)-4x_Ay_Ay_B]-{c_1}^2[-2x_A({y_B}^2-{x_B}^2)-4y_Ax_By_B]\}{x_P}^3 \\
&\qquad +\{{c_2}^2[-4x_Ay_Ax_B+2y_B({y_A}^2-{x_A}^2)] \\
&\qquad -{c_1}^2[-4x_Ax_By_B+2y_A({y_B}^2-{x_B}^2)]\}\sqrt{R^2-{x_P}^2}\,{x_P}^2 \\
&\qquad +\{{c_2}^2[A_4({y_A}^2-{x_A}^2)]-{c_1}^2[A_2({y_B}^2-{x_B}^2)]\}{x_P}^2 \\
&\qquad +\{{c_2}^2[2A_4x_Ay_A]-{c_1}^2[2A_2x_By_B]\}\sqrt{R^2-{x_P}^2}\,x_P \\
&\qquad +\{{c_2}^2[-2A_1x_B+4x_Ay_Ay_BR^2] \\
&\qquad -{c_1}^2[-2A_3x_A+4y_Ax_By_BR^2]\}x_P \\
&\qquad +\{{c_2}^2[2A_1y_B]-{c_1}^2[2A_3y_A]\}\sqrt{R^2-{x_P}^2} \\
&\qquad +\{{c_2}^2[A_1A_4]-{c_1}^2[A_2A_3]\}=0
\end{aligned}
\tag{5.16}
$$

Consequently, solving Equation 5.7 requires a solution to the following polynomial equation:

$$\begin{gathered} a_{\text{coef}}x^3 + b_{\text{coef}}\sqrt{R^2 - x^2}\, x^2 + c_{\text{coef}}x^2 + d_{\text{coef}}\sqrt{R^2 - x^2}\, x + e_{\text{coef}}x \\ + f_{\text{coef}}\sqrt{R^2 - x^2} + g_{\text{coef}} = 0 \end{gathered} \tag{5.17}$$

where

$a_{\text{coef}} = c_2{}^2[-2x_B(y_A{}^2 - x_A{}^2) - 4x_Ay_Ay_B] - c_1{}^2[-2x_A(y_B{}^2 - x_B{}^2) - 4y_Ax_By_B]$

$b_{\text{coef}} = c_2{}^2[-4x_Ay_Ax_B + 2y_B(y_A{}^2 - x_A{}^2)] - c_1{}^2[-4x_Ax_By_B + 2y_A(y_B{}^2 - x_B{}^2)]$

$c_{\text{coef}} = c_2{}^2[A_4(y_A{}^2 - x_A{}^2)] - c_1{}^2[A_2(y_B{}^2 - x_B{}^2)]$

$d_{\text{coef}} = c_2{}^2[2A_4x_Ay_A] - c_1{}^2[2A_2x_By_B]$

$e_{\text{coef}} = c_2{}^2[-2A_1x_B + 4x_Ay_Ay_BR^2] - c_1{}^2[-2A_3x_A + 4y_Ax_By_BR^2]$

$f_{\text{coef}} = c_2{}^2[2A_1y_B] - c_1{}^2[2A_3y_A]$

$g_{\text{coef}} = c_2{}^2[A_1A_4] - c_1{}^2[A_2A_3]$

$x = x_P$

To take advantage of numerical computing software to solve Equation 5.17, a deformation of the equation is executed as presented in Equation 5.18.

$$a_{\text{coef}}x^3 + c_{\text{coef}}x^2 + e_{\text{coef}}x + g_{\text{coef}} = -(b_{\text{coef}}\, x^2 + d_{\text{coef}}\, x + f_{\text{coef}})\sqrt{R^2 - x^2} \tag{5.18}$$

Execute square operation to both sides of Equation 5.18 to produce:

$$\left(a_{\mathrm{coef}}x^3 + c_{\mathrm{coef}}x^2 + e_{\mathrm{coef}}x + g_{\mathrm{coef}}\right)^2 = \left(-(b_{\mathrm{coef}}\, x^2 + d_{\mathrm{coef}}\, x + f_{\mathrm{coef}})\sqrt{R^2 - x^2}\right)^2 \tag{5.19}$$

The left-hand side of Equation 5.19 can be simplified to:

$$\begin{aligned}(a_{\mathrm{coef}}x^3 + c_{\mathrm{coef}}x^2 + e_{\mathrm{coef}}x + g_{\mathrm{coef}})^2 &= a_{\mathrm{coef}}{}^2x^6 + 2a_{\mathrm{coef}}c_{\mathrm{coef}}x^5 + (2a_{\mathrm{coef}}e_{\mathrm{coef}} + c_{\mathrm{coef}}{}^2)x^4 \\ &+ 2(a_{\mathrm{coef}}g_{\mathrm{coef}} + c_{\mathrm{coef}}e_{\mathrm{coef}})x^3 + (2c_{\mathrm{coef}}g_{\mathrm{coef}} + e_{\mathrm{coef}}{}^2)x^2 \\ &+ 2e_{\mathrm{coef}}g_{\mathrm{coef}}x + g_{\mathrm{coef}}{}^2\end{aligned} \tag{5.20}$$

And the right-hand side of Equation 5.19 can be simplified to:

$$\begin{aligned}\left(-(b_{\mathrm{coef}}\, x^2 + d_{\mathrm{coef}}\, x + f_{\mathrm{coef}})\sqrt{R^2 - x^2}\right)^2 &= -b_{\mathrm{coef}}{}^2x^6 - 2b_{\mathrm{coef}}d_{\mathrm{coef}}x^5 \\ &+ \left(b_{\mathrm{coef}}{}^2R^2 - 2b_{\mathrm{coef}}f_{\mathrm{coef}} - d_{\mathrm{coef}}{}^2\right)x^4 \\ &+ 2(b_{\mathrm{coef}}d_{\mathrm{coef}}R^2 - d_{\mathrm{coef}}f_{\mathrm{coef}})x^3 \\ &+ [\left(2b_{\mathrm{coef}}f_{\mathrm{coef}} + d_{\mathrm{coef}}{}^2\right)R^2 - f_{\mathrm{coef}}{}^2]x^2 + 2d_{\mathrm{coef}}f_{\mathrm{coef}}R^2x \\ &+ f_{\mathrm{coef}}{}^2R^2\end{aligned} \tag{5.21}$$

Substituting Equation 5.20 and Equation 5.21 into Equation 5.19 and arranging it as descending powers of x, we have:

$$\begin{aligned}&(a_{\mathrm{coef}}{}^2 + b_{\mathrm{coef}}{}^2)x_p{}^6 + 2(a_{\mathrm{coef}}c_{\mathrm{coef}} + b_{\mathrm{coef}}d_{\mathrm{coef}})x_p{}^5 \\ &\quad + \left(2a_{\mathrm{coef}}e_{\mathrm{coef}} + c_{\mathrm{coef}}{}^2 - b_{\mathrm{coef}}{}^2R^2 + 2b_{\mathrm{coef}}f_{\mathrm{coef}} + d_{\mathrm{coef}}{}^2\right)x_p{}^4 \\ &\quad + 2(a_{\mathrm{coef}}g_{\mathrm{coef}} + c_{\mathrm{coef}}e_{\mathrm{coef}} - b_{\mathrm{coef}}d_{\mathrm{coef}}R^2 + d_{\mathrm{coef}}f_{\mathrm{coef}})x_p{}^3 \\ &\quad + \left(2c_{\mathrm{coef}}g_{\mathrm{coef}} + e_{\mathrm{coef}}{}^2 - \left(2b_{\mathrm{coef}}f_{\mathrm{coef}} + d_{\mathrm{coef}}{}^2\right)R^2 + f_{\mathrm{coef}}{}^2\right)x_p{}^2 \\ &\quad + 2(e_{\mathrm{coef}}g_{\mathrm{coef}} - d_{\mathrm{coef}}f_{\mathrm{coef}}R^2)x_p + (g_{\mathrm{coef}}{}^2 - f_{\mathrm{coef}}{}^2R^2) = 0\end{aligned} \tag{5.22}$$

Finally, the above equation can be used in MATLAB to find multiple solutions since the highest order is 6. By calculating the wave propagation time of the closest three solutions, the least time is the value of the TFM time map. The MATLAB code for the time map calculation is presented in Appendix D. Figure 5.3 displays an example of the time map result for 1st of 32 elements. This innovative analytical solution is validated through simulation and experimental data and is demonstrated in Section 5.3.2.

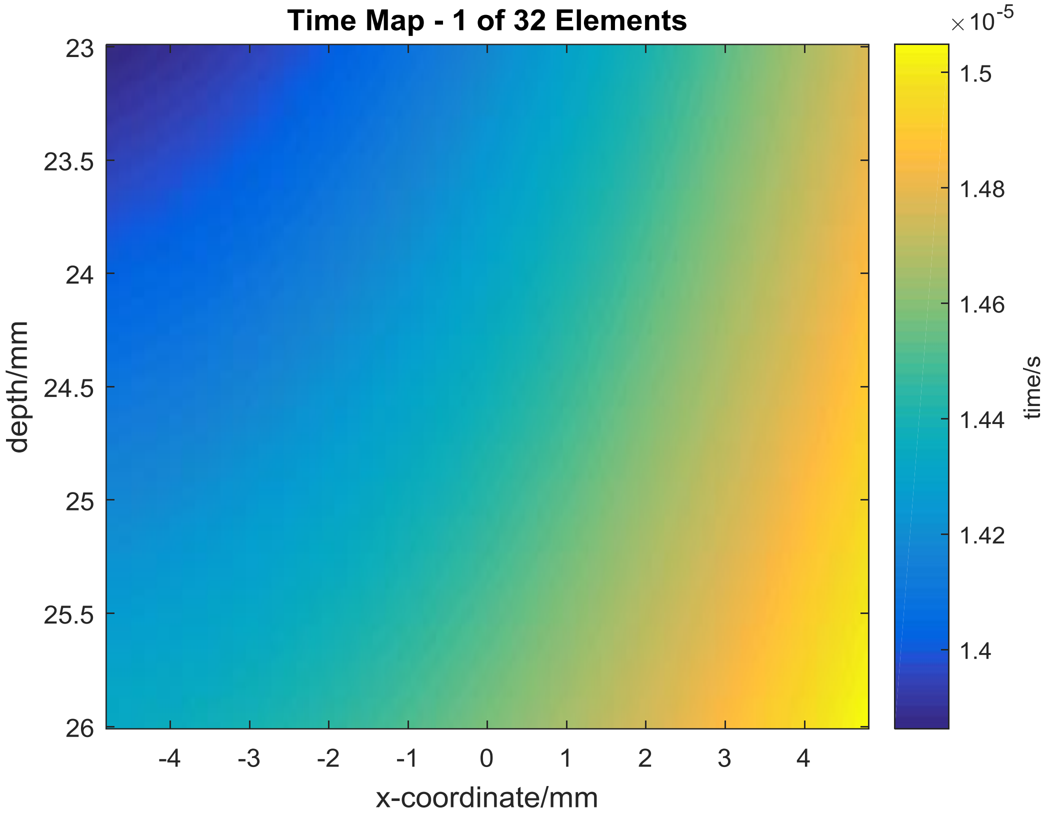

Figure 5.3 Example of time map of array element 1 of a 32 element array transducer for tube circumferential TFM

The only difference from Equation 4.4 is the change of the origin of the coordinate system. Therefore, when the coordinates of point $P - (x_P, y_P)$ are obtained, Equation 5.23 can be used for the calculation of TFM image pixel values on the OD surface in the circumferential direction.

$$
\begin{aligned}
& \mathrm{I}_{2nd\_circ}(\mathrm{x},\mathrm{y}) \\
& = \sum_{\mathrm{i}=1}^{\mathrm{N}}\sum_{\mathrm{j}=1}^{\mathrm{N}} \mathrm{f}_{\mathrm{Tx,Rx}}\left(\frac{\sqrt{\left(\mathrm{x}_{\mathrm{A,i}}-\mathrm{x}_{\mathrm{P,i}}\right)^2+\left(\mathrm{y}_{\mathrm{A,i}}-\mathrm{y}_{\mathrm{P,i}}\right)^2}+\sqrt{\left(\mathrm{x}_{\mathrm{A,j}}-\mathrm{x}_{\mathrm{P,j}}\right)^2+\left(\mathrm{y}_{\mathrm{A,j}}-\mathrm{y}_{\mathrm{P,j}}\right)^2}}{\mathrm{c}_1}\right. \\
& \left.+\frac{\sqrt{\left(\mathrm{x}_{\mathrm{B}}-\mathrm{x}_{\mathrm{P,i}}\right)^2+\left(\mathrm{y}_{\mathrm{B}}-\mathrm{y}_{\mathrm{P,i}}\right)^2}+\sqrt{\left(\mathrm{x}_{\mathrm{B}}-\mathrm{x}_{\mathrm{P,j}}\right)^2+\left(\mathrm{y}_{\mathrm{B}}-\mathrm{y}_{\mathrm{P,j}}\right)^2}}{\mathrm{c}_2}\right)
\end{aligned}
\qquad (5.23)
$$

where $\mathrm{c}_1 = \mathrm{c}_\mathrm{w}$, $\mathrm{c}_2 = \mathrm{c}_\mathrm{t}$.

This algorithm for time map is not sensitive to the tube sagging because the key parameter is the tube inner diameter *R* as presented in Equation 5.22, which is from array position plus the distance between array and tube surface. The distance between array and tube surface can be obtained accurately from the ID TFM image. This is a big advantage of applying array technology to replace current single element sensor head since it is able to focus at any distance. The only thing which needs to be considered in this algorithm is the distance between the circle of the tube cross-section and the array position. An incorrect value would slightly affect the curvature of the surface but does not affect the defect size measurement. An example of tube OD circumferential TFM image in Section 5.5.1 is demonstrated in Figure 5.4 for explanation of the effect of different distance values in the algorithm. From the images, there is no significant difference can be found when an offset ±3 mm of the array position exists. In addition, regarding to the pressure tube inspection, the transducer movement is much less serious comparing to the tube sagging. As long as the array is fixed on the scanner, the circle of the tube cross-section and the array have a fixed distance, which will lead to a good imaging result.

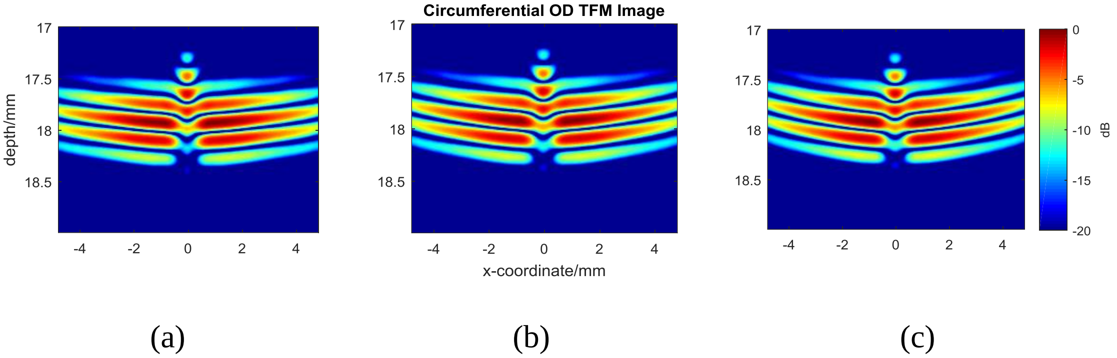

Figure 5.4 Tube OD circumferential TFM images with different distance values; (a) 3 mm shorter than; (b) same as; (c) 3 mm larger than real array position

5.2.2.2. Axial Full-skip TFM Imaging

The axial full-skip TFM means that the wave propagation path contains a reflection from the tube back wall for both transmitted and received array elements. As Figure 5.5 shows, the full-skip wave path from array element *A* to point *B* within the tube wall can be seen as path *APQB* via an incident point *P* and a back wall reflected point *Q*. Assuming point *B'* is the mirror point of *B* with respect to the tube back wall, then the path of wave propagation *APQB* can be considered as *APQB'*, which the time propagation in the second medium can be obtained by using the same algorithm approach for OD surface inspection on the axial direction. Equation 5.24 presents the calculation details of the pixel value of the full-skip TFM image.

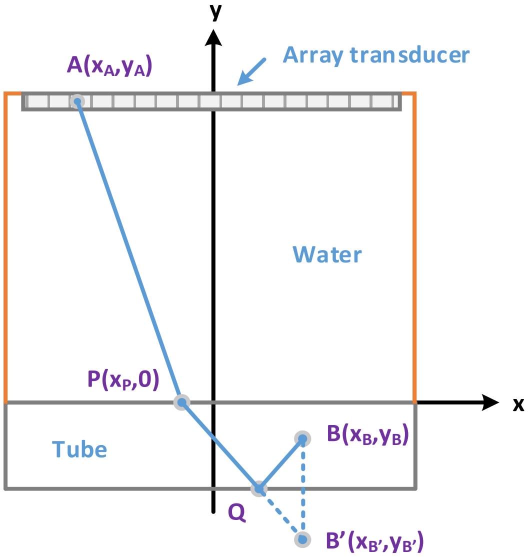

Figure 5.5 Axial full-skip TFM imaging

$$
\begin{aligned}
I_{FK}(x,y) \\
= \sum_{i=1}^{N}\sum_{j=1}^{N} f_{Tx,Rx} \Bigg(& \frac{\sqrt{\left(x_{A,i}-x_{P,i}\right)^2 + {y_{A,i}}^2} + \sqrt{\left(x_{A,j}-x_{P,j}\right)^2 + {y_{A,j}}^2}}{c_1} \\
+ & \frac{\sqrt{\left(x_{B'}-x_{P,i}\right)^2 + {y_{B'}}^2} + \sqrt{\left(x_{B'}-x_{P,j}\right)^2 + {y_{B'}}^2}}{c_2} \Bigg)
\end{aligned}
\tag{5.24}
$$

5.2.3. Array Signal SAFT Processing

In this Section, array TFM, single element SAFT and array SAFT are discussed in detail and specific reference to the application of array SAFT for pressure tube inspection provided.

5.2.3.1. Array TFM

When an array transducer is acquiring FMC data, the data can be archived as presented in Equation 5.25, which means all the transducer elements (N) receive A-scans from all combinations of the elements as transmitter and receiver[18]. Here, $\mathrm{f}_{\mathrm{i,j}}$ indicates the wave propagation function obtained by the combination of transmitter i and receiver j. The TFM algorithm effectively sums the echo information from this FMC dataset to generate an image focused at every pixel in the image space.

$$\begin{bmatrix} f_{11} & f_{12} & f_{13} & \cdots & f_{1N} \\ f_{21} & f_{22} & f_{23} & \cdots & f_{2N} \\ f_{31} & f_{32} & f_{33} & \cdots & f_{3N} \\ \vdots & \vdots & \vdots & \ddots & \vdots \\ f_{N1} & f_{N2} & f_{N3} & \cdots & f_{NN} \end{bmatrix} \tag{5.25}$$

5.2.3.2. Single Element SAFT in an Array

In an array configuration, the array elements can be considered as a single element transducer situated at different spatial positions. To provide a graphical explanation, an array transducer containing N elements is inspecting a target point, as shown in Figure 5.6 (a). The green dashed line indicates the ultrasound beam divergence from a single array element, while the red dashed lines is a mirror of it located at the target point. This means that the target point can only be detected by a limited number of elements situated within the red limits, as shown in the Figure. This beam width is called synthetic aperture length and is typically expressed as an angle.

Following the basic SAFT theory for a single element transducer introduced in Section 3.2.1.1, the traditional single array element SAFT can be described by Equation 5.26, which is the summation of all the echo information from the diagonal of the FMC matrix within the ultrasound beam[122]. Each pixel value of the image is calculated from the echo signal received within the ultrasound beam highlighted in the red rectangle in Equation 5.26, where array elements Q and K are the beginning and end elements within the synthetic aperture length, as shown in Figure 5.6 (b).

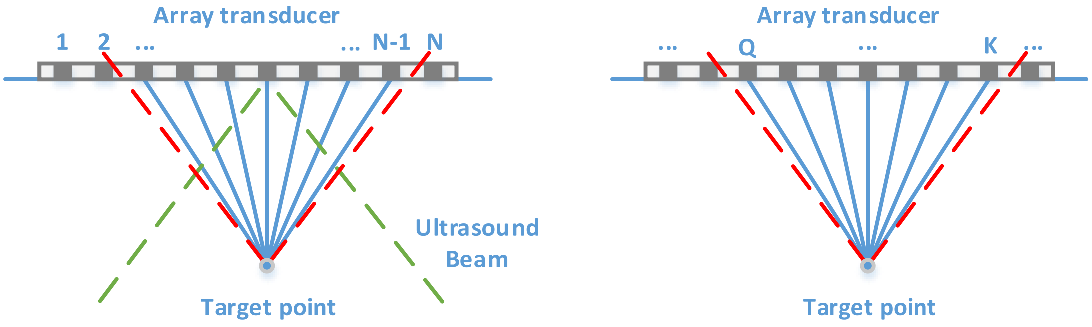

(a) (b)

Figure 5.6 SAFT for array transducer; Illustration of (a) Array SAFT with respect to a target point; (b) Illustration of array synthetic aperture length

$$\begin{bmatrix} f_{11} & \cdots & f_{1Q} & \cdots & f_{1K} & \cdots & f_{1N} \\ \vdots & & \vdots & \vdots & \vdots & \vdots & \vdots \\ f_{Q1} & \cdots & f_{QQ} & \cdots & f_{QK} & \cdots & f_{QN} \\ \vdots & \vdots & \vdots & \ddots & \vdots & \vdots & \vdots \\ f_{K1} & \cdots & f_{KQ} & \cdots & f_{KK} & \cdots & f_{KN} \\ \vdots & \vdots & \vdots & \vdots & \vdots & & \vdots \\ f_{N1} & \cdots & f_{NQ} & \cdots & f_{NK} & \cdots & f_{NN} \end{bmatrix} \tag{5.26}$$

5.2.3.3. Array SAFT

In terms of the SAFT algorithm when used with an array configuration, the data utilized by the algorithm is limited to all the combinations of transmit-receive echo signals within the synthetic aperture length associated with the target point. The biggest difference of array SAFT compared to TFM is the consideration of beam divergence of the array elements, which results in a subset of the FMC data being used for image pixel value calculation. The consideration of the beam divergence has been researched by S. Mosey[123] and Kerr et al.[124], while the former only considered the transmitted elements' beam divergence and the latter used a different submatrix from the one applied in this Thesis, which has a full coverage of the information from the array elements within the beam divergence. For the imaging algorithm, the target point is effectively every pixel in the imaging space. Therefore, a submatrix of the FMC dataset is employed for the calculation of image pixel intensity, as illustrated in Equation 5.27. This presumes that the number of array elements within the ultrasound beam is $(K - Q + 1)$ with respect to the target point. Then, all the echo signals from the $(K - Q + 1)$ x $(K - Q + 1)$ submatrix are used to calculate the new pixel value of the target at that spatial position.

$$\left[\begin{array}{ccccccc}
f_{11} & \cdots & f_{1Q} & \cdots & f_{1K} & \cdots & f_{1N} \\
\vdots & \ddots & \vdots & \Uparrow & \vdots & \vdots & \vdots \\ \cline{3-5}
f_{Q1} & \cdots & \multicolumn{1}{|c}{f_{QQ}} & \cdots & \multicolumn{1}{c|}{f_{QK}} & \cdots & f_{QN} \\
\vdots & \Leftarrow\vdots & \multicolumn{1}{|c}{\vdots} & \ddots & \multicolumn{1}{c|}{\vdots} & \vdots\Rightarrow & \vdots \\
f_{K1} & \cdots & \multicolumn{1}{|c}{f_{KQ}} & \cdots & \multicolumn{1}{c|}{f_{KK}} & \cdots & f_{KN} \\ \cline{3-5}
\vdots & \vdots & \vdots & \Downarrow & \vdots & \ddots & \vdots \\
f_{N1} & \cdots & f_{NQ} & \cdots & f_{NK} & \cdots & f_{NN}
\end{array}\right] \tag{5.27}$$

5.2.3.4. Application of Array SAFT Algorithm

According to the array imaging algorithm introduced in Section 5.2.2, the corresponding SAFT algorithm utilised in this work is presented here and includes wave propagation through two media on both the axial and circumferential directions.

When applying the SAFT algorithm in the first medium, either along the axial or circumferential directions of the tube, only the aperture width needs to be considered. In Figure 5.7 and Figure 5.8, θ_a is the beam angle of the effective synthetic aperture, which indicates the effective ultrasound beam width utilized for focusing. The pixel value of the image can be calculated by Equation 5.28, where $\theta_{a\mathrm{Tx}}$ and $\theta_{a\mathrm{Rx}}$ are the effective synthetic apertures for transmitter and receiver respectively, indicating a function of 1 within the beam angle and a function of 0 out of the beam area. $\mathrm{t_{ij}}(\mathrm{x},\mathrm{y})$ represents the total wave propagation time from transmitter i to receiver j through target pixel at position (x,y).

$$I_{ID\_SAFT}(\mathrm{x},\mathrm{y}) = \sum_{\mathrm{i}=1}^{\mathrm{N}}\sum_{\mathrm{j}=1}^{\mathrm{N}} \mathrm{f_{Tx,Rx}}\big(\mathrm{t_{ij}}(\mathrm{x},\mathrm{y})\big) \cdot \theta_{a\mathrm{Tx}} \cdot \theta_{a\mathrm{Rx}} \tag{5.28}$$

In the matter of applying the SAFT algorithm in the second medium, then refraction should be considered. For the axial direction, as shown in Figure 5.7, the wave transmitted from transducer element A has a beam angle θ_a in the first medium water. After entering the second medium (metallic tube) through point P at the interface, the beam angle is expanded and calculated by the incident angle θ_1 and refracted angle θ_2. Extending the refracted lines to have an intersection M, it is easy to determine the coordinates of M (x_M, y_M) by using the co-located angle $\theta_3 = \theta_2$.

$$x_M = x_A \tag{5.29}$$

$$y_M = \frac{|x_P - x_A|}{\tan\theta_3} \tag{5.30}$$

where x_A is known and x_P can be obtained by the computationally efficient method introduced in Section 4.3.3.2.

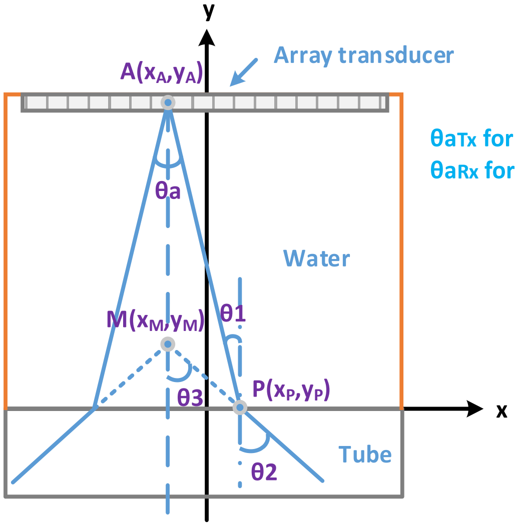

Figure 5.7 Array SAFT application on axial direction

Noting that the coverage area of the ultrasonic beam for the receiver is the same as the transmitter. On the axial direction, an arbitrary image pixel of the SAFT algorithm in the second medium can be calculated using Equation 5.31.

$$I_{OD\_SAFT}(\mathrm{x,y}) = \sum_{\mathrm{i}=1}^{\mathrm{N}}\sum_{\mathrm{j}=1}^{\mathrm{N}} \mathrm{f}_{\mathrm{Tx,Rx}}\big(\mathrm{t_{ij}}(\mathrm{x,y})\big)\cdot\theta_{\mathrm{\beta Tx\_M}}\cdot\theta_{\mathrm{\beta Rx\_M}} \tag{5.31}$$

where $\beta = 2\cdot\theta_3$ and $\theta_{\beta Tx\_M}$ and $\theta_{\beta Rx\_M}$ are the effective synthetic aperture of transmitter and receiver with respect to point M.

In the situation of implementing the SAFT algorithm in the second medium on the circumferential direction, the calculation of the coordinate of M is more complex than that on the axial direction, as shown in Figure 5.8. Firstly, the origin of the coordinate system is situated at the centre of the tube cross-section. Secondly, the shift of origin follows the array elements' position to take advantage of the angular relationship for obtaining the y-coordinate of M. Thirdly, the intersections on the tube surface has a different height, which causes a challenge when calculating the y-coordinate of M.

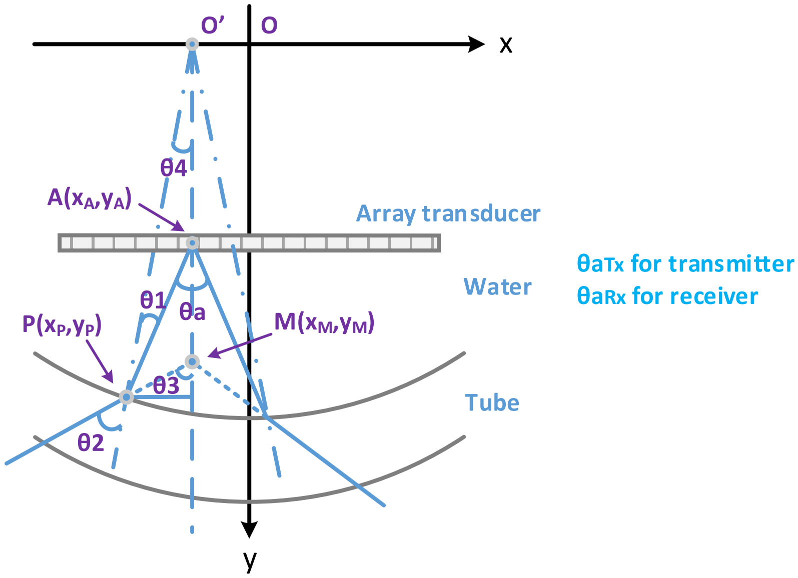

Figure 5.8 Array SAFT application on circumferential direction

In order to solve this problem, an effective way is to first have the intersection coordinate of the synthetic aperture and tube inner surface . Then, the following steps are utilized to find the coordinates of M. After defining the effective synthetic aperture θ_a, there are two intersections with the tube inner surface, with only one, point P, shown in Figure 5.8 and both of them satisfy Equation 5.32. Modifying the format as shown in Equation 5.33, then substituting into Equation 5.34 and considering $y_P < 0$, x_P can be obtained.

$$\frac{y_P - y_A}{x_P - x_A} = \pm\cot\frac{\theta_a}{2} \tag{5.32}$$

where ‘+’ indicates $x_P < x_A$ and ‘–’ indicates $x_P > x_A$.

$$y_P = \pm\cot\frac{\theta_a}{2}\cdot(x_P - x_A) + y_A \tag{5.33}$$

$${x_P}^2 + {y_P}^2 = R^2 \tag{5.34}$$

where R is the known tube inner diameter.

The solution includes two x_P values, which are $x_{P1} < x_A$ and $x_{P2} > x_A$. Considering a convenient way to find the coordinates of M, as in the example presented in Figure 5.8, selecting x_P for a smaller value of $|x_P - x_A|$ leads to the solution. Then, the corresponding y_P can be acquired through Equation 5.33.

For the sake of obtaining θ_3, the first step is to calculate θ_4 using Equation 5.35. After that, θ_1 can be calculated through Equation 5.36 following the exterior angle theorem, $\Delta O'PA$, and then θ_2 can be acquired by using Equation 5.37 following Snell’s law.

$$\theta_4 = \tan^{-1}\frac{-|x_P - x_A|}{y_P} \tag{5.35}$$

$$\theta_1 = \frac{\theta_a}{2} - \theta_4 \tag{5.36}$$

$$\theta_2 = \sin^{-1}\left(\frac{c_2}{c_1}\cdot\sin\theta_1\right) \tag{5.37}$$

where c_1 and c_2 are the wave velocity in water and tube respectively.

By using exterior angle theorem again in $\Delta O'PM$, θ_3 can be obtained.

$$\theta_3 = \angle O'PM + \theta_4 = \theta_2 + \theta_4 \tag{5.38}$$

Finally, the coordinates of M can be calculated using Equations 5.39 and 5.40, which are available for the second medium SAFT processing as described in Equation 5.31.

$$x_M = x_A \tag{5.39}$$

$$y_M = y_P + \frac{|x_P - x_A|}{\tan\theta_3} \tag{5.40}$$

5.3. Verification of Phased Array Imaging Methods

The verification of the TFM and SAFT array imaging methods, introduced in Section 5.2.2, is now presented through comparison of both simulation and experimental data. After this stage, the simulation platform will be used to evaluate a range of array inspection configurations, including the advanced TFM and SAFT post-processing algorithms. Hence, the key outcome for this Section is to validate both the simulation approach and the implementation of the array processing algorithms. For this validation work, a 32-element, 10 MHz array transducer has been utilised.

5.3.1. Simulation Configuration and Experiment Setup

It is difficult to acquire zirconium tubes for laboratory based experimentation due to the strict nuclear components management world-wide. Hence, titanium will be employed as an alternative. Table 5.3 shows an overview of the acoustic difference between zirconium and titanium[125].

Table 5.3 Acoustic difference between zirconium and titanium

Properties	**Zirconium**	**Titanium**
Longitudinal Velocity	4650 m/s	6070 m/s
Shear Velocity	2220 m/s	3310 m/s
Density	6480 kg/m^3	4500 kg/m^3
Acoustic Impedance	30.1 MRayl	27.32 MRayl

An additional simplification is used for the axial direction inspection, with a flat plate utilized instead of a tube section. This is considered appropriate due to the geometry in the axial direction and furthermore, simplifies the manufacture of artificial defects for this inspection scenario. A titanium tube with similar dimensions is used for circumferential defect inspection. Consequently, the geometry information for the array and titanium sample for both the simulation and experiment is presented in Figure 5.9 and Figure 5.10 provides details of the defects incorporated into the titanium samples. The 10 MHz array transducer, with an aperture of 9.6 mm, is immersed in water to inspect the tube with a water path distance of 20 mm, as illustrated in Figure 5.9. There are four configurations of the defect position shown in Figure 5.10, which are on the axial ID and OD surfaces, and the circumferential ID and OD surfaces with the specific size information listed in Table 5.4. The defect sizes are comparable with those identified within the CANDU pressure inspection guidelines, with a width range from 0.18 mm to 0.3 mm and a depth range from 0.24 mm to 0.5 mm, corresponding to a range from 1.2λ to 3.3λ. All the defects are manufactured by Centre for Ultrasonic Engineering and the exact size values are measured through a replication process (see Appendix C) combined with the use of an optical microscope. The full-skip TFM algorithm is validated by detecting the defect on the axial ID surface. Importantly, this combined modelling and experimental work can be used to verify the array imaging approach for pressure tube inspection.

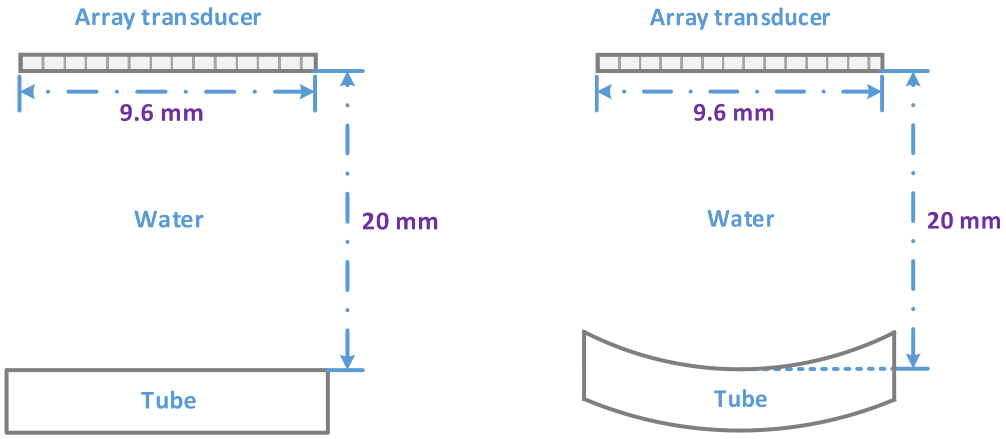

(a) (b)

Figure 5.9 Geometry of array transducer, water path and sample for both the simulation and experimental work (a) axial direction; (b) circumferential direction

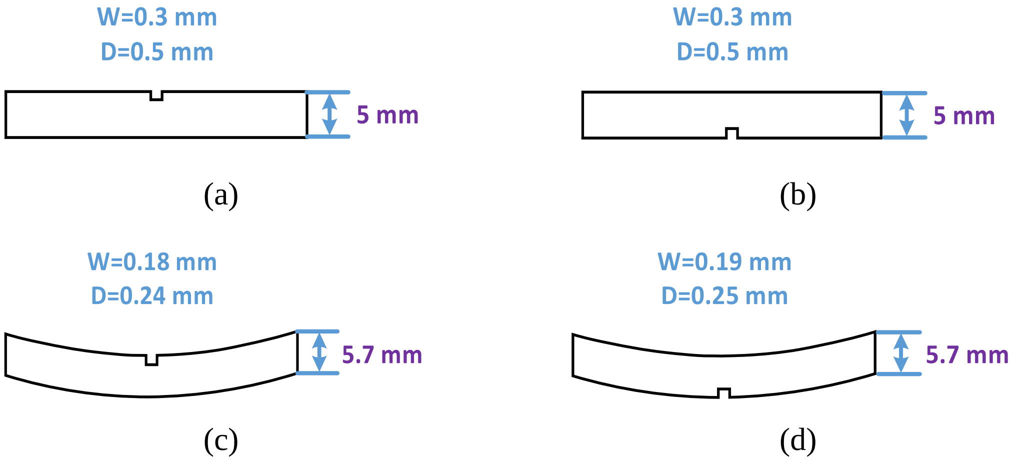

Figure 5.10 Geometry of titanium inspection target. W-width; D-depth. (a) axial ID; (b) axial OD; (c) circumferential ID; (d) circumferential OD

Table 5.4 Inspection parameters for both simulation and experimental scenarios

Item			**Parameter**	**Defect standard deviations**
Transducer	Central frequency		10 MHz	n.a.
	Element number		32	
	Pitch		0.3 mm	
	Element size		0.275 mm	
	Aperture		9.6 mm	
Water path			20 mm	
Axial	ID defect	Width	0.3 mm	0.0103 mm
		Depth	0.5 mm	0.0006 mm
	OD defect	Width	0.3 mm	0.0103 mm
		Depth	0.5 mm	0.0006 mm
	Tube thickness		5 mm	n.a.
Circumferential	ID defect	Width	0.18 mm	0.0076 mm
		Depth	0.24 mm	0.0052 mm
	OD defect	Width	0.19 mm	0.0087 mm
		Depth	0.25 mm	0.0314 mm
	Tube thickness		5.7 mm	n.a.
Wave velocity	Water		1480 m/s	
	Tube		6070 m/s	

The details of the simulation approach has been introduced in Chapter 4 and the experimental setup is presented in Figure 5.11 with an array transducer and a tube sample immersed in water to execute the inspection. The transducer was manufactured by Vermon (France) and has 128 elements, while the material of the tube is Titanium Grade 2 which is defined by American Society for Testing and Materials as unalloyed titanium with standard oxygen. The FI Toolbox array controller (Diagnostic Sonar Ltd, Livingstone, UK) is used to trigger the transducer to generate ultrasound waves and record the received echo signals. In addition, a computer with a proprietary software tool cueART[121] is used to provide a user interface for data acquisition. The key parameters of the ultrasonic inspection system are listed in Table 5.5.

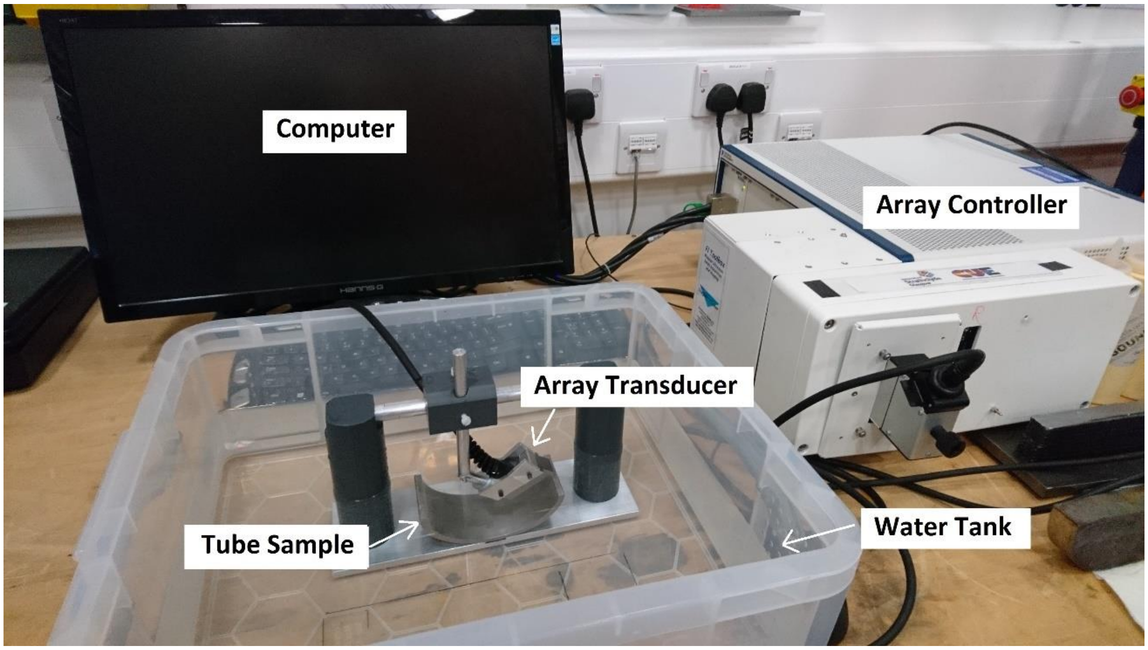

Figure 5.11 Experiment setup for validation

Table 5.5 Ultrasonic inspection system parameters

Items	**Parameters**
Array controller	FI Toolbox
Array transducer	Vermon 10 MHz 1-D linear transducer
Sample frequency	100 MHz
Transmitter voltage	40 V
Number of sample	1024 (32x32)
Data length	6000
User interface	cueART

5.3.2. Results Analysis

Using the titanium sample test configurations described in Section 5.3.1, both simulation and experimental FMC data has been acquired. The FMC data has subsequently been processed using TFM, including refraction and full-skip modalities where appropriate, and the results are presented in Figure 5.12 - Figure 5.15. In these Figures, the left hand column represents the simulated results, with the corresponding experimental result on the right hand column. Overall, good correlation between simulated and experimental results has been obtained. Each pair of images have the same *x*- and *y*- axes scales and each image has been individually normalised. Each inspection scenario, i.e. image pair, will now be individually discussed.

axial ID surface configuration: In the TFM image on the axial ID surface (Figure 5.12 (b)), a defect with a width of 0.3 mm and a depth of 0.5 mm is clearly seen and the surface signal is distinctly broken, where the same defect can be observed in the full-skip TFM images with the same features as shown in Figure 5.12 (d). Comparing the TFM images from the simulation to those from the experiment, they have a good correlation with the errors of 0.06 mm for width and 0.01 mm for depth. The image of axial ID surface (Figure 5.12 (a)) shows a strong front wall reflection signal and a broken surface, as replicated in the experiment. Considering the full-skip TFM image, the simulation data (Figure 5.12 (c)) presents a well matched result to the experimental data (Figure 5.12 (d)) to detect the defect on the ID surface.

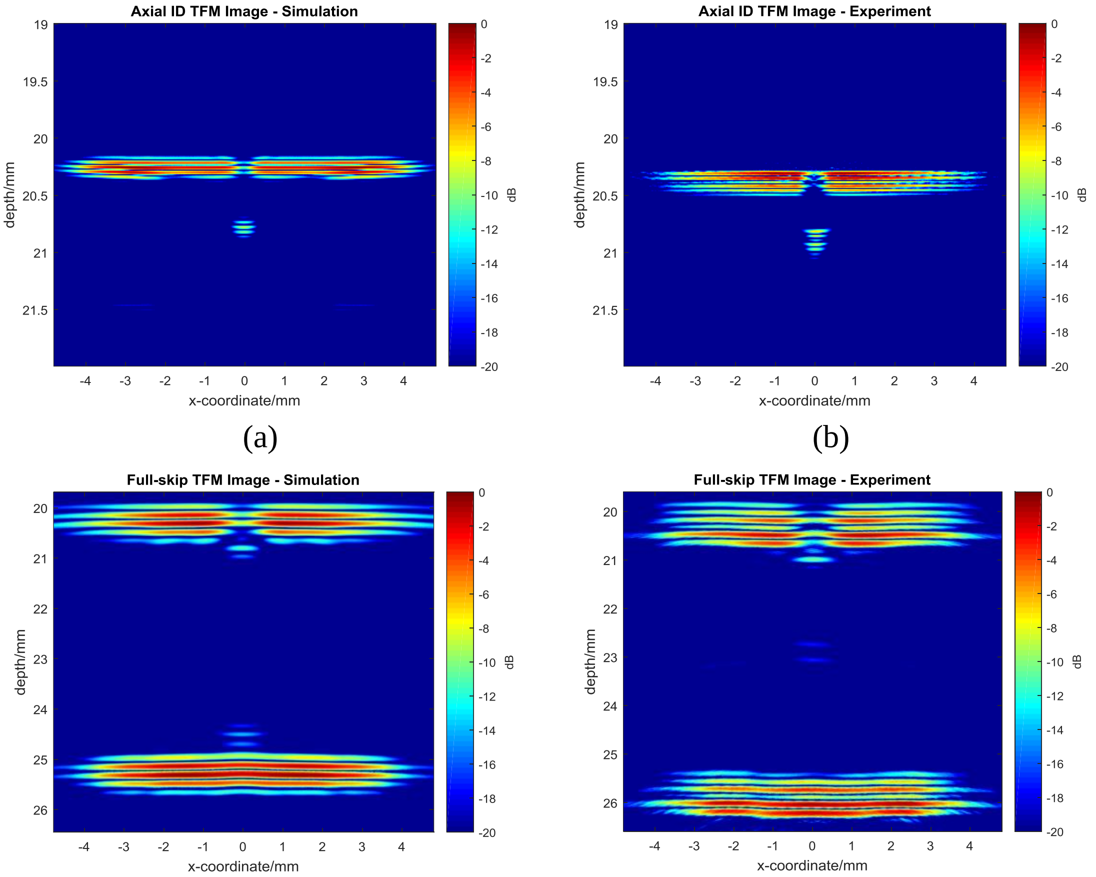

(a) (b)

(c) (d)

Figure 5.12 TFM image comparison of titanium inspections in axial ID (a) simulation and (b) experiment; full-skip (c) simulation and (d) experiment *axial OD surface configuration*: With regards to the experimental image of the axial OD surface with the same size defect (Figure 5.13 (b)), the defect and the broken surface are also identified, with the inspection errors of 0.5 mm for width and the correct depth measurement. Furthermore, the simulation image (Figure 5.13 (a)) reveals similar information. It should be noted that when comparing to the axial ID surface images, a larger wavelength can be found in the OD surface images due to the change in the speed of sound between the water and solid media.

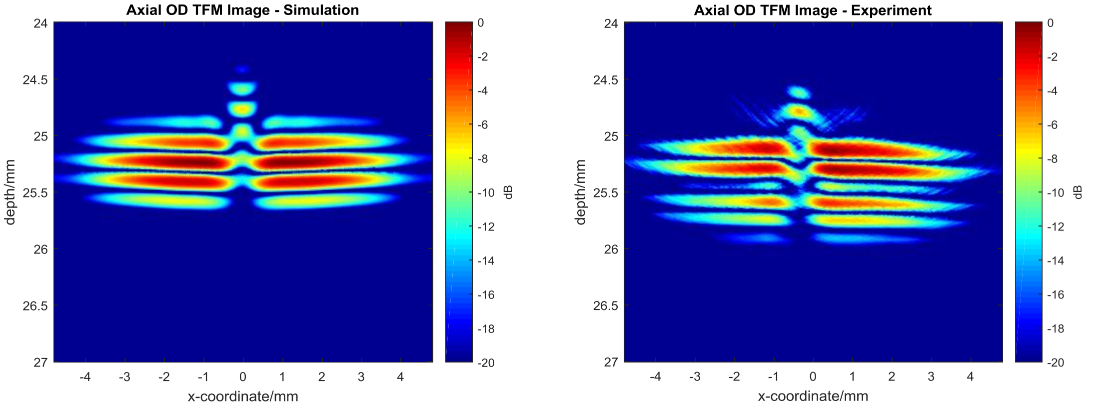

(a) (b)

Figure 5.13 TFM image comparison of titanium inspections in axial OD (a) simulation and (b) experiment

circumferential ID surface configuration: In terms of the inspection along the circumferential direction, for the experimental TFM image on the ID surface (Figure 5.14 (b)), the echo signal from the tube surface is stronger than that from the axial direction inspection since the curved surface leads to more energy being reflected back to the array transducer. Hence, the small defect with a width of 0.18 mm and a depth of 0.24 mm can be clearly identified. The simulation echo signal from the front wall surface (Figure 5.14 (a) is very close to the experiment, but with a weaker defect echo.

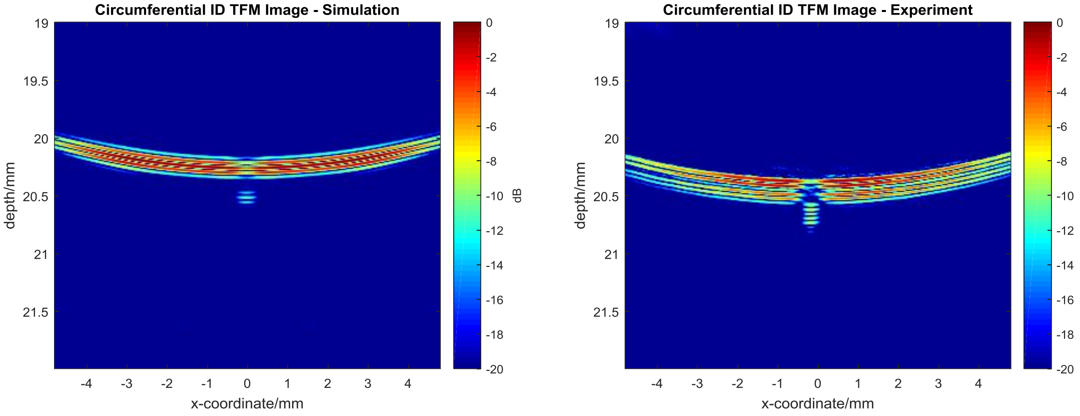

(a) (b)

Figure 5.14 TFM image comparison of titanium inspections in circumferential ID (a) simulation and (b) experiment

circumferential OD surface configuration: In respect of the images of the circumferential OD surfaces, the defect with a width of 0.19 mm and a depth of 0.25mm is difficult to find, but can be seen on the image (Figure 5.15) as the clear broken surface indicating that a defect is present at this location. Limited by manufacturing capability, only a defect width of 0.19 mm is made on the circumferential OD surface, which does not provide a strong defect echo. Notwithstanding the weak defect on OD surface, the imaging methods based on the simulation data can be used for subsequent post-processing algorithm investigations, since a defect width larger than 0.5 mm is more representative of this pressure tube inspection scenario.

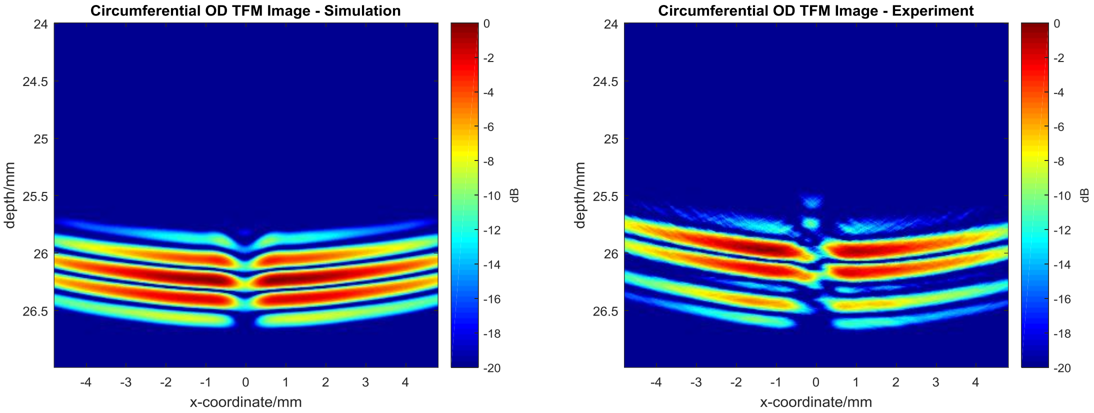

(a) (b)

Figure 5.15 TFM image comparison of titanium inspections in circumferential OD (a) simulation and (b) experiment

All of these TFM images obtained by simulation and experiment have proved that the imaging solution of phased array technique used for pressure tube inspection is reliable and the results demonstrate very high accuracy (see Table 5.6). Moreover, the simulation platform offers a high standard of defect detection ability and size measurement and importantly, both the imaging algorithms and simulation platform provide a strong foundation for the investigation of phased array inspection techniques applied to the pressure tube inspection.

The defect measurement results and associated errors for the results shown in Figure 5.12 – Figure 5.15 are listed in Table 5.6. Since the full-skip TFM image is utilized for supplying additional details about defect feature which will be demonstrated in Section 5.5.3, the direct TFM images are used to provide the defect measurement result. From the defect depth measurement results, an excellent accuracy is demonstrated for both ID and

OD surface inspections, with the errors within 0.03 mm in both cases. While the defect width measurement shows a bigger error due to the very small defect size especially for the OD inspection. However, the actual defects of concern will have widths larger than 0.5 mm and this will be represented in the following phased array simulation investigation. The measurement errors between simulation and experiment are presented in Figure 5.16 and clearly illustrates the accuracy of the simulation platform for predicting defect detection. The errors of defect depth measurement are within 0.03 mm and that of width measurement are within 0.15 mm.

Table 5.6 Defect measurement results of imaging methods verification

Direction	**Defect position**	**Dimension**	**Actual Results (mm)**	**Simulation**		**Experiment**	
				Results (mm)	**Error (mm)**	**Results (mm)**	**Error (mm)**
Axial	ID defect	Width	0.3	0.5	+0.2	0.44	0.14
		Depth	0.5	0.49	-0.01	0.5	0
	OD defect	Width	0.3	0.6	+0.3	0.7	+0.4
		Depth	0.5	0.47	-0.03	0.5	0
Circum-ferential	ID defect	Width	0.18	0.49	+0.31	0.35	+0.17
		Depth	0.24	0.25	+0.01	0.25	+0.01
	OD defect	Width	0.19	0.52	+0.33	0.45	+0.26
		Depth	0.25	0.23	-0.02	0.23	-0.02

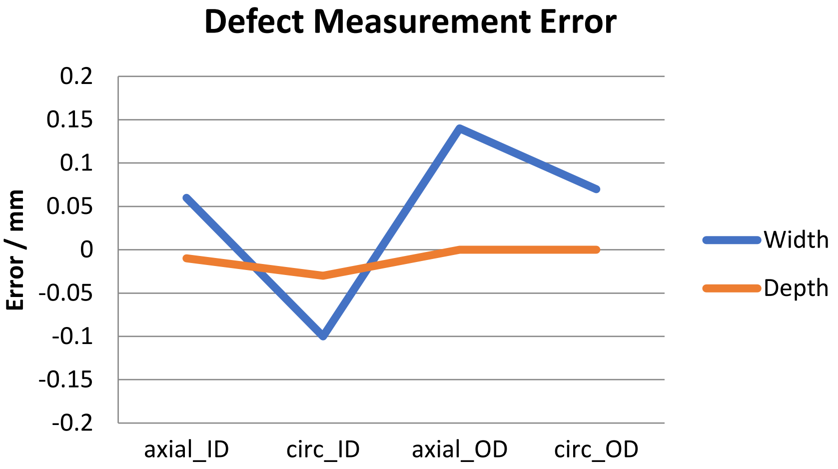

Figure 5.16 Defect measurement error (simulation comparing to experiment)

5.4. Comparison of Single Element and Array Inspection

Single element and array based pressure tube inspection are compared using simulation to consider the potential advantage in moving to an array inspection configuration. Considering the 20 MHz single element transducer offers the highest frequency with the highest resolution in the currently deployed system, a target defect on the tube ID surface is configured with dimensions of 2 mm width and 0.25 mm depth. A 32 element, 10 MHz array transducer is used in this comparison, because it can provide high accurate inspection results as presented in Section 5.3.2. The configuration details for both single element and array transducer systems are listed in Table 5.7. It should be noted that the single element transducer scenario is simulated at 3 different focal positions (20, 23 and 26 mm) to induce poorly-focused inspection data at 3 mm and 6 mm from the desired focal point of 20 mm.

Table 5.7 Configuration of parameters

Parameter		**Single element model**	**Array model**
Transducer	Frequency	20 MHz	10 MHz
	Aperture	6.3 mm	9.6 mm
	Pitch	-	0.3 mm
	Element size	-	0.275 mm
	Element number	1	32
	Focal length	20 mm	-
Water path		20/23/26 mm	20 mm
Defect	Width	2 mm	
	Depth	0.25 mm	

At the different focal distances between the single element transducer and the tube ID surface, the ultrasonic wave at the water-tube interface will have different wave shapes, as shown in Figure 5.17 using the -6 dB contour format. With regard to the desired 20 mm water path well-focused case, the width of the wave is only 0.34 mm, compared to the poorly-focused cases of 0.72 mm and 1.72 mm for 23 mm and 26 mm water paths respectively, and importantly, this impacts on the inspection system defect size resolution.

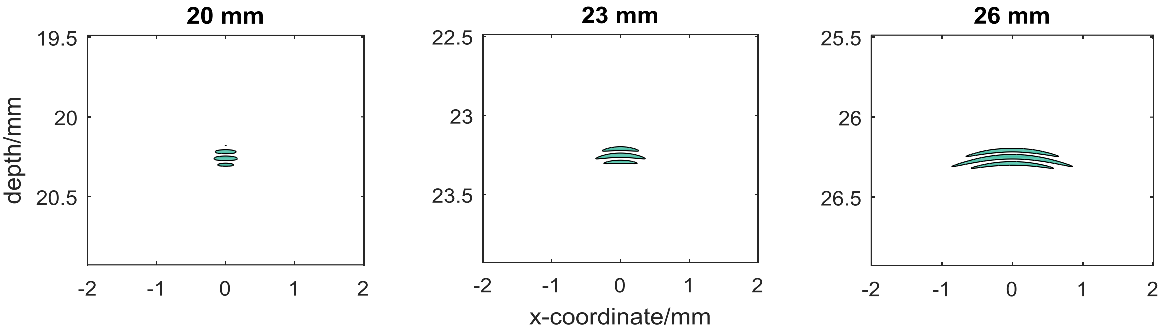

(a) (b) (c)

Figure 5.17 Ultrasonic wave at water-tube interface (a) 20 mm, well-focused; (b) 23 mm, poorly-focused; (c) 26 mm, poorly-focused

Figure 5.18 presents images of the inspection data from single element and array transducers. Firstly, through analysing the single element transducer inspections, the well-focused image (Figure 5.18 (a)) displays a stronger defect echo and OD surface echo, when compared to the poorly-focused examples shown in Figures 5.16 (b) and (c). Especially for the poorly-focused example at 6 mm beyond the focal point (Figure 5.18 (c)), it has a very weak defect echo, which causes the measurement results to be less accurate. When comparing the array inspection image (Figure 5.18 (d)) to the focused single element example, a clear break on the tube surface can be observed and importantly, this matches the defect width.

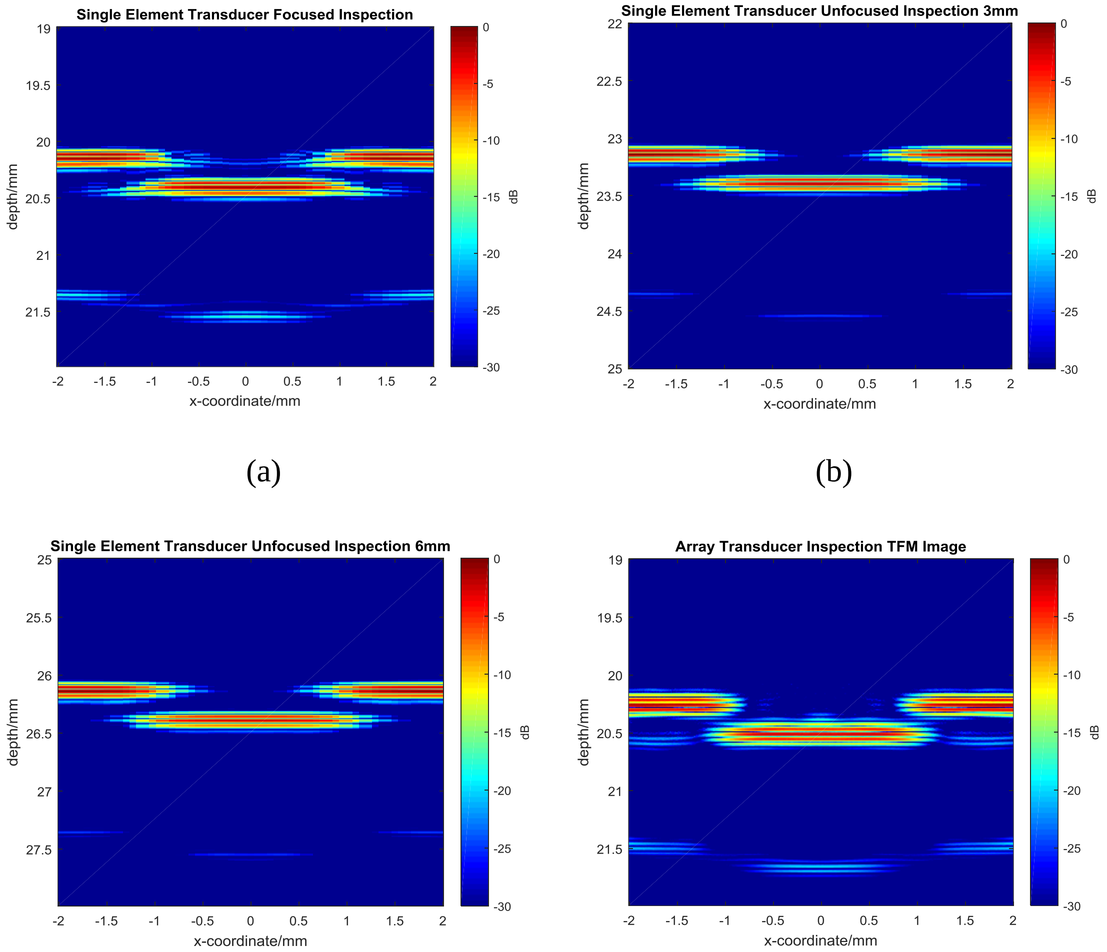

(a) (b)

(c) (d)

Figure 5.18 Comparison of single element and array inspection. Single element: (a) well-focused; poorly-focused, (b) 3 mm and (c) 6 mm beyond focal point; (d) array total focusing inspection

Through a comparison of the defect profile from the single element and array images presented in Figure 5.19, the array inspection demonstrates a good performance on the horizontal resolution, where the single element images show a lower resolution. Moreover, the defect signal energy has been reduced when compared to the ID surface signal for the poorly-focused images (3 mm and 6 mm), whereas the array image provides the same overall defect echo magnitude as the single element focused inspection. Additionally, using the A-scan signals to measure the defect depth is illustrated in Figure 5.20. All the reference signals (no defect) and defect signals are plotted to compare the relative depth measurement capabilities. To aid this comparison, all the results and errors are detailed in Table 5.8.

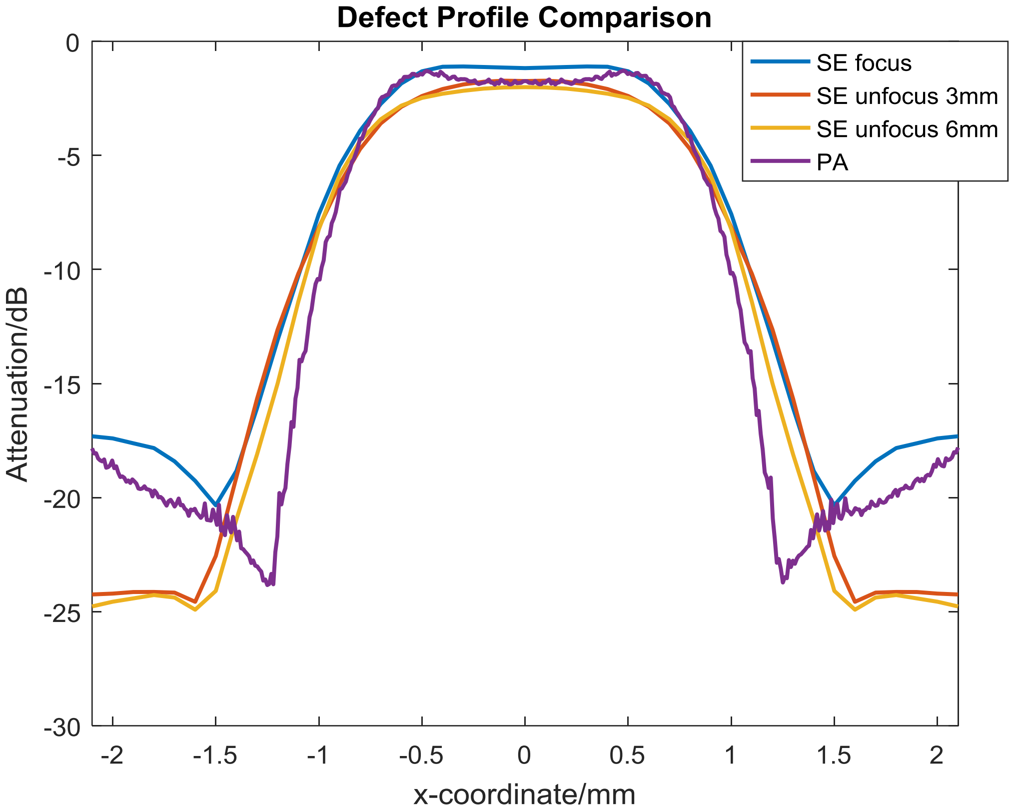

Figure 5.19 Defect profile comparison

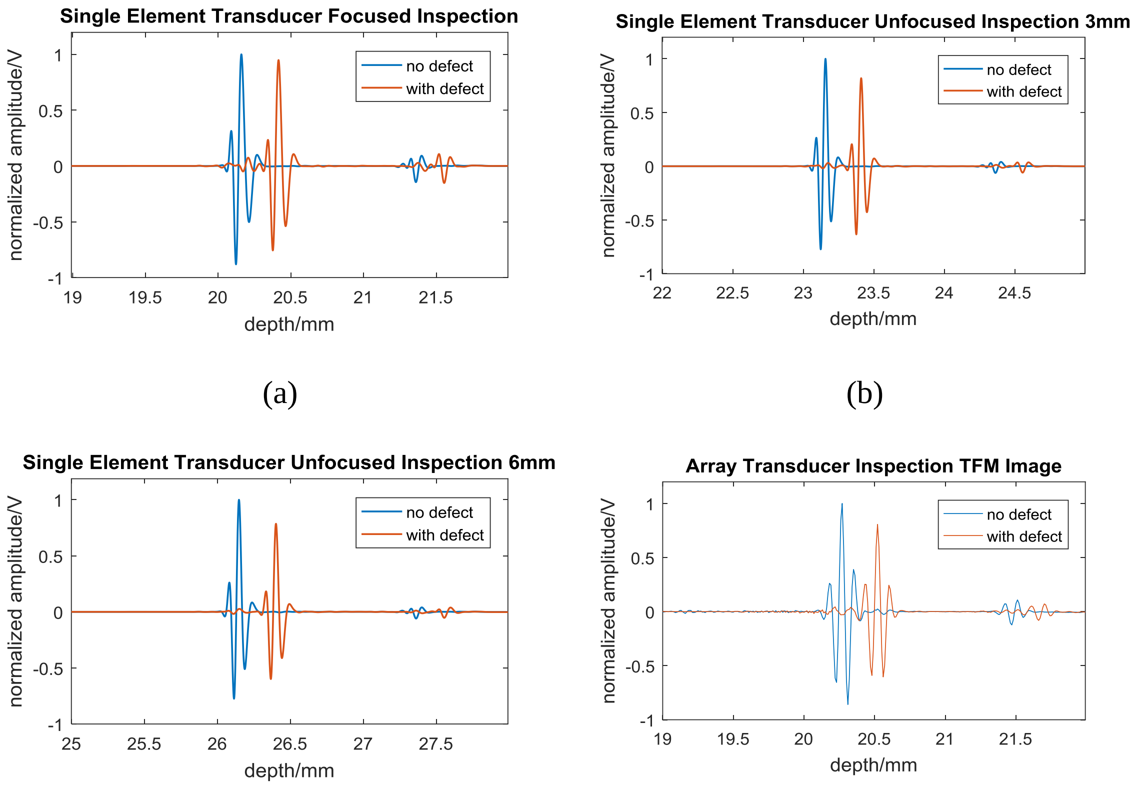

(a) (b)

(c) (d)

Figure 5.20 No defect and with defect signals for defect depth measurement. Single element: (a) well-focused; poorly-focused, (b) 3 mm and (c) 6 mm beyond focal point; (d) array total focusing inspection

From the simulation results presented in Table 5.8, the defect depth values are very similar, although the highest accuracy is obtained from the array TFM image. Whereas, the defect width predictions show the largest differences, albeit with the best result coming from the array image. Moreover, the amplitude ratio of the defect echo to the front wall echo for the array image is 86.3%, which presents an excellent contrast from which to detect and measure the defect.

Table 5.8 Defect depth and width simulated results, for a target defect dimension of 2 mm width and 0.25 mm depth

Inspection setup	**Defect depth measurement**		**Defect width measurement**		**Min attenuation (dB)**	**Amplitude Ratio**
	Result (mm)	**Error (mm)**	**Result (mm)**	**Error (mm)**		
Single element focused	0.26	+0.1	2.1	+0.1	-1.173	87.4%
Single element unfocused 3 mm	0.26	+0.1	2.2	+0.2	-1.739	81.9%
Single element unfocused 6 mm	0.26	+0.1	2.2	+0.2	-2.009	79.4%
Array TFM	0.25	0	1.9	-0.1	-1.281	86.3%

Overall, the phased array technology demonstrates very high resolution and accuracy for the defect size measurement. It does not only solve the focusing problem which exists in the single element inspection, but also provides flexibility through array post-processing for defect measurement improvements and feature identification. It is now proposed to use this simulation platform, and associated array imaging, to undertake a study of array configurations to determine a potential array system to replace the existing multiple single element transducer sensor head arrangement.

5.5. Simulation Data Analysis for a Range of Array Configurations

In order to select a suitable array configuration for inspection of pressure tubes, a number of simulations have been conducted to consider the impact of different array central frequencies and array element numbers on the detection of defects situated on the axial ID (aID), axial OD (aOD), circumferential ID (cID) and circumferential OD (cOD) surfaces. Figure 5.21 demonstrates the details of the array configurations, frequency (5 MHz, 7.5 MHz and 10 MHz) and number of elements (8, 16 and 32), used to predict the results of inspecting two different defect types, as shown in Figure 5.22. The defects are a rectangular defect (rect, depth 0.3 mm and width 0.5 mm) and a v-shaped defect (vshape, depth 0.5 mm and width 0.5 mm with a tip of radius 0.06 mm). These two defects are representative of the defects typically encountered in a nuclear pressure tube inspection to test the ability of the array technology and post-processing algorithms. There are 36 models to be run for inspecting each defect, so a total of 72 hybrid models will be used to analyse the defect characterisation performance from each array configuration and at the key axial and circumferential locations in the tube.

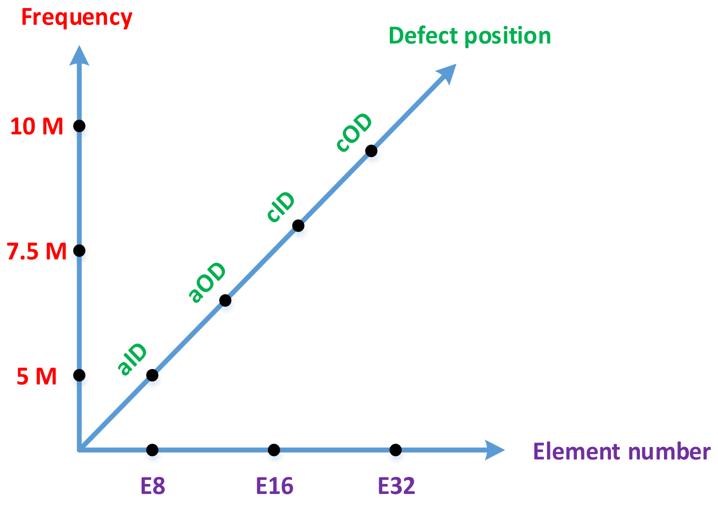

Figure 5.21 Representation of range of array configurations to be simulated

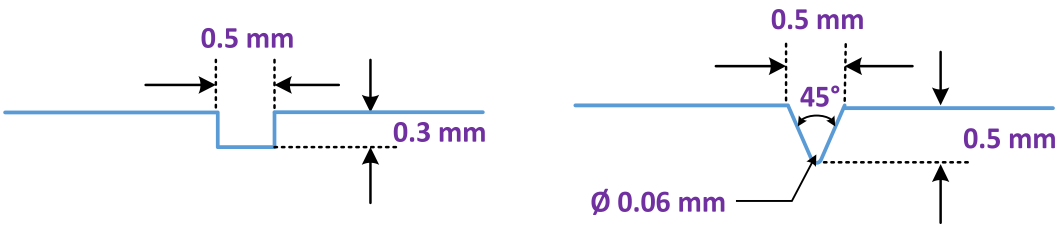

(a) (b)

Figure 5.22 Defect types and dimensions (a) rect defect; (b) vshape defect

With respect to the range of array configurations to be simulated, the practical array element dimensions are based on conventional array imaging design guidelines and are listed in Table 5.9. Here, the array element pitch is constant with respect to operating frequency and hence, an increase in the number of elements will increase the active array aperture.

Table 5.9 Diverse array parameters

	Diverse array configuration								
Central frequency (MHz)	5 MHz			7.5 MHz			10 MHz		
Element size (mm)	0.55			0.41			0.275		
Pitch (mm)	0.6			0.45			0.3		
Element number	8	16	32	8	16	32	8	16	32
Active Aperture (mm)	4.8	9.6	19.2	3.6	7.2	14.4	2.4	4.8	9.6

5.5.1. TFM Imaging Analysis

First of all, the measurement results of the single medium TFM imaging used for the defect inspection on the aID and cID surfaces are shown in Figure 5.23 and Figure 5.24, respectively. The full measurement results using TFM and array SAFT processing methods can be found in Appendix E combined with two size measurement examples. All the measurement are based on the -6 dB sizing method. The solid line indicates the depth result while the dotted line indicates the width result. From all four charts, consistent and reasonably accurate depth measurement results can be observed for all array configurations for both rect or vshape defects. For the rectangular defect, the predicted measurement accuracy is 97% on aID (Figure 5.23 (a)) and cID (Figure 5.24 (a)). However, the depth measurement result of the vshape defect is overestimated by 19% by both 7.5 MHz and 10 MHz configurations, whereas, the 5 MHz array is prediccted to provide a more accurate result, with only a 12% error with respect to the true defect depth of 0.5 mm.

In terms of the defect width results, an obvious trend is evident in Figure 5.23 and Figure 5.24 where the higher operating frequency tends towards the actual width value of 0.5 mm for both rect and vshape defects. Hence, larger array configurations are necessary for more accurate defect width measurement. In addtion, both of the 7.5 MHz and 10 MHz configurations demonstrate similar defect width measurement ability, with the highest resolution being achieved by using 32 elements.

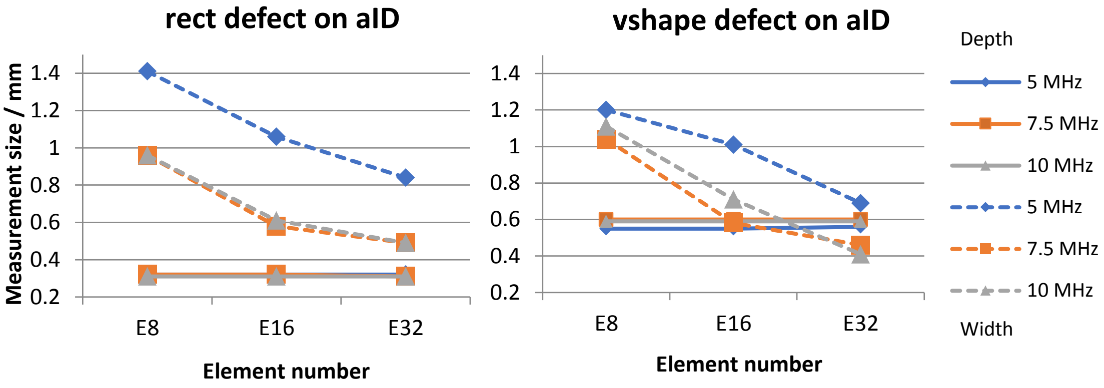

(a) (b)

Figure 5.23 Depth and width measurement results from aID (a) rect defect; (b) vshape defect

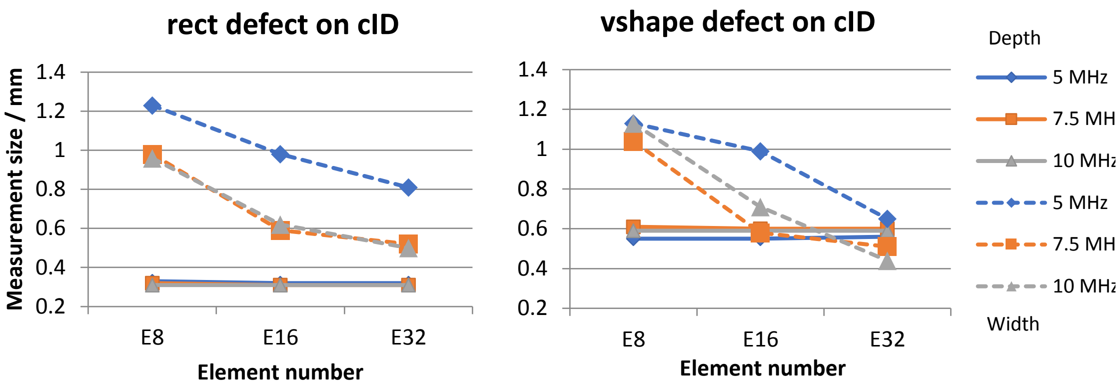

(a) (b)

Figure 5.24 Depth and width measurement results from cID (a) rect defect; (b) vshape defect

To present a direct view of the comparison of TFM imaging results by utilizing different numbers of elements, Figure 5.25 shows the 10 MHz TFM images of the cID surface. Both types of defects can be observed in the images generated by each configuration, with higher element numbers producing the highest fidelity images and accurate defect sizing. Furthermore, when using 32 elements, the ID interface has a fully broken surface which can enhance the defect detection capabilities in a practical situation.

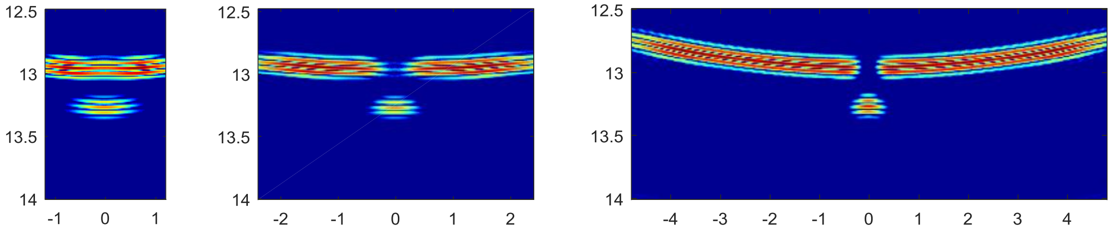

rect E8 rect E16 rect E32

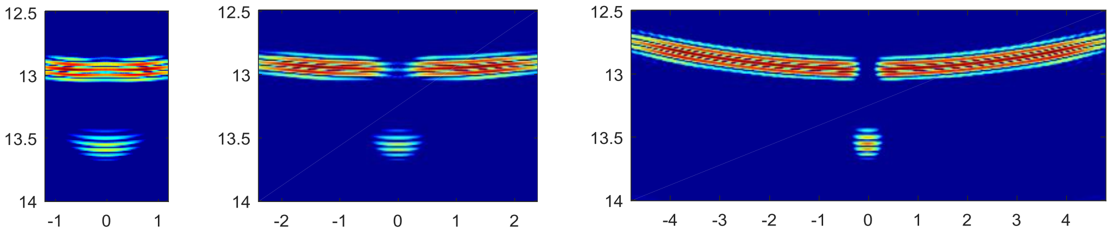

vshape E8 vshape E16 vshape E32

Figure 5.25 10 MHz cID TFM images by different transducer configurations (x-coordinate/mm, depth/mm)

The generation of OD TFM simulated images are more complex for both axial and circumferential inspections, due to reflection and refraction at the water-tube interface. Figure 5.26 presents the predicted rectangular defect width and depth measurements for the aOD inspection scenario. Interestingly, the predicted measurements are very similar for both 7.5 MHz and 10 MHz operating frequencies, with the 5MHz case showing the poorest results accuracy at the lowest element number due to its largest relative wavelength, as is illustrated in Figure 5.27. Nevertheless, the 5 MHz configuration provides an excellent defect width measurement result, when using either 16 and 32 elements, since the defect echo can be completely isolated from the OD surface, whereas this feature is not observed in the 7.5 MHz and 10 MHz image data. To aid understanding, a comparison of aOD TFM images at both 5 MHz and 10 MHz operating frequencies are compared in Figure 5.27.

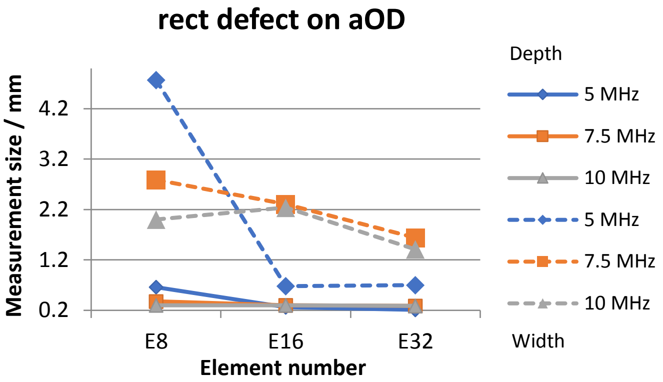

Figure 5.26 Depth and width measurement results from aOD for rect defect

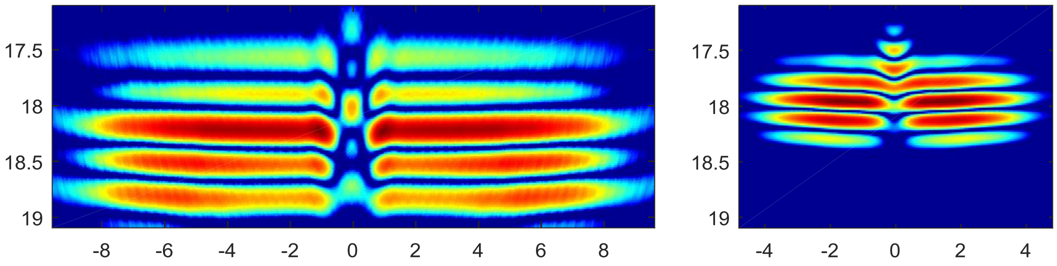

5 MHz rect E32

10 MHz rect E32

Figure 5.27 Comparison of 5 MHz and 10 MHz aOD TFM images for rect defect (x-coordinate/mm, depth/mm)

In terms of the vshape defect on the aOD surface, there is difficulty in finding the defect tip information, as the echoes from the defect tip are weakly received. Figure 5.28 gives an example of the aOD TFM image from a 10 MHz transducer using 32 elements. Even though there is no strong tip echo from the vshape defect, when applying more array elements, an obvious broken surface can be seen from the OD surface that indicates the presence of a defect.

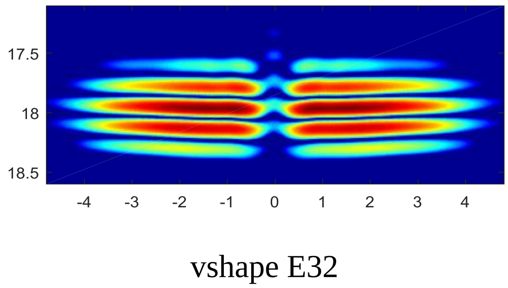

Figure 5.28 10 MHz 32 elements aOD TFM image for vshape defect (x-coordinate/mm, depth/mm)

Thanks to the curved inner diameter surface, the weak tip echo from the vshape defect situated at the cOD surface is focused back to the transducer and a weak, but identifiable signal can be observed on the cOD surface, as shown in Figure 5.29.

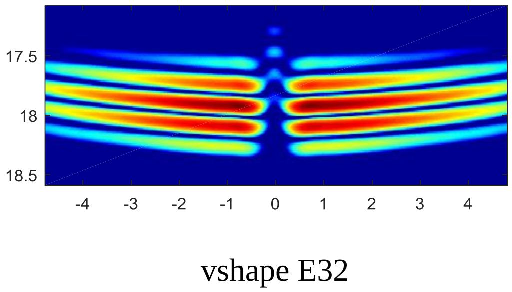

Figure 5.29 10 MHz 32 elements cOD TFM images vshape defect (x-coordinate/mm, depth/mm)

With regard to the TFM images from inspection of defects on the cOD surface, the defect depth measurement results are consistent when using 32 elements for rect defect inspection scenarios, with similar results for the vshape defect across all frequency configurations. Overall, lower numbers of elements make it difficult to identify either of the defects. All the rect defect depth measurement results are 0.02 mm smaller than the defined value (0.3 mm) and between 0.05 mm and 0.1 mm smaller than the configured vshape defect depth (0.5 mm) for the 10 MHz and 5 MHz array transducers, respectively.

For all the defect width measurements, 32 element arrays bring about more accurate results as illustrated in Figure 5.30. There is some inconsistency in the trend of the results between the 8 and 16 element configurations. The reason is that the weak echo signal from the defect is difficult to separate from the connected OD surface echo and leads to a large predicted measurement.

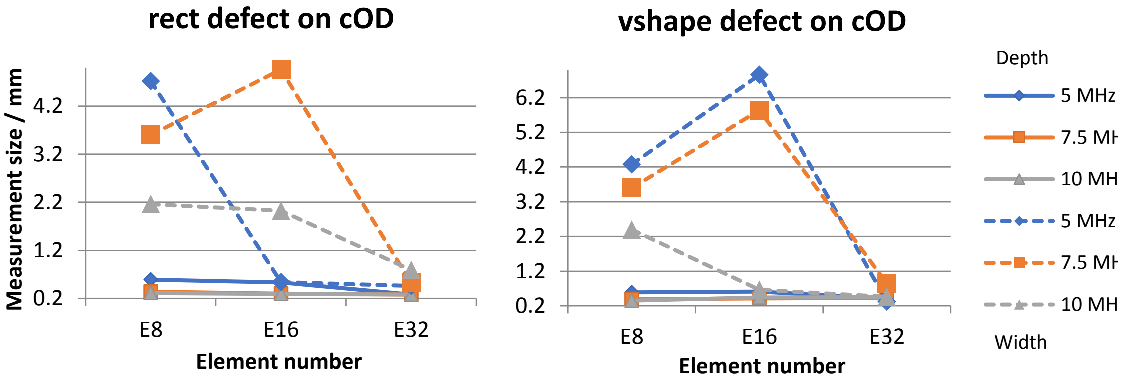

(a) (b)

Figure 5.30 Depth and width measurement results from cOD (a) rect defect; (b) vshape defect

A graphical view of the difference between using 5 MHz and 10 MHz array transducers is displayed in Figure 5.31. Here, the lower operating frequency provides a stronger penetration in which the broken OD surface feature is even present in the 8 element configuration and completely separated defect information can be identified in 16 and 32 elements configurations. Conversely, the higher frequency supplies a weaker penetration where the defect echo is not separated from the surface for the entire element configurations. However, the 10 MHz transducer has a higher resolution for the depth measurement due to its short operational wavelength.

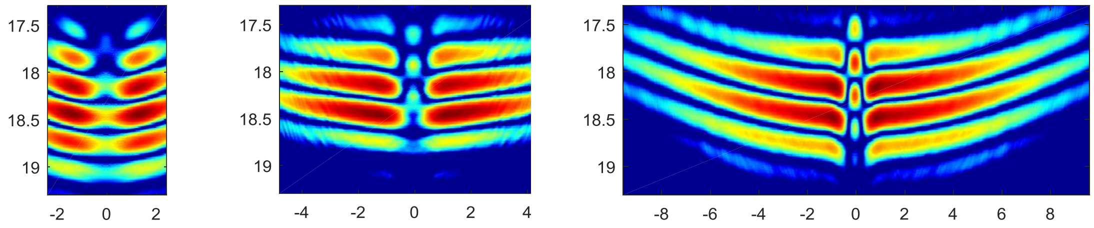

5 MHz rect E8 5 MHz rect E16 5 MHz rect E32

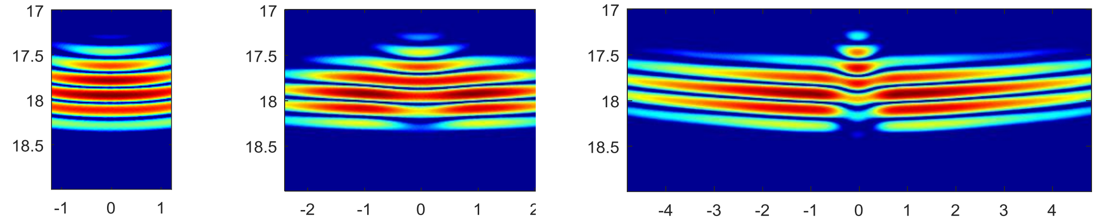

10 MHz rect E8 10 MHz rect E16 10 MHz rect E32

Figure 5.31 5 MHz and 10 MHz cOD TFM images by different transducer configurations (x-coordinate/mm, depth/mm)

5.5.2. Array SAFT Processing Analysis

Considering the operating frequency range of the three different array transducer configurations, the array synthetic aperture length has been determined for both ID and OD inspection scenarios using the approach illustrated in Figure 5.32. The 5 MHz transducer with 32 array elements will be used for analysing the effect of array SAFT processing due to its wider field of view providing flexibility of the selection of effective synthetic aperture. The rect defect presented in Figure 5.22 (a) situated at the centre of the aID, cID, aOD and cOD surfaces are configured in the hybrid model and different synthetic aperture lengths based on angle are utilized in the array SAFT processing algorithm to find the most effective synthetic aperture length to improve the defect width measurements.

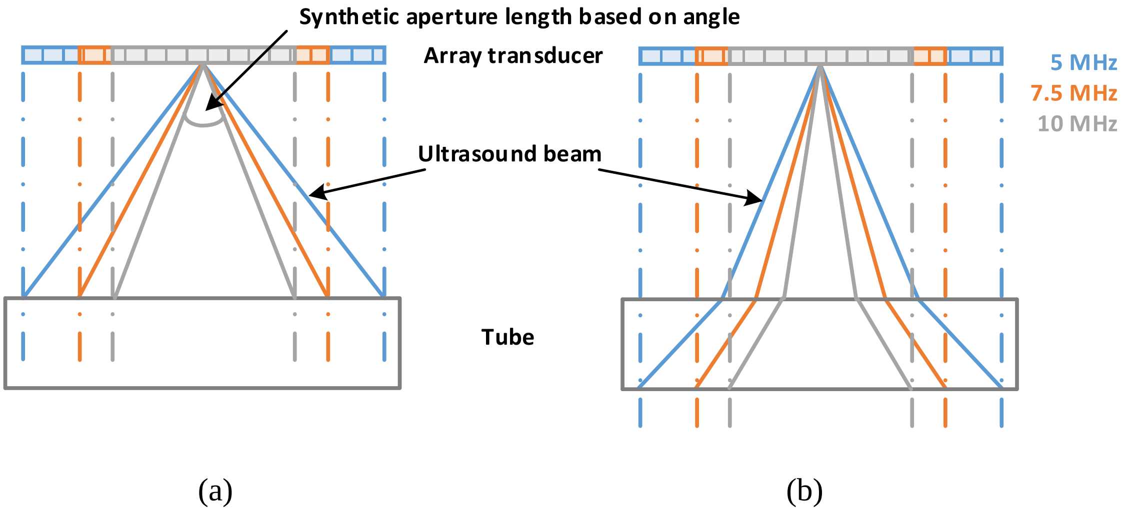

Figure 5.32 Maximum coverage range by different frequency array transducers; (a) ID and (b) OD surfaces

Regarding the array SAFT application for the measurement of defect on the ID surface, the synthetic aperture length is selected from 30° to 80° with a full reasonable coverage of the ultrasound beam. Figure 5.33 demonstrates the array SAFT processing of the rect defect on the aID surface with different synthetic aperture lengths, where the blue solid line indicates the SAFT measurement result, and the red and green dotted lines indicate the TFM result and the real width value. From this Figure, TFM overestimates the defect width by approximately 68%, which is roughly matched by the array SAFT at the extremities of the synthetic aperture range used in these simulations. However, at a synthetic aperture of 45^{o}, the measurement error is reduced to approximately 46%. Importantly, this improvement only needs to find the effective synthetic aperture of the array element, which can be executed with the calibration of FMC data[28][126].

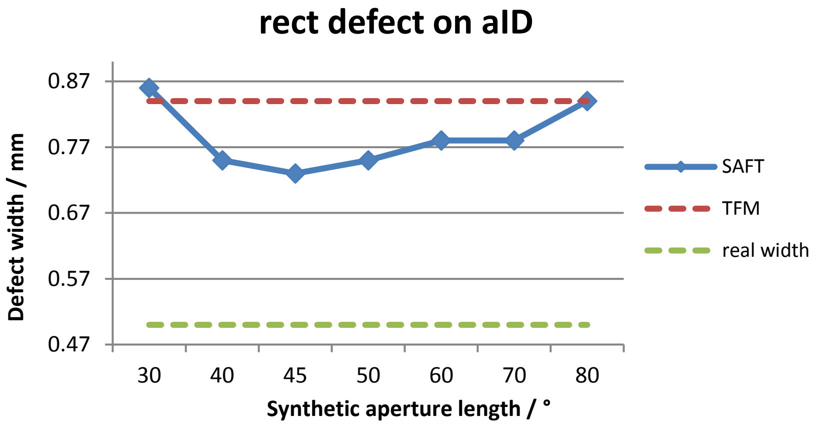

Figure 5.33 Comparison of SAFT and TFM measurement of defect width on aID surface

In order to compare the array SAFT algorithm to TFM imaging, the corresponding defect profiles are shown in Figure 5.34, using a 45° synthetic aperture length for the SAFT image. The TFM image demonstrates higher amplitudes of noise outside the defect peak, although the defect itself has a similar form for both imaging approaches. Interestingly, the defect signal associated with the TFM approach has a double peak at the maximum defect response and this can lead to measurement inaccuracies. The double peak is caused by the greater aspect ratio in TFM while array SAFT involves more relative beam waves to contribute a focused result.

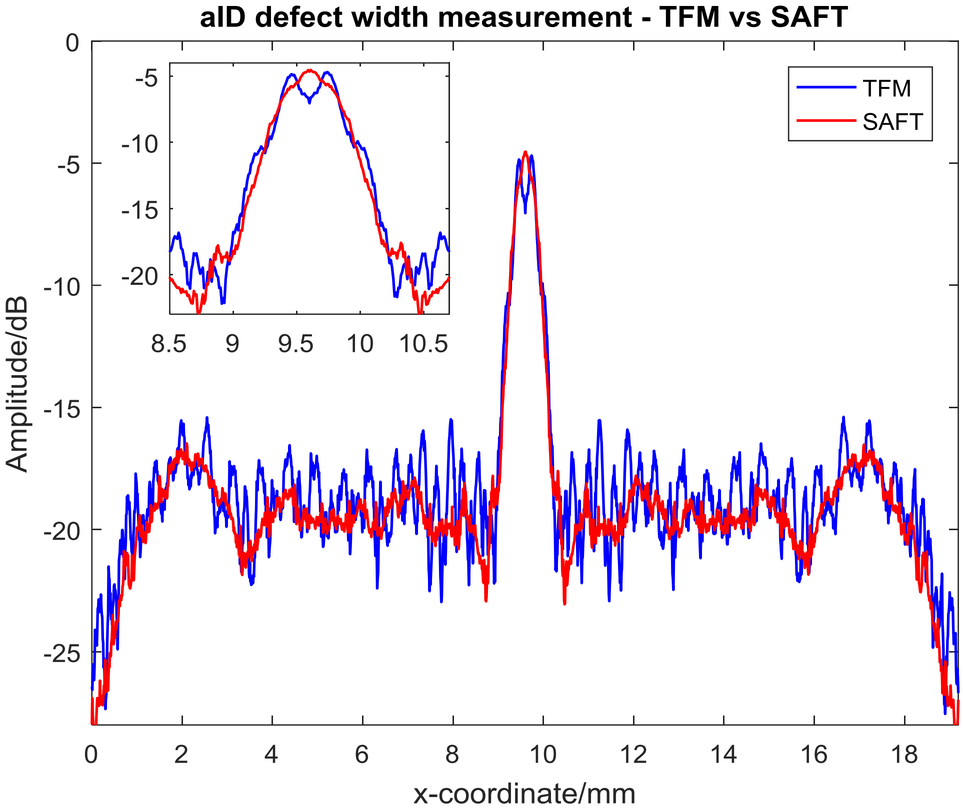

Figure 5.34 aID surface defect width measurement – TFM vs SAFT

The circumferential ID surface produces enhanced echo signals to be reflected and received by the transducer. Therefore, the TFM image produces a smaller measurement error (~60%) when compared to axial ID case, as shown in Figure 5.35, and furthermore, the array SAFT processing offers minimal improvement for defect width measurement.

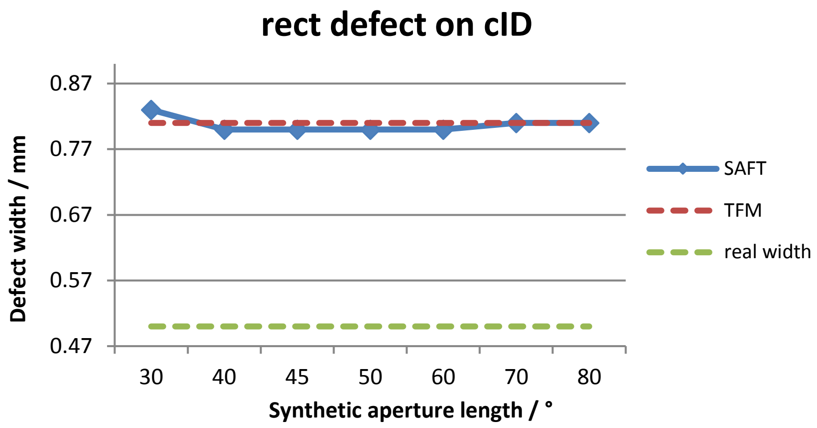

Figure 5.35 Comparison of SAFT and TFM measurement of defect width on cID surface

In terms of the array SAFT application on the inspection of OD surface, the range of the synthetic aperture length is smaller than that for ID surface because of refraction at the water-tube interface. Importantly, a synthetic aperture length of 28° can reach the critical angle in the tube. Consequently, the range of the synthetic aperture length for the array SAFT on the OD surface is selected between 16° to 26°.

The width measurement of the rectangular defect on the axial OD surface using both array SAFT and TFM methods is illustrated in Figure 5.36, where a similar trend to the axial ID surface inspection (see Figure 5.33) is observed. Here, the 20° aperture length demonstrates the most effective synthetic aperture and gives rise to the most accurate measurement result with a 25% error compared to 40% for the TFM case.

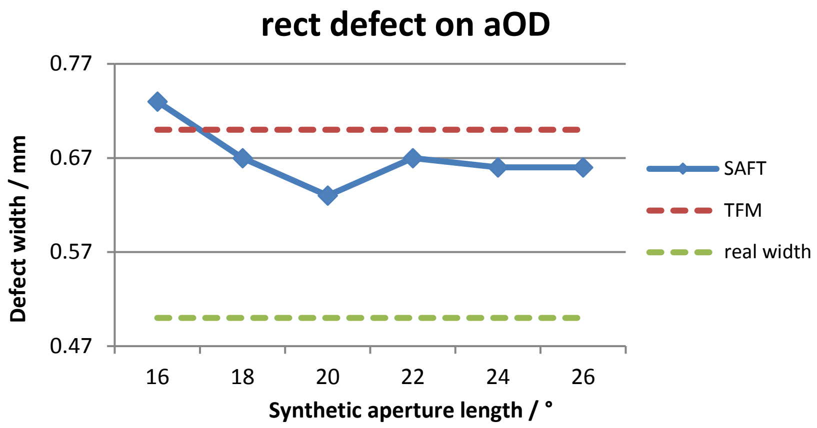

Figure 5.36 Comparison of SAFT and TFM measurement of defect width on aOD surface

Figure 5.37 presents the direct defect profile view comparing the 20° synthetic aperture length array SAFT and TFM results. The high amplitude is from the axial OD surface reflection, while the defect profile is situated at the centre of the image which can be seen in the zoomed part of the Figure. Although from initial observation both algorithms have a similar performance, the array SAFT image provides a narrow defect profile and a higher amplitude drop around the defect that means it has a better separation from the surface signal.

With respect to the circumferential OD surface inspection, the defect width result from TFM images is close to, although approximate 8% smaller than, the real value, as shown in Figure 5.38. The application of array SAFT processing with low synthetic aperture lengths, < 22°, has produced a measurement result to within 2% due to the more effective information being utilized for array focusing. However, as the synthetic aperture length increases above 22°, the measurement tends to the same value/error as the predicted by the TFM result.

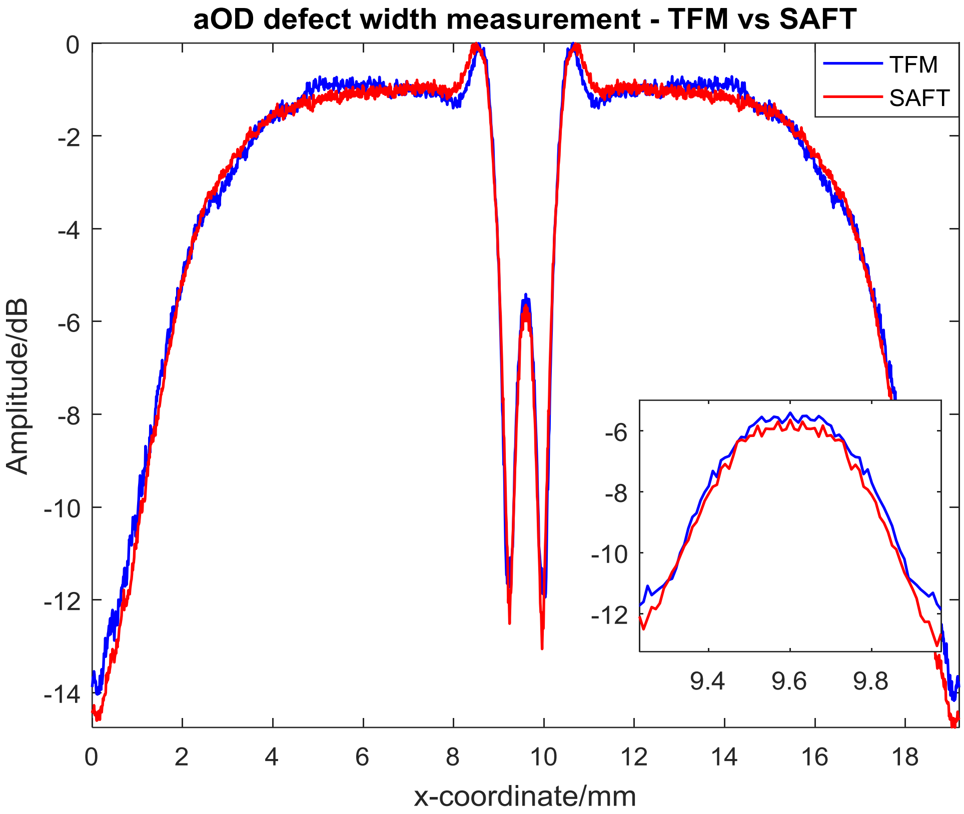

Figure 5.37 aOD surface defect width measurement – TFM vs SAFT

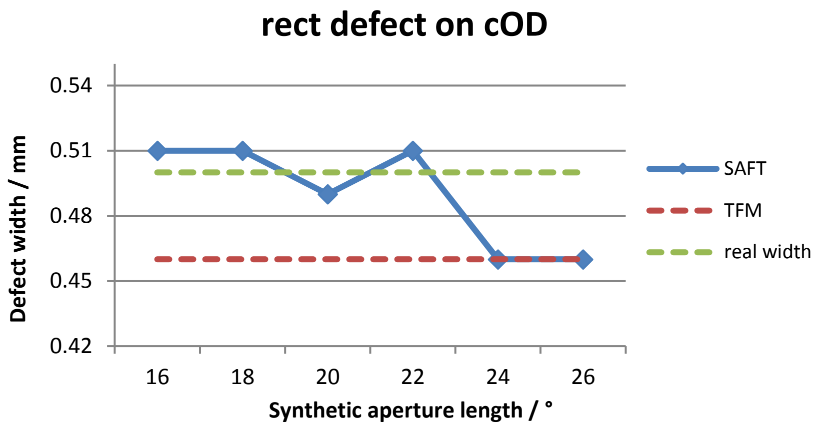

Figure 5.38 Comparison of SAFT and TFM measurement of defect width on cOD surface

5.5.3. Full-skip TFM for Defect Feature Analysis

The vshape defect is more critical than the rect defect since it is easier to generate a crack in the tube. Hence, the ability of the inspection technique to identify this critical defect is significant and the full-skip TFM can be helpful to find this kind of defect.

Figure 5.39 shows the direct and full-skip TFM images associated with inspecting defects on the ID surface. Both the rect defect and vshape defect are demonstrated with the dimensions introduced in Figure 5.22. When a clear defect echo is found in the ID surface from a direct TFM image, it is not easy to identify the defect shape. As shown in Figure 5.39 (a) and (b), both defects are discoverable but it is hard to discriminate between the rectangular shape and a defect containing a tip. Through observing the full-skip TFM images, a defect echo, indicated as an extension of the back wall signal, can be found near the ID surface (Figure 5.39 (c)) for a rect defect, because a strong defect reflection inside of the tube. However, the vshape defect does not provide an apparent defect echo in the full-skip TFM image (Figure 5.39 (d)) since the reflection from a tip inside of the tube is too weak to be detected.

The full-skip TFM is actually an inverted view of the scene between the tube ID and OD surface reflections, which can be supportive in terms of providing additional defect characteristic details. The critical vshape defect can be distinguished using the full-skip TFM image after an obvious defect echo on the ID surface is found from a direct TFM image.

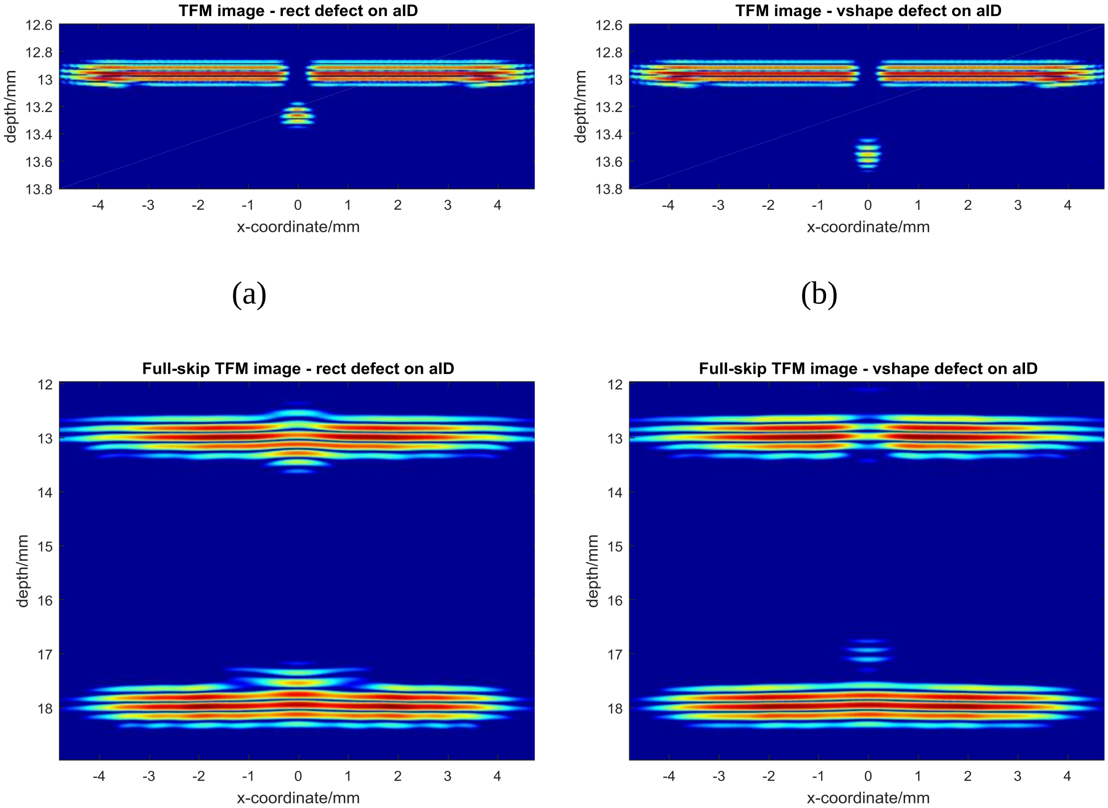

(a) (b)

(c) (d)

Figure 5.39 Direct TFM and Full-skip TFM images by 10 MHz transducer with 32 elements for defect on ID surface; (a) rect defect and (b) vshape defect TFM images; (c) rect defect and (d) vshape defect full-skip TFM images

5.6. Discussion

According to the previous analysis, a replacement of the current sensor system for pressure tube inspection by using phased array technology is proposed. The new sensor system will include two array transducers and corresponding array controllers for FMC data acquisition and signal processing. A 10 MHz array transducer is situated at the axial direction and a 5 MHz array transducer is situated at the circumferential direction as Figure 5.40 shown. Compromising between the defect detection ability and data processing efficiency, both of the transducers will contain 32 elements.

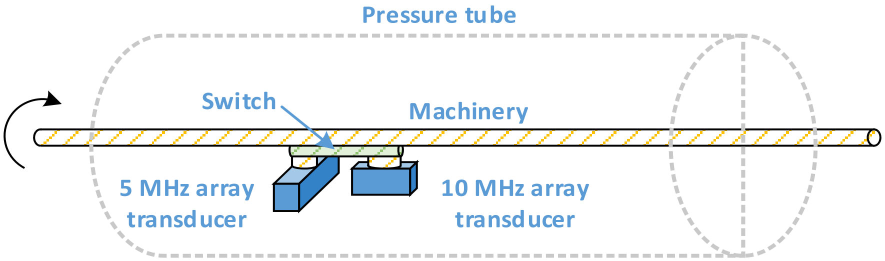

Figure 5.40 Proposed array sensor system

The reason to incorporate different array frequencies takes into account that their respective advantages, where 10 MHz array is sensible for defect on the ID surface while the 5 MHz array shows excellent defect size measurement on the OD surface. A switch could be designed to control the inspection modality (i.e. drive one array for a specific inspection task).

Since usually the length of a 5 MHz array is longer than a 10 MHz array for a same number of elements configuration, and the circumferential located transducer needs to keep recording the data during the helical scan, the longer 5 MHz array is suggested to inspect circumferentially to reduce the data acquisition times on every circle. Therefore, an improvement of inspection speed can be achieved. In terms of the 10 MHz array, it can cover a certain range (e.g. 9 mm for a 32 element array) on the axial direction during the inspection. Thus, when the sensor head is executing a helical scan, the data acquisition system would align with this mechanical step size.

Once the FMC data is acquired from both of the array transducers, the TFM imaging methods are able to show the tube ID and OD surface inspection results. The scanning speed including FMC data acquisition and TFM imaging is approximate 1/140 second (140 frames per second) by using the FI Toolbox in CUE with a 32 element transducer configuration. The proposed images have been introduced in this Chapter and the schematics can be found in Figure 5.1. In addition, combining SAFT processing algorithms can provide improved accuracy of defect size measurement.

5.7. Summary

The complete replacement of the single element transducer head currently utilised in the CIGAR pressure tube inspection system using the phased array technology, including advanced signal post-processing algorithms, has been investigated in this Chapter.

Compared to the B-scan imaging associated with the single element transducer system, only two phased array transducers would be required for imaging the ID and OD surfaces on both the axial and circumferential directions. For both arrays, two array processing techniques have been implemented and compared. The TFM algorithm provides a high resolution image of the ID or OD surface defects and the array SAFT approach has been used to improve the imaging performance by including the array element directivity and associated structural geometries to limit the number of elements contributing to the image of the defect.

72 different array configurations have been simulated using finite element modelling and used to investigate defect detection performance for both rectangular and vshape defects. Specifically, transducer frequency and the number of array elements are utilised in this parametric study. In terms of tube ID surface inspection, the defect depth is well measured by a higher element number configuration for any transducer frequencies. While the defect width measurement can be more accurately inspected through higher element number and higher frequency configuration. With regard to the tube OD surface inspection, a more accurate defect depth measurement can be obtained from higher element and higher frequency configuration due to the small operational wavelength. However, the defect width can be achieved by using a lower frequency transducer with higher element number as a result of stronger penetration. Comparing to the inspection along the axial direction, the circumferential inspection presents more reflected wave energy caused by the curved surface, from which is may be easier to determine an accurate defect size. The array SAFT algorithm is executed on the longest active aperture to have more flexibility for the application and the effects of using different synthetic aperture lengths are explained. When finding the most effective synthetic aperture length which can be obtained through calibration, an improvement of the defect width measurement can be achieved. In addition,

the full-skip TFM imaging is introduced to analyse the defect feature to identify critical defect.

A proposed complete replacement scheme incorporating an array sensor system is discussed at the end of the Chapter. The proposed scheme has been selected based on array imaging performance and has not considered the practical aspects of such an inspection system. In particular, radiation hardened array technology may have an influence on the ultrasonic system performance and the challenge of integrating a phased array controller into the head of the tool.

Chapter 6

Conclusion and Future Work

6.1. Overall Conclusion

The research work demonstrated in this Thesis concerned investigating enhanced ultrasonic techniques for inspection of pressure tubes within the CANDU nuclear reactor. Currently, single element transducers are utilised in the inspection and advanced phased array technology was suggested as a replacement sensor technology. A hybrid simulation platform was built through a combination of FE modelling and analytical extrapolation to provide a software platform to investigate the application of phased array inspection (Chapter 4). This platform then was used to generate FMC data acquisition from a variety of array transducer inspection scenarios, which was used for TFM imaging and array SAFT processing to find a potential solution for future pressure tube inspection systems (Chapter 5). Moreover, the issue of poorly-focused ultrasonic signals producing lower accuracy defect information in the current single element sensor tool head was diminished through application of the SAFT algorithm and the wavelet analysis method. Enhanced performance on industrial data from poorly-focused sensors was presented in Chapter 3.

The key results from this research work are:

- Development of SAFT algorithm employing a virtual source at the transducer focal point to correct the poorly-focused industrial data. Importantly, the effect of the focal length value to the algorithm was thoroughly analysed.
- A wavelet analysis method for extracting defect information by using the high frequency components in the received echo spectrum to improve depth measurement from poorly-focused industrial data. An investigation of different wavelets were compared and the Haar wavelet selected as the most effective one for this poorly-focused case.
- Innovative hybrid simulation platforms for analysis of immersed inspection of pressure tubes with single element transducer configuration, as well as phased array transducers, were developed.
- A new methodology to utilize phased array transducers to replace the currently used single element transducers was proposed. High quality TFM images of both ID and OD surfaces, on the axial and circumferential directions, show excellent promise for future inspection technology.
- Development of a novel numerical method for the time map calculation of TFM applied to a two-layer, curved propagation path.
- An array SAFT algorithm to improve the accuracy of defect size measurement was demonstrated. The effective synthetic aperture lengths were calculated for all pressure tube inspection scenarios and indicated an improved focusing effect to enhance defect measurement results.

The Thesis can be considered in two different timelines: improvements to current CANDU pressure tubes inspection data; and a new transducer inspection approach for future high fidelity inspection systems. Moreover, the signal processing approach utilised on the current datasets, where mechanical deformation of the tube results in poorly-focused inspection data, has been also translated into the future system approach to ensure consistency in the inspection performance across the different platforms.

The SAFT method applied on the industrial inspection data has provided an improved performance on the defect width measurement compared to the original poorly-focused image. The defect echo shown on the refocused B-scan ultrasonic image demonstrates a more intense energy that brings about a more accurate measurement result. The SAFT processing is easy to realize provided it is configured to use the appropriate value of the transducer focal length. While this currently needs to be manually checked, there is potential for this to be automatically detected. The wavelet analysis method used for defect depth measurement presents a significant improvement in extracting sizing information from the weak defect echo in the original poorly-focused A-scan signal. For this work, an optimal solution employing the Haar wavelet shows a significant advantage to obtain the strongest defect echo and also provides an improved estimate of the defect depth which meets the industrial inspection guidelines requirement.

The hybrid simulation platform combining finite element modelling with analytical extrapolation solves the problem of numerical dispersion errors associated with simulation over large propagation distances. This platform provides a reliable simulation of ultrasonic phased array transducer inspection and enables the analysis of Total Focusing Method and array SAFT processing to enhance defect detection and characterisation performance. Its application to evaluate a range of phased array imaging solutions provides useful information towards the selection of the next generation ultrasonic system to be incorporated into the inspection tool sensor head. After analysing the effects of applying different array element numbers and frequencies, a dual array system incorporating 32-element 5 and 10 MHz arrays shows important advantages to inspect the CANDU pressure tubes. The results from this Thesis conclude that the application of the phased array technology combined with signal processing algorithms will be significant to improve the quality of the inspection data and hence, reduce the requirement for the expensive replica process.

6.2. Chapter Conclusions

The conclusions from each Chapter of the whole Thesis are now described in detail.

In Chapter 3, SAFT and wavelet analysis methods employed for correcting the poorly-focused industrial data were introduced. Regarding the SAFT algorithm, the effects of different focal length values 10.4 mm, 12 mm and 13.5 mm were compared and it has been suggested that the difference of the focal length value utilized in the algorithm brought about significant differences of curvature in the resultant images. When the calculated aperture curvature is best matched with the actual defect echo signal, this was 12 mm focal length in the case presented in this Thesis, a re-focused B-scan image leads to more accurate measurement of the defect width with a significant improvement example from original 0.8° to a re-focused 0.3°. More importantly, the more serious the sagging in the tube results in a greater separation between the tube surface and the transducer focal point and this is where the SAFT algorithm can achieve better focusing results. The results of SAFT processing were based on the standard -6 dB method, which is also used by the Analyst – although they would also have additional historical information and their inspection experience to conclude their defect characterisation decision. For correct implementation of the SAFT algorithm on industrial data, a corresponding level of training for the Analyst would be required. In terms of wavelet analysis, decomposing the signal into different spectral regions results in a higher time resolution, where a Haar wavelet displayed a double bandwidth on level 1 caused a double time resolution. Four different wavelets were analysed, with the Haar wavelet producing the best measurement results with the highest SNR, whose signal amplitude is more than twice of the other wavelet techniques. A total of 46 industrial datasets from 8 pressure tubes have been processed in this Thesis, with 38 tubes showing improved defect detection, which can assist the Analyst’s work with the potential to reduce the replica process.

In order to overcome the limitation of using FE simulation for large models, a hybrid simulation method was demonstrated in Chapter 4. The large model of the pressure tube inspection scenario was decomposed into five parts with a combination of FE method and analytical extrapolation. Here, the ultrasound transmission, target interaction and ultrasonic reception were simulated using the FE method, while the transmission and reception wave propagations made use of the Kirchhoff extrapolation method to remove the necessity to model the propagation path using computationally expensive FE. The model was utilised for both single element transducer and phased array inspection scenarios. In the single element transducer simulation example, the focal area can be an approximation by a rectangular with dimensions of 0.58 mm and 0.04 mm, which shows the excellent matched result of measuring a 1 mm depth defect. Regarding the phased array transducer simulation, the simulation platform was configurable by the number of array elements and the FE model output combined with TFM imaging algorithms to image the ID and OD surfaces. The simulation platform performed an accurate simulation result of phased array inspection of the pressure tube, where a 32 element configuration brought about simulation errors of 0.03 mm and -0.04 mm for defect depth measurement on ID and OD surfaces, when compared to the actual defect size. Hence, this simulation platform gave a firm foundation to the following investigation of array sensor configuration.

In Chapter 5, the TFM imaging algorithms of tube ID and OD surfaces on axial direction and circumferential direction were presented and all the methods were validated by experimental data with an excellent accuracy. In addition, the pressure tube inspection by using the current single element transducer with different focus situations (to simulate tube sagging) and by using a phased array transducer were compared. The phased array technology showed the highest measurement resolution for defect depth and width measurement and a defect back wall amplitude ratio 86.3%. A range of simulated array configurations, frequency (5 MHz, 7.5 MHz and 10 MHz) and number of elements (8, 16 and 32), was applied for the inspection of two typical nuclear industry defect types (rectangular and v-shaped). The 10 MHz transducer showed the highest resolution for the depth measurement, while the 5 MHz transducer presented the strongest penetration for

OD surface inspection. Moreover, the 32 elements configuration brought about the most information from the defect echo, which resulted in the most accurate defect size measurement. However, a transducer containing more elements in the pressure tube inspections means more data needs to be archived in the array system. Currently, each group of experimental FMC data acquired in this Thesis is approximate 20 Megabyte for a 32 elements array inspection. When executing a helical scanning to a 6.3 m pressure tube with a step of 0.2 mm for each circle, the data size will be dramatically increased. For example, if a 5 MHz array transducer with 32 elements (transducer length 19.6 mm) is used, acquiring 20 groups of FMC data for each helical revolution will generate 12.6 Gigabyte data for one pressure tube. Furthermore, an array SAFT processing algorithm was proposed to reduce the overestimate of defect width from 68% (by TFM) to 46% for defect on the axial ID surface, and from 40% (by TFM) to 25% for defect on the axial OD surface. The full-skip TFM method also provided supplementary information for identifying defect features, where a critical v-shaped defect could be distinguished using the full-skip TFM image after an obvious defect echo on the ID surface is observed from a direct TFM image.

In the final discussion part of the simulated array inspection programme, a completed array sensor system was suggested. Combining the analysis of TFM imaging methods and array SAFT processing algorithms, a sensor head containing two array transducers was recommended for the replacement of current set of single element sensors. A 5 MHz array and a 10 MHz array both with 32 elements were proposed to be situated on circumferential and axial directions, respectively, where their positions can be switched if a re-scan for more information is needed. Through taking advantages of the strong penetration from the 5 MHz array and the high resolution from the 10 MHz array, the defects on both of the ID and OD surfaces can be accurately detected and measured, which will effectively reduce the time and cost consuming replica process.

6.3. Future Work

A few further developments of the methodologies introduced in this Thesis can be executed to provide improved and industrially practical solutions. These will focus on the use of the hybrid simulation platform to investigate more about the phased array technology on pressure tube inspection, the enhanced signal processing of current industrial data and the array transducer and the corresponding instrumentation in the high radiation nuclear environment.

The defect types and features used in this Thesis to investigate the phased array system approach, do not represent the wide range of features that can be detected from real industrial data. Hence, future work will aim at taking advantage of the established simulation platform to model more complex defect shapes for detection and characterization. Moreover, the simulated transducer signal can be modified to deliver more advanced excitation schemes, for example Golay code excitation, to investigate an advanced technique for enhanced signal penetration and potentially enhanced signal-to-noise.

The work presented in this Thesis has used longitudinal wave excitation and propagation. Using shear wave and including mode conversion within the wave propagation paths generated from array transducer systems could provide additional layers of defect and feature information to improve system resolution.

The FMC data size is an important factor to be considered when using phased array technology since an array transducer with N elements generates N x N A-scans, and if the element number increases, the data size will increase dramatically. Therefore, consideration about managing the data volume is required to make a trade-off between array element number and inspection accuracy and consider the impact of archiving all of the acquired FMC/TFM data.

The simulation platform shown in this Thesis is based on a 2-D point of view which is less realistic than 3-D simulation. The future work could be extending the platform to 3-D simulation that would provide a more realistic result. However, the computational burden of the simulation work should be considered as well.

The SAFT processing algorithm applied on the current industrial data to correct the poorly-focused single element transducer has been submitted to Bruce Power for further validation. However, manually checking for the right focal length consumes lots of time and an automatic algorithm to find the true focal length of the transducer by using a computer vision method would be recommended.

A methodology employing wavelet analysis to improve the defect depth measurement from industrial data has been introduced, where the application has been tested by using different wavelets. Haar wavelet demonstrates the highest time resolution comparing to other wavelets analysed in the Thesis. A future work stream could design a specific wavelet for this particular case to obtain an improved performance accuracy.

The phased array system investigated in this Thesis is based on general 1-D linear transducers and all the experiment are done in an ideal laboratory, which means all the transducers and corresponding instrumentations are not specified for using in a nuclear reactor with a high radiation environment. A future work could customize a phased array system with radiation protected transducers, cables and other instruments.

Appendix A: Calculation of Lens Geometry in PZFlex

The process of drawing a focal lens in PZFlex is firstly drawing a rectangle with material of lens, and then drawing a filled circle with material of water. As Figure A. 1 shown, The filled circle is tangential to the transducer at point C. The sound waves pass the lens and focus at point F which is on the central line of the wave path. Point O indicates the centre of the circle.

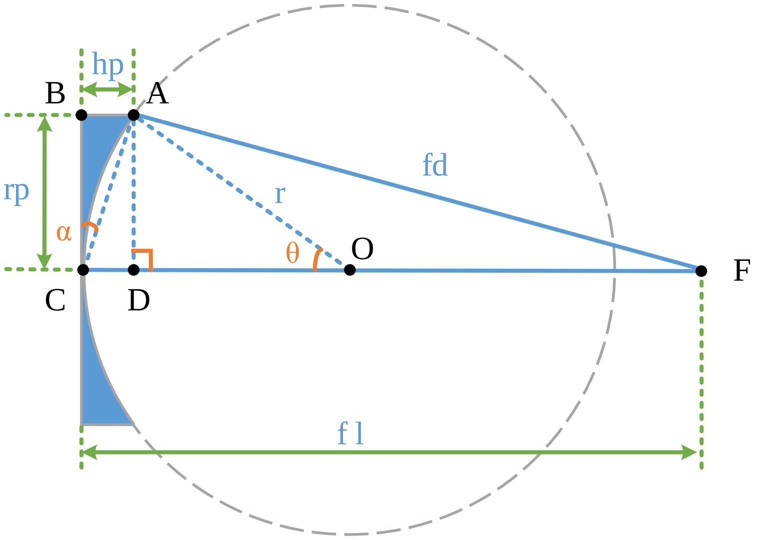

Figure A. 1 Calculation of the parameters of the lens

The target parameters used in PZFlex model are the thickness of the lens hp and the radius of the circle r. Considering the known conditions, the radius of the lens rp and focal length fl, and combining with the folowing geomety calculation, hp and r can be obtained.

Since O is the circle centre, there is $OA = OC$, which can conclude Equation A.2 through Equation A.1.

$$\angle OAC = \angle OCA \tag{A.1}$$

$$\angle\alpha = 90° - \angle OCA = 90° - \frac{(180° - \angle\theta)}{2} = \frac{\angle\theta}{2} \tag{A.2}$$

After the sound waves entering the lens in parallel, there are a number of paths to reach the focus F. Considering paths BAF and CDF for annlysis, these two waves enter into the lens from point B and C at the same time and spend equal time reaching the focus F. Assuming that the sound velocity in water is c_w and the velocity in lens is c_l, in terms of path BAF, the time of wave trasmitting in lens is $t_{\mathrm{BA}} = \frac{hp}{c_l}$ and the time of wave trasmitting in water is $t_{\mathrm{AF}} = \frac{fd}{c_w}$. Therefore, the time of transmitting path BAF is given by Equation A.3.

$$t_{BAF} = t_{BA} + t_{AF} = \frac{hp}{c_l} + \frac{fd}{c_w} \tag{A.3}$$

Regarding to path CDF, the wave can be seen as only transmiting in water. Thus, the time of transmitting path CDF is given by Equation A.4

$$t_{CDF} = \frac{fl}{c_w} \qquad (A.4)$$

As the above description, there is $t_{\mathrm{BAF}} = t_{\mathrm{CDF}}$. A combination of Equation A.3 and Equation A.4 is given by:

$$\frac{hp}{c_l} + \frac{fd}{c_w} = \frac{fl}{c_w} \qquad (A.5)$$

Following the geomatry information in Figure A. 1, Equation A.6 and A.7 can be easily obtained.

$$hp = rp * \tan(\alpha) = rp * \tan(\frac{\theta}{2}) \qquad (A.6)$$

$$fd = \sqrt{AD^2 + DF^2} = \sqrt{rp^2 + (fl - hp)^2} \qquad (A.7)$$

Put Equations A.6 and A.7 into Equation A.5, θ can be calculated. And finally, refer to Equation A.6, hp can be calculated and r can be calculated following Equation A.8 as well.

$$r = \frac{rp}{\sin(\theta)} \qquad (A.8)$$

Appendix B: Kirchhoff Extrapolation

Huygens' principle (Figure B. 1) states that for a straight wave front, every point on the wave front can be seen as a new source of a spherical wave. So the stored data from the FE model is available to be the new source for wave propagation.

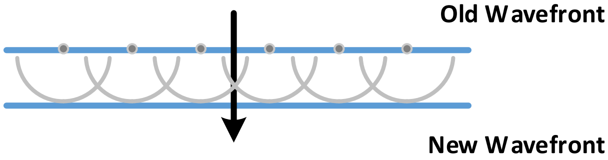

Figure B. 1 Huygens' principle

The method of Kirchhoff extrapolation uses Green's function, Equation B.1, for the derivation of the following integral[117]:

$$\int_V f\,\nabla^2 g - g\,\nabla^2 f\,dV = \oint_S (f\,\nabla g - g\,\nabla f)\cdot \boldsymbol{n}\,dS \qquad (B.1)$$

where V is the volume of a medium not containing sound sources; S is the surface surrounded volume V (see Figure B. 2); f is the sound pressure field $P(\boldsymbol{r},\omega)$ within the volume; g is a Green's function $G_{\boldsymbol{r_0}}(r,\omega)$ for the wave equation; and ω is the angular frequency. V should satisfy Equations B.2 and B.3.

$$\nabla^2 \mathrm{P} + \mathrm{k}^2 \mathrm{P} = 0 \qquad (B.2)$$

$$\nabla^2 G_{\mathbf{r_0}} + k^2 G_{\mathbf{r_0}} = -4\pi\delta(r - r_0) \qquad (B.3)$$

where k is the wavenumber.

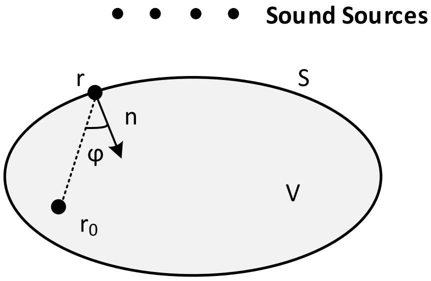

Figure B. 2 A volume V surrounded by a surface S

The wave propagation in the frequency domain is described by

$$-\nabla P = j\omega\rho_0\mathbf{V} \qquad (B.4)$$

where ρ_0 is the mass density.

Substituting Equations B.2 and B.3 into Green's function and combining with Equation B.4, the sound pressure field can be described as:

$$P(\boldsymbol{r_0}, \omega) = \frac{1}{4\pi}\oint_S \left(P\,\frac{\partial G_{\boldsymbol{r_0}}}{\partial n} + jk\rho_0 c V_n G_{\boldsymbol{r_0}}\right) dS \qquad (B.5)$$

where c is the wave velocity.

By applying Green's function Equation B.6 into Equation B.5 to solve the derivatives, the forward Kirchhoff integral can be expressed by Equation B.7.

$$G_{\boldsymbol{r_0}}(\boldsymbol{r}, \omega) = \frac{e^{-jk\|\boldsymbol{r}-\boldsymbol{r_0}\|}}{\|\boldsymbol{r}-\boldsymbol{r_0}\|} \qquad (B.6)$$

$$P(\boldsymbol{r_0},\omega) = \frac{1}{4\pi}\oint_S \left(jk\rho_0 cV_n(\boldsymbol{r},\omega) + P(\boldsymbol{r},\omega)\frac{1+jk\|\boldsymbol{r}-\boldsymbol{r_0}\|}{\|\boldsymbol{r}-\boldsymbol{r_0}\|}cos\varphi\right)\frac{e^{-jk\|\boldsymbol{r}-\boldsymbol{r_0}\|}}{\|\boldsymbol{r}-\boldsymbol{r_0}\|}dS \tag{B.7}$$

This demonstrates that the sound pressure at any point of source free volume V can be calculated from the pressure and velocity on the boundary surface S.

Appendix C: Defect Size Measurement by Replication

This Appendix demonstrates an example of the defect size measurement by replication process.

As shown in Figure C. 1 (a), a sample of a tube contains a horizontal defect on the ID surface. Through using a gun with synthetic rubber replicating compound (Figure C. 1 (b)), the surface defect can be replicated (Figure C. 1 (c)).

Then, a Meiji Techno microscope (Figure C. 1 (d)) is applied for the size measurement of the replicated defect. Firstly, a 1 mm pixel calibration ruler (Figure C. 1 (e)) is employed to calibrate the relationship between pixels and distance. Secondly, measure the defect at five different positions (Figure C. 1 (f)). Finally, the defect size can be obtained through the average measurement results.

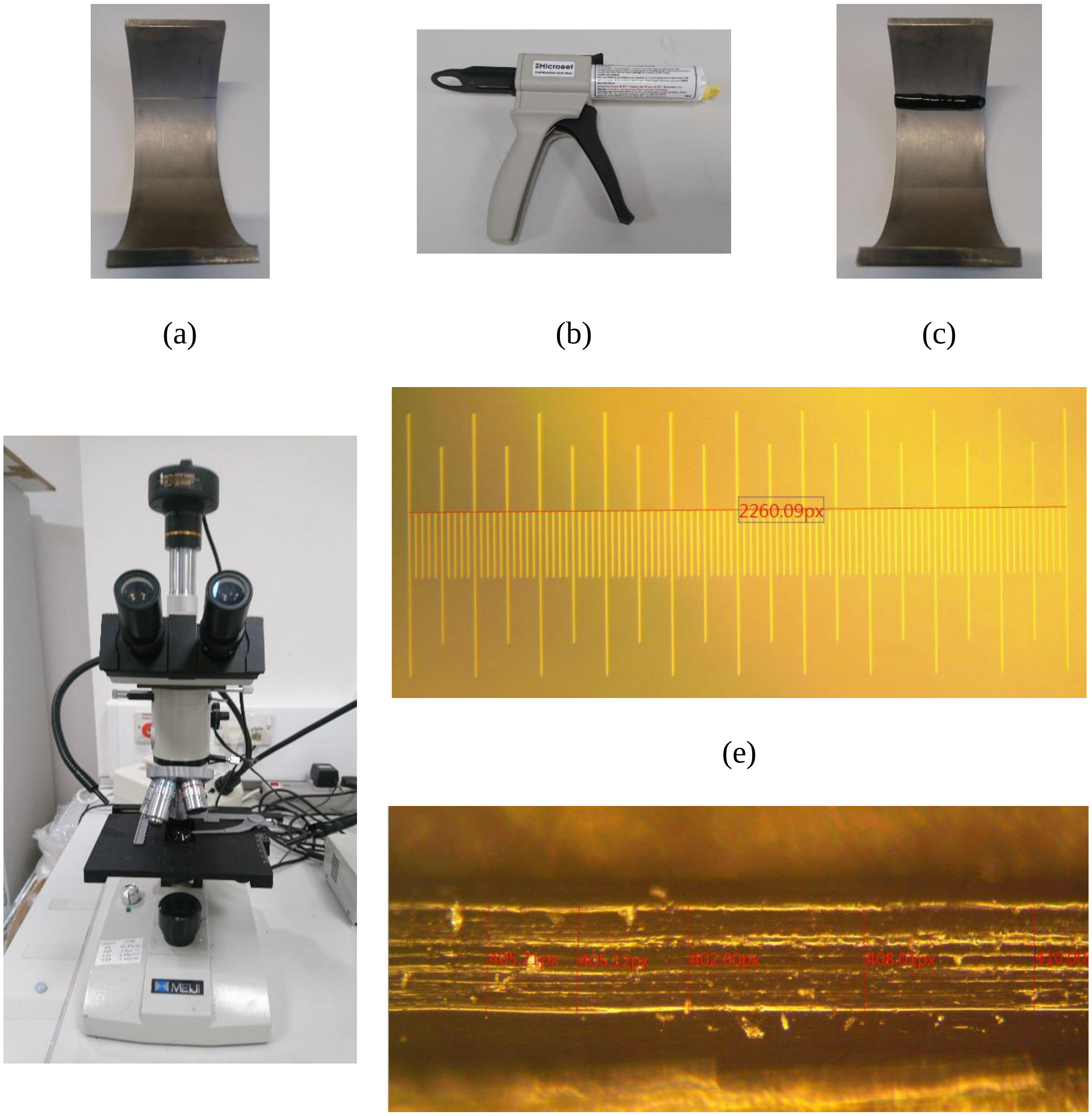

(a) (b) (c)

(e)

(d) (f)

Figure C. 1 Replication process example (a) tube sample; (b) gun with replicating compound; (c) replica of defect; (d) microscope; (e) calibration ruler; (f) defect measurement

Appendix D: MATLAB Code of Circumferential TFM Time Map Calculation

This Appendix presents the MATLAB code for the calculation of TFM time map for the second medium on the circumferential direction.

```
% Define A1/A2/A3/A4
A1 = R^2 * xA^2;
A2 = R^2 + xA^2 + yA^2;
A3 = R^2 * xB.^2;
A4 = R^2 + xB.^2 + yB.^2;
% Define polynomial coefficients for Equation 5.17
a_coef = c2^2*(-2*xB*(yA^2-xA^2)-4*xA*yA.*yB) - c1^2*(-2*xA*(yB.^2-xB.^2)-
4*yA.*xB.*yB);
b_coef = c2^2*(-4*xA*yA.*xB+2*yB*(yA^2-xA^2)) - c1^2*(-4*xA.*xB.*yB+2*yA*(yB.^2-
xB.^2));
c_coef = c2^2*(A4*(yA^2-xA^2)) - c1^2*(A2*(yB.^2-xB.^2));
d_coef = c2^2*(2*A4*xA*yA) - c1^2*(2*A2.*xB.*yB);
e_coef = c2^2*(-2*A1.*xB+4*xA*yA.*yB*R^2) - c1^2*(-2*A3*xA+4*yA.*xB.*yB*R^2);
f_coef = c2^2*(2*A1.*yB) - c1^2*(2*A3*yA);
g_coef = c2^2*(A1*A4) - c1^2*(A2*A3);
% Define polynomial coefficients for Equation 5.22
q6 = a_coef.^2 + b_coef.^2;
q5 = 2*a_coef.*c_coef + 2*b_coef.*d_coef;
```

```
q4 = - R^2*b_coef.^2 + 2*f_coef.*b_coef + c_coef.^2 + d_coef.^2 + 2*a_coef.*e_coef;

q3 = - 2*b_coef.*d_coef.*R^2 + 2*a_coef.*g_coef + 2*c_coef.*e_coef + 2*d_coef.*f_coef;

q2 = - R^2*d_coef.^2 - 2*b_coef.*R^2.*f_coef + e_coef.^2 + f_coef.^2 + 2*c_coef.*g_coef;

q1 = - 2*d_coef.*f_coef.*R^2 + 2*e_coef.*g_coef;

q0 = - R^2*f_coef.^2 + g_coef.^2;

% Solve Equation 5.22

% Originally multiple solutions

x0 = roots([q6(i,j) q5(i,j) q4(i,j) q3(i,j) q2(i,j) q1(i,j) q0(i,j)]);

% Since there are multiple solutions for Equation 5.22, to find the least time of the sound path (following Fermat's principle), a xM value between xA and xB is defined. The closest three results will be considered for comparison to find out the least time.

xM = xA + (xB(i,j)-xA)*c1/c2;

[val, index] = sort(abs(x0- xM));

xP1(i,j)  = x0(index(1));

xP2(i,j)  = x0(index(2));

xP3(i,j)  = x0(index(3));

% Time calculation of three closest positions

yP = -sqrt(R^2-xP1.^2);

L1 = sqrt((xP1-xA).^2 + (yP-yA).^2);

t1 = L1/c1;

L2 = sqrt((xP1-xB).^2 + (yP-yB).^2);

t2 = L2/c2;

tsum1 = t1 + t2;

% Same way to obtain tsum2 and tsum3

% Compare three results to find the shortest time

tsum1(tsum2<tsum1) = tsum2(tsum2<tsum1);

tsum1(tsum3<tsum1) = tsum3(tsum3<tsum1);

time(:,:,ch) = tsum1;
```

Appendix E: TFM and Array SAFT Measurement Results and Example

Table E. 1 Rect defect TFM imaging measurement results

Frequency		5 MHz			7.5 MHz			10 MHz		
Element number		E8	E16	E32	E8	E16	E32	E8	E16	E32
aID	Depth	0.32	0.32	0.32	0.32	0.32	0.31	0.31	0.31	0.31
	Width	1.41	1.06	0.84	0.96	0.58	0.49	0.96	0.61	0.49
aOD	Depth	0.66	0.26	0.21	0.38	0.3	0.29	0.3	0.3	0.29
	Width	4.77	0.68	0.7	2.79	2.31	1.64	2	2.24	1.41
cID	Depth	0.33	0.32	0.32	0.32	0.31	0.31	0.31	0.31	0.31
	Width	1.23	0.98	0.81	0.98	0.59	0.52	0.96	0.62	0.5
cOD	Depth	0.59	0.53	0.28	0.34	0.3	0.28	0.31	0.29	0.28
	Width	4.72	0.54	0.46	3.6	4.96	0.52	2.16	2.02	0.79

Table E. 2 Vshape defect TFM imaging measurement results

Frequency		5 MHz			7.5 MHz			10 MHz		
Element number		E8	E16	E32	E8	E16	E32	E8	E16	E32
aID	Depth	0.55	0.55	0.56	0.6	0.6	0.6	0.59	0.59	0.59
	Width	1.2	1.01	0.69	1.04	0.58	0.46	1.11	0.71	0.41
aOD	Depth	Difficult to identify the defect								
	Width									
cID	Depth	0.55	0.55	0.56	0.61	0.6	0.6	0.59	0.59	0.59
	Width	1.13	0.99	0.65	1.04	0.58	0.51	1.13	0.71	0.44
cOD	Depth	0.59	0.61	0.4	0.39	0.41	0.43	0.35	0.44	0.45
	Width	4.28	6.86	0.32	3.6	5.84	0.84	2.4	0.66	0.46

Table E. 3 aID array SAFT processing results

Angle (°)	**30**	**40**	**45**	**50**	**60**	**70**	**80**
SAFT (mm)	0.86	0.75	0.73	0.75	0.78	0.78	0.84
TFM (mm)	0.84						
Real width (mm)	0.5						

Table E. 4 cID array SAFT processing results

Angle (°)	**30**	**40**	**45**	**50**	**60**	**70**	**80**
SAFT (mm)	0.83	0.8	0.8	0.8	0.8	0.81	0.81
TFM (mm)	0.81						
real width (mm)	0.5						

Table E. 5 aOD array SAFT processing results

Angle (°)	**16**	**18**	**20**	**22**	**24**	**26**
SAFT (mm)	0.73	0.67	0.63	0.67	0.66	0.66
TFM (mm)	0.7					
real width (mm)	0.5					

Table E. 6 cOD array SAFT processing results

Angle (°)	**16**	**18**	**20**	**22**	**24**	**26**
SAFT (mm)	0.51	0.51	0.49	0.51	0.46	0.46
TFM (mm)	0.46					
real width (mm)	0.5					

The details of the -6 dB method for defect size measurement are explained from two examples presented in Figure E. 1 and Figure E. 2 for ID and OD surfaces respectively with a comparison of TFM and SAFT results. In terms of the defect on the ID surface, it is easy to find the defect profile as shown on the left hand side of Figure E. 1 with the peaks indicating defect echoes. The first step is to detect the maximum defect echo signal, as displayed on the right hand side of Figure E. 1, -4.688 dB is for TFM and -4.53 dB is for SAFT. Then, looking for the nearest -6 dB values of the peak on each side and the defect width is the difference between the two values. In this case, the data cursors below the points are for TFM and above the points are for SAFT. So the TFM result is 0.84 mm (10.04 - 9.2) and the SAFT result is 0.73 mm (9.98 - 9.25).

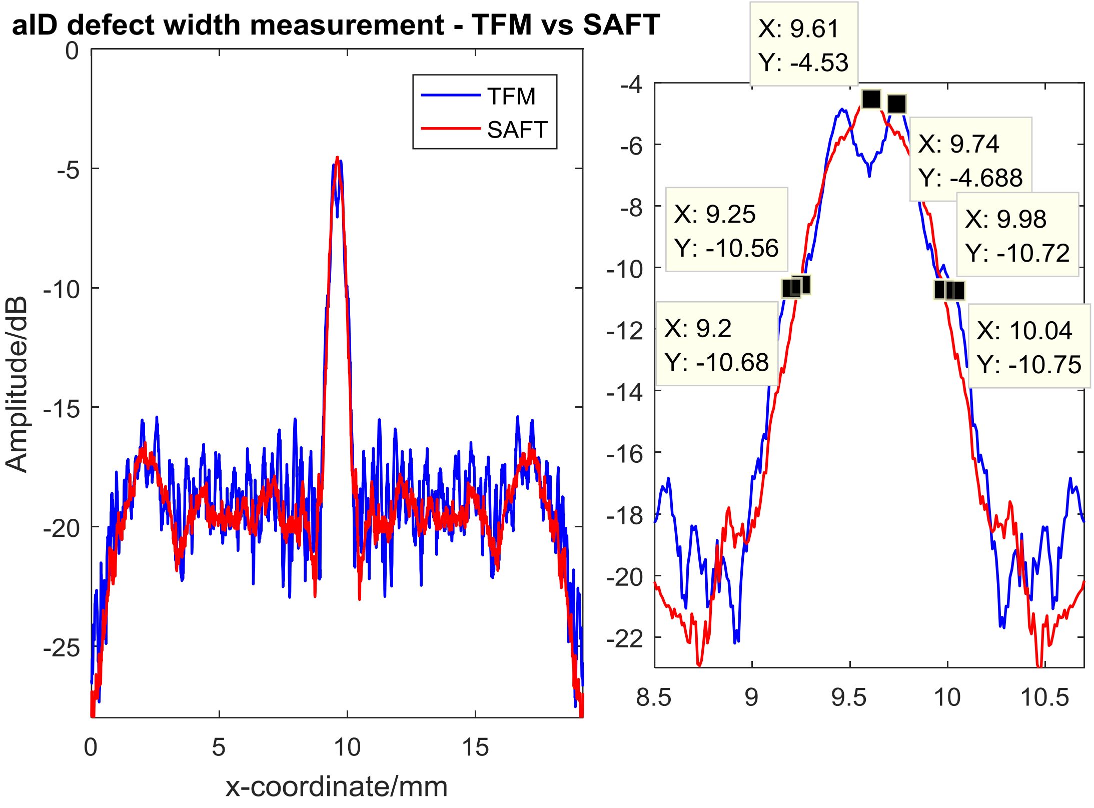

Figure E. 1 Example of ID surface defect size measurement

Regarding to the defect on the OD surface, the size measurement steps are similar to the ID surface example, while the difference is the defect profile is combined together with the surface echo (Figure E. 2). The first step is the same as the ID surface case to detect the maximum defect echo signal, as displayed on the right hand side of Figure E. 2, -5.411 dB is for TFM and -5.645 dB is for SAFT. In this example, the data cursors above the points are for TFM and below the points are for SAFT. So the TFM result is 0.7 mm (9.95 - 9.25) and the SAFT result is 0.63 mm (9.91 - 9.28).

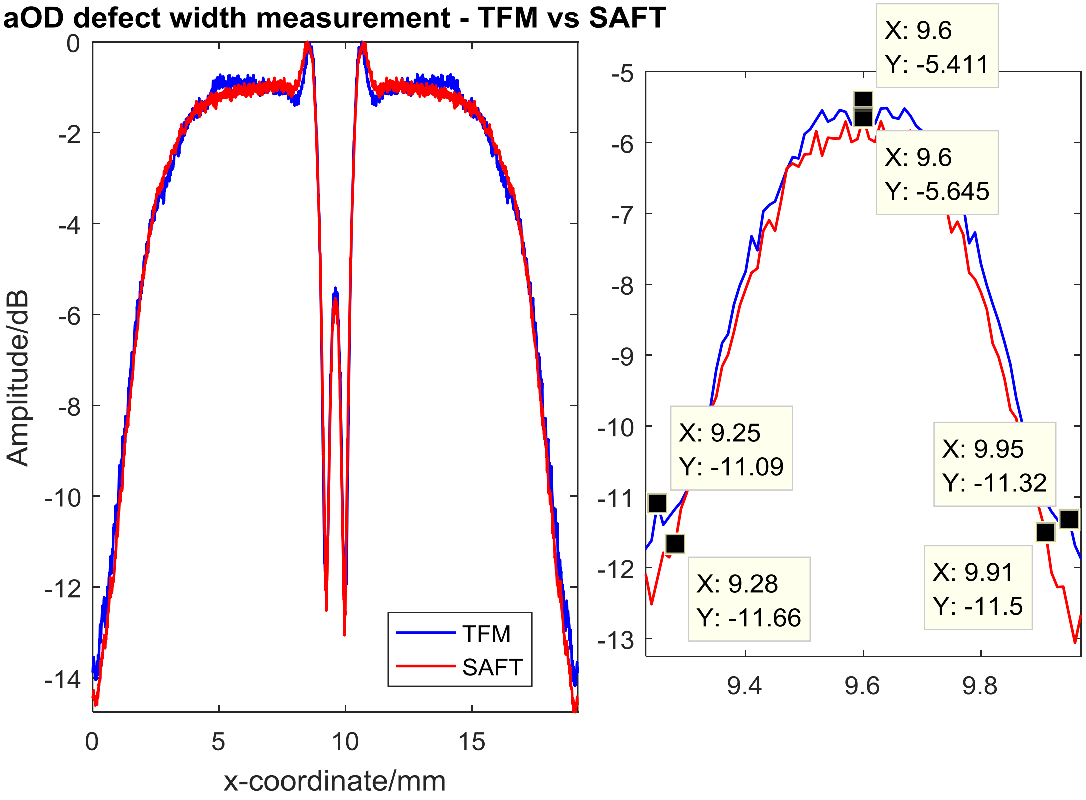

Figure E. 2 Example of OD surface defect size measurement

References

[1] BP Statistical Review of World Energy, "BP Statistical Review of World Energy 2018," 2018.

[2] International Energy Agency, "World Energy Balances 2018," 2018.

[3] Mycle Schneider, "The world nuclear industry status report 2018," 2018.

[4] IAEA - International Atomic Energy Agency, "Nuclear Power Reactors in the World," 2018.

[5] IAEA - International Atomic Energy Agency, "Heavy water reactors : status and project development," 2002.

[6] M. Trelinski, "Application of Ultrasonic Testing Methods for Volumetric and Surface Inspection of CANDU Pressure Tubes," in *1st Pan American Conference for Nondestructive Testing*, 1998, vol. Toronto, O, no. Id, p. 8.

[7] IAEA - International Atomic Energy Agency, "Assessment and management of ageing of major nuclear power plant components important to safety: CANDU pressure tubes," 1998.

[8] IAEA - International Atomic Energy Agency, "Delayed hydride cracking in zirconium alloys in pressure tube nuclear reactors," 2004.

[9] A. C. Wallace, S. Xu, N. P. Singh, and L. Gutkin, "Inspection Specification for

CANDU Fuel Channels," 2008.

[10] C. D. E. Ensaios, N. Ã. O. Destrutivos, D. A. América, U. E. Caribe, and G. N. Jarvis, "Inspection of CANDU Nuclear Reactor Fuel Channels," 1986.

[11] M. Trelinski, "Inspection of CANDU Reactor Pressure Tubes Using Ultrasonics," in *17th World Conference on Nondestructive Testing*, 2008, p. 8.

[12] Candu Energy Inc., "Operating Procedure CIGAR Analysis- PT Inspection Data Analysis - Analysis of Ultrasonic Indications Engineering and Technical Delivery," 2014.

[13] M. Trelinski, "Pressure tube flaws and artifacts observed in CANDU fuel channels ; detection , sizing and characterization issues," 2007.

[14] S. Sung-Jin, H. J. Shin, and Y. H. Jang, "Development of an ultrasonic phased array system for non-destructive tests of nuclear power plant components," *Nucl. Eng. Des.*, vol. 214, pp. 151–161, 2002.

[15] S. Mahaut, O. Roy, C. Beroni, and B. Rotter, "Development of phased array techniques to improve characterization of defect located in a component of complex geometry," *Ultrasonics*, vol. 40, no. 1–8, pp. 165–169, 2002.

[16] B. W. Drinkwater and P. D. Wilcox, "Ultrasonic arrays for non-destructive evaluation: A review," *NDT E Int.*, vol. 39, no. 7, pp. 525–541, 2006.

[17] Lester W. and J. Schmerr, *Fundamentals of Ultrasonic Phased Arrays*, vol. 215. Springer, 2015.

[18] C. Holmes, B. W. Drinkwater, and P. D. Wilcox, “Post-processing of the full matrix of ultrasonic transmit-receive array data for non-destructive evaluation,” *NDT&E Int.*, vol. 38, pp. 701–711, 2005.

[19] R. Boehm, D. Brackrock, J. Kitze, G. Brekow, and M. Kreutzbruck, “The SAFT Approach for Advanced Crack Analysis,” in *Proceedings of the National Seminar and Exhibition on Non-Destructive Evaluation*, 2009, pp. 315–318.

[20] C. J. Hellier, *Handbook of Nondestructive Evaluation*. 2012.

[21] T. G. Leighton, “What is ultrasound?,” *Prog. Biophys. Mol. Biol.*, vol. 93, no. 1–3, pp. 3–83, 2007.

[22] H. D. Young and R. A. Freedman, *University Physics with Modern Physics - 13th Edition*. 2012.

[23] R. Halmshaw, *Non-Destructive Testing (Second Edition)*. Edward Arnold, 1991.

[24] J. L. Rose, *Ultrasonic waves in solid media*. Cambridge University Press, 1999.

[25] P. Taylor and A. I. Lvovsky, “Fresnel Equations,” *Encycl. Opt. Eng.*, no. August, pp. 37–41, 2013.

[26] A. Romano and R. Cavaliere, “Fermat’s Principle and General Considerations Regarding Centered Optical Systems,” in *Geometric Optics*, Birkhäuser, Cham, 2016, pp. 1–21.

[27] J. Krautkrämer and H. Krautkrämer, *Ultrasonic testing of materials*, 4th fully. Springer-Verlag, 1990.

[28] M. Weston, “Advanced Ultrasonic Digital Imaging and Signal Processing for Applications in the Field of Non-Destructive Testing,” University of Manchester, 2011.

[29] K. F. Graff, “A History of Ultrasonics,” in *Physical Acoustics*, 1981.

[30] S. Cochran, “Piezoelectricity and basic configurations for piezoelectric ultrasonic transducers,” in *Ultrasonic Transducers*, Woodhead Publishing Limited, 2012, p. 33.

[31] A. A. Vives, *Piezoelectric transducers and applications*. 2004.

[32] S. Song, *Ultrasonic Nondestructive Evaluation Systems - Models and Measurements*. Springer, 2007.

[33] M. Moore, B. Phares, and G. Washer, “Guidelines for Ultrasonic Inspection of Hanger Pins,” US Department of Transportation, 2004.

[34] O. Esquivel and R. W. Seibold, “Capabilities and Limitations of Nondestructive Evaluation Methods for Inspecting Components Beneath Thermal Protection Systems,” 2004.

[35] Olympus NDT, *Introduction to Phased Array Ultrasonic Technology Applications*. Olympus NDT, 2007.

[36] S. C. Mondal, P. D. Wilcox, and B. W. Drinkwater, “Design of Two-Dimensional Ultrasonic Phased Array Transducers,” *J. Press. Vessel Technol.*, vol. 127, no. 3, p. 336, 2005.

[37] J. Zhang, B. W. Drinkwater, P. D. Wilcox, and A. J. Hunter, “Defect detection using ultrasonic arrays: The multi-mode total focusing method,” *NDT E Int.*, vol. 43, no. 2, pp. 123–133, 2010.

[38] M. V. Felice, A. Velichko, and P. D. Wilcox, “Accurate depth measurement of small surface-breaking cracks using an ultrasonic array post-processing technique,” *NDT E Int.*, vol. 68, pp. 105–112, 2014.

[39] T. Schmitte, O. Nemitz, N. Chichkov, and T. Orth, “Application of the Total Focusing Method for Improved Defect Characterization in the Production of Steel Tubes , Pipes and Plates,” in *19th World Conference on Non-Destructive Testing 2016*, 2016, pp. 1–8.

[40] X. Han, W. Wu, P. Li, and J. Lin, “Combination of direct , half-skip and full-skip TFM to characterize multi-faceted crack,” in *2015 IEEE International Ultrasonics Symposium Proceedings*, 2015, p. 4.

[41] G. P. Singh and S. Udpa, “The role of digital signal processing in NDT,” *NDT Int.*, vol. 19, no. 3, pp. 125–132, 1986.

[42] A. V. Oppenheim, A. S. Willsky, and S. Hamid Nawab, *Signals and Systems (International Edition)*. Pearson, 1997.

[43] L. Cohen, *Time-frequency Analysis*. Prentice Hall PTR, 1995.

[44] C. Scott, *Introduction to Optics and Optical Imaging*. Wiley-IEEE Press, 1998.

[45] Merrill I. Skolnik, *Introduction to Radar Systems*. 1980.

[46] S. Song and P. Que, “Wavelet based noise suppression technique and its application to ultrasonic flaw detection.,” *Ultrasonics*, vol. 44, pp. 188–93, 2006.

[47] W. Liang and P. wen Que, “Optimal scale wavelet transform for the identification of weak ultrasonic signals,” *Meas. J. Int. Meas. Confed.*, vol. 42, no. 1, pp. 164–169, 2009.

[48] Y. Wang, “Wavelet Transform Based Feature Extraction for Ultrasonic Flaw Signal Classification,” *J. Comput.*, vol. 9, no. 3, pp. 725–732, 2014.

[49] I. Daubechies, *Ten Lectures on Wavelets*. Society for Industrial and Applied Mathematics, 1992.

[50] M. R. Canal, “Comparison of wavelet and short time Fourier Transform methods in the analysis of EMG signals,” *J. Med. Syst.*, vol. 34, no. 1, pp. 91–94, 2010.

[51] Y. Zhang, Z. Guo, W. Wang, S. He, T. Lee, and M. Loew, “A comparison of the wavelet and short-time fourier transforms for Doppler spectral analysis,” *Med. Eng. Phys.*, vol. 25, no. 7, pp. 547–557, 2003.

[52] M. H. S. Siqueira, C. E. N. Gatts, R. R. Da Silva, and J. M. A. Rebello, “The use of ultrasonic guided waves and wavelets analysis in pipe inspection,” *Ultrasonics*, vol. 41, no. 10, pp. 785–797, 2004.

[53] H. Chen, M. J. Zuo, X. Wang, and M. R. Hoseini, “An adaptive Morlet wavelet filter for time-of-flight estimation in ultrasonic damage assessment,” *Meas. J. Int. Meas. Confed.*, vol. 43, no. 4, pp. 570–585, 2010.

[54] A. White, J. W. Hong, S. Hong, and J. Choi, “Parameter estimation for wavelet transformed ultrasonic signals,” *NDT E Int.*, vol. 44, no. 1, pp. 32–40, 2011.

[55] J. A. Johnson and B. A. Barna, “The Effects of Surface Mapping Corrections with Synthetic-Aperture Focusing Techniques on Ultrasonic Imaging,” *IEEE Trans. Sonics Ultrason.*, vol. 30, no. 5, pp. 283–294, 1983.

[56] P. L. J. Busse, H. D. Collins, and S. R. Doctor, “Review and Discussion of the Development of Synthetic Aperture Focusing Technique for Ultrasonic Testing (SAFT-UT),” 1984.

[57] I. Bolotina *et al.*, “Ultrasonic arrays for quantitative nondestructive testing an engineering approach,” *Russ. J. Nondestruct. Test.*, vol. 49, no. 3, pp. 145–158, 2013.

[58] M. Spies, “Analytical methods for modeling of ultrasonic nondestructive testing of anisotropic media,” *Ultrasonics*, vol. 42, no. 1–9, pp. 213–219, 2004.

[59] M. Spies and W. Jager, “Synthetic aperture focusing for defect reconstruction in anisotropic media,” *Ultrasonics*, vol. 41, no. 2, pp. 125–131, 2003.

[60] M. Spies and H. Rieder, “Synthetic aperture focusing of ultrasonic inspection data to enhance the probability of detection of defects in strongly attenuating materials,” *NDT E Int.*, vol. 43, no. 5, pp. 425–431, 2010.

[61] C. Holmes, B. W. Drinkwater, and P. D. Wilcox, “Advanced post-processing for scanned ultrasonic arrays: Application to defect detection and classification in non-destructive evaluation,” *Ultrasonics*, vol. 48, no. 6–7, pp. 636–642, 2008.

[62] J. Prager, J. Kitze, C. Acheroy, D. Brackrock, G. Brekow, and M. Kreutzbruck, "SAFT and TOFD - A comparative study of two defect sizing techniques on a reactor pressure vessel mock-up," *J. Nondestruct. Eval.*, vol. 32, no. 1, pp. 1–13, 2013.

[63] K. Hoegh and L. Khazanovich, "Extended synthetic aperture focusing technique for ultrasonic imaging of concrete," *NDT E Int.*, vol. 74, pp. 33–42, 2015.

[64] T. Olofsson, "Phase shift migration for imaging layered objects and objects immersed in water," *IEEE Trans. Ultrason. Ferroelectr. Freq. Control*, vol. 57, no. 11, pp. 2522–2530, 2010.

[65] M. H. Skjelvareid, Y. Birkelund, and Y. Larsen, "Internal pipeline inspection using virtual source synthetic aperture ultrasound imaging," *NDT E Int.*, vol. 54, pp. 151–158, 2013.

[66] T. Stepinski, "An Implementation of Synthetic Aperture Technique in Frequency Domain," *IEEE Trans. UFFC*, vol. 54 (7), no. 7, pp. 1399–1408, 2007.

[67] M. H. Skjelvareid, T. Olofsson, Y. Birkelund, and Y. Larsen, "Synthetic aperture focusing of ultrasonic data from multilayered media using an omega-K algorithm," *IEEE Trans. Ultrason. Ferroelectr. Freq. Control*, vol. 58, no. 5, pp. 1037–1048, 2011.

[68] C. H. Frazier and W. D. O'Brien, "Synthetic aperture techniques with a virtual source element," *IEEE Trans. Ultrason. Ferroelectr. Freq. Control*, vol. 45, no. 1, pp. 196–207, 1998.

[69] M. Li, W. Guan, and P. Li, “Improved Synthetic Aperture Focusing Technique with Applications in High-Frequency Ultrasound Imaging,” *Engineering*, vol. 51, no. 1, pp. 63–70, 2004.

[70] T. Scharrer, M. Schrapp, S. J. Rupitsch, A. Sutor, and R. Lerch, “Ultrasonic imaging of complex specimens by processing multiple incident angles in full-angle synthetic aperture focusing technique,” *IEEE Trans. Ultrason. Ferroelectr. Freq. Control*, vol. 61, no. 5, pp. 830–839, 2014.

[71] M. H. Bae and M.-K. Jeong, “A study of synthetic-aperture imaging with virtual source elements in B-mode ultrasound imaging systems,” *IEEE Trans. Ultrason. Ferroelectr. Freq. Control*, vol. 47, no. 6, pp. 1510–1519, 2000.

[72] S. Wu, H. Wu, H. Jin, K. Yang, and E. Wu, “Frequency-domain synthetic aperture focusing technique for immersion testing using focused transducer,” *J. Zhejiang Univ. (Engineering Sci.*, vol. 49, no. 1, pp. 110–115, 2015.

[73] Harumi K., “Computer simulation of ultrasonic in a solid,” *NDT Int.*, vol. 19, no. 5, pp. 315–332, 1986.

[74] W. Lord, R. Ludwig, and Z. You, “Developments in ultrasonic modeling with finite element analysis,” *J. Nondestruct. Eval.*, vol. 9, no. 2–3, pp. 129–143, 1990.

[75] P. Calmon, A. Lhémery, I. Lecœur-Taïbi, R. Raillon, and L. Paradis, “Models for the computation of ultrasonic fields and their interaction with defects in realistic NDT configurations,” *Nucl. Eng. Des.*, vol. 180, pp. 271–283, 1998.

[76] P. Wendling *et al.*, “Non-destructive testing modeling with finite element method

(problem 8)," *2005 Int. Conf. Electr. Mach. Syst.*, vol. 3, no. Problem 8, pp. 2097–2100, 2005.

[77] W. Choi, E. Skelton, M. J. S. Lowe, and R. V Craster, "Development of efficient hybrid finite element modelling for simulation of ultrasonic Non-Destructive Evaluation," no. Ecndt, pp. 2–8, 2014.

[78] P. N. Bilgunde and L. J. Bond, "A 2D finite element simulation of liquid coupled ultrasonic NDT system," in *41st Annual Review of Progress in Quantitative Nondestructive Evaluation*, 2015, vol. 1650, no. September, pp. 1543–1552.

[79] J. Dobson *et al.*, "Finite element analysis simulations for ultrasonic array NDE inspections," *AIP Conf. Proc.*, vol. 1706, 2016.

[80] A. Van Pamel, P. Huthwaite, C. R. Brett, and M. J. S. Lowe, "Numerical simulations of ultrasonic array imaging of highly scattering materials," *NDT E Int.*, vol. 81, pp. 9–19, 2016.

[81] K. J. Kirk and N. Schmarje, "Experimental and simulated performance of lithium niobate 1-3 piezocomposites for 2 MHz non-destructive testing applications," *Ultrasonics*, vol. 53, no. 1, pp. 185–190, 2013.

[82] W. Ke, M. Castaings, and C. Bacon, "3D finite element simulations of an air-coupled ultrasonic NDT system," *NDT E Int.*, vol. 42, no. 6, pp. 524–533, 2009.

[83] S. M. Subair, K. Balasubramaniam, P. Rajagopal, A. Kumar, B. P. Rao, and T. Jayakumar, "Finite element simulations to predict Probability of Detection (PoD) curves for ultrasonic inspection of nuclear components," in *1st International*

Conference on Structural Integrity, 2014, vol. 86, pp. 461–468.

[84] A. Nandy, S. Mullick, and D. Datta, “Numerical simulation of ultrasonic wave propagation in flawed domain,” in *National Seminar & Exhibition on Non-Destructive Evaluation,* 2009, pp. 160–163.

[85] H. Chen, K. Sun, C. Ke, and Y. Shang, “Simulation of ultrasonic testing technique by finite element method,” in *IEEE 2012 Prognostics and System Health Management Conference,* 2012, pp. 1–5.

[86] J. Xu and R. Huanhuan, “Design and finite element simulation of an ultrasonic transducer of two piezoelectric discs,” *J. Meas. Eng.,* vol. 5, no. 4, pp. 266–272, 2017.

[87] P. Calmon, S. Mahaut, S. Chatillon, and R. Raillon, “CIVA: An expertise platform for simulation and processing NDT data,” *Ultrasonics,* vol. 44, no. SUPPL., pp. 975–979, 2006.

[88] J. N. Reddy, *An Introduction to the Finite Element Method*. McGraw-Hill Higher Education, 1994.

[89] D. L. Logan, *A First Course in the Finite Element Methods*. CL Engineering, 2010.

[90] I. Harari, “Dispersion, Pollution, and Resolution,” in *Computational Acoustics of Noise Propagation in Fluids – Finite and Boundary ElementMethods,* S. Marburg and B. Nolte, Eds. Springer, 2008, pp. 37–56.

[91] L. L. Thompson, “A review of finite-element methods for time-harmonic acoustics,”

J. Acoust. Soc. Am., vol. 119, no. 3, pp. 1315–1330, 2006.

[92] P. Rajagopal, E. A. Skelton, W. Choi, M. J. S. Lowe, and R. V. Craster, “A generic hybrid model for bulk elastodynamics, with application to ultrasonic nondestructive evaluation,” *IEEE Trans. Ultrason. Ferroelectr. Freq. Control*, vol. 59, no. 6, pp. 1239–1252, 2012.

[93] J. H. Han, Y. J. Kim, and M. Karkoub, “Wave propagation modeling of fluid-filled pipes using hybrid analytical/two-dimensional finite element method,” *Wave Motion*, vol. 51, no. 7, pp. 1193–1208, 2014.

[94] M. Masmoudi and M. Castaings, “Three-dimensional hybrid model for predicting air-coupled generation of guided waves in composite material plates,” *Ultrasonics*, vol. 52, no. 1, pp. 81–92, 2012.

[95] J. S. Lee, E. Deckers, S. Jonckheere, W. Desmet, and Y. Y. Kim, “A direct hybrid finite element-wave based modelling technique for efficient analysis of poroelastic materials in steady-state acoustic problems,” *Comput. Methods Appl. Mech. Eng.*, vol. 304, pp. 55–80, 2016.

[96] P. Zuo, X. Yu, and Z. Fan, “Numerical modeling of embedded solid waveguides using SAFE-PML approach using a commercially available finite element package,” *NDT E Int.*, vol. 90, no. March, pp. 11–23, 2017.

[97] Y. Shen and V. Giurgiutiu, “Combined analytical FEM approach for efficient simulation of Lamb wave damage detection,” *Ultrasonics*, vol. 69, pp. 116–128, 2016.

[98] F. Shi, W. Choi, E. A. Skelton, M. J. S. Lowe, and R. V Craster, “A time domain finite element boundary integration method for ultrasonic non-destructive evaluation,” *IEEE Trans. Ultrason. Ferroelectr. Freq. Control*, vol. 61, no. 12, pp. 2054–2066, 2014.

[99] G. Hayward, “Unidimensional modeling of 1-3 composite transducers,” *J. Acoust. Soc. Am.*, vol. 88, no. 2, p. 599, 1990.

[100] P. P. Delsanto, T. Whitcombe, H. H. Chaskelis, and R. B. Mignogna, “Connection machine simulation of ultrasonic wave propagation in materials. I: the one-dimensional case,” *Wave Motion*, vol. 16, no. 1, pp. 65–80, 1992.

[101] G. Dobie *et al.*, “Simulation of ultrasonic lamb wave generation, propagation and detection for a reconfigurable air coupled scanner,” *Ultrasonics*, vol. 51, no. 3, pp. 258–269, 2011.

[102] T. Stepinski, “Technique in Ultrasonic Inspection of Coarse Grained Materials,” 2008.

[103] M. a Fischler and R. C. Bolles, “Random Sample Consensus: A Paradigm for Model Fitting with Applications to Image Analysis and Automated Cartography,” 1980.

[104] M. Trelinski, “Application of Ultrasonic Testing Methods for Volumetric and Surface Inspection of CANDU Pressure Tubes,” in *9th European NDT Conference*, 2006, pp. 1–13.

[105] Y. T. Chan, *Wavelet Basics*. Kluwer academic publishers, 1995.

[106] D. Gabor, “Theory of Communication,” *J. Inst. Electr. Eng. - Part III Radio Commun. Eng.*, vol. 93, no. 26, pp. 429–457, 1946.

[107] L. Ülo and H. Helle, *Haar Wavelets: With Applications*, Illustrate. Springer Science & Business Media, 2014, 2014.

[108] A. Erhard, G. Schenk, T. Hauser, and U. Völz, “New applications using phased array techniques,” *Nucl. Eng. Des.*, vol. 206, no. 2–3, pp. 325–336, 2001.

[109] Y. Zhang *et al.*, “Application of Phased Array Ultrasonic Testing Technology on Inservice Wheel,” in *18th World Conference on Nondestructive Testing*, 2012, no. April, pp. 16–20.

[110] A. Mcgilp, J. Dziewierz, T. Lardner, A. Gachagan, and C. Bird, “Inspection of Complex Components using 2D Arrays and TFM,” in *53rd Annual Conference of the British Institute of Non-Destructive Testing*, 2014, pp. 1–9.

[111] O. Casula, G. Toullelan, O. Roy, and P. Dumas, “Ultrasonic Nondestructive Testing of Complex Components with Flexible Phased Array Transducers,” *Ultrasonics*, vol. 38, pp. 131–134, 2000.

[112] J. Zhang, B. Drinkwater, and P. D. Wilcox, “Comparison of ultrasonic array imaging algorithms for nondestructive evaluation,” *IEEE Trans. Ultrason. Ferroelectr. Freq. Control*, vol. 60, no. 8, pp. 1732–1745, 2013.

[113] A. J. Hunter, B. W. Drinkwater, and P. D. Wilcox, “Autofocusing ultrasonic imagery for non-destructive testing and evaluation of specimens with complicated geometries,” *NDT E Int.*, vol. 43, no. 2, pp. 78–85, 2010.

[114] X. L. Han, W. T. Wu, P. Li, and J. Lin, “Application of ultrasonic phased array total focusing method in weld inspection using an inclined wedge,” in *Proceedings of the 2014 Symposium on Piezoelectricity, Acoustic Waves and Device Applications, SPAWDA 2014*, 2014, pp. 114–117.

[115] R. H. Brown, J. Dobson, S. G. Pierce, B. Dutton, and I. Collison, “Quantifying performance of ultrasonic immersion inspection using phased arrays for curvilinear disc forgings,” in *AIP Conference Proceedings*, 2016, vol. 1806, p. 7.

[116] J. Dobson, A. Gachagan, R. O. Leary, A. Tweedie, G. Harvey, and T. Tomasetti, “Finite element analysis of ultrasonic CFRP laminate inspection,” in *55th Annual British Conference of Non-Destructive Testing*, 2016, pp. 1–12.

[117] E. Hulsebos, “Auralization using wave field synthesis,” 2004.

[118] OnScale, “Introduction to FEA,” 2018. [Online]. Available: https://onscaleus.sharepoint.com/sites/External/Shared Documents/Public Examples/Training/OnScale_Training_A.pdf?cid=f98be473-ed53-468d-8c4a-6ce987f17865. [Accessed: 25-Apr-2019].

[119] M. Sutcliffe, M. Weston, B. Dutton, and I. Cooper, “Real-time full matrix capture with auto-focussing of known geometry throuogh dual layered media,” *Bindt*, no. 1, pp. 1–8, 2012.

[120] J. Dziewierz and A. Gachagan, “Computationally Efficient Solution of Snell’s Law of Refraction,” *IEEE Trans. Ultrason. Ferroelectr. Freq. Control*, vol. 60, no. 6, pp. 1256–1259, 2013.

[121] J. Dziewierz, A. Gachagan, N. Lord, and J. A. Mullholland, “An application-specific design approach for 2D ultrasonic arrays,” in *51st Annual Conference of the British Institute of Non-Destructive Testing*, 2012, vol. 2012, p. 8.

[122] T. Stratoudaki, M. Clark, and P. D. Wilcox, “Laser induced ultrasonic phased array using full matrix capture data acquisition and total focusing method,” *Opt. Express*, vol. 24, no. 19, p. 18, 2016.

[123] S. A. Mosey, “Resolution Enhancement of B-Mode Ultrasound Images,” 2013.

[124] W. Kerr, S. G. Pierce, and P. Rowe, “Investigation of synthetic aperture methods in ultrasound surface imaging using elementary surface types,” *Ultrasonics*, vol. 72, pp. 165–176, 2016.

[125] N. R. Center, “Accoustic Properties for Metals in Solid Form,” 2019. [Online]. Available: http://www.ndt-ed.org/GeneralResources/MaterialProperties/UT/ut_matlprop_metals.htm.

[126] M. Ingram *et al.*, “Calibration of Ultrasonic Phased Arrays for Industrial Applications,” in *2017 IEEE SENSORS*, 2017, pp. 1–3.